On the Theory of the Electrohydrodynamic Instability in Nematic Liquid Crystals near Onset

Der Universität Bayreuth
zur Erlangung des Grades eines
Doktors der Naturwissenschaften (Dr. rer. nat.)
genehmigte Abhandlung

vorgelegt von

Martin Treiber

geboren in Nürnberg

1. Gutachter:	Prof. L. Kramer PhD.
2. Gutachter:	Prof. Dr. H. Schamel

Tag der Einreichung:	26. 2. 1996
Tag des Kolloquiums:	02. 7. 1996

Theorie elektrohydrodynamischer Instabilitäten in nematischen Flüssigkristallen nahe des Einsatzpunktes

(Deutsche Zusammenfassung)

In dieser Dissertation untersuche ich einige grundlegende Aspekte strukturbildender Prozesse in Elektrokonvektion nematischer Flüssigkristalle. Das System besteht aus einem Nematen mit negativer oder nur leicht positiver dielektrischer Anisotropie zwischen zwei transparenten Elektroden. In der hier untersuchten Konfiguration ist die lokale Orientierung (der Direktor) des Nematen an den Elektroden planarhomogen ausgerichtet. Legt man eine Wechselspannung an und erhöht die effektive Spannung oberhalb eines bestimmten Schwellenwertes, so setzt eine Instabilität zu einem periodischen Muster ein, welches mit optischen Methoden gemessen werden kann. Die Muster hängen von den Materialparametern, der Schichtdicke und der Frequenz der angelegten Spannung ab. In dieser Arbeit wird der "konduktive Bereich" niedriger Frequenzen behandelt. Das vorgestellte Modell sollte jedoch auch für andere Fälle anwendbar sein.

Ein lange Zeit ungelöstes Problem in Elektrokonvektion ist die Hopfbifurkation zu laufenden Wellen, die man in dünnen Zellen mit relativ niedriger Leitfähigkeit beobachtet. Die übliche hydrodynamische Beschreibung von Helfrich, hier Standardmodell (SM) genannt, behandelt den Nematen wie einen anisotropen ohmschen Leiter und sagt in allen Fällen eine stationäre Bifurkation voraus. Eine andere mit dem SM nicht erklärbare Beobachtung stellt die in manchen Parameterbereichen mit empfindlichen Experimenten gemessene Hysteresis dar.

Dies war die Motivation, in dieser Dissertation eine Verallgemeinerung des SM zu formulieren und anzuwenden, das Modell des schwachen Elektrolyten (Weak Electrolyte Model, WEM).

Im Kapitel 2 gebe ich eine Skizze der Herleitung des Standardmodells mit den Methoden der generalisierten Hydrodynamik. Ziel ist es, die vielen Näherungen auf dem Weg von den erten Prinzipien (hydrodynamische Erhaltungssätze und Bilanzgleichungen sowie die mikroskopischen Maxwell-Gleichungen) zu den Grundgleichungen des SM aufzuzeigen.

Im Kapitel 3 formuliere ich das WEM. Im Gegensatz zu dem im SM angenommenen ohmschen Verhalten werden die Leitfähigkeitseigenschaften des Nematen im WEM durch zwei frei bewegliche Ladungsträgersorten mit entgegengesetzter Ladung beschrieben. Sie entstehen aus Verunreinigungen oder dotierten Molekülen durch eine Dissoziations-Rekombinations-Reaktion und bewegen sich, wie in schwachen Elektrolyten, relativ zu dem sie umgebenden Fluid mit einer Geschwindigkeit, die

proportional zu ihren Mobilitäten und dem elektrischen Feld sind. Die Mobilitäten $\underline{\underline{\mu}}^{\pm}$ der zwei Ladungsträgersorten sind tensoriell mit den Hauptwerten $\mu_{\perp}^{\pm}$ und $\mu_{\parallel}^{\pm}$ senkrecht und parallel zum Direktor. Experimentelle Evidenz für die Wichtigkeit elektrolytischer Effekte gibt es seit mehr als 20 Jahren.

Das WEM drückt die Raumladungsdichte, die auch im SM erscheint, durch die Differenz der Teilchendichten der beiden Ladungsträgersorten aus. Die Migration der Ladungsträger führt zu einer Ladungstrennung und regt ein neues Feld ("Ladungsträger-Mode") an, welches durch die lokale Leitfähigkeit ausgedrückt werden kann. Die lokale Leitfähigkeit ist proportional zu der mit den Mobilitäten $\mu_{\perp}^{\pm}$ gewichtete Summe der Teilchendichten der Ladungsträger.

Das WEM enthält zwei neue dimensionslose Parameter, die nicht im SM enthalten sind,

$$\tilde{\alpha} = \sqrt{\frac{\mu_{\perp}^{+}\mu_{\perp}^{-}\gamma_1\pi^2}{\sigma_{\perp}^{\mathrm{eq}}d^2}}, \quad \tilde{r} = \frac{\tau_d}{\tau_{\mathrm{rec}}} = \frac{\gamma_1 d^2}{K_{11}\pi^2\tau_{\mathrm{rec}}},$$

mit der Rotationsviskosität γ_1 , der Orientierungselastizität K_{11} für Splay-Verzerrungen des Direktors, der Schichtdicke d und der Leitfähigkeit $\sigma_{\perp}^{\mathrm{eq}}$ im Gleichgewicht. Der Mobilitätsparameter $\tilde{\alpha}$ ist proportional zum geometrischen Mittel der Mobilitäten und beschreibt die Stärke der Anregung der Ladungsträger-Mode. Der Rekombinationsparameter ist definiert als die inverse Rekombinationszeit $(\tau_{\mathrm{rec}})^{-1}$ in Einheiten der inversen Direktor-Relaxationszeit $(\tau_d)^{-1}$ und beschreibt die Relaxation der Ladungsträger-Mode zum Gleichgewicht der Dissoziations-Rekombinations-Reaktion.

Im allgemeinen ist der nicht konvektierende Grundzustand des WEM nichttrivial und enthält Randschichten, in denen die Ladungsträger nicht die Gleichgewichtskonzentration haben. Im Kapitel 4 zeige ich, daß diese Randschichten in den meisten relevanten Experimenten vernachlässigt werden können. Dies ist ein wichtiges Ergebnis, da es die Voraussagen des WEM unabhängig von den Randbedingungen für die Ladungsträger macht, die von den komplizierten und unbekannten elektrochemischen Prozessen an den Elektroden abhängen. Experimente unterstützen diese Annahme. Im restlichen Teil dieser Arbeit benutze ich physikalisch saubere isolierende Randbedingungen, bei denen die Ladungsträger die Elektroden nicht durchdringen können.

Im Kapitel 5 linearisiere ich die Grundgleichungen des WEM um den trivialen Grundzustand, d.h. unter Vernachlässigung der Randschichten. Um analytische Resultate zu erhalten, verwende ich Modenapproximationen in niedrigster Ordnung. Zunächst zeige ich, daß man trotzdem quantitativ richtige Ergebnisse erhält. Die lineare Analyse gibt die Schwellenspannung, bei der die Instabilität einsetzt und den Wellenvektor des entstehenden Rollenmusters; im Falle einer Hopfbifurkation zusätzlich die Frequenz der laufenden Wellen.

Das WEM sagt, in Abhängigkeit von den Parametern, sowohl stationäre Bifurkationen als auch Hopfbifurkationen voraus. Die Bedingung für eine Hopfbifurkation

ist in guter Näherung

$$C'(\omega_0)\left(\frac{\pi}{d}\right)^3 K_{11}\sqrt{\frac{\mu_\perp^+\mu_\perp^-}{\gamma_1\sigma_\perp^{\rm eq}}} > \frac{1}{\tau_{\rm rec}},$$

wobei die dimensionslose Funktion $C'(\omega_0)$ von der Grössenordnung 10 ist. Falls die dielektrische Anisotropie negativ ist, nimmt $C'(\omega_0)$ mit der Frequenz ω_0 der angelegten Wechselspannung zu. Unter der Annahme langer Rekombinationszeiten (wofür es für MBBA experimentelle Evidenz gibt), erklärt diese Gleichung qualitativ, warum Hopfbifurkationen nur in dünnen Zellen und für relativ niedrige Leitfähigkeiten von der Grössenordnung $10^{-8}(\Omega\mathrm{m})^{-1}$ beobachtet werden, und daß die Tendenz zu einer Hopfbifurkation mit steigender äußeren Frequenz zunimmt. Die experimentellen Ergebnisse für die Parameter am Kodimension-2 Punkt (der Grenze zwischen stationären und laufenden Rollen) sind konsistent mit einer Rekombinationszeit von 10s.

Ist man im Hopf-Bereich und nicht zu nahe am Kodimension-2 Punkt, so kann man die Rekombinationseffekte vernachlässigen und erhält quantitative Voraussagen für die Hopffrequenz. Die Hopffrequenz ist in diesem Fall durch die linke Seite der letzten Ungleichung gegeben, d.h. sie ist proportional zu d^{-3}, $(\sigma_\perp^{\rm eq})^{-1/2}$, $C'(\omega_0)$, und zu $(\mu_\perp^+\mu_\perp^-)^{1/2}$. Das geometrische Mittel $(\mu_\perp^+\mu_\perp^-)^{1/2}$ der Mobilitäten ist der einzige nicht im SM enthaltene Parameter.

Quantitative Vergleiche werden mit Experimenten an MBBA und I52 durchgeführt. Da nicht alle Materialparameter des SM für I52 bekannt sind, werden diese zunächst bestimmt, indem man die Voraussage des WEM an die gemessenen Thresholdspannungen und Rollenwinkel (Winkel der Rollenachsen zur Gleichgewichtsorientierung) als Funktion von ω_0 für verschiedene Temperaturen anpaßt. Es ist möglich, dafür das SM zu nutzen, da es nahezu den gleichen Threshold und den gleichen Rollenwinkel voraussagt wie das WEM.

In beiden Materialien stimmen die vorausgesagte mit den gemessene Hopffrequenzen überein, falls $(\mu_\perp^+\mu_\perp^-)^{1/2}$ von der Grössenordnung $10^{-10}\mathrm{m}^2/(\mathrm{Vs})$ ist. Dies ist konsistent mit unabhängigen Messungen der Mobilitäten. Nachdem man die Mobilität an einen Datenpunkt angepaßt hat, sind die Voraussagen für andere Werte von ω_0 und d fest. Die Figuren 5.9 - 5.11 zeigen, daß die Voraussage des WEM und die gemessenen Werte in weiten Parameterbereichen um typischerweise weniger als 10 % differieren. Insbesondere variierte man in den Experimenten d^3 um den Faktor 8 (zwei verschiedene Zellen), $\sqrt{\sigma_\perp}^{\rm eq}$ um den Faktor 2.2 (Variation der Temperatur), und $C'(\omega_0)$ um den Faktor 2.5 (Variation der Frequenz der Wechselspannung). In MBBA ändert sich die Hopffrequenz viel rapider mit steigendem ω_0. Die Figuren 5.7 und 5.8 zeigen, daß das WEM diesen Anstieg nahezu quantitativ in einem Bereich beschreibt, der mehr als einen Faktor 10 in der Hopffrequenz umfaßt. Das verschiedene Verhalten der beiden Materialien läßt sich auf die dielektrischen Anisotropie zurückführen, die in MBBA viel negativer ist.

Es stellte sich heraus, daß der Mechanismus der Hopfbifurkation ähnlich den Mechanismen anderer Systeme ist, die eine Hopfbifurkation zeigen (Figur 12): Der für die Instabilität verantwortliche primäre Carr-Helfrich-Mechanismus ist an eine sekundäre stabilisierende Rückkopplungsschleife angebunden, die vom langsam relaxierenden Ladungsträgerdichte-Feld erzeugt wird. In vielerlei Hinsicht ist die Rolle des Ladungsträger-Feldes analog zu der des Konzentrationsfeldes in thermischer Konvektion in binären Mischungen.

In Kapitel 6 wird die schwach-nichtlineare Analyse der wichtigsten Terme der WEM - Grundgleichungen durchgeführt. Ein wichtiges Ergebnis sind die Koeffizienten einer eindimensionalen komplexen Ginzburg–Landau Gleichung (CGL), die die Dynamik der Einhüllenden links- oder rechtslaufender Wellen beschreibt. Die schwach-nichtlineare Analyse sagt voraus, daß die für lange Rekombinationszeiten $\tau_{\rm rec}$ erwartete Hopfbifurkation immer kontinuierlich (vorwärts) ist und daß die nichtlineare Sättigung stärker ist als im SM, d.h., die Amplituden sind bei gleichem Abstand vom Threshold kleiner. Für kleineres $\tau_{\rm rec}$ wird die Bifurkation stationär und im allgemeinen (schwach) hysteretisch. Für noch kürzere Rekombinationszeiten wird die Bifurkation wieder kontinuierlich und im Grenzfall $\tau_{\rm rec} \to 0$ geht das WEM in das SM über (Figur 6.4).

Dies stimmt qualitativ mit den I52 Experimenten überein. Schlußfolgernd kann gesagt werden, daß drei verschiedene Voraussagen zu einer Rekombinationszeit in der Größenordnung 10-20s führen: Die Amplitude des nichtlinearen Zustands nach dem Sprung im hysteretisch-stationären Bereich, die Abnahme der gemessenen Frequenz der laufenden Wellen mit der angelegten Spannung im Hopf-Bereich, und die (lineare) Bedingung für eine Hopfbifurkation.

Zwei Experimente an MBBA zeigen ein verwirrenderes Verhalten. Die Korrelationen *subkritischer* Fluktuationen lassen sich nur mit einer oszillierenden linearen Dynamik erklären, aber die deterministische Bifurkation ist stationär-hysteretisch. Ich zeige, daß folgende Interpretation konsistent mit dem WEM ist: Die Hopfbifurkation ist *tasächlich* kontinuierlich, aber es erfolgt ein Sprung zu einem stationären nichtlinearen Zustand bei einer Spannung, die experimentell nicht von der Threshold-Spannung unterschieden werden kann. Aktuelle Experimente am Nematen Phase 5 bestätigen diese Vermutung.

Die gemessene Fluktuationsstärke der oben erwähnten subkritischen Fluktuation war nur 30% bis 40% höher, als man es von einer naiven Abschätzung mit Hilde des Gleichverteilungssatzes für *thermische* Fluktuation des Direktors (unter Vernachlässigung der Fluktuationen der Ladungsträger) enerwarten würde. Kann dieses Ergebnis, nach dem die thermischen Fluktuationen in diesem System nahezu die eines Gleichgewichtssystems sind, verstanden werden? Um ein besseres Verständnis thermischer Fluktuationen in diesen und anderen hydrodynamischen Systemen zu erhalten, wende ich im Kapitel 7 Landaus Methode hydrodynamischer Fluktuationen

auf die Grundgleichungen des SM an. Das Ergebnis ist, das, in der Tat, die Direktorfluktuationen mit einem geeignet verallgemeinertem Gleichverteilungssatz bestimmt werden können, und daß die Fluktuationen der Raumladungen nur zu 3% bzw. zu 10 % in den beiden Systemen beitragen. Das WEM würde zu einen Faktor 2 führen, da man *zwei* kritische Moden (links-und rechtslaufende Wellen) hat. Dieser Faktor wird jedoch kompensiert durch die Korrelationszeit im Nenner von Gl. (7.41), die nach der Voraussage des WEM doppelt so lang ist wie im SM. Diese Zeit wurde ebenfalls experimentell bestimmt. Sie stimmt in beiden Experimenten mit dem WEM, nicht mit dem SM, überein.

Im abschließendem 8. Kapitel versuche ich, Hinweise auf interessante, noch offene Probleme zu geben. Die Koeffizienten der CGL wurden in dieser Dissertation für den einfachst-möglichen Fall der links oder rechtslaufende Wellen in einer Dimension ermittelt. Im allgemeinen muß man die Kopplung der links- und rechtslaufenden Wellen (für Schrägrollen gibt es sogar vier lineare kritische Moden), sowie möglicherweise die Kopplung an andere langsam relaxierende Moden, berücksichtigen. Gekoppelte Gleichungen dieser Art können möglicherweise das in Experimenten an I52 beobachtete raumzeitlich Chaos *lokalisierter* Zustände erklären. Besonders faszinierend ist die Möglichkeit, das ebenfalls beobachtete raumzeitliche Chaos *ausgedehnter* Zustände auf die Benjamin–Feir Instabilität der CGL zurückzuführen. Damit könnte man die Voraussagen der nach der Kuramoto-Sivashinsky-Gleichung einfachsten generischen Gleichung für raumzeitliches Chaos quantitativ mit Experimenten vergleichen.

Abstract

In this thesis I study some fundamental aspects of pattern formation in electroconvection of nematic liquid crystals. The system consists of a nematic liquid crystal with negative or only mildly positive dielectric anisotropy sandwiched between two transparent electrodes and aligned planar-homogeneously. Some electric conductivity is needed. When applying an AC voltage and increasing its rms value above a certain threshold, there is an instability leading to a spatially periodic state which can be measured by optical methods. The patterns depend on the material parameters of the nematic, the thickness d of the layer, and on the applied frequency. I treat the case of relatively low frequencies, i.e., the so-called conductive range. The physical model introduced in this thesis should be valid for other cases, too.

A long-standing problem in electroconvection is the Hopf bifurcation leading to travelling rolls, observed in thin cells with relatively low conductivity. The standard hydrodynamic description ("Standard model" SM) going back to Helfrich where the nematic is treated as an anisotropic ohmic conductor, always predicts a stationary bifurcation leading to stationary rolls. Also the inclusion of additional effects like flexoelectricity has up to now not improved the situation. Similarily, the small hysteresis observed in very sensitive experiments in some parameter ranges cannot be understood with the standard description, which always predicts a continuous bifurcation.

This gave rise to develop and explore in this thesis a generalization of the SM, the Weak Electrolyte Model (WEM).

In Chapter 2, I review the derivation of the SM with the methods of generalized hydrodynamics. There are several approximations along the path from the "first principles" (the hydrodynamic conservation laws and balance equations, and the microscopic Maxwell equations) to the basic equations of the SM. This chapter is intended to show these approximations.

In Chapter 3, I formulate the WEM. In contrast to the ohmic behaviour assumed in the SM, the WEM describes the conductive properties of the nematic by the dynamics of two species of oppositely charged freely mobile ions. They originate from impurities or dopants by a dissociation-recombination reaction and migrate relative to the fluid, as in usual weak electrolytes, with velocities proportional to their mobilities and proportional to the electric field. The ionic species are assumed to have constant, possibly different, mobility tensors $\mu^{\pm}$ with principal values perpendicular and parallel to the director, $\mu_{\perp}^{\pm}$ and $\mu_{\parallel}^{\pm}$, respectively. Experimental evidence for the relevance of weak electrolytic effects in nematics with long recombination times τ_{rec} actually goes back more than 20 years.

The WEM expresses the total space-charge density, which already appears in the SM, as the difference of the number densities of the two ionic species. In addition, migration leads to a charge separation and gives rise to a new field, which can be expressed in terms of the local conductivity $\sigma_\perp(\boldsymbol{r},t)$ ("charge-carrier mode") proportional to the sum of the number densities weighted with the mobilities $\mu_\perp^+$ and $\mu_\perp^-$. The WEM contains two new dimensionless parameters,

$$\tilde{\alpha} = \sqrt{\frac{\mu_\perp^+ \mu_\perp^- \gamma_1 \pi^2}{\sigma_\perp^{\mathrm{eq}} d^2}}, \quad \tilde{r} = \frac{\tau_d}{\tau_{\mathrm{rec}}} = \frac{\gamma_1 d^2}{K_{11}\pi^2 \tau_{\mathrm{rec}}}.$$

Here, γ_1 is a rotational viscosity, K_{11} the splay constant, d the layer thickness, and $\sigma_\perp^{\mathrm{eq}}$ the conductivity in the equilibrium state. The mobility parameter $\tilde{\alpha}$ is proportional to the geometric mean of the mobilities $\mu_\perp^+$ and $\mu_\perp^-$ and describes the rate at which the charge-carrier mode is excited. The recombination parameter $\tilde{r}$ is the inverse recombination time τ_{rec} in units of the inverse of the director relaxation time τ_d, and describes the relaxation of the charge-carrier mode towards equilibrium $[\sigma_\perp(\boldsymbol{r},t) = \sigma_\perp^{\mathrm{eq}}]$ by the dissociation-recombination reaction.

Apart from the case of very special boundary conditions, the non-convecting (motionless) basic state of the WEM is nontrivial and implies boundary layers of the charge carriers. I investigate these boundary layers in Chapter 4 and conclude that they can be neglected in the relevant experiments. This is an important result since it means that the predictions of the WEM are rather independent of the boundary conditions for the charge carriers, involving, in general, the complicated and unknown electrochemistry of the electrodes. This conclusion is supported by experimental evidence. In addition, the linear and weakly-nonlinear analysis in the following chapters is simplified considerably by this assumption. In the rest of this work, I use physically clean "blocking" boundary conditions where the charge carriers cannot cross the electrodes.

In Chapter 5, I linearize the WEM around the trivial basic state (without boundary layers) using lowest-order expansions for the space and time dependence of all fields. This allows for an analytic approach. The analysis gives the onset of instability and the wavevector and frequency (in the case of the Hopf bifurcation) of the new solution describing a stationary or travelling pattern. The possibility for a Hopf bifurcation can be seen quite easily. A first version of this analysis restricted to normal rolls (roll axis perpendicular to the homogeneous alignment) has been published [1].

The WEM predicts both, Hopf and stationary bifurcations, depending on the parameters. The condition for a Hopf bifurcation is, in a good approximation,

$$C'(\omega_0)\left(\frac{\pi}{d}\right)^3 K_{11}\sqrt{\frac{\mu_\perp^+ \mu_\perp^-}{\gamma_1 \sigma_\perp^{\mathrm{eq}}}} > \frac{1}{\tau_{\mathrm{rec}}},$$

where the dimensionless function $C'(\omega_0)$ is of order 10. It increases with the external frequency ω_0 of the AC voltage if the dielectric anisotropy is negative, and depends otherwise only on scaled material parameters of the SM. Assuming long recombination times of the order of seconds, this equation explains why travelling rolls are observed for all external frequencies in thin cells and for liquid crystals with a relatively low equilibrium conductivity $\sigma_\perp^{\rm eq}$ [of the order of $10^{-8}(\Omega{\rm m})^{-1}$], while they are observed only for higher frequencies in an intermediate range of $\sigma_\perp^{\rm eq}$ and d. The precise value and the temperature dependence of the recombination time $\tau_{\rm rec}$ are unknown; so no quantitative predictions of the system parameters at the transition from the Hopf bifurcation to the stationary one (codimension-two point) could be made. The experimental findings on the nematics MBBA and I52 (see p. 5 or Ref. 2 for the chemical formula for this compound) were consistent with $\tau_{\rm rec}$ of the order of 10 s.

In the Hopf regime and not too near to the codimension-two point, the recombination effects drop out (one can set $\tau_{\rm rec} = \infty$ in the formulas) enabling a quantitative experimental test of the predicted oscillation frequency of the travelling rolls (Hopf frequency). In this case, the Hopf frequency is given by the left-hand side of the previous equation (see also Eq. (39) in Ref. [1]), i.e., it is proportional to d^{-3}, $(\sigma_\perp^{\rm eq})^{-1/2}$, $C'(\omega_0)$, and to $(\mu_\perp^+\mu_\perp^-)^{1/2}$. Here the geometric mean $(\mu_\perp^+\mu_\perp^-)^{1/2}$ is the only parameter that is not contained in the SM.

Quantitative comparisons with experiments are made for MBBA and I52. For I52, some material parameters of the SM are not known. They were determined by fitting the prediction of the SM to the experimental results for the threshold voltage and the roll angle (with respect to the homogeneous alignment) as function of the AC frequency ω_0 at different temperatures. It is possible to use the SM since it predicts nearly the same threshold and roll angle as the WEM.

Fits to the measured Hopf frequency give values for $(\mu_\perp^+\mu_\perp^-)^{1/2}$ of the order of $10^{-10}{\rm m}^2/({\rm Vs})$ in MBBA and I52, consistent with published data. With $(\mu_\perp^+\mu_\perp^-)^{1/2}$ fitted for each temperature to one data point, the Figures 5.7 - 5.11 (see also Figs. 2a and 2b in Ref. [2]) show for I52, that the difference between the WEM prediction and the measured values differed typically by less than 10% for changes of d^3 by a factor of 8 (two different cells), of $(\sigma_\perp^{\rm eq})^{1/2}$ by a factor of 2.2 (variation of the temperature), and of $C'(\omega_0)$ by a factor of 2.5 (variation of the external frequency). In MBBA, the Hopf frequency increases much faster with ω_0. In the Figures 5.7 and 5.8 it is shown that the WEM predicts this increase nearly quantitatively in a range covering more than a factor of 10. The different behaviour of the two materials is mainly due to the different dielectric anisotropies: $\epsilon_a \approx -0.52$ for MBBA, $\epsilon_a \approx -0.056$ (30°C)$\cdots$0 (60°C) for I52.

The mechanism of the Hopf bifurcation is found to be similar to that of other pattern-forming systems showing a Hopf bifurcation: a primary destabilization feedback mechanism is coupled to a stabilizing second feedback cycle which is here me-

diated by the charge-carrier field, with a slow intrinsic time scale (Figure 5.12). In many aspects, the σ field is reminiscent of the slow concentration field of thermal convection in binary fluid mixtures.

Chapter 6 is devoted to the weakly-nonlinear analysis of the most important contributions of the WEM equations. I calculate approximate analytic expressions of the coefficients of a one-dimensional complex Ginzburg–Landau equation (CGL) describing the dynamics of the envelope (including of course the actual amplitude) of, say, the left-travelling waves. The weakly-nonlinear analysis predicts that the Hopf bifurcation expected for long recombination times $\tau_{\rm rec}$ is always continuous and that the nonlinear saturation is stronger than in the SM (smaller amplitude). Decreasing $\tau_{\rm rec}$, the bifurcation becomes stationary and, in general, also (slightly) hysteretic. For even shorter recombination times, it becomes continuous (Figures 6.4 and 6.5) and in the limit $\tau_{\rm rec} \to 0$, the WEM approaches the SM.

This agrees qualitatively with the experiments on I52. It can be concluded that three different predictions: the amplitude of the nonlinear state after the jump in the stationary-hysteretic regime, the decrease of the oscillation frequency on increasing the voltage in the Hopf regime, and the (linear) condition for a Hopf bifurcation, agree with the experiments assuming a recombination time of 10–20s.

Two experiments with MBBA cells showed a more puzzling behaviour. The linear dynamics assessed by *subcritical* fluctuations is oscillatory, but the deterministic bifurcation seemed to be stationary-hysteretic. I show that the following interpretation is compatible with the WEM: the Hopf bifurcation is actually continuous, but a subsequent jump to a nonlinear state takes place at a value of the control parameter which can not be distinguished experimentally from the threshold value. Recent experiments on the nematic mixture Merck Phase 5 confirm this interpretation.

The oscillatory behaviour (Hopf bifurcation) in the two MBBA eperiments mentioned above was obtained from the correlation function of fluctuations below threshold, which anticipate the linear-deterministic dynamics. The strength of the fluctuations was observed to be (only) 30% to 40% higher than expected from naive estimates based on the equipartition theorem for thermal fluctuations of the director only (without considering charge-density fluctuations). Can this result which indicates that thermal fluctuations are nearly those of an equilibrium system, be understood? To give a better understanding of thermal fluctuations in this (and other hydrodynamic nonequilibrium systems) I apply in Chapter 7 the Landau approach of fluctuating hydrodynamics to the SM equations. The conclusion is that a "generalized equipartition theorem can indeed be applied to the director fluctuations and that charge-density fluctuations indeed contribute in the two experiments only by, respectively, 3% and 10% [3,4]. Using the WEM would lead to a factor of two (two critical left- and right travelling modes instead of one stationary mode) that is cancelled by the correlation time in the denominator of Eq. (7.41), which the WEM

predicts to be twice as long as in the SM. The correlation time, determined in the experiments by the correlation function as well, agrees with the WEM, and not the SM.

A concluding chapter attempts to give some directions for future research. The coefficients for the CGL were derived in this thesis for the most simple case of either left- or right-travelling waves. However, one has to consider the interaction of degenerate critical modes, and, for finite amplitudes, also slowly-relaxing modes excited by the nonlinearities. Coupled equations for these modes can possibly explain quantitatively the spatio-temporal chaos (STC) of *localized* states observed in I52 at lower temperatures. The CGL predicts also a small region where travelling waves are unstable to long-wavelength modulations (Benjamin–Feir instability). It would be fascinating to explain the amplitude-STC of *extended* states observed in I52 at higher temperatures, by a CGL in the Benjamin–Feir unstable range. This would enable a quantitative experimental comparison with the predictions of one of the most simple and generic equations producing STC.

[1] M. Treiber and L. Kramer, Mol. Cryst. Liq. Cryst **261**, 311 (1995).

[2] M. Dennin, M. Treiber, L. Kramer, G. Ahlers, and D. Cannell, Phys. Rev. Lett. (1996), in press.

[3] M. Treiber and L. Kramer, Phys. Rev. E **49**, 3184 (1994).

[4] M. Treiber, Thermal Fluctuations in Pattern Forming Instabilities, in L. Kramer and A. Buka, editors, *Pattern Formation in Liquid Crystals*, Springer, (NY 1996).

0

Chapter 1

Introduction

1.1 Nonlinear dynamics and pattern formation

> *I am an old man now and when I will die and go to Heaven I hope that two things will be understood in the future. One is quantum electrodynamics and the other turbulent motion. With respect to the first, I am really rather optimistic.*
>
> (Said allegedly by the British Mathematican and Physicist Sir Horace Lamb, 1932.)

There are three directions in which physics pushes the limits to explore nature: towards the very large and fast, towards the very small, and towards the complex. With respect to the first two directions, one leaves the familiar space of the intermediate dimensions where our intuition is formed. Relativity and the uncertainty relation are two of the unexpected and counter-intuitive facts with which nature provided us.

Starting about thirty years ago, the third direction became more and more important and gave rise to a new field of physics: nonlinear dynamics, the study of nonlinear systems and equations. In this case one does not leave the familiar dimensions, and the underlying (classical) physical laws are well known. Nevertheless, also here one is lead to unexpected, often counter-intuitive, and therefore fascinating phenomena. The central role is played by the inherent nonlinearity of the systems, so that our basic concept of superposition cannot be applied. The system as a whole behaves differently from "the sum of its parts" [1]; qualitatively new phenomena emerge and its long-term behaviour may become unpredictable, even if the system is governed by deterministic equations.

This was already known by Poincaré [2] who showed that certain Hamiltonian systems cannot be separated into modes evolving independently from each other,

as is the case for any linear system. It took more than seventy years before the meteorologist Lorenz applied these ideas to dissipative systems. He showed that even a set of three ordinary differential equations, the so-called Lorenz model, can lead to irregular motion and to a sensitive dependence on the initial conditions. He coined the word "butterfly effect" meaning that even the motion of a single butterfly can influence the global evolution of the weather in the future.

Nowadays this behaviour is referred to as "deterministic chaos" [3] and, supported by the increase in computer power, the dynamics of low dimensional nonlinear systems (ordinary differential equations or iterated discrete maps) is fairly well understood. Typically, the behaviour depends on control parameters which, in the physical context, are external forces driving the system out of equilibrium. For low values the long-term behaviour of the system is stationary, described mathematically by an fixed point. Upon increasing the stress, many systems react with a cascade of increasingly complex states and eventually the dynamics is chaotic and is described by a fractal "strange attractor" [4]. There are at least three generic routes to chaos, the Ruelle–Takens route involving a few Hopf bifurcations [5], the intermittency route of Pomeau and Manneville [6] and the Feigenbaum scenario with an infinite cascade of period doublings [7]. Often it is even possible to reconstruct the attractor, or even the dynamics of a low-dimensional chaotic system, by measuring a time series of only one dynamical variable [8].

The next logical step towards complexity consists of the study of spatially extended nonlinear dissipative systems described by partial differential equations or high-dimensional discrete models. As in the low-dimensional case, typical systems are in an ordered (often featureless) state for low external stress. In reaction to an increasing control parameter, the systems develop spatially and spatio-temporally ordered structures, and eventually, spatio-temporal chaos or turbulence [9]. While to date little is known about these two "Holy Grails" of the field [9] we have an increasing number of analytical and numerical tools to investigate the spatio-temporal structures appearing spontaneously for an external stress higher than that for the unstructured state and lower than that for chaos, the domain of pattern formation [9, 10].

Patterns are ubiquitous in nature. Some examples are water waves driven by wind [11], cloud formations, sand dunes [12], the ripples appearing in stream beds and on dirt roads (the infamous "wash boards"), erosion structures, and snow flakes as well as other interfacial phenomena. Biological examples are population distributions [13], stripes and spots on animal coats [9, 14] or the (partially fractal) shape of fern leaves [15]. Geophysical examples include convection structures of the mantle of

the earth [16] or of the atmospheres of the large planets [17]. Other examples may lead to practical applications like modelling the stop-and-go waves of traffic flow on motorways [18], suppressing the spiral waves occurring in some heart deseases [19], or controlling chaos in general [8].

1.2 Hydrodynamic systems

For a quantitative understanding of pattern formation, one needs systems where (i) the basic equations describing the macroscopic dynamics are well established, and that (ii) allow reproducible precision experiments. The first point is best fulfilled for hydrodynamic systems. The second point restricts the investigations to rather few paradigmatic "standard" systems. It would be also useful to find general aspects not depending on particular systems. Such universal behaviour is typically found near the threshold to the first instability, so this range is particularly interesting.

The most prominent system of pattern formation is probably thermal convection in a simple fluid heated from below, known as Rayleigh–Bénard convection (RBC). RBC was investigated as early as 1900 [20, 21] and is the isotropic test system for natural phenomena such as cloud streets and convection phenomena in the mantle of the earth, but also for the transition to turbulence. For a review see Ref. [9] and the references therein. While the classic RBC predicts stationary patterns, variations like thermal convection in binary fluid mixtures [22], or in nematic liquid crystals [23, 24], show in some parameter ranges a bifurcation to oscillatory patterns (see also Chapter 5.6).

Another test system showing a rich scenario of patterns is the Taylor-Couette system where a fluid is confined to a gap between two concentric cylinders which rotate with different angular velocities [9]. In contrast to the buoyancy force of RBC, the instability is driven by centrifugal forces. From all systems, it is probably that system, whose basic equations (Navier–Stokes equations with no-slip boundary conditions) describe the dynamics most accurately.

The paradigma for anisotropic systems is electrohydrodynamic convection (EHC) in nematic liquid crystals (NLCs). The main advantages of EHC with respect to other systems are the convenient time scales in the experiments, many accessible control parameters, and the large aspect ratio (typically, of the order 1000), that can be realized experimentally. The main disadvantage of EHC are the complicated structure of the basic equations, the many (often unknown) material parameters, and the obviously incomplete standard hydrodynamic description. This last point is the motivation for most of the work in this thesis.

1.3 Electrohydrodynamic convection

Nematic liquid crystals

The liquid-crystal state is sometimes called the fourth state of matter [25]. In fact, liquid crystals posses properties of both crystals and liquids. In nematic liquid crystals (nematics, NLC), considered exclusively in this work, the crystal-like properties come from the long-range uniaxial orientational order of the rod-like (or disc-like) molecules. The positional order of the centers of gravity of the molecules is short ranged which means, that the NLC can flow like a liquid.

I will consider the hydrodynamic description [26, 27, 25] which is based on local averages visualized by fluid elements. These fluid elements contain many individual molecules, so local averages can be introduced, but they are small enough to allow for a continuum treatment on the scale of the entire fluid.

The molecules of the NLC are not aligned perfectly. The degree of alignment is denoted by the scalar order parameter S [25], and the locally-averaged orientation by the director field $\boldsymbol{n}$. Strictly speaking, $\boldsymbol{n}$ is not a vector, but it can be represented as an unit vector with an additional inversion symmetry (the molecular alignment does not distinguish right from left). While the order parameter can be assumed to remain constant for the phenomena studied in this work, the dynamics of the director field must be incorporated into a hydrodynamic description of a NLC.

The orientational order is associated with an orientational elasticity, i.e., the NLC responds with a restoring force upon distortions of the director field. In addition, the orientational order makes the material properties uniaxially anisotropic. The material properties are described by tensors depending on $\boldsymbol{n}$ which will be given in Chapter 2. Since the order parameter depends on the temperature (especially near transition to other phases [25]), the relative anisotropy of the material tensors depends on the temperature as well. For the viscosities and conductivities, an Arrhenius-like temperature dependence is superimposed [28, 29] that is usually much stronger and will be important for comparing the proposed model with experiments (Chapter 5.5).

The NLCs used in the relevant experiments are the standard substance *4-methoxybenzylidene4′-n-butyl-aniline* (MBBA), and the newly introduced material *4-ethyl-2-fluoro-4′-[2-(trans-4-pentylcyclohexyl)-ethyl] biphenyl* (I52). I52 was found to be a good material for EHC experiments [30, 31, 32] with some properties complementary to that of MBBA. MBBA is the only room-temperature nematic with negative dielectric anisotropy where all material parameters have been measured; in I52, some parameters had to be fitted, see Appendix A.1. In the usual prepa-

rations of cells MBBA develops a sufficiently high electric conductivity for EHC [$\approx 10^{-8}(\Omega\mathrm{m})^{-1}$] while I52 must be doped with an ionizable dopant [30].

The experimental system

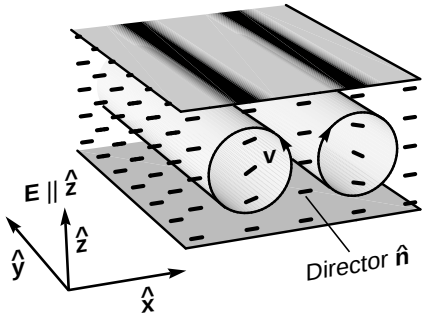

Fig.1.1a: Cell geometry for planar EHC with a section of a roll pattern $\mathbf{v}$ = velocity

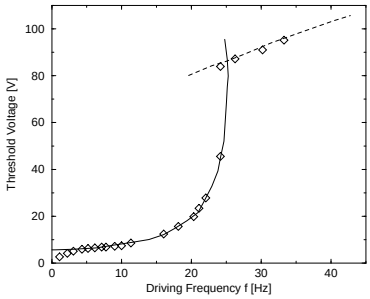

Fig.1.1b: Typical threshold curves for MBBA; — : conductive range, - - - : dielectric range.

The system consists of a nematic liquid crystal with negative or only mildly positive dielectric anisotropy sandwiched between two glass plates with transparent electrodes. When applying an AC voltage (typically, $\overline{V} = 10$V with a frequency of $10 \cdots 1000$ Hz) and increasing the rms $\overline{V}$ above a certain threshold, the non-convecting basic state becomes unstable in favour of a periodic state.

Throughout this work, I consider a planar-homogeneous alignment of the director at the electrodes inducing the anisotropy of the system and defining the x axis, see Fig. 1.1a. A very detailed description of the experimental setup dealing also with the intricacies in making cells of I52, is given in the PhD thesis of M. Dennin [31]; see also [30].

Patterns

The driving force for EHC is the electric volume force acting on space charges that are generated by initial director distortions together with a positive conductivity anisotropy. This mechanism was suggested by Carr [33] and incorporated into a one-dimensional model by Helfrich [34]. See the Chapters 5.3 and 5.6 for a discussion.

The first experiments of Williams and Kapustin [35, 36] were interpreted to show normal rolls, i.e., the roll axis is perpendicular to the equilibrium alignment of the director. Later on, one observed oblique rolls [37] where the roll axis is tilted with respect to the y direction (Fig. 1.1a).

Most notable are travelling rolls which have been observed as early as 1978 [38]. They were found in a broad parameter range in different NLCs (MBBA, Phase 5, and I52) by different groups [39, 40, 41, 30, 42] and seem to be generic for relatively thin and clean cells. In most experiments, the bifurcation appears to be continuous (forward), but in very sensitive experiments, one found a small hysteresis [43, 39].

Finally, EHC is the best (and, until recently, the only) system where thermal fluctuations could be observed directly [39, 44]. For an overview of some experiments, see Ref. [40].

Theoretical description

The one-dimensional model of Helfrich was generalized to include AC driving [45], to two dimensions [46], and finally to a fully three-dimensional treatment [47, 48, 49]. In this work, the standard hydrodynamic description [26, 27, 25] together with the three-dimensional formulation for EHC is referred to as the Standard Model (SM). For a review, see, e.g., [50, 24] or, for the older works, the books of Blinov [28] and Chandrasekhar [51].

The linear analysis in Chapter 5 results in an eigenvalue equation for the growth rate $\lambda(\boldsymbol{q}, R) = \sigma(\boldsymbol{q}, R) \pm i\omega(\boldsymbol{q}, R)$ of periodic perturbations with the wavevector $\boldsymbol{q} = (q_x, q_y)$. The growth rate depends on the primary control parameter $R \propto \overline{V}^2$ describing the external driving and on the AC frequency ω_0. The real part σ of one of the eigenvalues crosses zero upon increase of R at fixed $\boldsymbol{q}$ beyond a value $R_0(\boldsymbol{q})$, while the real parts of the other eigenvalues with the same wavevector $\boldsymbol{q}$ remain negative. The neutral surface $R_0(\boldsymbol{q})$ is defined, for any $\boldsymbol{q}$, by the condition that the most unstable mode has a vanishing growth rate, $\sigma(\boldsymbol{q}, R_0) = 0$. Minimizing $R_0(\boldsymbol{q})$ with respect to $\boldsymbol{q}$ gives the threshold $R_c = R_0(\boldsymbol{q}_c)$ with the critical wavevector $\boldsymbol{q}_c$ and the critical frequency (Hopf frequency) $\omega_c = \omega(\boldsymbol{q}_c, R_c)$ of the pattern.

In the SM, ω_c is always equal to zero indicating a stationary bifurcation (this is of course not accidental, but consitutes a generic case in systems with reflection symmetry). The z and time symmetries of the mode becoming first unstable depends on ω_0. I treat the case of relatively low frequencies, i.e., the so-called conductive range (solid curve in Fig. 1.1b). The modes for higher frequencies are called dielectric modes (dashed in Fig. 1.1b).

In the case of a nonzero ω_c, two degenerate oscillatory modes with frequency $\pm\omega_c$ become unstable simultanously at threshold, which is the definition for a Hopf bifurcation (see, e.g., [10]). The two modes can be identified as the left- and right travelling waves. Even with extreme values of the material parameters and inclusion of flexoelectric terms one never found a Hopf bifurcation as first instability in the

SM [52]. This gave rise to develop and explore in this thesis a generalization of the SM, the Weak Electrolyte Model (WEM).

Chapter 2

The standard (Helfrich-Carr) description of electroconvection

The Helfrich-Carr model of electroconvection combines the static [53] and dynamic [26, 27] macroscopic description of NLCs with the quasi-static Maxwell equations under the assumption of an ohmic conductivity. Since nearly all past theoretical investigations are based on this model (see Ref. [50] and the references therein), it is referred to as the Standard Model (SM).

In this chapter I give the essential steps of the derivation of the SM. The main purpose is to show the various approximations and to discuss their possible relevance for a mechanism leading to travelling rolls.

In the first section, I discuss the choice of the macroscopic fields. One has to make sure that they contain all slow processes involved in the instability mechanism. In the following section, I give the canonical derivation in the framework of generalized hydrodynamics [54, 55, 56] (for more details see [57, 58]). Impatient readers may skip these two sections and go directly to Chapter 2.3 which gives a self-contained description of the SM in the form used throughout the rest of this work.

2.1 Macroscopic variables

In generalized hydrodynamics, one distinguishes three types of slow fields [55].

- Conserved quantities. They cannot be created or destroyed locally, so their dynamics is of the form $\partial_t X + \boldsymbol{\nabla} \cdot \boldsymbol{J}_X = 0$ where $\boldsymbol{J}_x$ is the current associated to X. In EHC as in other hydrodynamic systems, the components of the

momentum density $g_i = \rho_m v_i$ [1] are such variables. Its currents define the tensor T_{ij} of the momentum flux, which is equal to the negative stress tensor.

- Broken-symmetry variables. They break a continuous symmetry but are not conserved, so their dynamical equations are of the form $\partial_t X + Y_X = 0$ where Y_X is sometimes called a "quasi current" [58]. Since, according to the Noether theorem, outer symmetries are related to conservation laws, this type of field can exist only in complex fluids with some inner symmetries. In NLCs without external fields, the director breaking the local rotational symmetry is such a field.

- Slowly relaxing variables. In contrast to the first two classes they are not truly hydrodynamic in that they relax in the homogeneous limit in a finite time. Nevertheless they cannot be neglected in EHC (and other confined systems), if their relaxation time is comparable to that of hydrodynamic fields with *nonzero* wavenumbers varying at length scales of the order of the distance d between the two electrodes. The dynamical equation is of the same form as that for broken-symmetry variables but, in contrast to the former, the static contribution to the energy density does not vanish in the homogeneous limit. The component of the director parallel to an electric (or magnetic) field is such a variable.

In both the SM and the WEM, the quasi-static Maxwell equations $\boldsymbol{\nabla}\times\boldsymbol{E} = \boldsymbol{\nabla}\times\boldsymbol{H} = 0$, $\partial_t\rho + \boldsymbol{\nabla}\cdot\tilde{\boldsymbol{J}} = 0$ are used, where $\tilde{\boldsymbol{J}} = \rho\boldsymbol{v} + \boldsymbol{J}$ and $\rho = \boldsymbol{\nabla}\cdot\boldsymbol{D}$ (Poisson equation). This means that there is only one independent slow electric quantity for which the charge density ρ can be taken. [2] With the normalization condition $\boldsymbol{n}^2 = 1$ and the further assumption of incompressibility, $\boldsymbol{\nabla}\cdot\boldsymbol{v} = 0$, the SM contains five independent fields, namely the charge density ρ, two director components, and two momentum densities g_i with the equations [3]

$$\partial_t\rho + \boldsymbol{\nabla}\cdot(\rho\boldsymbol{v} + \boldsymbol{J}) = 0, \tag{2.1}$$

$$(\partial_t + \boldsymbol{v}\cdot\boldsymbol{\nabla})n_i + Y_i = 0, \tag{2.2}$$

$$\partial_t g_i + \partial_j(g_i v_j + T_{ij}) = 0, \tag{2.3}$$

[1] In general (e.g. for nonzero magnetic fields), $\boldsymbol{g}$ is not equal to $\rho_m\boldsymbol{v}$ [59]. Within the quasi-static approximation for the Maxwell equations, we have always $\boldsymbol{g} = \rho_m\boldsymbol{v}$.

[2] Later on, the potential ϕ of the induced field inhomogeneity will be used as independent electric variable.

[3] Throughout this work, summation over doubly occurring indices is assumed; the notation $\partial_j = \partial/\partial x_j$, $n_{i,j} = \partial_j n_i$ will be used freely.

where the convective currents proportional to $\boldsymbol{v}$ are shown explicitly and ρ as well as the (quasi-) currents $\boldsymbol{J}, \boldsymbol{Y}$ and $\underline{\underline{T}}$, are yet to be determined.

One has to watch for other slow processes. The mere existence of a slow field is, of course, not dangerous. To become relevant for EHC, the slow field must be excited by the SM variables and must couple back. A possible candidate is the order parameter S which becomes a slowly relaxing field near the clearing point [58]. It couples to the other fields via the S dependent relative anisotropies of the material parameters [25] and was suggested as a possible explanation for travelling waves [52]. The temperature (or internal energy) is slow as well, which is exploited in RBC of NLCs [60]. With planar boundary conditions (BC), the director enhances the buoyancy mechanism of isotropic RBC by a factor of the order of $\tau_d/\tau_{therm} \approx 1000$ (!) via heat focussing caused by the anisotropic thermal conductivity [61, 24]. Without an external temperature gradient, temperature inhomogenities are produced only in nonlinear order by the dissipative heat production R (Chapter 2.2). A simple order-of-magnitude estimation shows, that this contribution is negligible even in weakly-nonlinear calcuations [62]. With an external electric field, however, generalized hydrodynamics allows for a linear mechanism driven by thermoelectric effects [an electric field drives a thermal current and a temperature gradient drives an electric current, see Eq. (2.16) below], which may become important for thick cells.

Even the classic Maxwell equations have some subtleties if applied to polarizable media [59]. Only rather recently, the treatment of the fields $\boldsymbol{D}$ and $\boldsymbol{B}$ on equal footing as the other hydrodynamical variables has been carried through [63] leading in NLCs to new "dissipative" parts of the electromagnetic fields [57], which are not *a priori* small. Furthermore, such fields can induce a coupling between, e.g., a velocity gradient and the electric current, which clearly is relevant for EHC. There exist, however, no measurements of the material parametes involved, or even an experimental evidence of these effects; they are just allowed by symmetries. This concept will not be pursued in this work.

Finally, in this framework, the WEM is based on the assumption that the local conductivity becomes slowly relaxing. It is excited by charge-carrier migration effects and couples back to the other equations via the change of the conductivity in the charge conservation.

2.2 Derivation of the Standard Model

The framework set by Eqations (2.1) to (2.3) is valid for many systems. Now we specify them to NLCs by determining ρ and the (quasi) currents $\boldsymbol{J}, \boldsymbol{Y}$ and $\underline{\underline{T}}$. The functional dependence on the NLC material parameters is completely determined by symmetries [55, 58] and its derivation will be sketched in the following.

2.2.1 Statics

The thermodynamical potential suitable for equilibrium at a given temperature and for a given electric field is the free electric enthalpy $G = \int d^3r \{\epsilon - Ts - \boldsymbol{E}\cdot\boldsymbol{D}\}$ where ϵ and s are the densities of the energy and the entropy, respectively.[4] Near equilibrium, G is a quadratic form of the thermodynamic variables $\boldsymbol{n}$, $\rho_m\boldsymbol{v}$, and $\boldsymbol{E}$. Furthermore, it is extensive, $G = \int d^3r g$, and the scalar density g is invariant under rotations. Since $\boldsymbol{n}$ is a symmetry variable without an electric field, the elastic contribution of G depends only on gradients of $\boldsymbol{n}$. Respecting the uniaxiality of the state, the $\boldsymbol{n} \leftrightarrow -\boldsymbol{n}$ symmetry and the inversion symmetry in space and time, and restricting to the lowest-order expansion in the gradients, one obtains

$$G = \int d^3r \left\{ \frac{1}{2}\rho_m \boldsymbol{v}^2 + \frac{1}{2}K_{ijkl}n_{i,j}n_{k,l} - \frac{1}{2}\epsilon_{ij}E_iE_j - e_{ijk}n_{i,j}E_k \right\} \tag{2.4}$$

with

$$K_{ijkl}n_{i,j}n_{k,l} = K_{11}(\boldsymbol{\nabla}\cdot\boldsymbol{n})^2 + K_{22}[\boldsymbol{n}\times(\boldsymbol{\nabla}\times\boldsymbol{n})]^2 + K_{33}[\boldsymbol{n}\cdot(\boldsymbol{\nabla}\times\boldsymbol{n})]^2, \tag{2.5}$$

$$\epsilon_{ij} = \epsilon_\perp\delta_{ij} + \epsilon_a n_i n_j, \tag{2.6}$$

$$e_{ijk} = e_1\delta_{ij}n_k + e_3\delta_{ik}n_j. \tag{2.7}$$

Comparing Equation (2.4) with the general form of the free electric enthalpy gives the constitutive equation for $\boldsymbol{D}$ (and thus for ρ) and defines the "molecular field" $\boldsymbol{h}$ [25] as the thermodynamic conjugate of $\boldsymbol{n}$,

$$D_i = -\frac{\delta G}{\delta E_i} = \epsilon_{ij}E_j + e_{jki}n_{j,k} := \epsilon_{ij}E_j + P_i^{flexo}, \tag{2.8}$$

$$h_i = \frac{\delta G}{\delta n_i} = \frac{\partial g}{\partial n_i} - \partial_j\left(\frac{\partial g}{\partial n_{i,j}}\right). \tag{2.9}$$

The term (2.5) is the orientational-elastic Frank energy [53] due to splay (K_{11}), twist (K_{22}), and bend (K_{33}) deformations of the director; $\underline{\epsilon}$ is the uniaxial tensor of the

[4] In the Chapters 5-7, the control parameter is denoted by ϵ as well. A confusion should not arise.

dielectric permittivity, and e_{ijk} describes the flexoelectric effect. The flexoelectric polarization $\boldsymbol{P}^{flexo}$ leads to an additional charge density $\boldsymbol{\nabla}\cdot\boldsymbol{P}^{flexo}$ in Eq. (2.1)) that is not *a priori* small. In fact, the flexoeffect has been investigated rather extensively as a possible candidate to explain the travelling waves [64, 49, 65]. It cancels out, however, for AC driving in the "lowest order time expansion" (Chapter 5.2) which will be considered exclusively in this thesis. In addition, the flexoelectric coefficients are hard to measure [66].

2.2.2 Dynamics

The suitable potential to derive the dynamics is the energy

$$dE = \int d^3r \left\{ T\delta s + \tilde{\phi}\delta\rho + h\delta n + v_i\delta g_i \right\} := \int d^3r\epsilon, \tag{2.10}$$

since its natural variables are those of the conservation laws and balance equations (2.1) - (2.3).

The central relation is the entropy balance

$$\partial_t s + \boldsymbol{\nabla}\cdot(s\boldsymbol{v} + \boldsymbol{J}_s) = \frac{R}{T}, \tag{2.11}$$

were the dissipation function R is the local heat production per volume from dissipative processes. With Eq. (2.10), $\partial_t s$ can be substituted by $T^{-1}(\partial_t\epsilon - \boldsymbol{v}\cdot\rho_m\partial_t\boldsymbol{v} - \boldsymbol{h}\cdot\partial_t\boldsymbol{n} - \tilde{\phi}\partial_t\rho)$. After eliminating the time derivatives with the energy balance $\partial_t\epsilon + \boldsymbol{\nabla}(\epsilon\boldsymbol{v} + \boldsymbol{J}_\epsilon) = 0$ and with the Eqs (2.1) - (2.3), we arrive (with the constitutive equation $g_i = \rho_m v_i$) at

$$\begin{aligned} R &= T\boldsymbol{\nabla}(s\boldsymbol{v} + \boldsymbol{J}_s) - \boldsymbol{\nabla}(\epsilon\boldsymbol{v} + \boldsymbol{J}_\epsilon) + \tilde{\phi}\boldsymbol{\nabla}(\rho\boldsymbol{v} + \boldsymbol{J}) \\ &+ \boldsymbol{h}(\boldsymbol{v}.\boldsymbol{\nabla}\boldsymbol{n} + \boldsymbol{Y}) + v_i(\rho_m v_j\partial_j v_i + \partial_j T_{ij}). \end{aligned} \tag{2.12}$$

The (quasi-) currents [5] on the right-hand side of Eq. (2.12) can be separated into independent dissipative parts (the superscript D will be used) and reversible parts, and the latter can be separated into transport parts shown explicitly in (2.12) and parts existing also in the frame of reference comoving with the local velocity [dashed in Eq. (2.21) below]. Now I determine the three parts separately.

Dissipative parts

The dissipative currents make up the entropy production. Near or in local equilibrium, the entropy production is a quadratic form of the generalized forces driving

[5] Henceforth, I will not distinguish explicitly betwee currents and quasi-currents

the system out of (global) equilibrium. *In* equilibrium, the conjugates of conserved variables are constant and that of symmetry breaking or slowly relaxing variables are zero, so *near* local equilibrium, the Onsager forces of the conserved variables ρ, $g_i = \rho_m v_i$, and s are the gradients of the conjugate fields, $-\boldsymbol{\nabla}\tilde{\phi}$, $-\partial_i v_j$ and $-\boldsymbol{\nabla}T$, and the force of the director is the conjugate h itself. If one writes the forces as

$$F_\alpha := (E_i, h_i, -\partial_i v_j, -\partial_i T), \tag{2.13}$$

the dissipation function (the entropy production multiplied by T) takes the form

$$R = F_\alpha M_{\alpha\beta} F_\beta := F_\alpha J_\alpha \tag{2.14}$$

which defines the Onsager fluxes J_α. The matrix $M_{\alpha\beta}$ has to fulfil the Onsager relations [67, 68, 69]

$$M_{\alpha\beta} = t_\alpha t_\beta M_{\beta\alpha}, \tag{2.15}$$

where $t_\alpha = 1$ (-1) for forces of variables that are symmetric (antisymmetric) under time reversal. The signs (and possible prefactors) of F_α are defined such that the Onsager fluxes J_α are just the curents $\boldsymbol{J}, \boldsymbol{Y}, T_{ij}$ and $\boldsymbol{J}_{therm}$ as will be shown below. Applying the symmetry restrictions and Eq. (2.15), we obtain analogously to Eq. (2.4) in lowest order

$$\begin{aligned} R \;&= \tfrac{1}{2}\sigma_{ij}E_iE_j + \tfrac{1}{2\gamma_1}h_i\delta^\perp_{ij}h_j + \tfrac{1}{2}\eta_{ij,kl}v_{i,j}v_{k,l} \\ &\quad + \tfrac{1}{2}\kappa_{ij}(\partial_i T)(\partial_j T) + \kappa^{el}_{ij}E_i\partial_j T. \end{aligned} \tag{2.16}$$

The first term with the usual uniaxial form for the conductivity tensor $\sigma_{ij} = \sigma_\perp\delta_{ij} + \sigma_a n_i n_j$ is due to ohmic heating. The second term with the rotational viscosity γ_1 describes the rotational friction of the director relative to the moving fluid. To satisfy $\boldsymbol{n}^2 = 1$, the variational derivative in the definition of the molecular field must be restricted to variations perpendicular to the director itself. This means $\boldsymbol{h} \perp \boldsymbol{n}$ and is guaranteed by applying to $\boldsymbol{h}$ the tensor $\delta^\perp_{ij} = \delta_{ij} - n_i n_j$ projecting onto the plane perpendicular to the director. The third term with three viscosities (see below) describes the viscous heating. The two temperature-gradient terms are neglected, although, for a nonzero external electric field, the thermoelectric coupling $\propto \kappa^{el}_{ij}$ induces a thermal current in linear order (Chapter 2.1). [6]

[6] Sometimes, a further term $\tilde{e}_{ijk}h_i\partial_j E_k$ describing the dynamic analog of the flexoelectric effect, is introduced [58]. It is of higher order if there are no field gradients in the basic state; the corresponding material parameter has not been measured.

The dissipative currents are determined by rearranging Eq. (2.12) without the convective terms in a gradient and a sum of Onsager forces multiplied by fluxes,

$$\begin{aligned} R &= \partial_j \left(T J^D_{sj} + \tilde{\phi} J^D_j + v_i T^D_{ij} - \frac{\partial \epsilon}{\partial n_{i,j}} Y_i - J^D_{\epsilon j} \right) \\ &+ \boldsymbol{J}^D \cdot \boldsymbol{E}. + \boldsymbol{h} \cdot \boldsymbol{Y}^D - T^D_{ij} \partial_j v_i - \boldsymbol{J}^D_s \cdot \boldsymbol{\nabla} T, \end{aligned} \tag{2.17}$$

and comparing the result with Eq. (2.16). The gradient parts are balanced by $\boldsymbol{J}_\epsilon$, and the dissipative currents are (in the approximations of the SM)

$$J^D_i = \frac{\partial R}{\partial E_i} = \sigma_{ij} E_j, \tag{2.18}$$

$$Y^D_i = \frac{\partial R}{\partial h_i} = \gamma_1^{-1} \delta^\perp_{ij} h_j, \tag{2.19}$$

$$\begin{aligned} -T^D_{ij} = \frac{\partial R}{\partial v_{i,j}} &= \eta_{ijkl} v_{k,l} = \alpha_4 A_{ij} + (\alpha_1 + \gamma_1 \lambda^2) n_i n_j n_k n_l A_{kl} \\ &+ (\alpha_5 - \frac{\gamma_1 \lambda (1+\lambda)}{2})(n_i A_{jk} n_k + n_j A_{ik} n_k), \end{aligned} \tag{2.20}$$

where $A_{ij} = (\partial_i v_j + \partial_j v_i)/2$. As a result of the symmetry restrictions, one gets in Eq. (2.20) three general shear-viscosity coefficients. They have been expressed in terms of the more familiar Erickson-Leslie coefficients α_1, α_4 and α_5 [26, 27], and by γ_1 and a reversible parameter λ to be defined below.

Reversible parts for zero transport

The Onsager symmetries (2.15) are valid also for the reactive Onsager fluxes $J'_\alpha = M'_{\alpha\beta} F_\beta$, but now, of course, the heat production Eq. (2.14) has to vanish. This implies that the reactive Onsager matrix $M'_{\alpha\beta}$ has no diagonal terms and only those cross terms that couple variables with opposite time-reversal symmetry. This leads to $\boldsymbol{J}'_s = \boldsymbol{J}' = 0$, and to

$$\begin{pmatrix} Y'_i \\ T'_{ij} \end{pmatrix} = \begin{pmatrix} 0 & \frac{1}{2}\lambda_{ijk} \\ -\frac{1}{2}\lambda_{kji} & 0 \end{pmatrix} \begin{pmatrix} h_k \\ -\partial_j v_k \end{pmatrix}. \tag{2.21}$$

The symmetries lead to $\lambda_{ijk} = \lambda_1 \delta^\perp_{ij} n_k + \lambda_2 \delta^\perp_{ik} n_j$ and the condition of vanishing relative motion of the director in the case of a rigidly rotating fluid, $\partial_t \boldsymbol{n} = \boldsymbol{\omega} \times \boldsymbol{n}$ for $\partial_i v_j = \partial_j v_i$ and $\boldsymbol{\nabla} \times \boldsymbol{v} = 2\boldsymbol{\omega}$, leads to $\lambda_2 - \lambda_1 = 2$.[7] Thus $\underline{\underline{\lambda}}$ can be written as

$$\lambda_{ijk} = (\lambda - 1)\delta^\perp_{ij} n_k + (\lambda + 1)\delta^\perp_{ik} n_j. \tag{2.22}$$

[7] A more formal derivation using conservation of the angular momentum can be found in [58].

Often, the sum of the reactive and dissipative parts of the momentum-flux tensor is expressed in terms of the Erickson-Leslie coefficients $\alpha_1, ..., \alpha_6$ [26, 27], given in Eq. (2.28) below. Although this formulation is less systematic, it will be used throughout this thesis, mainly to enable an easy comparison with existing work. An intuitive picture of the various viscosities is given e.g. in [70, 31].

Transport parts

The transport or convective currents are related to Galilean invariance and therefore reversible as well. The condition that the dissipation function of the convective currents, Eq. (2.12) with $\boldsymbol{J}_s = \boldsymbol{J} = \boldsymbol{Y} = 0$, vanishes for any $\boldsymbol{v}$, can only be satisfied by an extra part T^t_{ij} of the momentum-flux tensor. The momentum-flux tensor (including the isotropic pressure) is the only non-convective current which gives contributions $\propto \boldsymbol{v}$ in (2.12) and thus can balance all other advective contributions. This leads to

$$T^t_{ij} = p\delta_{ij} + \pi_{ij} - E_i D_j, \qquad \pi_{ij} = \frac{\partial \epsilon}{\partial n_{k,j}} n_{k,i}, \tag{2.23}$$

where the pressure is given by the Gibbs relation [71, 59] $p = -\epsilon + Ts + \rho_m v^2 + \rho\tilde{\phi}$, and some transport parts were expressed by $\partial_i p = D_j \partial_i E_j - h_j \partial_i n_j + \rho_m v_j \partial_i v_j + s\partial_i T$.

The pressure will be eliminated later. The second term in Eq. (2.23), the Erickson stress [25], is the (nonlinear) counter term of the director advection term $\boldsymbol{v} \cdot \boldsymbol{\nabla} \boldsymbol{n}$. In physical terms, velocity gradients change the elastic energy by changing the local director distortions which must be balanced by the mechanical power (i.e. velocity times a force) $v_i \partial_j \pi_{ij}$. The third term $E_i D_j := -T^{el}_{ij}$ is the balance to the charge advection. Its gradient, the electric volume force, is the main driving force of EHC.

By redefining the pressure as $\tilde{p} = p - \frac{1}{2}\epsilon_0 \epsilon_\perp E^2$, the volume force can be written as $-\partial_j T^{el}_{ij} = \rho E_i + P_j \partial_j E_i$, where the "polarization" $P_i = \epsilon_a n_i n_j E_j$ contains the inhomogeneity of the dielectric displacements. The polarization part is nonlinear and will be neglected in the following.

2.3 Basic equations

In summary, the equations of the SM are

$$(\partial_t + \boldsymbol{v} \cdot \boldsymbol{\nabla})\rho = -\boldsymbol{\nabla} \cdot (\underline{\sigma} \boldsymbol{E}), \tag{2.24}$$

$$(\partial_t + \boldsymbol{v} \cdot \boldsymbol{\nabla})\boldsymbol{n} = \boldsymbol{\omega} \times \boldsymbol{n} + \underline{\underline{\delta}}^{\perp}(\lambda \underline{\underline{A}} \boldsymbol{n} - \frac{1}{\gamma_1} \boldsymbol{h}), \tag{2.25}$$

$$\rho_m(\partial_t + \boldsymbol{v} \cdot \boldsymbol{\nabla})v_i = -\partial_i p - \partial_j(\pi_{ij} + T^{visc}_{ij}) + \rho E_i, \tag{2.26}$$

with the static conditions $\rho = \partial_i \epsilon_{ij} E_j$ (Poisson equation), $E_i = E_0(t)\delta_{i3} - \partial_i \phi$ (exploiting $\boldsymbol{\nabla} \times \boldsymbol{E} = 0$ and separating $\boldsymbol{E}$ into an external field and a field inhomogeneity), $\boldsymbol{n}^2 = 1$ (constant order parameter), and $\boldsymbol{\nabla} \cdot \boldsymbol{v} = 0$ (incompressibility).

Eq. (2.24) is just the charge balance for a weak anisotropic ohmic conductor where both the charge density and the current are relevant. Without forces, the director in Eq. (2.25) would move with the surrounding fluid like a rod in a river, $\boldsymbol{N} \equiv (\partial_t + \boldsymbol{v} \cdot \boldsymbol{\nabla})\boldsymbol{n} - \omega \times \boldsymbol{n} = 0$, where $\boldsymbol{\omega} = (\boldsymbol{\nabla} \times \boldsymbol{v})/2$ is the local fluid rotation. The forces onto the director in Eq. (2.25) come from the orientational elasticity described by the molecular field $\boldsymbol{h}$, and from a coupling of the director to the fluid shear $A_{ij} = (\partial_i v_j + \partial_j v_i)/2$ ("flow alignment"). The projection tensor $\delta_{ij}^{\perp} = \delta_{ij} - n_i n_j$ guarantees $n^2 = 1$. The molecular field is given by

$$h_i = \frac{\delta}{\delta n_i} \left(K_{mnkl} n_{m,n} n_{k,l} \right) - \epsilon_a (\boldsymbol{n} \cdot \boldsymbol{E}) E_i, \tag{2.27}$$

with $K_{ijkl} n_{i,j} n_{k,l}$ from Eq. (2.5). Sometimes, Eq. (2.25) is written as $\boldsymbol{n} \times (\boldsymbol{h} + \gamma_1 \boldsymbol{N} + \gamma_2 \underline{\underline{A}} \boldsymbol{n}) = 0$ with $\gamma_2 = -\lambda \gamma_1$ [72, 25, 73]. Both forms of the director equation can be expressed in terms of the Erickson-Leslie coefficients with the relations $\gamma_1 = \alpha_3 - \alpha_2$ and $\lambda = (\alpha_2 + \alpha_3)/(\alpha_2 - \alpha_3)$ obtained with the help of angular momentum conservation.

The negative viscous stress tensor (momentum-flux tensor) T_{ij}^{visc} has a reactive part T'_{ij} and a dissipative part T_{ij}^{D} given by the Eqs. (2.21) and (2.20), respectively. Often, the molecular field in T'_{ij} is expressed with the help of Eq. (2.25) in terms of $\boldsymbol{N}$ and $\underline{\underline{A}} \boldsymbol{n}$ and the two parts are written together in terms of the Leslie coefficients,

$$\begin{aligned} -T_{ij}^{visc} &= \alpha_1 n_i n_j n_k n_l A_{kl} + \alpha_2 n_j N_i + \alpha_3 n_i N_j \\ &\quad + \alpha_4 A_{ij} + \alpha_5 n_j n_k A_{ki} + \alpha_6 n_i n_k A_{kj}. \end{aligned} \tag{2.28}$$

In this formulation, the Onsager symmetries have to be condidered separately leading to the so-called Parodi relation [74] $\alpha_2 + \alpha_3 = \alpha_6 - \alpha_5$. At last, the nonlinear Erickson stress π_{ij} in Eq. (2.26) is given by Eq. (2.23). In the Eqs. (2.24)–(2.26), some small contributions have been neglected, e.g., the flexoeffect and the polarization part of the electric volume force (Chapter 2.2.2).

Equations (2.24) to (2.26) represent five independent equations for the potential ϕ of the electric field inhomogeneity, two director components (n_y and n_z for the planar geometry), and two velocity fields or a suitable representation for them, e.g. the toroidal and a poloidal potential g and f for divergence-free fluids[75]

$$\boldsymbol{v} = \boldsymbol{\nabla} \times \hat{\mathbf{z}} g + \boldsymbol{\nabla} \times (\boldsymbol{\nabla} \times \hat{\mathbf{z}} f) \equiv \boldsymbol{\epsilon} g + \boldsymbol{\delta} f, \tag{2.29}$$

$$\boldsymbol{\epsilon} = (\partial_y, -\partial_x, 0), \quad \boldsymbol{\delta} = (\partial_{xy}^2, \partial_{yz}^2, -\partial_{xx}^2 - \partial_{yy}^2). \tag{2.30}$$

class of response	effect	given by		in EHC leading to
static	orientational elasticity	$K_{ijkl} = (2.5)$	K_{11} K_{22} K_{33}	restoring torque from director distortions
	dielectric permittivity	$\epsilon_{ij} =$ $\epsilon_\perp \delta_{ij} + \epsilon_a n_i n_j$	$\epsilon_\perp$ ϵ_a	dielectric torque
dynamic, reactive	flow alignment	$\lambda_{ijk} =$(2.22)	λ †	torque onto the director due to fluid shear
dynamic, dissipative	rotational viscosity		γ_1 †	torque onto the director due to relative rotation
	shear viscosity	$\eta_{ijkl} = (2.20)$	α_1 α_4 α_5	Damping of the fluid motion
	conductivity	$\sigma_{ij} =$ $\sigma_\perp \delta_{ij} + \sigma_a n_i n_j$	$\sigma_\perp$ σ_a	charge focussing; electric volume force
† $\lambda = (\alpha_2 + \alpha_3)/(\alpha_2 - \alpha_3), \quad \gamma_1 = \alpha_3 - \alpha_2$				

To eliminate the pressure, one takes the y and z components of the curl of (2.26) [48] or applies the Hermitean conjugate of the operators $\boldsymbol{\delta}$ and $\boldsymbol{\epsilon}$ [76, 77, 62].

The planar-homogeneous "rigid" BC, used exclusively in this work, are

$$\begin{aligned} \phi(z = \pm d/2) &= 0 \qquad \text{(ideally conducting plates)}, \\ \boldsymbol{n}(z = \pm d/2) &= (1, 0, 0) \qquad \text{(rigid anchoring)}, \\ \boldsymbol{v}(z = \pm d/2) &= 0 \qquad \text{(finite viscosity)}. \end{aligned} \tag{2.31}$$

In the horizontal x and y directions, I assume the system to be infinite (translationally invariant). To avoid destruction of the NLC by electrolytic effects, the cell is driven with an AC voltage,

$$E_0(t) = \frac{\overline{V}\sqrt{2}}{d} \cos \omega_0 t, \tag{2.32}$$

which conveniently introduces the external frequency as a second control parameter (typically, $\omega_0/2\pi = 10...1000$ Hz). The instability mechanism, however, is active also for DC.

In the table, the material parameters of the NLC are summarized that are contained in the SM.

Chapter 3

The Weak Electrolyte Model

I know that I know nearly nothing, and hardly this.

K. R. Popper

Many features of EHC in the conductive range of low frequencies are quantitatively described by the SM, in particular the threshold voltage as function of the external frequency, and the existence and angle of oblique rolls. Nevertheless, even qualitative features remain unexplained. Most notable are travelling rolls which have been observed as early as 1978 [38]. Later on, they were found in a broad parameter range in different liquid crystals (MBBA, Phase 5 and I52) by different groups [42, 39, 40, 41, 30], and seem to be generic for relatively thin and clean cells. Despite this, they have withstood a theoretical understanding until recently.

3.1 Physical assumptions

A theory of travelling rolls in EHC must explain the following facts.

- The travelling rolls are really produced by a Hopf bifurcation that breaks spontaneously the reflection symmetry. This is shown by spatiotemporal correlations of subcritical director fluctuations which are left-right symmetric [39]. This is confirmed by experiments where the control parameter (rms voltage) is modulated in time and, for a modulation with the double Hopf frequency, parametric resonance leads to standing waves as predicted by theory for a Hopf bifurcation [40]. This means that the travelling rolls really originate from a Hopf bifurcation to degenerate right and left travelling rolls. Drift effects due to broken left-right symmetry (e.g., nonideal planar boundary conditions with a pretilt [52, 76]) are excluded.

- Travelling rolls are only found in thin cells, e.g., in MBBA in cells with $d = 13\mu m$ [39], but not in cells with $d \geq 20\mu m$ [41, 43], and in I52 for $d = 28\mu m$, but not for $d = 57\mu m$ [30, 42].

- For a fixed cell thickness, travelling rolls are observed for conductivities below a certain threshold [30]. From experiments, it was suggested [31], that deviations from the SM scale with $(\sigma_\perp d^2)^{-1}$ and, in particular, that for a given material the codimension-two curve separating stationary from travelling rolls is given by $\sigma_\perp d^2 = \text{const}$.

- For a stongly negative dielectric anisotropy (MBBA with $\epsilon_a = -0.53$ or Phase 5 with ϵ_a of the order of -0.2) one observes travelling rolls only in a certain frequency range $\omega_{0,min} < \omega_0 < \omega_{cutoff}$ (e.g. between 350 and 420 Hz in [40]), or, the Hopf frequency becomes very low for low frequencies [41, 78]. For I52 at low temperatures (slightly negative ϵ_a) there are travelling rolls with a significantly nonzero Hopf frequency for all frequencies and the Hopf frequency increases with the external frequency. At high temperatures (ϵ_a essentially zero) the Hopf curve of I52 is essentially flat [30, 42].

- Furthermore, there is an excellent quantitative agreement between the SM and experiments for *thermal* convection in NLCs [23, 79, 24], so any new model must reduce to the SM for zero electric fields, and for large values of $\sigma_\perp$ and d^2.

In the SM, the static and dynamic electric properties of the NLC are described by $\boldsymbol{D} = \underline{\underline{\epsilon}}\boldsymbol{E}$ and $\boldsymbol{J} = \underline{\underline{\sigma}}\boldsymbol{E}$, respectively. Obviously, a new model must generalize either of these two relations.

The static relation has been generalized to include flexoelectric effects (see Chapter 2.2), $\boldsymbol{D} = \underline{\underline{\epsilon}}\boldsymbol{E} + P_{flexo}$ [49, 65]. The *rationale* was that the flexoelectric terms break the combined symmetry $z \rightarrow -z,\ t \rightarrow t + \pi/\omega_0$ and that the resulting coupling of two linear modes, namely the conductive IA and dielectric IIB modes (see Chapter 5.2) may lead to oscillations at threshold [52]. However, this can be the case only for external frequencies where both modes get unstable nearly simultaneously (crossover), i.e. only near the cutoff frequency. In addition, there are other problems with the flexoeffect that are described in Chapter 2.2. Anyway, evaluating the SM including the flexoeffect has not led to travelling rolls.

A generalization of $\boldsymbol{J} = \underline{\underline{\sigma}}\boldsymbol{E}$, i.e., a non-ohmic conductivity, was suggested already in the Refs. [48, 52] and will be the basis of the development of the WEM. The intrinsic conductivity of thermotropic NLCs is extremely low (for I52 less than $10^{-9}(\Omega m)^{-1}$

[31]; To obtain a sufficient and well-controlled conductivity, one adds often an ionizable dopant to the NLC. For MBBA with the dopant *Tetrabutyl-Ammonium Tetraphenyl-Boride* (TBATPB), the conductivity increases with the square root of the TBATPB concentration [80]; with a molar concentration of 10^{-5} moles per liter one obtains a conductivity of $1.5 \times 10^{-7} (\Omega \mathrm{m})^{-1}$. For I52, it proved to be very difficult to find a dopant providing enough conductivity for EHC, probably because I52 consists of nonpolar molecules, in contrast to MBBA. At last (after 17 tries with other dopants) a concentration of 2% (!) Iodine (I_2) was successful in the experiments of Mike Dennin [31].

For MBBA with the dopant TBATPB, the measured dependence of the equilibrium conductivity from the square root of the TBATPB concentration can be naturally explained by a simple dissociation-recombination reaction. Ref [80] suggests the reaction

$$(C_4H_9)_4\ N(C_6H_5)_4B \rightleftharpoons (C_4H_9)_4\ N^+ + (C_6H_4)_4B^-,$$

which has the generic form [80]

$$AB \rightleftharpoons A^+ + B^-.$$

In equilibrium, the product of the number densities n^+ and n^- of the ions A^+ and B^- is proportional to the density n_{AB} of the undissociated molecules, $n^+ n^- / n_{AB} = \text{const.} := K$ (mass-action law). The conductivity is caused by the drift of the dissociated ions, is proportional to the sum of n^+, n^-, weighted with the mobilities. With typical values for the mobilities (see Table 3.1) one finds that only a small fraction of the impurities is dissociated into ionic charge carriers (weak-electrolyte limit) and one obtains from the mass-action law the observed square-root behaviour. In the I_2 doped I 52, the molecules form a charge-transfer complex and then undergo a dissociation-recombination reaction [31]. Although this is a multistep process, the net effect should be described by the above simple binary reaction.

In any case, the current should be described as in the SM (Ohm's law with anisotropic conductivities) for homogeneous stationary systems, or, approximatively, for thick cells. This motivates following assumptions for the WEM.

- The electric current is caused by two species of ionic charge carriers A^+ and B^- with charges $\pm e$ [1] and number densities n^+ and n^-. The electric current $\boldsymbol{J}^\pm$ of each species is caused by advection with the fluid velocity, migration

[1] Charges of $\pm ne$ can be taken care of by renormalizing the mobility by a factor of $1/n$.

(drift) by electric fields $\boldsymbol{E}$, and diffusion due to carrier-density gradients [81],

$$\begin{aligned} \boldsymbol{J} = \boldsymbol{J}^+ + \boldsymbol{J}^- &= e(n^+ - n^-)\boldsymbol{v} + e\left(\underline{\underline{\mu}}^+ n^+ + \underline{\underline{\mu}}^- n^-\right)\boldsymbol{E} \\ &- e\left(\underline{\underline{D}}^+ \boldsymbol{\nabla} n^+ - \underline{\underline{D}}^- \boldsymbol{\nabla} n^-\right). \end{aligned} \tag{3.1}$$

- The charge carriers originate from dissociation of impurity ions and can be described by the net reaction AB $\rightleftharpoons$ $A^+ + B^-$ with the dissociation rate $\dot{n}_{diss} = k_d n_{AB}$ and the recombination rate $\dot{n}_{\rm rec} = k_r n^+ n^-$. In addition, overall neutrality, $\int d^3r(n^+ - n^-) = 0$, is assumed.

- The mobilities (and diffusivities) are uniaxial tensors whose principal values $\mu_\perp^\pm$ and $\mu_\parallel^\pm$ ($D_\perp^\pm$ and $D_\parallel^\pm$) do not depend on $\boldsymbol{E}$, n^+ or n^-. I assume equal relative anisotropies [80, 28], which must be given by the measured relative anisotropy of the conductivities to be consistent with the SM limit,

$$\mu_{ij}^+ = \mu_\perp^+ \mu'_{ij}, \quad \mu_{ij}^- = \mu_\perp^- \mu'_{ij} \quad \text{with} \quad \mu'_{ij} = \delta_{ij} + \frac{\sigma_a^{eq}}{\sigma_\perp^{eq}} n_i n_j. \tag{3.2}$$

- The number density of dissociated ions is much lower than the density of the remaining undissociated impurities (weak-electrolyte limit),

$$n_{AB} >> n^+, n^-. \tag{3.3}$$

Introducing the dissociation constant $K = k_d/k_r$, the equilibrium charge carrier density of the neutral NLC, $n_0 := n_{eq}^+ = n_{eq}^- = \sqrt{n_{AB}^{eq} K}$, the total concentration of the dopant, $c = n_{AB} + (n^+ + n^-)/2$ (a conserved quantity), and the degree of ionization in equilibrium, $\beta_c = n_0/c$ [28], we have in equilibrium ($E_0 = 0$), but not restricted to weak electrolytes

$$\beta_c = \frac{K}{2c}\left(\sqrt{1 + 4\frac{c}{K}} - 1\right). \tag{3.4}$$

The weak-electrolyte limit is given by $\beta_c \approx \sqrt{K/c} << 1$, i.e. $K << c$ which is well satisfied for I52, see Table 3.1. The generalized condition (3.3) for $\boldsymbol{E} \neq 0$ requires knowledge of the solutions of the WEM equations, i.e. can be verified only *a posteriori*.

3.2 Formulation of the WEM

3.2.1 Dynamical equations for the charge- carrier densities

The hydrodynamic part of the equations for the carrier densities (without dissociation and recombination) can be formulated in the framework of generalized hydro-

dynamics. The electric part $\tilde{\phi} d\rho$ of the SM energy density (2.10) becomes

$$d\epsilon_{el} = \tilde{\phi} e(dn^+ - dn^-) + k_B T d(n^+ \ln n^+ + n^- \ln n^-), \tag{3.5}$$

where the second term equals T times the additional entropy from the two (non-interacting) carrier densities. Without dissociation and recombination, the fields $n^\pm$ are true hydrodynamic variables obeying the continuity eqations $\partial_t n^\pm + \boldsymbol{\nabla} \cdot (n^\pm \boldsymbol{v} + \boldsymbol{J}_{n^\pm}) = 0$, where the currents are linear combinations of the thermodynamic forces,

$$\boldsymbol{F}^\pm = -\boldsymbol{\nabla} \left(\frac{\partial \epsilon}{\partial n^\pm} \right) = \pm e \boldsymbol{E} - k_B T \boldsymbol{\nabla} \ln n^\pm. \tag{3.6}$$

Cross couplings between, e.g., $\boldsymbol{J}_{n^+}$ and $\boldsymbol{F}^-$ are not forbidden, but it seems reasonable to neglect them, putting $\boldsymbol{J}_{n^\pm} = \underline{\underline{M}}^\pm \boldsymbol{F}^\pm$. The Onsager matrices $\underline{\underline{M}}^\pm$ are determined by the condition that the ohmic SM conductivity should be recovered in the homogeneous limit and by the assumption of constant mobilities ($\boldsymbol{J}_{n^\pm} \propto n^\pm$). This leads to $\underline{\underline{M}}^\pm = \frac{1}{e} \underline{\underline{\mu}}^\pm n^\pm$ or

$$\boldsymbol{J}_{n^\pm} = \pm \underline{\underline{\mu}}^\pm \left(n^\pm \boldsymbol{E} - \frac{k_B T}{e} \boldsymbol{\nabla} n^\pm \right) \tag{3.7}$$

Comparison of (3.7) with (3.1) gives a relation of the diffusivities with the mobilities, the anisotropic form of the Einstein law [28],

$$\underline{\underline{D}}^\pm = V_T \underline{\underline{\mu}}^\pm, \quad V_T = \frac{k_B T}{e} \approx 26\text{mV}, \tag{3.8}$$

where V_T is the thermal voltage. The (non-hydrodynamic) dissociation and recombination parts are given in a homogeneous (stirred) system by the usual kinetic equations $\partial_t n^\pm = k_d n_{AB} - k_r n^+ n^-$. The weak-electrolyte assumption implies that $n_{AB} \approx n_{AB}^{eq} = \text{const}$, or $k_d n_{AB} - k_r n^+ n^- \approx k_r (n_0^2 - n^+ n^-)$.

Combining the hydrodynamic and the non-hydrodynamic parts and substituting Eq. (3.7) for the currents give the dynamical equations for the carrier densities,

$$\partial_t n^\pm + \boldsymbol{\nabla} \cdot \left[\boldsymbol{v} n^\pm + \mu_\perp^\pm \underline{\underline{\mu}}' (\pm \boldsymbol{E} - V_T \boldsymbol{\nabla}) n^\pm \right] = k_r (n_0^2 - n^+ n^-). \tag{3.9}$$

Note that, using $\boldsymbol{\nabla} \cdot \boldsymbol{v} = 0$, the left-hand side of (3.9) can be written in the "advective" form
$(\partial_t + \boldsymbol{v}^\pm \cdot \boldsymbol{\nabla}) n^\pm + \mu_\perp^\pm \left(\pm n^\pm \boldsymbol{\nabla} (\underline{\underline{\mu}}' \boldsymbol{E}) - V_T (\boldsymbol{\nabla} n^\pm)(\boldsymbol{\nabla} \underline{\underline{\mu}}') \right)$ where $\boldsymbol{v}^\pm = \boldsymbol{v} + \mu_\perp^\pm \underline{\underline{\mu}}' (\pm \boldsymbol{E} - V_T \boldsymbol{\nabla})$ are the total velocities of the carriers.

In view of coupling Eqs.(3.9) to the director and momentum-balance equations of the SM, it is convenient to write the equation as a continuity equation for the

charge density $\rho(\boldsymbol{r},t) = e(n^+ - n^-)$ and a balance equation for the local conductivity $\sigma_\perp(\boldsymbol{r},t) = e(\mu_\perp^+ n^+ + \mu_\perp^- n^-)$,

$$\begin{aligned} \partial_t \rho &+ \boldsymbol{\nabla}\cdot\left[\rho\boldsymbol{v} + \underline{\underline{\mu}}'\boldsymbol{E}\sigma_\perp - V_T\underline{\underline{\mu}}'\boldsymbol{\nabla}\left(d_1\sigma_\perp + 2\mu s_1\rho\right)\right] = 0, \qquad (3.10)\\ \partial_t\sigma_\perp &+ \boldsymbol{\nabla}\cdot\left[\sigma_\perp\boldsymbol{v} + \mu\underline{\underline{\mu}}'\boldsymbol{E}(d_1\sigma_\perp + \mu s_1\rho) - \mu V_T\underline{\underline{\mu}}'\boldsymbol{\nabla}\left(s_2\sigma_\perp + d_1\mu s_1\rho\right)\right]\\ &= k_r n_0 \sigma_\perp^{eq}\left[1 - \frac{(\sigma_\perp + \mu_\perp^-\rho)(\sigma_\perp - \mu_\perp^+\rho)}{(\sigma_\perp^{eq})^2}\right], \qquad (3.11)\end{aligned}$$

where we introduced the effective mobility $\mu = \mu_\perp^+ + \mu_\perp^-$, the equilibrium conductivity $\sigma_\perp^{eq} = \mu e n_0$ and the mobility ratio $\gamma = \mu_\perp^-/\mu_\perp^+$ together with $d_1 = (1-\gamma)/(1+\gamma)$, $s_1 = \gamma/(1+\gamma)^2$, and $s_2 = (1+\gamma^2)/(1+\gamma)^2$. Note that the terms $\propto s_1, s_2 (\propto d_1)$ are (anti-) symmetric with respect to a change $n^+ \leftrightarrow n^-$ corresponding to $\gamma \to 1/\gamma$. $\sqrt{s_1}$ is the ratio of the geometric mean to the sum of the mobilities.

3.2.2 Boundary conditions

In the structureless state with no variations in x and y, we have $\rho = \epsilon_\perp \partial_z E_z$, and Eqs. (3.10) and (3.11) represent, with respect to the z derivatives, a third-order equation for E_z and a second-order equation for $\sigma_\perp$. Thus we need at the confining plates five BCs for the electrical variables in addition to the usual fully-rigid planar SM-BCs $\boldsymbol{n} = (1,0,0)$ and $\boldsymbol{v} = 0$ ($z = \pm d/2$). The integral condition

$$\int_{-d/2}^{d/2} dz\ E_z = V(t) \qquad (3.12)$$

is always valid. the remaining four electrical BC are relations between current, electric field and density for each species at the electrodes which can depend in a complicated way on electrochemical processes and may be parametrised e.g., for $z = d/2$ as

$$J_z^\pm = \sigma_{\text{surface}}^\pm E_z - D_{surface}^\pm (n_{ext}^\pm - n^\pm), \qquad (3.13)$$

where $\boldsymbol{J}^+ = e\boldsymbol{J}_n^+$ ($\boldsymbol{J}^- = -e\boldsymbol{J}_n^-$) are the electric currents carried by the positive (negative) carriers. Some special cases are

- Strongly injecting electrodes where σ_{surface} is very large at one or at both electrodes leading to $E_z = 0$ ("space-charge limiting conditions"). In the isotropic-unipolar case, such BCs are adopted, e.g., in the Refs. [81, 82].
- Electrodes absorbing outflowing carriers, $\sigma_{\text{surface}}^\pm = e\mu_\perp^\pm n^\pm$ for $\boldsymbol{E}\cdot\hat{e} > 0$, and $\sigma_{\text{surface}} = 0$ for $\boldsymbol{E}\cdot\hat{e} < 0$ ($\hat{e}$ is the outwards-pointing normal vector). This kind of electrodes is used for electrodyalitic purification [83].

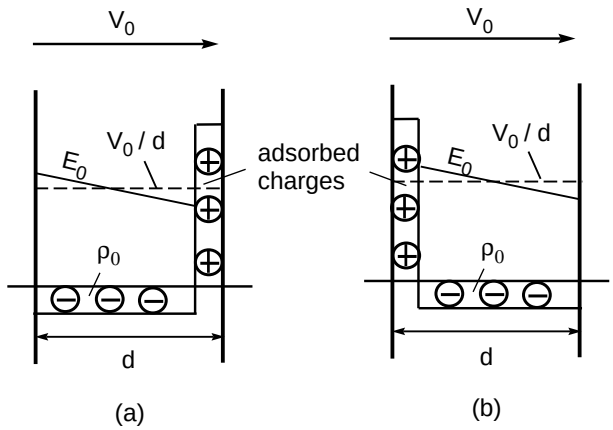

Figure 3.1 Effects of adsorbed surface charges on the electric field and the volume charges under the assumption of an otherwise trivial basic state (discussed in Chapter 4. (a): Charges adsorbed at the right (top) plate; (b): Charges adsorbed at the left (bottom) plate. For illustrative purposes, the δ-distributed surface charge is drawn as a layer of finite thickness.

- The BCs of the SM. For zero diffusivities, the five electric BC lead to an overdetermined system. This fixes the BC to the "ohmic BC" $\sigma^{\pm}_{\text{surface}} = e\mu^{\pm}_{\perp} n^{\pm}$ or $J_z = \sigma_{\perp} E_z$.

- Blocking electrodes. No transfer of any charge through the electrodes [84, 85, 86],

$$J_z^+(z = \pm d/2) = J_z^-(z = \pm d/2) = 0. \tag{3.14}$$

These last BCs do not involve unknown electrochemical processes and will be assumed in the rest of this paper. They are also relevant for the I52 experiments (insulating SI O_2 - layer at the electrodes [30]) and it is known that, for AC driving, blocking electrodes do not influence EHC [87]. These BC imply that the total charge $\int_{cell} d^3r\rho := \int dx\ dyQ$ is a conserved quantity. Usually, overall neutrality ($Q = 0$) is assumed, but the electrodes may contain as well permanently adsorbed charges [86]. This can be incorporated into the WEM by setting

$$E_z(d/2) - E_z(-d/2) = -\frac{Q_{ad}}{\epsilon_0 \epsilon_{\perp}}, \tag{3.15}$$

where Q_{ad} is the average adsorbed total charge per area and E_z is the field just inside the layers. Remarkably, Eq. (3.15) is the same whether the charges are adsorbed at the top or bottom plates or on both, see Fig. 3.1. Like the flexoeffect, adsorbed charges break the z symmetry of the system, but leave the combined symmetry $z \to -z,\ t \to t + \pi/\omega_0$ intact. Adsorbed charge layers increase the Fre'edericksz threshold in a simple model [86]. Their effect on EHC has not been investigated.

Table 3.1: Material parameters related to conduction

parameter	material	value and source
total mobility μ ##	MBBA ++ MBBA 5CB theory for MBBA	3.71 [80]; 0.18 [83]; 1..10 [87]; 10 [81]; 1 [28] 0.6 [84]; 2.5 [86] 11 (Stokes friction) [80] 0.2 (dielectric friction) [87]
geometric mean $\sqrt{\mu_\perp^+ \mu_\perp^-}$	I52	0.40 ... 0.47 (Hopf frequency) [42]
assumed mobility ratio γ	MBBA# 5CB	1 [80] $>> 1$ [84]
mobility anisotropy $\frac{\mu_a}{\mu_\perp}$	MBBA	0.33 [80]; 0.5 [88]
dissociation constant $K = \frac{k_d}{k_r}$	MBBA# MBBA ††	$3.4 \times 10^{21}\mathrm{m}^{-3}$ [80] $(2..4) \times 10^{20}\mathrm{m}^{-3}$ [28]
recombination- rate constant k_r	MBBA † dielectric liquids	$1.5 \times 10^{-27}\mathrm{m}^3\mathrm{s}^{-1}$ [83] $10^{-15}\mathrm{m}^3\mathrm{s}^{-1}$ [81]
carrier lifetime $\tau_{\mathrm{rec}} = (2k_r n_0)^{-1}$	MBBA † MBBA 5CB	2.7×10^4 s [83] 10^{-3}s [81] 0.05 s [86]
equilibrium density n_0	MBBA 5CB	$6 \times 10^{20}\mathrm{m}^{-3}$ [28] $10^{20}\mathrm{m}^{-3}$ [84]; $8 \times 10^{20}\mathrm{m}^{-3}$ [85]
degree of ionization $\beta_c = \frac{n_0}{c}$, Eq. (3.4)	MBBA *, # I52 ,+	0.001 0.2
diffusion constant D	5CB	$4.5 \times 10^{-13}\mathrm{m}^2\mathrm{s}^{-1}$ [84]

In units of $10^{-10}\mathrm{m}^2/(\mathrm{Vs})$; # dopant TBATPB;
†† dopants TBAP and TBAB; ++ does not depend on the TBATPB concentration;
† electrodialysed to $\sigma = 5 \times 10^{-9}(\Omega\mathrm{m})^{-1}$, 50 °C(3K above the clearing point);
** dopant 2% I_2; * For $\sigma_\perp = 10^{-7}(\Omega\mathrm{m})^{-1}$, $\mu_\perp = 3.71 \times 10^{-10}\mathrm{m}^2/(\mathrm{Vs})$;
+ T=40C, $\sigma_\perp = 0.49 \times 10^{-8}(\Omega\mathrm{m})^{-1}$

3.2.3 Material parameters related to conductivity

In addition to the SM material parameters (see e.g. Ref. [48] for MBBA), the Eqs. (3.10) and (3.11) contain the WEM parameters $\mu_\perp^+, \mu_\perp^-$, and $k_r n_0$. As will be shown later, only the products $\mu_\perp^+\mu_\perp^-$ and $k_r n_0$ are relevant, in most cases.

The dissociation constant K and the total mobility $\mu = \mu_\perp^+ + \mu_\perp^-$ (and thus n_0) were measured in MBBA doped with TBATPB [80] by fitting the experimentally obtained conductivity *vs.* concentration curve to the expression obtained from (3.4),

$$\sigma_\perp^{eq}(c) = e\mu n_0 = e\mu\beta_c c = \frac{e\mu K}{2}\left(\sqrt{1+4\frac{c}{K}} - 1\right). \tag{3.16}$$

The quantities μ, $k_D n_{AB} \approx k_d c$ and k_r were determined by measuring the stationary current and the current response to various voltage signals in electrodialytic cells with charge-absorbing BC [83]. Another group used the current response in cells with blocking BC to measure μ, n_0 and indirectly the diffusion constant D via the thickness of the diffusive boundary layers [84, 85, 86] which are assumed to decay exponentially with the Debye length λ_D, see Table 3.2. The resulting diffusivity is smaller by a factor of three than that obtained with the Einstein relation. As discussed in Chapter 4, the thickness of the diffusive boundary layers can be obtained also by measuring the capacitance as a function of the external frequency [31].

There exist also theoretical estimates for the mobility. In the simplest case one assumes that the dissipation leading to a finite mobility is caused by Stokes's friction of a sphere with the effective ion radius (of the order of 5 Å). For NLCs, the resulting mobilities are two to three orders of magnitude too high [80]. The correct order of magnitude is obtained [87] by assuming additional dissipation from the lag of the polarization cloud in the surrounding solvent [89]. This theory of "dielectric friction", however, predicts an isotropic mobility depending on microscopic parameters like the ion radius and the Debye relaxation time ($\approx 10^{-6}$ s in NLCs [29]) which causes the lag, It is applicable only to polar solvents (MBBA, not I52). Finally, the WEM relates the geometric mean $\sqrt{\mu_\perp^+\mu_\perp^-}$ to the Hopf frequency, see Chapter 5.

Table 3.1 contains a summary of relevant measurements. There seem to be no measurements of γ although this seems to be possible by the current-response experiments.

3.2.4 Intrinsic times and lengths, scaling

In the Table 3.2 I show the various intrinsic time, length and voltage scales of the WEM subsystems. One sees that the full WEM has the potential for rich behaviour.

Table 3.2: Intrinsic scales of the WEM

quantity	definition	typical value*
threshold voltage	$V_{c0} = \sqrt{\frac{K_{11}\pi^2}{\epsilon_0\epsilon_\perp}}$	2.63 V
thermal voltage	$V_T = \frac{k_B T}{e}$	26 mV
diffusion time	$\tau_{\text{diff}} = \frac{d^2}{D^{phys}} \approx \frac{V_{c0}}{V_T}\tau_t$	342 s
recombination time	$\tau_{\text{rec}} = (2k_r n_0)^{-1}$	$10^{-3}...2 \times 10^4$ s
carrier transition time	$\tau_t = \frac{d^2}{\mu V_{c0}}$	3.39 s
director relaxation time	$\tau_d = \frac{\gamma_1 d^2}{K_{11}\pi^2}$	0.561 s
charge relaxation time	$\tau_q = \frac{\epsilon_0\epsilon_\perp}{\sigma_\perp}$	5.35×10^{-3} s
momentum diffusion time	$\tau_{\text{visc}} = \frac{d^2\rho_m}{\gamma_1}$	6×10^{-6} s
diffusion layer	$\lambda_D = \sqrt{\frac{V_T\epsilon_0\epsilon_\perp}{2en_0}} = \sqrt{\frac{V_T\epsilon_0\epsilon_\perp\mu}{2\sigma_\perp^{eq}}}$	0.1 μm
* NLC I52 for $d = 28$ μm at $T = 40°$C (see Appendix A.1)		

Note that, by virtue of the Einstein law, the diffusion scales are not connected with new material parameters. It is useful to scale lengths, times, the electric potential and the total charge concentration in such a way that they become of the order of unity for EHC. The chosen scaling is given in Table 3.3. Many properties of the SM do not depend on the absolute values of the material parameters (in contrast to the WEM), so the material constants will be scaled as well. Dependent quantities are scaled accordingly, e.g., $\boldsymbol{E}$ in units of $V_{c0}\pi/d$ and ρ in units of $V_{c0}\pi^2\epsilon_0\epsilon_\perp/d^2$. Furthermore, it is sometimes useful to express the local conductivity in terms of the deviation from its equilibrium value,

$$\delta\sigma(\boldsymbol{r}, t) := \frac{\sigma_\perp(\boldsymbol{r}, t)}{\sigma_\perp^{eq}} - 1. \tag{3.17}$$

Unless explicitely stated otherwise, all variables with the exception of the scaling units $\epsilon_\perp, \sigma_\perp^{\text{eq}}, \gamma_1$, and K_{11} are understood as scaled variables in the rest of this thesis.

The resulting scaled WEM equations, which replace the SM equations (2.24)-(2.26), are an important building block of this work and the basis for the investigations in the next three chapters. They read

Table 3.3: Scaling

quantity	scaling unit	typical value *
lengths	d/π	$(10...100\mu\text{m})/\pi$
time	$\tau_d = \frac{\gamma_1 d^2}{K_{11}\pi^2}$	0.166 s $\left(\frac{d}{10\mu m}\right)^2$
voltage	$V_{c0} = \sqrt{\frac{\pi^2 K_{11}}{\sigma_\perp \tau_q}} = \sqrt{\frac{\pi^2 K_{11}}{\epsilon_0 \epsilon_\perp}}$	1.19 V
conductivities	$\sigma_\perp^{\text{eq}} = \mu e n_0$	$10^{-9}...10^{-7}(\Omega\text{m})^{-1}$
orientational elasticities	K_{11}	6.66×10^{-12}N
dielectric constants	$\epsilon_0 \epsilon_\perp$	4.65×10^{-11}As/Vm
viscosities	$\gamma_1 = \alpha_3 - \alpha_2$	0.109 kg (m s)$^{-1}$
* parameter set MBBA I (Appendix A.1)		

$$P_1(\partial_t + \boldsymbol{v}\cdot\boldsymbol{\nabla})\rho = -\boldsymbol{\nabla}\cdot(\underline{\underline{\mu}}'\boldsymbol{E}\sigma) + \tilde{D}\boldsymbol{\nabla}\underline{\underline{\mu}}'\boldsymbol{\nabla}\left(\rho + \frac{\tilde{d}\sigma}{2P_1\pi^2\tilde{\alpha}^2}\right) \quad (3.18)$$

$$(\partial_t + \boldsymbol{v}\cdot\boldsymbol{\nabla})(\sigma - \tilde{d}\rho) = -\tilde{\alpha}^2\pi^2\boldsymbol{\nabla}\cdot(\underline{\underline{\mu}}'\boldsymbol{E}\rho) + \frac{\tilde{D}}{P_1}\boldsymbol{\nabla}\underline{\underline{\mu}}'\boldsymbol{\nabla}\left(\sigma - \frac{\tilde{d}\rho}{2}\right) \quad (3.19)$$

$$- \frac{\tilde{r}}{2}\left[(\sigma+1)(\sigma-1) - \tilde{d}\rho\sigma - P_1\pi^2\tilde{\alpha}^2\rho^2\right]$$

$$(\partial_t + \boldsymbol{v}\cdot\boldsymbol{\nabla})\boldsymbol{n} = \boldsymbol{\omega}\times\boldsymbol{n} + \underline{\delta}^\perp\left(\lambda\underline{\underline{A}}\boldsymbol{n} - \boldsymbol{h}\right) \quad (3.20)$$

$$\frac{\tau_{\text{visc}}}{\tau_d}(\partial_t + \boldsymbol{v}\cdot\boldsymbol{\nabla})v_i = -\partial_i p - \partial_j(T_{ij}^{\text{visc}} + \pi_{ij}) + \pi^2\rho E_i, \quad (3.21)$$

The system parameters R, ω_0, P_1, $\tilde{\alpha}$ and $\tilde{r}$ are given in Table 3.4, $\tilde{d} = (P_1/\gamma)^{1/2}\pi(1-\gamma)\tilde{\alpha}$ is a mobility-difference parameter and $\tilde{D} = 4s_1(\pi\lambda_D/d)^2$ the scaled diffusion constant. [2] The constitutive equations for ρ, $\boldsymbol{h}$ and T_{ij}^{visc} are, respectively, given by $\boldsymbol{\nabla}\cdot(\underline{\underline{\epsilon}}\boldsymbol{E})$, Eq. (2.27), and Eq. (2.28) with the scaled material parameters and ϵ_a replaced by $\pi^2\epsilon_a$ in Eq. (2.27). The electric field

$$\boldsymbol{E} = \sqrt{2R}\cos\omega_0 t\hat{z} - \boldsymbol{\nabla}\phi \quad (3.22)$$

contains the two SM-control parameters. The fully rigid BC for homogeneous alignment and blocking electrodes are

[2] In contrast to the SM Eq. (2.24), the diffusion currents have been kept in Eqs. (3.18) and (3.19). The approximation of zero diffusivities is usually assumed in the bulk. This may not be justified for very thin cells where the thicknes of the boundary layers can become of the same order as d (Chapter 4.) Furthermore, in the dielectric regime where the size of the patterns can be $<< d$. the neglect of the diffusivities becomes questionable even in the bulk.

$$\int_{-\pi/2}^{\pi/2} dz\ E_z = \sqrt{2R}\cos\omega_0 t, \tag{3.23}$$

$$[J_z]_{z=\pm\pi/2} = \left[E_z\sigma - \tilde{D}\partial_z\left(\rho + \frac{\tilde{d}\sigma}{2P_1\pi^2\tilde{\alpha}^2}\right)\right]_{z=\pm\pi/2} = 0, \tag{3.24}$$

$$[J_z^\sigma]_{z=\pm\pi/2} = \left[-\tilde{\alpha}^2\pi^2 E_z\rho + \frac{\tilde{D}}{P_1}\partial_z(\sigma - \tilde{d}\rho/2)\right]_{z=\pm\pi/2} = 0, \tag{3.25}$$

$$\boldsymbol{n}(\pm\pi/2) = (1,0,0), \quad \boldsymbol{v}(\pm\pi/2) = 0. \tag{3.26}$$

3.3 Discussion

The physical contents of the new Eq. (3.19) is an excitation of the charge-carrier mode (σ mode) by the ρ mode $\propto \tilde{\alpha}^2$, diffusion $\propto \tilde{D} \propto \tilde{\alpha}^2$ and recombination $\propto \tilde{r}$. [3]

The WEM equations (3.18) - (3.26) contain much more parameters as other fluid-dynamical systems. For example, the scaled Boussinesq equations for RBC in simple fluids depend only on the Rayleigh number and the Prandtl number $\tau_{\rm therm}/\tau_{\rm visc}$. The WEM contains two "Rayleigh-number like" control parameters R and ω_0, four "Prandtl-number like" time-scale ratios of subsystems, P_1, $\tilde{\alpha}$, $\tilde{r}$ and $\tau_{\rm visc}/\tau_d$, one ratio of WEM material parameters, γ, and a total of eight ratios of SM material parameters, $K_{22}, K_{33}, \epsilon_\perp, \sigma_\perp$ and four viscosities.

Fortunately, the dynamics is mainly determined by the first two classes ("system parameters"), summarized in Table 3.4. The ratio $\tau_{\rm visc}/\tau_d$ can always be neglected (at least in the conductive range), i.e. the velocities can be adiabatically eliminated. In many cases, also the charge can be adiabatically eliminated, $P_1 = 0$.

The full WEM equations (3.18) to (3.21) seem too complex for direct theoretical investigations. Fortunately, the typical parameters given in the tables in the last section suggest some simplifications, depending on the particular situation. In the following, I discuss the approximations of zero diffusivity, of a linear recombination term and of zero mobility difference parameter $\tilde{d}$, which are used for the linear and nonlinear calculations in Chapters 4 - 6. The approximations are valid in the conductive regime, for not too extemely different mobilities and for $\tilde{\alpha} << 1$, i.e. for not too thin cells and not too high mobilities. In addition, I discuss the limits where the SM is recovered and relate various models used in the literature to special cases of the WEM.

[3] For a nonzero mobility difference, these effects act on a linear combination of the carrier and the charge-density fields, but it will be shown that the parts $\propto \tilde{d}$ can be neglected in most cases.

Table 3.4: System parameters of the WEM

parameter	physical process	MBBA#	I52##
$R = \frac{\overline{V}^2}{V_{c0}^2} = \frac{\overline{V}^2 \epsilon_0 \epsilon_\perp}{K_{11}\pi^2}$	control parameter	≥ 31	≥ 14
$\omega_0 P_1 = \omega_0^{phys} \tau_q = \frac{\omega_0 \epsilon_0 \epsilon_\perp}{\sigma_\perp}$	control parameter	$0 \cdots 2.5$	$0 \cdots 4$
$P_1 = \frac{\tau_q}{\tau_d} = \frac{\epsilon_0 \epsilon_\perp K_{11}\pi^2}{\sigma_\perp \gamma_1 d^2}$	charge relaxation	0.0095	0.00356
$\tilde{\alpha} = \frac{\sqrt{s_1 \tau_q \tau_d}\pi}{\tau_t} = \sqrt{\frac{\mu_\perp^+ \mu_\perp^- \gamma_1 \pi^2}{\sigma_\perp^{eq} d^2}}$	ion migration	0.0253	0.024
$\tilde{r} = \frac{\tau_d}{\tau_{\rm rec}} = 2k_r n_0 \tau_d$	recombination	0.05*	0.05*

Parameter set MBBA I with $d = 13\mu$m,
$\sigma_\perp = 10^{-8}(\Omega\text{m})^{-1}, \mu = 10^{-10} m^2/(Vs)$, $\gamma = 1$.
Parameters from Appendix A.1 for 40C; especially
$d = 28\mu$m, $\sigma_\perp^{eq} = 0.493 \times 10^{-8}(\Omega\text{m})^{-1}$, $\mu = 0.88 \times 10^{-10} m^2/(Vs)$, $\gamma = 1$.
* Estimates, see Chapter 5.5

3.3.1 Approximations for low mobilities in the conductive range

The thickness of the boundary layers, as deduced from the capacitance measurements [31], is about 1 μm. This is of the same order as the thickness of the boundary layer estimated from the WEM (see Chapter 4). The value of the diffusivity given directly in Table 3.1 as well as that obtained indirectly from the mobilities by the Einstein relation (3.8) lead to Debye lengths even well below 1 μm (Table 3.4). So it seems reasonable, to neglect the diffusive boundary layers, at least in the conductive range and for not too thin cells. There are some subtleties connected with the BC. The equations (3.23) to (3.25) lead to an overdetermined system and impose the BC $E_z = 0$ or $\rho = 0$ and $\sigma = 0$. This is, of course, plausible since the drift current cannot be balanced by a diffusive current to satisfy the blocking BC, so its z component must be zero. This is fulfilled either for $E_z = 0$ or, if there are no carriers at all. On the other hand, a vanishing diffusivity *and* a vanishing mobility (leaving $\sigma_\perp$ constant) means boundary layers of vanishing thickness representing a capacitor of infinite capacity. For the carriers, this is an infinite sink and leads, as in the SM, to "free" electric BC $\partial_z E_z = \partial_z \sigma = 0$, no matter what the real BCs are.

There is one *caveat* connected with ion drift. For zero dissociation and recombination, a DC voltage together with blocking BC would lead to a complete charge separation (the bulk is free of carriers) after the time $\tau_t/\sqrt{R}$. For a nonzero dissociation with $\tau_{\rm rec}/\tau_t << 1$, the total density of the (dissociated and non-dissociated)

impurities will decay on a (larger) time scale $\tau_t/(\sqrt{R}\beta_c)$ (electrodialysis). [4] With an AC voltage these separation effects occur only near the electrodes, within the distance over which a carrier can migrate in one half-cycle, see Eq. (4.6) below. For most experiments (especially for those on I52) this distance is comparable to that of the thickness of the diffusion layer and both boundary effects can be neglected.

If $\tilde{\alpha} << 1$ (which is fulfilled unless the mobilities are extremely high or the cell is extremely thin), the recombination term can be treated in linear order, even for nonlinear calculations. For EHC in the conductive regime, the typical amplitude of the carrier mode normalized to the charge-density mode is $||\sigma||/||\rho|| = \mathcal{O}(\pi\tilde{\alpha}^2\sqrt{R_c}/\tilde{r})$ or $\mathcal{O}(\pi\tilde{\alpha}^2\sqrt{R_c}/\omega_H) = \mathcal{O}(\pi\tilde{\alpha}/\sqrt{R_c})$, whichever is lower ($\omega_H$ is related to the Hopf frequency, Chapter 5 below and $||*||$ here denotes the amplitude). This means that even in the fully nonlinear regime where $||\rho|| = \mathcal{O}(1)$ all recombination terms in the bracket of (3.19) are of the order of $\tilde{\alpha}^2 << 1$.

The only mobility-difference term surviving the above approximations is that on the left-hand side of (3.19). If $\tilde{r}$ is sufficiently low, so that the condition for a Hopf bifurcation is fulfilled (Chapter 5), the relative magnitude $\tilde{d}||\rho||/||\delta\sigma|| = \mathcal{O}(P_1 R_c/\gamma)^{1/2}/(1-\gamma)/\pi)$ is usually small. In addition, the $\tilde{d}$ term has the z and time symmetry opposite to that of as the σ mode and does not couple back to the WEM mechanism. With all these approximations the WEM equations (3.18) - (3.20) become

$$P_1(\partial_t + \boldsymbol{v}\cdot\boldsymbol{\nabla})\rho = -\boldsymbol{\nabla}\cdot(\underline{\underline{\mu}}'\boldsymbol{E}\sigma) \tag{3.27}$$

$$(\partial_t + \boldsymbol{v}\cdot\boldsymbol{\nabla})\sigma = -\tilde{\alpha}^2\pi^2\boldsymbol{\nabla}\cdot(\underline{\underline{\mu}}'\boldsymbol{E}\rho) - \tilde{r}\delta\sigma, \tag{3.28}$$

$$(\partial_t + \boldsymbol{v}\cdot\boldsymbol{\nabla})\boldsymbol{n} = \boldsymbol{\omega}\times\boldsymbol{n} + \underline{\underline{\delta}}^{\perp}\left(\lambda\underline{\underline{A}}\boldsymbol{n} - \boldsymbol{h}\right), \tag{3.29}$$

$$\rho|_{z=\pm\pi/2} = \partial_z\sigma|_{z=\pm\pi/2} = 0. \tag{3.30}$$

3.3.2 The limit of the Standard Model

Equation (3.27) reduces to the charge conservation of the SM for $\sigma = 1$ or $\delta\sigma = 0$. Since the magnitude of $\delta\sigma$ scales with $\tilde{\alpha}^2/\tilde{r}$, this is the case for $\tilde{\alpha} \to 0$ while $\tilde{r} \neq 0$. In Chapter (3.3.1) it is argued that the boundaries behave effectively as the ohmic BC of the SM if the boundary layers have a thickness $<< d$. With the results from Chapter 4 this is fulfilled for $\tilde{\alpha} << 1$, $\tilde{\alpha}/\tilde{r} << 1$ and $\tilde{\alpha}\sqrt{P_1}/(\omega_0^{phys}\tau_q) << 1$ (ω_0^{phys} is the external frequency in unscaled physical units).

[4] In this and further order-of-magnitude estimates of drift distances, I assume, for simplicity, the upper bound μ for the mobility of the faster drifting charge-carrier species.

All above conditions for the SM limit can be summarized as

$$\tilde{\alpha} \to 0, \quad \tilde{r} \neq 0, \quad \omega_0 \neq 0. \tag{3.31}$$

3.3.3 Relation with models assuming fast recombination

In the limit of fast dissociation and recombination, the carrier mode can be adiabatically eliminated by setting the bracket of Eq. (3.19) equal to zero. Inserting the resulting $\sigma(\rho)$ into (3.18) (where in contrast to (3.27) the diffusivity is retained) leads to a "bipolar charge conservation" equation for ρ, which is different from the SM for $\tilde{\alpha} \neq 0$. Coupling this equation to an isotropic momentum balance equation (Eq. (3.21) with $\alpha_4 \to 2\eta$ and all other viscosities set equal to zero) gives for a DC voltage the model investigated by Turnbull [81]. Linear analysis for injecting (rather than blocking) BC gives a convective DC instability [81], which, of course, takes place also in isotropic fluids containing carriers.

In the unipolar limit $\rho \to \infty,\ n^+ >> n^-$ ($\rho \to -\infty,\ n^+ << n^-$) corresponding to strongly injecting electrodes, this model reduces to that considered by Felici and contains also a DC instability [90, 82].

At last, the fast-recombination limit of the WEM is obtained by coupling the bipolar charge conservation $\sigma(\rho)$ to the Eqs. (3.20) and (3.21) and assuming an AC voltage and blocking BC. This model leads to an increase for the threshold of EHC, but again, no Hopf bifurcation [91]. The threshold shift is plausible since, in contrast to the injecting BC for the DC instabilities [82, 90], the change of the volume force in the direction of the force is positive, $\rho E_z \partial_z(\rho E_z) > 0$ i.e. the volume forces of the basic state act in the stabilizing direction.

Chapter 4

Basic state

In contrast to the SM, the basic state of planar EHC in the WEM description is in general not trivial, i.e. $\sigma = 1$, $\phi = 0$, $\boldsymbol{n} = (1, 0, 0)$ and $\boldsymbol{v} = 0$ is not a solution of the WEM equations. For blocking electrodes this is obvious because charge conservation together with finite conductivity leads to an accumulation of charges near the electrodes. The only exception are plates having conductive properties as though the NLC would extend behind the electrodes to infinity in the z direction. Actually, this kind of "ohmic" BC is assumed in the SM. Any other BC lead to boundary layers (BL) with the general form

$$\sigma = \sigma_0(z,t) \equiv 1 + \delta\sigma_0(z,t), \quad \phi = \delta\phi_0(z,t), \quad \boldsymbol{n} = (1,0,0), \quad \boldsymbol{v} = 0. \tag{4.1}$$

Global properties of the BL can be measured. The component of the dipole momentum per area that is in phase with the external voltage leads for low frequencies to a deviation of the capacitance from its dielectric value; the component with a phase lag of $\pi/2$ leads to a contribution to the AC conductivity for low frequencies. Of course, the DC conductivity equals zero for blocking BC.

In Chapter 4.1 I formulate the problem and discuss general properties of the basic state. In the Chapters 4.2 and 4.3 the BLs arising from blocking BC are discussed in the limits of slow and fast recombination. The latter case has been investigated extensively in different contexts in the literature and I will show how the models used there are related to special cases of the WEM. Chapter 4.4 gives the current response of the NLC cell in the basic state for blocking BC in form of analytic approximations for the low-frequency behaviour of the capacitance and the conductivity. Fits to the experiments give a thickness of about 1 μm consistent with the values calculated with the WEM. It is concluded, that, at least in the I52 experiments, the BLs are not relevant for EHC. This means that, in a good approximation, the subsequent

linearization of the WEM in Chapter 5 can be carried out with respect to the trivial basic state. Thus the main part of the material contained in Chapter 5 is independent of the presentation in this chapter, and readers not interested in the problem of the basic state can continue with Chapter 5. The linear stability analysis starting from the nontrivial basic state is formulated in Appendix A.2.

4.1 Boundary layers

The investigations in this chapter are based on the general scaled WEM equations (3.18) and (3.19), without the approximations made in Chapter 3.3.1. The Eqs. (3.27) - (3.30) resulting from these approximations are the basis for the Chapters 5 and 6.

Inserting the ansatz (4.1) for the nontrivial basic state into the equations (3.18) and (3.19) results in

$$P_1\partial_t\rho_0 = -\partial_z\left(E_0\sigma_0\right) + D\partial_z^2\left(2s_1\rho_0 + \frac{d_1\sigma_0}{\alpha}\right), \tag{4.2}$$

$$\begin{aligned} P_1\partial_t(\sigma_0 - \alpha d_1\rho_0) &= -\alpha^2 s_1\partial_z(E_0\rho_0) + Ds_1\partial_z^2\left(2\sigma_0 - \alpha d_1\rho_0\right) \\ &- \frac{\tilde{r}P_1}{2}\left[\sigma_0^2 - 1 - \alpha d_1\rho_0 - \alpha^2 s_1\rho_0^2\right]. \end{aligned} \tag{4.3}$$

In contrast to the linearization in Chapter 5, the director relaxation plays no role, and the charge relaxation time rather than the geometric mean $\sqrt{\tau_q\tau_d}$ and the sum of the mobilities rather than their geometric mean is relevant for the basic state. Furthermore, the diffusion length in the basic state is directly related to λ_D. So I introduced as new mobility parameter the ratio of the charge relaxation time to the transition time for the mobility sum μ under the voltage V_{c0}, and as new diffusion parameter the scaled Debye length [92],

$$\alpha = \frac{\tau_q}{\tau_t}\pi^2 = \frac{\mu V_{c0}\tau_q\pi^2}{d^2} = \sqrt{\frac{P_1\pi^2}{s_1}}\tilde{\alpha}, \tag{4.4}$$

$$D = 2\left(\frac{\pi\lambda_D}{d}\right)^2 = \frac{\tilde{D}}{2s_1}. \tag{4.5}$$

Assuming $\gamma = 1$, α varies from 0.016 for $T = 30°\mathrm{C}$ to 0.0032 for $T = 60°\mathrm{C}$ and $D \approx 0.01\alpha$ in the I52 experiments [31, 42]. Equations (4.2) and (4.3) are a set of partial differential equations with inhomogeneous BC for $\rho_0 = -\partial_z^2\phi_0$ and σ_0. With respect to the z derivatives, they are of forth order in ϕ_0 and of second order in σ_0. The necessary six BC are $\phi_0(z = \pm\pi/2, t) = 0$, and the four BCs (3.24) and (3.25).

The nonlinearities arise from the recombination terms in the bracket and from the "drift advection terms" $\partial_z(E_0\rho_0)$ and $\partial_z(E_0\sigma_0)$.

A first estimate of the (scaled) BL thickness, valid for any recombination rates, is set by the amplitude λ_{mig} of the carrier-drift oscillations under the AC field, [1].

$$\lambda_{mig} = \frac{\alpha\sqrt{R}}{\pi\omega_0^{phys}\tau_q}. \tag{4.6}$$

Since the charge-density parts of the BL relax while they migrate, the effective thickness of the ρ-BL caused by the drift effects cannot exceed the distance $\lambda_q = \alpha\sqrt{R}$ travelled in one charge relaxation time.

4.2 Estimates for slow recombination

Assuming $\tau_{\rm rec} >> \tau_q$, the carrier-density mode cannot follow the oscillations of the external field, so $\sigma_0(z)$ is assumed to be approximately constant in time. The blocking BC induce oscillating charges, so $\rho_0(z,t)$ oscillates with the external field. We are only interested whether there are boundary layers that are much thicker than the ρ-BL whose thickness is bounded by λ_{mig}, Eq. (4.6). Outside the ρ-BL, the Eqs. (4.2) and (4.3) can be linearized. The ansatz

$$\begin{array}{ll} \rho_0 & = (\rho_0^+ \cos\omega_0 t + \rho_0^- \sin\omega_0 t)e^{-k(z-\pi/2)}, \\ \delta\sigma_0 & = \sigma_0^0 e^{-k(z-\pi/2)} \end{array} \tag{4.7}$$

leads to three eigenvalues k_n corresponding to three characteristic lengths $\lambda_{\rm BL,n} = 1/k_n$. There are two modes dominated by ρ with $\lambda_{\rm BL}$ of the order of λ_D, and much less than λ_D, respectively. The third mode dominated by σ has the decay length

$$\lambda_{BL,\sigma} = \sqrt{\frac{s_1(R\alpha^2 + 2D)}{\tilde{r}P_1}}. \tag{4.8}$$

For a zero electric field, the three modes are decoupled and $\lambda_{BL,\sigma}$ results from the interplay of diffusion and recombination relaxation of the σ field. For $\tilde{r} = 0.05$ relevant for an experiment using I52 (see Chapter 5.5), the thickness of the σ-BL would be nearly 40% of the cell thickness, but this mode is not excited for blocking BC. Nevertheless, this problem should be investigated numerically.

[1] In this estimate, $2\sqrt{2}/\pi$ is set equal to one.

4.3 Limit of fast recombination

If $\tau_{\rm rec} << \omega_0^{-1}$ and $\tau_{\rm rec} << \tau_d$, the carriers are in local equilibrium with respect to the dissociation-recombination reaction so that $n^+n^- = n_0^2$. This corresponds to $\tilde{r} \to \infty$, i.e., the bracket in Eq. (4.3) must become zero. This is automatically fulfilled by expressing the carrier densities in terms of the "diffusion potential" u, defined by $n^\pm = n_0 e^{\pm u}$, or

$$\rho_0(u) = \frac{2\sinh u}{\alpha}, \tag{4.9}$$

$$\sigma_0(u) = \frac{e^u + \gamma e^{-u}}{1+\gamma}. \tag{4.10}$$

The right-hand side of (4.2) becomes $-\partial_z J_0$ where the current is given by

$$J_0(u) = \sigma_0(u)\left[E_0 - \frac{D}{\alpha}\partial_z u\right] = \sigma_0(u)\left[E_0 - \frac{V_T}{V_{c0}}\partial_z u\right], \tag{4.11}$$

and Eq. (4.2) itself can be written as

$$P_1 \partial_t \sinh u = -\sigma_0(u)\left[\frac{\alpha}{2}\ \frac{J_0(u)\partial_z\sigma_0(u)}{\sigma_0^2(u)} + \sinh u - \frac{D}{2}\partial_z^2 u\right]. \tag{4.12}$$

The form of the current is obvious from the derivation of the WEM. In the fast-recombination limit, the thermodynamic forces $\boldsymbol{F}^\pm$, Eqs. (3.6), are given by $\boldsymbol{F}^\pm = \mp e\boldsymbol{\nabla}(\tilde{\phi_0} + V_T u)$, so $J_0 = \mu_\perp^+ \partial_z F_z^+ - \mu_\perp^- \partial_z F_z^- = \sigma_\perp \partial_z (E_0 - V_T \partial_z u)$, which is just Eq. (4.11) in physical units.

The electric field in the Eqs. (4.11) and (4.12) is given by

$$E_0(z,t) = E_b(t) + \int_{-\pi/2}^{z} dz \rho_0(u) \tag{4.13}$$

where the field $E_b(t) = E_0(z = -\pi/2)$ is determined by the condition $J_0(u) = 0$ at $z = -\pi/2$ with J_0 from Eq. (4.11). After some transformations using the condition of overall neutrality $E_0(z = -\pi/2) = E_0(z = \pi/2)$, the result is

$$E_b(t) = \frac{1}{\pi}\left(p(t) - \sqrt{2R}\cos\omega_0 t\right), \tag{4.14}$$

$$p(t) = \int_{\pi/2}^{\pi/2} dz z \rho_0 = 2\int_{\pi/2}^{\pi/2} dz z \frac{\sinh u}{\alpha}. \tag{4.15}$$

$p(t)$ has the physical meaning of a dipole momentum per area.

Equation (4.12) with (4.11), (4.9) and (4.10) represents a partial integro-differential equation for the field $u(z,t)$. The "integro" part comes from the electric field, Eq.

(4.13) and the BC (4.14). It was solved numerically with a finite-difference method in real space. The z derivatives are represented as centered differences of second order and the integral parts are calculated using the trapezoid rule. For the time steps, an implicit second-order Crank-Nicholson method was applied for all local terms and an Euler step for the nonlocal parts. For the numerical calculations [93], space was scaled by λ_D, time by τ_q and the voltage by V_T, and then the equations (4.12) and (4.14) take the compact form ($u' \equiv \partial_z u$)

$$\partial_t \sinh u = -\sigma_0(u)[\sinh u - u''] + \left[u' - u'_b - \int_0^z dz \sinh u\right] \frac{\partial \sigma_0}{\partial u} u', \quad (4.16)$$

$$u'_b = \frac{\lambda_D}{d}\left[\int_{-d/2\lambda_D}^{d/2\lambda_D} dz z \sinh u - \frac{\overline{V}\sqrt{2}}{V_T}\cos \omega_0^{phys} \tau_q t\right]. \quad (4.17)$$

Note that in this scaling the integro-PDE itself contains only the ratio γ while the BC (4.17) contains the three system parameters of the basic state, $\frac{d}{\lambda_D}$, $\frac{\overline{V}}{V_T}$ and $\omega_0^{phys}\tau_q$. The BCs are implemented by calculating from (4.17) two "virtual" points just one grid unit outside of either electrode and using these points in the z derivatives of the next step. As initial conditions, all fields were set equal to zero and several external periods (typically 10 corresponding to 10^4 time steps) were simulated before the actual period which is plotted to obtain approximately steady-state conditions.

In the following, I present results for $\gamma = 1$. In this case, further simplifications are possible (see below), which are not essential for the numerical solution, but can be used to make contact with previous work.

Figure 4.1 (a) shows the field $u(z,t)$ and Figure 4.1 (b) the electric field $E_0(z,t)$ in the WEM scaling for the parameters $d/\lambda_D = 26$, $\overline{V}/V_T = 143$, and $\omega_0^{phys}\tau_q = 0.2\pi$. Figure 4.2 shows $u(z,t)$, $E_0(z,t)$, and the local current density $I_0(z,t)$, for a higher frequency of the AC voltage. In physical units, the voltage is half of the threshold voltage in the MBBA experiments [39, 40]. The thickness of 13μm in these experiments corresponds to $\lambda_D = 0.5$ μm or, with the formula for λ_D in Table 3.2 and for $\sigma_\perp = 10^{-8}(\Omega\mathrm{m})^{-1}$, to $\mu = 3 \times 10^{-9}\mathrm{m}^2/(\mathrm{Vs})$.

Since in a rather large part of the bulk region the fields are nearly those of the trivial SM state, the electric field in units of V_T/λ_D, rather than the voltage, determines the dynamics of the BLs. The spatio-temporal behaviour of the scaled fields in the Figs. 4.1, 4.2, and Fig. 4.3 is invariant under a transformation $\overline{V} \to \beta\overline{V}'$, $\lambda_D \to \beta^{-1}\lambda'_D$ corresponding to $\mu \to \beta^{-2}\mu'$.

Figure 4.3 illustrates how the blocking BCs lead to a charge accumulation. In contrast to strongly injecting electrodes which can lead to the Felici instability [82], the blocking BC lead to a volume force which points always towards the electrodes and thus acts stabilizing.

Figure 4.1 (a) Diffusion potential u = $\ln(n^+/n^-)$ and (b) local electric field, $\boldsymbol{E} = E_0\hat{\boldsymbol{z}}$ of the WEM basic state in the fast-recombination limit for blocking electrodes and for an applied voltage corresponding to half of the threshold voltage. Assumed is an Debye length of $\lambda_D = 0.5$ μm .

Figure 4.2 (a) Diffusion potential, (b) local electric field, and (c) local current for the MBBA cell of Fig. 4.1 above, but for a higher external frequency of $\omega_0 \tau_q = \pi$.

Note that, in principle, Equation (4.12) can be written as a PDE of third-order with respect to the z derivatives by solving for E_0, differentiating both sides, and setting $\partial_z E_0 = \rho_0 = 2\sinh u/\alpha$. This form is, however, numerically less stable.

Special cases

For equal mobilities ($\gamma = 1$), the condition $n^+n^- = n_0^2$ can be written as $\sigma_0 = (1+\tilde{\rho}_0^2)^{1/2}$ and (4.2) becomes

$$P_1\partial_t\tilde{\rho}_0 = -\tilde{\rho}_0\sqrt{1+\tilde{\rho}_0^2} - \frac{\alpha E_0\tilde{\rho}_0}{2\sqrt{1+\tilde{\rho}_0^2}}\partial_z\tilde{\rho}_0 + \frac{D}{2}\partial_z^2\tilde{\rho}_0. \tag{4.18}$$

The three terms on the right-hand side can be interpreted as relaxation of the charges with the linear relaxation rate enhanced by a factor of $(1+\tilde{\rho}_0^2)^{1/2}$, while the carriers drift with the velocity μ^+E_0 of either species times a factor $\tilde{\rho}_0/(1+\tilde{\rho}_0^2)^{1/2}$, and diffuse with a constant rate. The slowing down of the effective velocity for decreasing $\tilde{\rho}_0^2$ is illustrated by the "charge wave" in Fig. 4.2 for t=0...π near the left electrode and in Figure 4.3, where the charge wave moves quickly to the right if $\tilde{\rho}_0^2$ is large (Figures 4.3a - 4.3c) and slows down and eventually relaxes (Figures 4.3d and 4.3e).

In the stationary case (DC driving), charge conservation implies a constant current and Eq. (4.12) reduces to the condition that the bracket be zero. Neglecting diffusivities, this condition can be writen as

$$du\left(\frac{e^u - \gamma e^{-u}}{(e^u+\gamma e^{-u})^2(e^u-e^{-u})}\right) = -\frac{dz}{J_0\alpha(1+\gamma)}. \tag{4.19}$$

The integration gives the rather lengthy Eq. (14) in Ref. [81]. In the unipolar limit this gives the well-known basic state $\rho_0 = (J_0/(2\alpha)^{1/2}$ of the Felici instability [82].

At last, the linearization of (4.12) in the stationary limit ($E_0 = \sqrt{R}/\pi$) gives two decay length scales associated with the combined effects of diffusion, drift and relaxation.

4.4 Low-frequency behaviour of the resistance and the capacitance

Throughout this section I use unscaled (physical) units. The general current response for any BC is the sum of the conductivity current and the displacement current. For a NLC cell with an area A in the x and y directions, one obtains

$$I(t) = A\left[j_z + \partial_t\epsilon_0\left(\underline{\underline{\epsilon}}\boldsymbol{E}\right)_z\right], \tag{4.20}$$

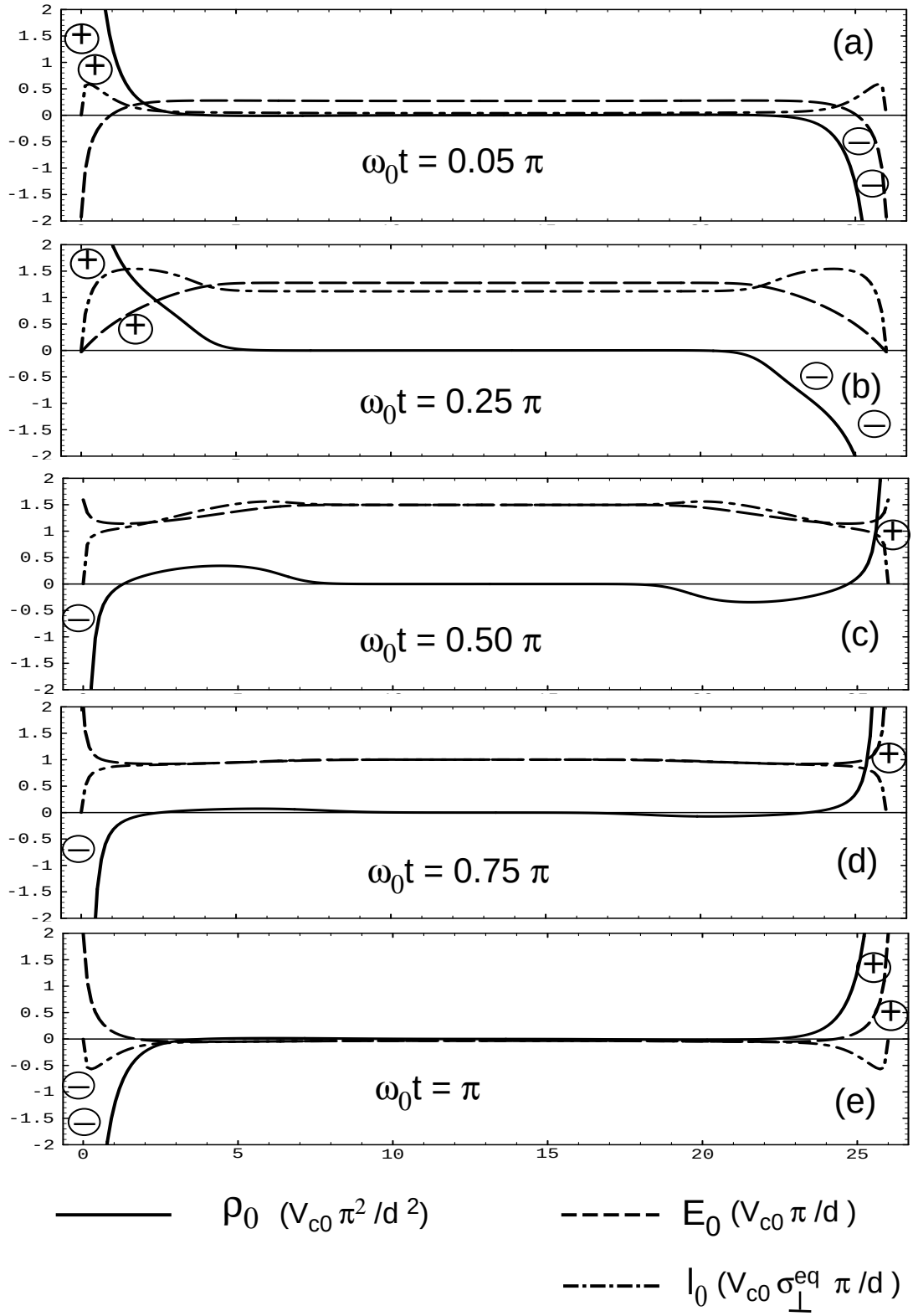

Figure 4.3 Snapshots of the WEM basic state of Fig. 4.1 for five times covering a half period. Shown is the space charge $\tilde{\rho}_0 = \sinh u$ (solid), the local field E_0 (dashed), and the local current I_0 (point-dashed).

where $\boldsymbol{j}$ and $\partial_t \epsilon_0 \underline{\underline{\epsilon}} \boldsymbol{E}$ are the conductivity and displacement currents. With the help of charge conservation, Eq. (4.20) can be transformed into

$$I(t) = A\left[\overline{j}_{BC} + \partial_t\left(\epsilon_0\overline{\epsilon_{3j}E_j} + \frac{p(t)}{d}\right)\right], \tag{4.21}$$

where $\overline{x}$ denotes the average of the quantity x over the cell volume and $\overline{j}_{BC}$ is the horizontally averaged current density through the boundaries ($\overline{j}_{BC} = 0$ for blocking BC). Overall neutrality implies $\overline{j}_{BC}(z = -d/2) = \overline{j}_{BC}(z = +d/2)$.

Below threshold, the averaged displacement current $\epsilon_0\partial_t\overline{\epsilon_{3j}E_j} = \epsilon_0\epsilon_\perp\partial_t V(t)/d$ is strictly in phase with the time derivative of the voltage and leads to the dielectric capacitance. For blocking BC, all nontrivial parts of the resistance and the capacitance are related to $p(t)$.

4.4.1 AC Resistance and capacitance

The AC resistance R [2] and capacitance C are defined by the Fourier-transformed current response $I(\omega)$,

$$\frac{1}{R} = \mathrm{Re}\frac{I(\omega)}{V(\omega)}, \tag{4.22}$$

$$C = \frac{1}{\omega}\mathrm{Im}\frac{I(\omega)}{V(\omega)}. \tag{4.23}$$

With Eq. (4.21), one arrives at

$$\frac{1}{R} = \frac{A}{d}\left[-\omega\mathrm{Im}\left(\frac{p(\omega)}{V(\omega)}\right) + \mathrm{Re}\left(\frac{\overline{j}_{BC}(\omega)d}{V(\omega)}\right)\right], \tag{4.24}$$

$$C = C_{diel} + \frac{A}{d}\left[\mathrm{Re}\left(\frac{p(\omega)}{V(\omega)}\right) + \frac{1}{\omega}\mathrm{Im}\left(\frac{\overline{j}_{BC}(\omega)d}{V(\omega)}\right)\right], \tag{4.25}$$

where $C_{diel} = A\epsilon_0\epsilon_\perp/d$.

4.4.2 Analytic approximations for blocking boundaries

The considerations in the previous sections show, that in a good approximation $\lambda_{\mathrm{BL}} << 1$ for the relevant modes. In addition, I assume for the BLs the functional form

$$\rho_0 = \rho_l(t)e^{-(z-d/2)/\lambda_{BL}} + \rho_r(t)e^{-(d/2-z)/\lambda_{BL}}, \quad \rho_l = -\rho_r. \tag{4.26}$$

[2] In this section, R is not the control parameter

(in view of, e.g., Figure 4.1, this is a rather crude approximation). Charge conservation leads to a dynamical equation for ρ_l which can be expressed as one for the dipole moment per area,

$$\partial_t p = -\frac{2\lambda_{BL}}{\tau_q d} p + V(t)\sigma_\perp. \tag{4.27}$$

Substituting this into (4.24) and (4.25) yields the result

$$R = R_\infty \left(1 + \left(\frac{\lambda'}{\omega_0 \tau_q}\right)^2\right), \tag{4.28}$$

$$C = C_{diel} \left(1 + \frac{\lambda'}{(\omega_0 \tau_q)^2 + \lambda'^2}\right), \tag{4.29}$$

where $R_\infty = d/(A\sigma_\perp)$ is the high-frequency resistance and $\lambda' = 2\lambda_{\mathrm{BL}}/d$ is the fraction of the cell volume occupied by the BLs.

Fitting these relations to the capacitance and resistivity measurements of Dennin [31] gives an effective thickness of the charge BL of about 0.9 μm . In the experiments, the external frequency always satisfies $\omega_0^{phys}\tau_q >> \lambda'$, so Eq. (4.29) predicts $C - C_{diel} \approx \lambda'/(\omega_0^{phys}\tau_q)^2$. The measured low-frequency behaviour, however, fits better to a $(\omega_0^{phys}\tau_q)^{-1}$ law. The discrepancy is possibly a result of the the crude approximation (4.26).

Chapter 5

Linear analysis

In this chapter, I present the linearization of the WEM in the conductive range which is for materials with $\epsilon_a < 0$ restricted to relatively low external frequencies. The emphasis lies on approximate analytic results, to see the functional dependence of the various quantities. After several approximations (well-controlled for usual parameter ranges), one arrives at a linear $2\times$ 2 normal form for the amplitudes of the charge-carrier mode and of the critical conductive mode of the SM. Solving this 2×2 equation with the ansatz $e^{\lambda t}$ leads at threshold (Re λ =0) for certain ranges of the system parameters to a nonzero imaginary part ω_H which can be identified as the Hopf frequency. More specifically, the condition for the Hopf bifurcation is $\tilde{r} < R_c\tilde{\alpha}C'$ (where C' is of the order of unity) and if this condition is well satisfied, ($\tilde{r} \leq 0.5R_c\tilde{\alpha}C'$ will do for practical purposes), the Hopf frequency is proportional to $\tilde{\alpha} \propto \sqrt{\mu_\perp^+\mu_\perp^-}$ and has a functional dependence on the external frequency ω_0 depending only on SM parameters.

These predictions are compared with two sets of experiments employing the NLCs MBBA and I 52. The dependence of the Hopf frequency and of the capacitance on ω_0 agrees nearly quantitatively with the experiments and the fit to the frequency of the measured travelling waves gives a geometric mean of the mobilities of about $1.6 \times 10^{-10}\mathrm{m}^2/(\mathrm{Vs})$ for MBBA and of $0.45 \times 10^{-10}\mathrm{m}^2/(\mathrm{Vs})$ for I 52, consistent with the reported data of Table 3.1. The mechanism leading to a Hopf bifurcation is quite similar to that of other periodic-oscillatory pattern-forming systems. This will be discussed by comparing the WEM with three thermal convection systems.

As a "by-product" of this approach, an analytic approximation of the three-dimensional linear stability analysis of the SM, performed some time ago [47, 48], is given in the form of a new, intuitive threshold formula.

Readers not interested in the details of the linearization of the SM and the WEM

(or who are abhorred by longer equations) can start with the 2×2 equations (5.38) in Chapter 5.4, bearing in mind that this system results from the basic equations by applying a Fourier transform in x, y, and in time, a lowest-order Galerkin expansion, and adiabatically eliminating the velocities and the charge density.

5.1 Linearization of the WEM equations

We decompose the fields of the scaled WEM model, Eqs. (3.18) - (3.21) into the basic state Eq. (4.1), denoted by an index 0, and into linearized perturbations, denoted by a superscipt $^{(1)}$. The basic state is a superposition of the trivial basic state (basic state of the SM together with $\sigma = 1$) and of the WEM boundary layers which are denoted by δ,

$$\begin{array}{lll} \boldsymbol{E} & = E_0(z,t)\boldsymbol{e}_z - \boldsymbol{\nabla}\phi^{(1)}(\boldsymbol{r},t) & = [\pi^{-1}\sqrt{2R}\cos\omega_0 t + \delta E_0(z,t)]\boldsymbol{e}_z - \boldsymbol{\nabla}\phi^{(1)}(\boldsymbol{r},t), \\ \rho & = \delta\rho_0(z,t) + \rho^{(1)}(\boldsymbol{r},t) & = \delta\rho_0(z,t) + \hat{\epsilon}\phi^{(1)} + \epsilon_a E_0 \partial_x n_z^{(1)}, \\ \sigma & = \sigma_0(z,t) + \sigma^{(1)}(\boldsymbol{r},t) & = 1 + \delta\sigma_0(z,t) + \sigma^{(1)}(\boldsymbol{r},t), \\ \boldsymbol{n} & = (1,0,0) + (0, n_y^{(1)}, n_z^{(1)}), & \\ \boldsymbol{v} & = \boldsymbol{v}^{(1)}. & \end{array} \tag{5.1}$$

The charge density of the boundary layers is denoted with $\delta\rho_0 = \partial_z \delta E_0$, and $\hat{\epsilon} = -\epsilon'_{ij}(\boldsymbol{n}_0)\partial_i\partial_j = -(\boldsymbol{\nabla}^2 + \epsilon_a\partial_x^2)$. The linearized WEM equations are obtained by inserting the decomposition (5.1) into the Eqs. (3.18) - (3.21) and the BCs (3.23) – (3.26). For a nontrivial basic state, these equations are rather lengthy. They are given for normal rolls in Appendix A.2.

In the following, I assume the trivial SM basic state which is a good approximation if the cell thickness is much larger than the sum of the thicknesses of the two BLs, $2d_{BL} \leq 2\ \mu$m (Chapter 4). Furthermore, I neglect all diffusivity terms, a good approximation if the smallest length scale of the rolls is much larger than the Debye length, $2\pi/|\boldsymbol{q}_c| >> 0.2\ \mu$m , which is always fulfilled in the conductive range. The intrinsic time scale of the velocities, given by the diffusion time τ_{visc} in Table 3.2, is always negligibly small compared to the director relaxation time, so the velocities can be adiabatically eliminated by setting $(\partial_t + \boldsymbol{v}\cdot\boldsymbol{\nabla})\boldsymbol{v}$ equal to zero in the momentum-balance equations.

After a Fourier transform of the linearized WEM fields $\boldsymbol{u}^{(1)} \equiv (\phi^{(1)}, \sigma^{(1)}, n_z^{(1)}, n_y^{(1)}, \boldsymbol{v}^{(1)})$,

$$\boldsymbol{u}^{(1)}(\boldsymbol{r},t) = e^{iq\cdot x}\overline{\boldsymbol{u}}(z,t) + \text{c.c.}, \tag{5.2}$$

the equations of the linearized WEM equations for the charge density, the local conductivity, the director fields n_z and n_y, the z and y components of the curl of the

momentum balance, and the incompressibility condition, are given by

$$
\begin{aligned}
[P_1\partial_t\hat{\epsilon}_q+\hat{\sigma}_q]\,\overline{\phi}+E_0\partial_z\overline{\sigma}+\left[P_1\epsilon_a(\dot{E}_0+E_0\partial_t)+\sigma_aE_0\right]iq\overline{n}_z &= 0, && (5.3)\\
\left[\tilde{\alpha}^2\pi^2E_0\partial_z-\tilde{d}\partial_t\right]\hat{\epsilon}_q\overline{\phi}+[\partial_t+\tilde{r}]\,\overline{\sigma}+\left[\epsilon_a(\tilde{\alpha}^2\pi^2E_0^2\partial_z-\tilde{d}\partial_tE_0)\right]iq\overline{n}_z &= 0, && (5.4)\\
-\epsilon_a\pi^2E_0q^2\overline{\phi}+\left[\partial_t+\hat{K}_{zz}-\epsilon_a\pi^2E_0^2\right]iq\overline{n}_z+\hat{K}_{zy}p\overline{n}_y & && \\
+\alpha_3iq\partial_z\overline{v}_x+|\alpha_2|q^2\overline{v}_z &= 0, && (5.5)\\
-\hat{K}_{zy}ip\overline{n}_z+\left[\partial_t+\hat{K}_{yy}\right]qn_y+\alpha_3iqp\overline{v}_x-|\alpha_2|q^2i\overline{v}_y &= 0, && (5.6)\\
\alpha_3p\partial_z\partial_t\overline{n}_z-\left[\alpha_2q^2-\alpha_3p^2\right]\partial_ti\overline{n}_y & && \\
-\left[(\eta_0-\eta_1-\alpha_2)q^2+\eta_2(p^2-\partial_z^2)\right]p\overline{v}_x & && \\
+\left[\eta_1q^2-(\eta_2-\alpha_3-\alpha_4)p^2-\frac{\alpha_4}{2}\partial_z^2\right]q\overline{v}_y+\left[q(\eta_2-\alpha_3-\frac{\alpha_4}{2})\partial_z\right]ip\overline{v}_z &= 0, && (5.7)\\
-\pi^2E_0q^2\hat{\epsilon}_q\overline{\phi}-\left[(\alpha_2q^2+\alpha_3\partial_z^2)\partial_t+\epsilon_a\pi^2E_0^2q^2\right]iq\overline{n}_z & && \\
+\alpha_3pq\partial_z\partial_t\overline{n}_y+\left[(\eta_0-\eta_1-\alpha_2)q^2+\eta_2(p^2-\partial_z^2)\right]\partial_ziq\overline{v}_x & && \\
+\left[q(\eta_2-\alpha_3-\frac{\alpha_4}{2})\partial_z\right]iqp\overline{v}_y+\left[(\eta_2-\alpha_3-\alpha_4)\partial_z^2+\eta_1q^2+\frac{\alpha_4}{2}p^2\right]q^2\overline{v}_z &= 0, && (5.8)\\
iq\overline{v}_x+ip\overline{v}_y+\partial_z\overline{v}_z &= 0, && (5.9)
\end{aligned}
$$

where

$$
\begin{aligned}
\hat{\epsilon}_q &= (1+\epsilon_a)q^2+p^2-\partial_z^2, \quad \hat{\sigma}_q=(1+\sigma_a)q^2+p^2-\partial_z^2, && (5.10)\\
\hat{K}_{zz} &= K_{33}q^2+K_{22}p^2-\partial_z^2, \quad \hat{K}_{zy}=(1-K_{22})q\partial_z, & \\
\hat{K}_{yy} &= K_{33}q^2+p^2-K_{22}\partial_z^2, && (5.11)\\
\eta_1 &= (-\alpha_2+\alpha_4+\alpha_5)/2, \quad \eta_2=(\alpha_3+\alpha_4+\alpha_6)/2, & \\
\eta_0 &= \alpha_1+\alpha_4+\alpha_5+\alpha_6. && (5.12)
\end{aligned}
$$

The coefficients η_1, η_2, and $\alpha_4/2 := \eta_3$ are sometimes called Miesowicz coefficients and can be measured directly by simple shear experiments (see, e.g., [25]). The BCs at $z=\pm\pi/2$ are

$$\overline{\phi}=\partial_z\overline{\sigma}=\overline{n}_z=\overline{n}_y=\overline{\boldsymbol{v}}=0. \tag{5.13}$$

The SM part of this set is given, with a different scaling, in Eqs. (3.2a-f) of Ref. [48]. The transformations $\phi\to\pi\overline{\phi}$, $\theta\to-i\overline{n}_z$, $\psi\to\overline{n}_y$, $v_{x/y}\to-i\overline{v}_{x/y}$, $v_z\to\overline{v}_z$, $\sqrt{2}/\pi\overline{V}e^{i\omega t}\to\pi E_0$, $\overline{V}^2/\pi^2(1+e^{2i\omega t})\to\pi^2E_0^2$, $d\to\pi$, $\partial_t\to P_1\partial_t$ in Eq. (3.2a), $\rho_md^2/\pi^2\to P_2\approx 0$, and ϵ_0, $\epsilon_\perp$, $\sigma_\perp$, γ_1, and K_{11} set to unity, brings these equations into our notation.

5.2 Approximate analytic approach

Equations (5.3) - (5.9) with $\pi E_0 = \sqrt{2R}\cos\omega_0 t$ [see Eq. (5.1) for the trivial basic state $\delta\boldsymbol{E}_0 = 0$] represent a linear system with periodic coefficients allowing the Floquet ansatz

$$\overline{\boldsymbol{u}}(z,t) = \tilde{\boldsymbol{u}}(z,\omega_0 t)e^{\lambda(\boldsymbol{q},R)t} = \Sigma_n \tilde{\boldsymbol{u}}^{(n)}(z)e^{[\lambda(\boldsymbol{q},R)+in\omega_0]t}, \tag{5.14}$$

where the Floquet functions $\tilde{\boldsymbol{u}}$ are 2π periodic in the second argument. Of course, there are infinitely many branches $m = 1, 2, ...$ with growth rates $\lambda_m(\boldsymbol{q}, R)$. The special symmetries of the SM (without flexoeffect) lead to a separation of the eigenspace of the SM modes into four orthogonal subspaces, called IA, IB, IIA, IIB in [52, 94]. In class I, ("symmetric"), the fields $\tilde{\phi}, \tilde{n}_z, \tilde{v}_z$ are symmetric in z while the horizontal components of $\tilde{\boldsymbol{n}}$ and $\tilde{\boldsymbol{v}}$ are antisymmetric. In class A ("conductive"), the electric fields $\tilde{\phi}, \tilde{\rho}$, etc. are antisymmetric with respect to a time translation by a half external period, $t \to t + \pi/\omega_0$, and all other fields are symmetric. In class II ("antisymmetric") and B ("dielectric"), the symmetries are opposite. The terms $\propto \tilde{\alpha}$ in the WEM equation (5.4) retain this symmetry separations. The σ field corresponding to the IA modes of the SM is antisymmetric in z and symmetric with respect to the time translation $t \to t + \pi/\omega_0$. The terms $\propto \tilde{d}$ in (5.4) couple the IA to the IIB modes and the IB to the IIA modes. In particular, the ϕ field of the IA mode excites a σ field symmetric in z and antisymmetric with respect to $t \to t + \pi/\omega_0$ which couples back to the ϕ field of the IIB mode of the SM. Like the flexoelectric terms [94], the terms $\propto \tilde{d}$ break both symmetries while retaining the symmetry with respect to a simultaneous reflexion in z and time translation by a half external period. Usually, the terms $\propto \tilde{d}$ are small (see Chapter 3.3) and will be neglected in the following. This corresponds to a linearization of the simpler equations (3.27) – (3.30) together with the fluid equation (3.21) and the BCs (3.26), instead of the Eqs. (3.18)-(3.26).

To obtain analytic results for the conductive regime (where the IA mode has the lowest threshold), I apply to the Floquet functions the "lowest-order Fourier expansion" in time, where only the lowest-order nontrivial IA contributions of each field are retained [48]. The approximation is justified if $\tau_d >> 2\pi/\omega_0 >> \tau_q$ [48] i.e. necessarily $P_1 = \tau_q/\tau_d << 1$, which is usually fulfilled.

After eliminating $\overline{v}_x$ by the incompressibility condition (5.9), the z dependence of each field is approximated by a test function satisfying the symmetries and the BC (which can be seen as a lowest-order Galerkin expansion). Specifically, I represent the fields by the following lowest-order terms of the combined Fourier expansion in t and Galerkin expansion in z,

$$\tilde{\boldsymbol{u}}(z,\omega_0 t)=\sqrt{\frac{2}{\pi}}\begin{pmatrix}\sigma^{(0)}\sin z\\ \cos z(\phi^+\cos\omega_0 t+\phi^-\sin\omega_0 t)\\ n_z^{(0)}\cos z\\ n_y^{(0)}\sin 2z\\ v_y^{(0)}\sin 2z\\ v_z^{(0)}\sqrt{\frac{\pi}{2}}C_1(z)\end{pmatrix}, \tag{5.15}$$

where ϕ^+ and ϕ^- are defined by (compare Eq. (5.14)) $\phi^+\cos z=\tilde{\phi}^{(1)}+\tilde{\phi}^{(-1)}$, $\phi^-\cos z=i(\tilde{\phi}^{(1)}-\tilde{\phi}^{(-1)})$, and $C_1(z)$ is the lowest-order Chandrasekhar function [73],

$$C_1(z)=\frac{\cosh(\lambda_1 z)}{\cosh\left(\lambda_1\frac{\pi}{2}\right)}-\frac{\cos(\lambda_1 z)}{\cos\left(\lambda_1\frac{\pi}{2}\right)};\quad \lambda_1=1.50562. \tag{5.16}$$

By projecting Eq. (5.3) onto $\cos z e^{\pm i\omega_0 t}$ and the Eqs. (5.4), (5.5), (5.6), (5.7) and (5.8) onto $\sin z$, $\cos z$, $\sin 2z$, $\sin 2z$, and $C_1(z)$, respectively, one obtains a 7×7 eigenvalue system of the form

$$\left[\lambda(\boldsymbol{q},R)\underline{\underline{B}}(\boldsymbol{q},R,\omega_0)-\underline{\underline{L}}(\boldsymbol{q},R,\omega_0)\right](\sigma^{(0)},\phi^+,\phi^-,n_z^{(0)},n_y^{(0)},v_y^{(0)},v_z^{(0)})=0 \tag{5.17}$$

for the growth rate $\lambda(\boldsymbol{q},R)$.

Although the above approximations may appear rather crude, they nevertheless lead to quantitatively good results. This is shown in Table 5.1 for the threshold voltage $V_c=V_{c0}\sqrt{R_c^{\mathrm{SM}}}$ and the corresponding wavevectors q_c and p_c resulting from the minimum R_c of the neutral surface $R_0^{\mathrm{SM}}(q,p)$. Compared are the analytic formula for the neutral surface of this work, Eq. (5.21) below, with numerical results, with the formula resulting from the choice of $\sin^2 z$ instead of $C_1(z)$ as test function for v_z, and also with the exactly solvable case of "free" BC [48]. Another possibility consists in representing v_x by a test function, e.g., $\sin 2z$, rather than using the (exact) incompressibility condition [48]. Furthermore, one can express the velocities in terms of the potentials f and g, given as Eq. (2.29), and approximate the z dependence of f and g by the test functions $C_1(z)$ and $\sin 2z$, respectively [95]. The accuracy is similar to Eq. (5.21); the threshold formula contains more projection integrals but the representation of $\boldsymbol{v}$ in terms of f and g is preferable as a starting point for the nonlinear Galerkin analysis. The bottom line is, that it is preferable to satisfy the incompressibility condition exactly but that the choice of test functions is not critical, as long as they satisfy the correct rigid BC (2.31).

Within the Galerkin approximation, the adiabatically eliminated velocities can

Table 5.1: Comparison of different analytic threshold formulas

approximation	MBBA I, $\omega_0\tau_q = 0.5$		MBBA I, $\omega_0\tau_q = 2$		I52, 30°C, $\omega_0\tau_q = 0.5$		
	V_c	q_c	V_c	q_c	V_c	q_c	p_c
Eq. (5.21) (See also [50])	7.205	1.591	30.95	3.114	14.61	1.068	0.734
Ref. [95]	7.375	1.603	33.62	3.24			
Ref. [48]	7.382	1.475	17.66	2.125			
Eq. (5.21) with $\sin^2 z$ for v_z	7.353	1.619	31.70	3.188	14.87	1.072	0.773
free BC	6.244	1.314	28.02	2.779	12.57	0.801	0.708
numerical result	7.171	1.592	31.81	3.15			

then be expressed in terms of "effective viscosities" with the result

$$v_z^{(0)} = \frac{\frac{\pi^2\overline{E}}{\sqrt{2}}\rho^+ + \lambda\left(-a_2 iqn_z^{(0)} + a_2'\frac{\eta_{zy}}{\eta_{yy}}pn_y^{(0)}\right)}{\eta_z^{(\mathrm{eff})}\,q^2}, \tag{5.18}$$

$$iv_y^{(0)} = \frac{p}{q}\frac{\eta_{zy}}{\eta_{yy}}v_z^{(0)} + \frac{\lambda\left(\alpha_3 I_2 ipn_z^{(0)} + (\alpha_3 p^2 - \alpha_2 q^2)n_y^{(0)}\right)}{\eta_{yy}q^3}. \tag{5.19}$$

The effective shear viscosities $\eta_z^{(\mathrm{eff})}$ and η_{yy} and the effective rotational viscosities a_2 and a_2' are given, together with the other "effective" quantities, in Chapter 5.3; $\overline{E} = \sqrt{R}/\pi$ is the rms. of the external field, and ρ^+ is the in-phase part of the oscillatory charge density. The expression for $v_z^{(0)}$ is very intuitive and is reminiscent of the former one dimensional [34] and two dimensional [46] models. For stationary conditions, the time-independent part $\rho^+\overline{E}$ of the volume force is balanced by the viscosity force $\eta_z^{(\mathrm{eff})}\,q^2 v_z^{(0)}$, discussed further in Chapter 5.3. A nonzero director rotation (λ corresponds to ∂_t) leads *via* the orientational viscosities to a further drag onto the fluid which is, again, balanced by the viscous force.

Apart from very thin cells ($d \leq 10$ μm), the charge relaxation time is also much shorter than τ_d ($P_1 << 1$) and the charge variables ϕ^+ and ϕ^- can be adiabatically eliminated as well,

$$\rho^+ = \epsilon_q\phi^+ + \epsilon_a\overline{E}\sqrt{2}iqn_z^{(0)} = -\overline{E}\sqrt{2}\left(\sigma_a^{(\mathrm{eff})}\,iqn_z^{(0)} + \frac{\epsilon_q}{\sigma_q(1+\omega'^2)}\sigma^{(0)}\right), \tag{5.20}$$

where $\epsilon_q = (1+\epsilon_a)q^2 + p^2 + 1$ and $\sigma_q = (1+\sigma_a)q^2 + p^2 + 1$ are the Galerkin projections of the operators $\hat{\epsilon}_q$ and $\hat{\sigma}_q$. The SM part $-\overline{E}\sqrt{2}\sigma_a^{(\mathrm{eff})}\,iqn_z^{(0)}$ with the effective conductivity $\sigma_a^{(\mathrm{eff})}$, Eq. (5.23), contains the Carr-Helfrich mechanism which

will be discussed in the following Chapter 5.3. The second part of Eq. (5.20) describes the charge separation due to the gradients of the total carrier density and gives rise to a second feedback cycle involving the carrier-density mode. This second stabilizing feedback provides the possibility for a nonzero Hopf frequency and will be discussed in Chapter 5.4.

5.3 Carr-Helfrich mechanism and analytic threshold formula

Above a certain (frequency dependent) threshold for the rms value $\sqrt{R}$ of the applied voltage, the growth rate $\lambda(\boldsymbol{q}, R)$ of the fastest-growing branch with a wavevector $\boldsymbol{q} = (q, p)$ crosses zero. This defines the neutral surface $R = R_0(\omega_0, q, p)$. The global minimum of R_0 with respect to q and p defines the critical wavenumbers q_c and p_c and the threshold $R_c = R_0(q_c, p_c)$. Inserting the adiabatically eliminated field inhomogeneity ϕ^+, Eq. (5.20), and the adiabatically eliminated velocities, Eqs. (5.18) and (5.19), into the Galerkin projection of the Eqs. (5.5) and (5.6), and setting $\sigma^{(0)} = 0$ leads to a 2×2 eigenvalue equation of the form $\left[\underline{\underline{B}}(\boldsymbol{q})\lambda + \underline{\underline{L}}(\boldsymbol{q}, R, \omega_0)\right](n_z^{(0)}, n_y^{(0)}) = 0$ where the components of $\underline{\underline{B}}$ and $\underline{\underline{L}}$ are just numbers (this equation is the SM part of the 3×3 equations in Appendix A.3). Since the SM does not lead to an oscillatory instability, the neutral curve R_0^{SM} is defined by $\lambda = 0$ and the ensuing determinantal condition $\mathrm{Det}[\underline{\underline{L}}(\boldsymbol{q}, R, \omega_0)] = 0$ leads to the result [1]

$$R_0^{\mathrm{SM}} = \frac{K^{(\mathrm{eff})}}{\epsilon_a^{(\mathrm{eff})} + \frac{a_2 \sigma_a^{(\mathrm{eff})}}{\eta^{(\mathrm{eff})}}}, \tag{5.21}$$

with the effective orientational elasticity

$$\begin{aligned} K^{(\mathrm{eff})} &= K_{zz} - \frac{p^2 K_{zy}^2}{q^2 K_{yy}}, \\ K_{zz} &= K_{33} q^2 + K_{22} p^2 + 1, \\ K_{yy} &= K_{33} q^2 + p^2 + 4K_{22}, \\ K_{zy} &= (1 - K_{22}) q I_2, \end{aligned} \tag{5.22}$$

the effective anisotropy of the conductivity

$$\sigma_a^{(\mathrm{eff})} = \frac{\sigma_a}{1 + \omega'^2} \left(\frac{\epsilon_q}{\sigma_q} - \frac{\epsilon_a}{\sigma_a} \right), \tag{5.23}$$

[1] Here and in the following, the projection integral $I = 0.986$ of $\sqrt{2/\pi} \cos z$ and $C_1(z)$ is set equal to one

$$\omega' = \omega_0 \tau_q \epsilon_q / \sigma_q, \tag{5.24}$$

$$\sigma_q = (1+\sigma_a)q^2 + p^2 + 1, \quad \epsilon_q = (1+\epsilon_a)q^2 + p^2 + 1, \tag{5.25}$$

the effective dielectric constant

$$\epsilon_a^{(\mathrm{eff})} = \epsilon_a \left(q^2+p^2+1\right)\left(\frac{\sigma_q^{-1} + \omega'^2 \epsilon_q}{1+\omega'^2}\right), \tag{5.26}$$

the effective orientational viscosity coupling the director to the fluid,

$$a_2 = -\alpha_2 + \alpha_3 \left(\frac{1}{q^2} - \frac{\eta_{zy} p^2 I_2}{\eta_{yy} q^3}\right), \tag{5.27}$$

and the effective viscosity

$$\eta^{(\mathrm{eff})} = \frac{\eta_z^{(\mathrm{eff})}}{1 + \frac{p^2 K_{zy} \eta_{zy} a_2'}{q^2 K_{yy} \eta_{yy} a_2}}, \tag{5.28}$$

$$a_2' = -\alpha_2 + \alpha_3 \left(\frac{p^2}{q^2} - \frac{\eta_{yy}}{\eta_{zy}} \frac{I_p}{q}\right), \tag{5.29}$$

$$\eta_z^{(\mathrm{eff})} = \eta_{zz} - \frac{p^2 \eta_{zy}^2}{q^2 \eta_{yy}}, \tag{5.30}$$

$$\eta_{zz} = \eta_1 + (\eta_1 + \eta_2 + \alpha_1)\frac{I_1}{q^2} + \frac{\alpha_4}{2}\frac{p^2}{q^2} + \eta_2 \frac{\lambda_1^4 + I_1 p^2}{q^4}, \tag{5.31}$$

$$\eta_{yy} = \eta_1 + (\eta_1 + \eta_2 + \alpha_1)\frac{p^2}{q^2} + \frac{2\alpha_4}{q^2} + \eta_2 \frac{p^4 + 4p^2}{q^4}, \tag{5.32}$$

$$\eta_{zy} = (\eta_1 + \eta_2 + \alpha_1 - \alpha_4/2)\frac{I_p}{q} + \eta_2 I_p \frac{4+p^2}{q^3}, \tag{5.33}$$

$$\tag{5.34}$$

where η_0, η_1, and η_2 are given in Eq. (5.12). The projection integrals are given by

$$\begin{array}{ll} I_1 = -\langle C_1, \partial_z^2 C_1 \rangle & = 1.2465, \\ I_2 = \frac{2}{\pi}\langle \cos z, \partial_z \sin 2z \rangle & = 0.848, \\ I_p = \sqrt{\frac{2}{\pi}}\langle C_1, \partial_z \sin 2z \rangle & = 1.1119, \\ \lambda_1^4 = \langle C_1, \partial_z^4 C_1 \rangle & = 5.1388, \end{array} \tag{5.35}$$

where $\langle ... \rangle$ stands for the integration over z from $-\pi/2$ to $\pi/2$.

Equation (5.21) is written in such a way that the major effects contributing to the Carr-Helfrich mechanism are separated out. $K^{(\mathrm{eff})}$ describes the elastic torque on the director, which, at threshold, is balanced by the electric forces due to charge accumulation $\propto \sigma_a^{(\mathrm{eff})}\, \overline{E}^2$ and due to the dielectric anisotropy, $\propto \epsilon_a^{(\mathrm{eff})}\, \overline{E}^2$.

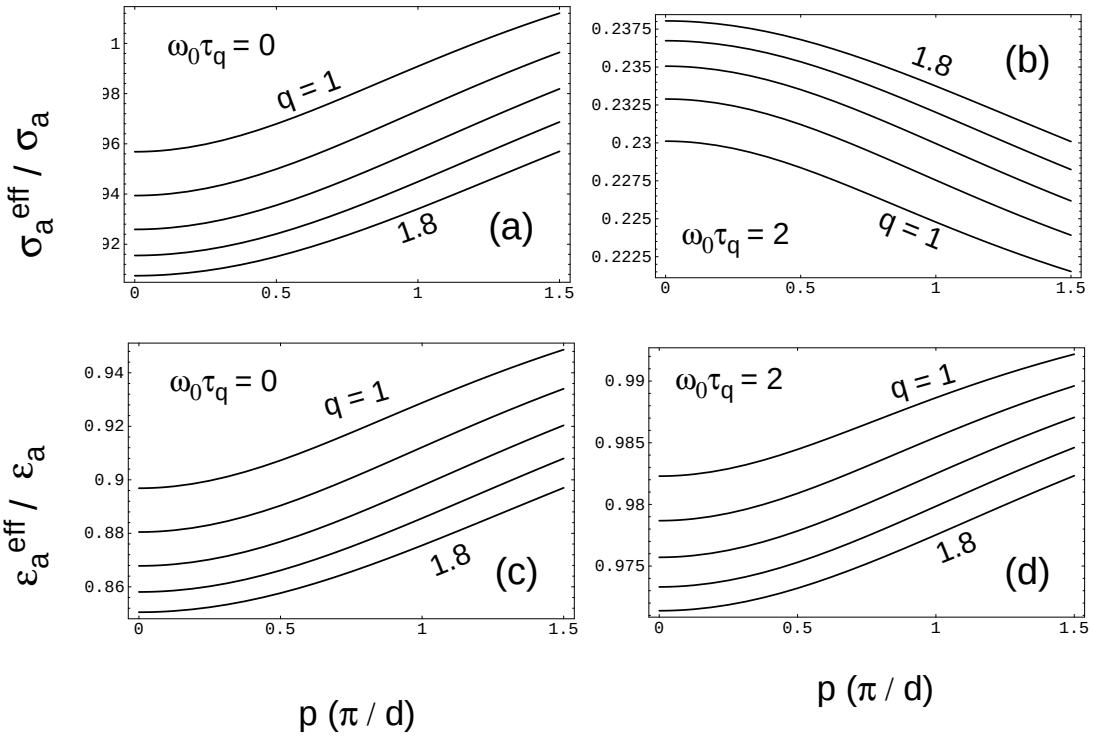

Figure 5.1 The dependence of the effective conductivity anisotropy, Eq. (5.23), and of the effective dielectric anisotropy, Eq. (5.26), on q, p, and ω_0.

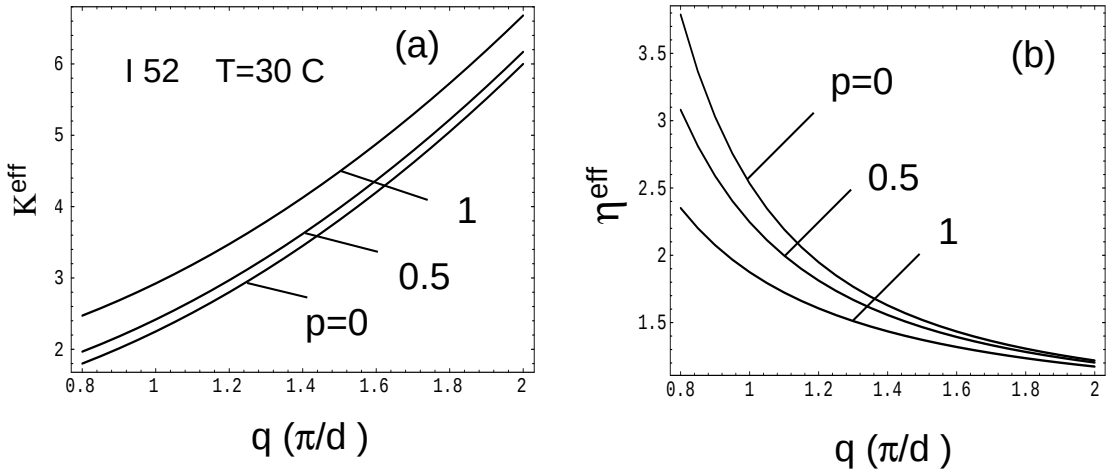

Figure 5.2 (a) The effective orientational elasticity, Eq. (5.22); (b) the effective viscosity, Eq. (5.28). The divergences of $K^{(\mathrm{eff})}$ for $q \to 0$ and of $\eta^{(\mathrm{eff})}$ for $q \to \infty$ lead to a finite, nonzero q_c.

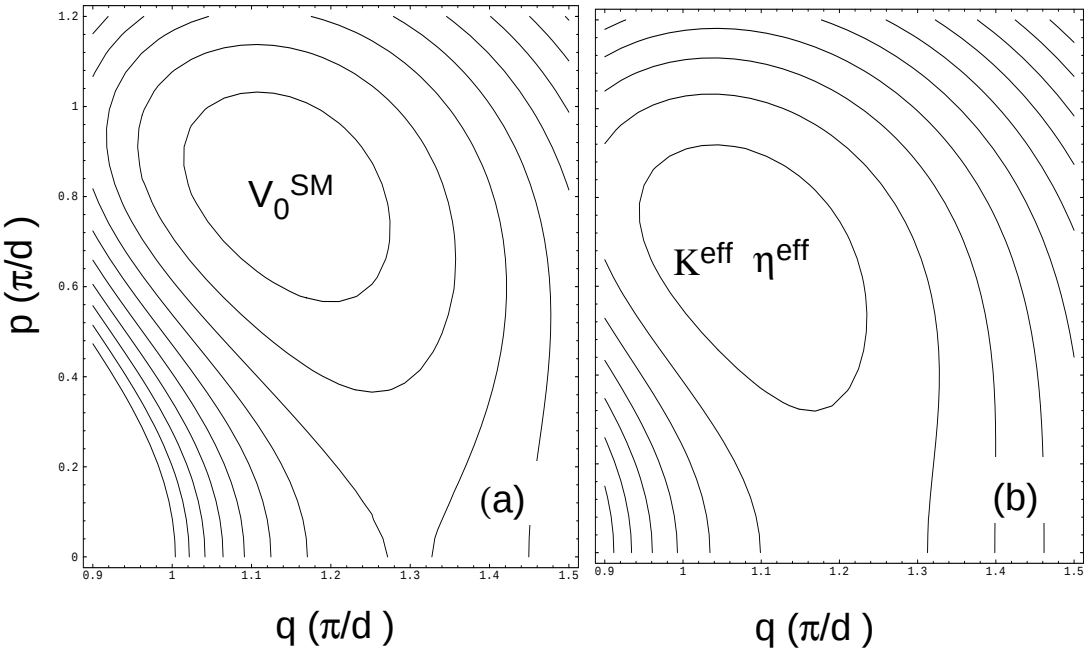

Figure 5.3 Contour plots of (a) the neutral surface, Eq. (5.21), and (b), the product $K^{(\mathrm{eff})}\,\eta^{(\mathrm{eff})}$. The parameters are for I 52 at 30°C. The external frequency $\omega_0\tau_q = 0.5$.

For $\epsilon_a < 0$, the dielectric energy has a minimum for $\boldsymbol{n}\cdot\boldsymbol{E} = 0$. The main contribution of the dielectric torque, $\epsilon_a\pi^2 E_0^2(t)iq\overline{n}_z$ in Eq. (5.5), tends to align the director perpendicular to the undistorted electric field. Additional contributions due to field distortions ($\boldsymbol{\nabla}\phi \neq 0$) lead, in the lowest-order Fourier and Galerkin expansions, to a total dielectric torque $\epsilon_a^{(\mathrm{eff})}\,\pi^2\overline{E}^2 iqn_z^{(0)}$ thus defining $\epsilon_a^{(\mathrm{eff})}$. As shown in Fig. 5.1, $\epsilon_a^{(\mathrm{eff})}$ is essentially equal to ϵ_a for all q, p, and ω_0. For $\epsilon_a < 0$, this contribution is stabilizing.

With the help of the Eqs. (5.18) and (5.20), the dominant contribution of the Carr-Helfrich part $|\alpha_2|q^2\overline{v}_z$ of the director equation Eq. (5.5) with v_z can be written as

$$\gamma^{(\text{Carr Helfrich})} = \frac{a_2\sigma_a^{(\mathrm{eff})}\,\pi^2\overline{E}^2 iqn_z^{(0)}}{\eta^{(\mathrm{eff})}}. \tag{5.36}$$

$\gamma^{\text{Carr Helfrich}}$ is an electrically induced torque onto the director that acts indirectly *via* the fluid (compare the Figs. 5.4 and 5.12): A director bend leads *via* the conductivity anisotropy to a divergence of the electric current (with the main contribution $\sigma_a E_0(t)iq\overline{n}_z$ in Eq. (5.3)), which gives rise to a charge accumulation and to a volume force $\rho\boldsymbol{E}$ onto the fluid. In the lowest-order of the Fourier expansion in t, only the part $\propto \rho^+\overline{E}$ of the volume force not oscillating with the electric

field, and deriving from the in-phase part of the accumulated charge density, sets the fluid into motion. So I defined $\sigma_a^{(\mathrm{eff})}$ to be proportional to the SM part of Eq. (5.20), $\rho^+ = -\sigma_a^{(\mathrm{eff})}\,\overline{E}\sqrt{2}iqn_z^{(0)}$. In the stationary case, the non-oscillating part $-\sigma_a^{(\mathrm{eff})}\,\overline{E}^2\pi^2 iqn_z^{(0)}$ of the volume force is balanced by the viscous forces of the rotating fluid which can be written as $\eta_z^{(\mathrm{eff})}\,q^2 v_z^{(0)}$ thus defining $\eta_z^{(\mathrm{eff})}$. The velocity gradients of the fluid lead *via* the rotational viscosities to a torque onto the director which I wrote as $-a_2 q^2 v_z^{(0)}$ defining a_2. For $\alpha_3 = 0$ ($a_2 = -\alpha_2$), and with the Fourier and Galerkin approximations, this is just the contribution $\alpha_2 q^2 \overline{v}_z$ in Eq. (5.5). With $v_z^{(0)} = -\sigma_a^{(\mathrm{eff})}\,\pi^2\overline{E}^2 iqn_z^{(0)}/(\eta_z^{(\mathrm{eff})}\,q^2)$, this contribution is equal to Eq. (5.36) with $\eta^{(\mathrm{eff})}$ substituted by $\eta_z^{(\mathrm{eff})}$. In addition, the total destabilizing Carr-Helfrich contribution (5.36) of the torque contains the Fourier and Galerkin approximations of the coupling term $-\hat{K}_{zy}p\overline{n}_y$ in Eq. (5.5). This term can be put formally into the definition of $\eta^{(\mathrm{eff})}$ leading to the difference between $\eta^{(\mathrm{eff})}$ and $\eta_z^{(\mathrm{eff})}$.

The fact that only the in-phase part of ρ is relevant, leads to the denominator $(1+\omega'^2)$ in Eq. (5.23) for $\sigma_a^{(\mathrm{eff})}$ making the Carr-Helfrich effect less effective for increasing external frequencies ($\eta^{(\mathrm{eff})}$ in Fig. 5.1). On the other hand, the effective viscosity decreases monotonically with increasing q (Fig. 5.2) approaching the asymptotic value $\eta_1 = (\alpha_4 + \alpha_5 - \alpha_2)/2$ for $q \to \infty$ and making this aspect of the Carr-Helfrich mechanism more effective for large wave numbers. [2] This explains the increase of the critical wavenumber q_c with increasing ω_0, and the existence of a "cutoff frequency" for $\epsilon_a < 0$. On increasing ω_0, the strength of the Carr-Helfrich effect decreases due to the decrease of $\sigma_a^{(\mathrm{eff})}$; to overcome the stabilizing and essentially q and ω_0 independent dielectric effect ($\epsilon_a^{(\mathrm{eff})}$ in Fig. 5.1), q_c increases with increasing ω_0. The effective viscosity, however, remains finite for $q \to \infty$. As a result there exists, for $\epsilon_a < 0$, a finite cutoff frequency ω_{cutoff} [45], where the Carr-Helfrich mechanism cannot overcome the dielectric force even for $q \to \infty$ and where R_c^{SM} diverges for the conductive mode. For a discussion, see, e.g., Ref. [48].

In general, $\eta^{(\mathrm{eff})}$ decreases with the roll angle $\arctan(p/q)$ for constant q (Fig. 5.2) while the behaviour of $\sigma_a^{(\mathrm{eff})}$ depends on the external frequency. For low (high) external frequencies, $\sigma_a^{(\mathrm{eff})}$ increases (decreases) favouring oblique (normal) rolls, see Fig. 5.1. For some NLCs (I 52, but not MBBA), the product of the restoring forces $K^{(\mathrm{eff})}\,\eta^{(\mathrm{eff})}$ has a minimum for nonzero p_c (Fig. 5.3). In I 52, this leads to oblique rolls except for very high frequencies where $\sigma_a^{(\mathrm{eff})}$ strongly favours normal rolls.

[2] For a negative Miesowicz coefficient $\eta_2 = (\alpha_3+\alpha_4+\alpha_6)/2$, the effective viscosity would become negative for q values *smaller* than some q_{min}. Note, however, that positive definiteness of the entropy production (2.17) leads to the Miescowicz coefficient $\eta_2 > 0$ [58] and forbids this unphysical behaviour.

For $q = 0$, Eq. (5.21) becomes $R_0^{\rm SM} = K^{(\rm eff)}/\epsilon_a$ which is positive (i.e. corresponds to a threshold) for $\epsilon_a > 0$. Usually, the effective restoring force $K^{(\rm eff)}$ increases with p and the minimum of $R_0^{\rm SM}(q = 0, p)$ lies at $p = 0$ corresponding to the usual Fréedericksz effect. If the value of the twist module is extremely low, $K_{22}/K_{33} < 0.298$, [3] the minima of $K^{(\rm eff)}$ $(q = 0, p)$ and of $R_0^{\rm SM}(q = 0, p)$ are at a nonzero wave number p corresponding to the "periodic splay-twist transition", as decsribed e.g., in Ref. [48].

5.4 Charge separation mechanism and Hopf frequency

5.4.1 Coupled equations for the director bend and the charge-carrier density

As in Chapter 5.3, I substituted the adiabatically eliminated ϕ^+, Eq. (5.20), and the adiabatically eliminated velocities, Eqs. (5.18) and (5.19), into the Galerkin projection of the linear basic equations (5.4), (5.5) and (5.6), but this time I retain the amplitude $\sigma^{(0)}$ of the charge-carrier-density mode. This leads to a 3×3 eigenvalue system for the linear growth rate λ with the eigenvector $\left(\sigma^{(0)}, n_z^{(0)}, n_y^{(0)}\right)$ which is given explicitly in the Appendix A.3.

Near threshold, where the reduced control parameter

$$\epsilon = \frac{R}{R_c} - 1 \tag{5.37}$$

satisfies $\epsilon << 1$, this system can be further reduced systematically to a 2×2 normal form for the amplitude $A_n(t)$ of the SM mode and the amplitude $A_\sigma(t)$ of the charge-carrier mode (see Appendix A.3),

$$\begin{aligned} \partial_t A_\sigma &= \lambda_\sigma(R) A_\sigma - \tilde{\alpha}^2 R \sigma_a^{(\rm eff)} A_n, \\ \partial_t A_n &= \frac{R}{\sigma_a^{(\rm eff)}} \left(\frac{C}{1+\omega'^2}\right)^2 A_\sigma + \lambda_n(R) A_n. \end{aligned} \tag{5.38}$$

The critical SM mode $A_n(t)$ is the amplitude of the director bend with a small admixture of twist,

$$\begin{pmatrix} iq\overline{n}_z(z,t) \\ q\overline{n}_y(z,t) \end{pmatrix} = \begin{pmatrix} \cos z \\ \alpha_n \sin 2z \end{pmatrix} A_n(t), \tag{5.39}$$

[3] This value is the result for the Galerkin approximations. The problem is exactly solvable with the result $K_{22}/K_{33} < (\beta_0^2 + \beta_0)^{1/2} - \beta_0 = 0.303$ with $\beta_0 = \pi^2/8 - 1$ [96].

where $\alpha_n = in_z^{(0)}/n_y^{(0)}$ is given by the eigenvector of the 3×3 system (A.5) - (A.7). The charge-carrier mode is given by

$$\overline{\sigma}(z,t) = A_\sigma(t) \sin z. \tag{5.40}$$

Neglecting some small terms $\propto \alpha_3 p$, the growth rates λ_σ and λ_n of the charge-carrier and SM modes, and the coupling coefficient C, are given by [4]

$$\begin{aligned}
\lambda_\sigma &= -\left(\tilde{r} + \frac{\tilde{\alpha}^2 R \epsilon_q}{\sigma_q(1+\omega'^2)}\right) \approx -\tilde{r}, && (5.41)\\
\lambda_n &= \frac{\epsilon}{\tau_0^{\rm SM}}, && (5.42)\\
C^2 &= \frac{K_{zz}}{K^{(\rm eff)}\,|\lambda_{0z}|\tau_0^{\rm SM}}\left(C_z^2 + \frac{p^2 K_{zy}\lambda_{0z}}{q^2 K_{zz}\lambda_{0y}} C_y^2\right), && (5.43)\\
C_z^2 &= \frac{\sigma_a \epsilon_q^2 |\lambda_{0z}|}{\sigma_q^2 \eta_z^{(\rm eff)}\, K_{zz}}\left(1 - \frac{\epsilon_a}{\epsilon_q}\frac{\sigma_q}{\sigma_a}\right)\left(a_2 - \frac{\epsilon_a q^2 \eta_z^{(\rm eff)}}{\epsilon_q}\right), && (5.44)\\
C_y^2 &= \frac{\sigma_a \epsilon_q^2 |\lambda_{0y}|}{\sigma_q^2 \eta_z^{(\rm eff)}\, K_{yy}}\left(1 - \frac{\epsilon_a}{\epsilon_q}\frac{\sigma_q}{\sigma_a}\right)\frac{\eta_{zy}}{\eta_{yy}} a_2', && (5.45)
\end{aligned}$$

and the zero-field growth rates λ_{0z} and λ_{0y} are given by

$$\lambda_{0z} = -\frac{K_{zz}\eta_z^{(\rm eff)}}{\eta_z^{(\rm eff)} - a_2^2}, \quad \lambda_{0y} = -\frac{K_{yy}\eta_z^{(\rm eff)}}{\eta_z^{(\rm eff)}\left(1 - \frac{a_2'^2}{\eta_{yy}}\right) - \frac{p^2}{q^2}\frac{\eta_{zy}^2}{\eta_{yy}^2}a_2'^2}. \tag{5.46}$$

For normal rolls $K^{(\rm eff)} = K_{zz}$ and $\tau_0^{\rm SM} = -1/\lambda_{0z}$ so that $C^2 = C_z^2$ is equivalent to the normal-roll expression in Ref [92], if one identifies $\eta_z^{(\rm eff)}$ with $1/L_{nn}$. [5] The question may arise whether the denominators proportional to $(\eta_z^{(\rm eff)} - a_2^2)$ in the growth rate λ_{0z} (and thus in C_z^2) can become zero or negative leading to unphysical results. This question is most critical for $q \to \infty$ and $p = 0$ (Fig. 5.2), where, in physical units, $\eta_1 > \alpha_2^2/\gamma_1$ is required to avoid unphysical results. It can be shown that the requirement of a positive fluid contribution $-T_{ij}^D \partial_j v_i$ of the entropy production (2.17) leads indeed to $\eta_1 > \alpha_2^2/\gamma_1$ [6]

[4] Due to a different scaling of the voltages and the time, the definition of C differs from that used in the Refs. [92] and [42] by a factor of $(\sigma_a/\sigma_\perp^{\rm eq})^{1/2}$.

[5] There is a printing error in Eq. (38) of Ref. [92]. The factor $(1 - \frac{\epsilon_a}{\epsilon_q} L_{nn} q^2)$ should be replaced by $(L_{nn} - \frac{\epsilon_a}{\epsilon_q} q^2)$.

[6] The contribution $\eta_1 - \alpha_2^2/\gamma_1$ is sometimes called η_3, e.g., in Ref. [58].

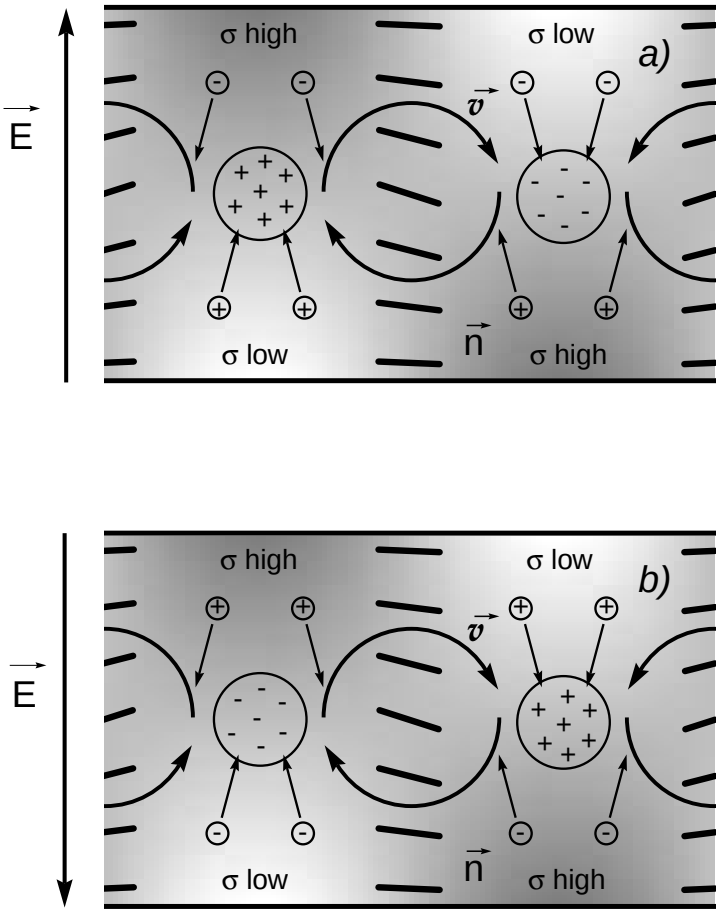

Figure 5.4 Sketch of the spatial distribution of the physical quantities inside the nematic layer (conductive regime). The straight arrows indicate the contributions to the current carried by each species. The shading illustrates the charge-carrier mode (dark = σ high, light = σ low).

5.4.2 The dynamics of the charge-carrier mode

The charge-separation mechanism of the WEM leading for low recombination rates to a nonzero Hopf frequency, can be explained essentially with the help of Fig. 5.4, Eq. (5.20) for the adiabatically eliminated charge density, and the 2×2 system (5.38). Like the Carr-Helfrich effect, this mechanism is active also for DC.

Consider $E_0 > 0$ and a region in the cell where the director bend A_n is negative which is connected by Eqs. (5.20) and (5.39) to a positive SM part of the charge density (left side of upper picture in Fig. 5.4). For $z > 0$, the gradient of the density of the upwards drifting positive carriers is negative and that of the downwards drifting negative carriers is positive. Migration of both species leads, for $z > 0$, to an increase in the total number density $\sigma(\boldsymbol{r}, t)$ of the carriers, illustrated by the shading (dark corresponds to a high density). The sign of the effect (accumulation or depletion of the carriers) depends on the signs of $\partial_z \rho$ and E_0. This means, in the conductive

regime, that the excited charge-carrier density mode $\sigma(\boldsymbol{r},t)$ is antisymmetric in z and does not follow the external oscillations in the lowest-order Fourier expansion in t (compare the upper and lower part of Fig. 5.4). This justifies the ansatz (5.15) for the σ mode and Eq. (5.40) for the amplitude A_σ. Within the ansatz (5.15), the driving force for the A_σ mode is proportional to ρ^+, $\partial_t A_\sigma = \tilde{\alpha}^2\pi^2\overline{E}\rho^+/\sqrt{2}$. The SM part of Eq. (5.20) for the adiabatically eliminated ρ^+ leads to the term $-\tilde{\alpha}^2 R\sigma_a^{(\mathrm{eff})} A_n$ in the upper line of Eq. (5.38). The WEM part leads to the part $\propto \tilde{\alpha}^2$ in Eq. (5.41) for the relaxation of the σ mode.

The stabilizing feedback of the A_σ mode on the charge density and on A_n is mediated, in the basic equation (5.4), by the WEM part $E_z\partial_z\overline{\sigma}$ of the divergence of the current. Together with the relaxational part it decreases the accumulated charge. With adiabatically eliminated charge density and velocities, this is equivalent to a decrease of all SM fields, and the WEM part of $\boldsymbol{\nabla}\cdot\boldsymbol{J}$ leads to the first term in the equation for $\partial_t A_n$. This term is positive, but since the director bend A_n is proportional to $-\rho^+$, the feedback is indeed negative, i.e., stabilizing. It leads to a nonzero Hopf frequency, provided the A_σ mode can build up sufficiently, i.e. the relaxation of the σ mode is sufficiently slow. [7]

5.4.3 Hopf frequency and threshold shift

The growth rates of modes $\propto e^{\lambda t}$ in (5.38) are given by

$$\lambda = \frac{\lambda_\sigma + \lambda_n}{2} \pm \sqrt{\frac{(\lambda_n - \lambda_\sigma)^2}{4} - \tilde{\omega}^2} \tag{5.47}$$

with

$$\tilde{\omega} = \frac{R_c\tilde{\alpha}C}{1+\omega'^2}. \tag{5.48}$$

The condition for a Hopf bifurcation at threshold ($Re\lambda = 0$, $Im\lambda = \pm\omega_H \neq 0$) are $\lambda_n = -\lambda_\sigma$ and $|\lambda_\sigma| < \tilde{\omega}$ which sets an upper bound on the recombination rate. The resulting Hopf frequency is

$$\omega_H = \tilde{\omega}\sqrt{1 - \left(\frac{\lambda_\sigma}{\tilde{\omega}}\right)^2} \approx \tilde{\omega}\sqrt{1 - \left(\frac{\tilde{r}}{\tilde{\omega}}\right)^2}, \tag{5.49}$$

[7] To put it anthropomorphically for normal rolls: If the A_σ mode builds up sufficiently, it is more advantageous for the Carr-Helfrich mechanism if the SM fields were shifted to the left or to the right. The travelling velocity (proportional to the Hopf frequency) is determined by the rate at which the A_σ mode can build up at the new location. This rate is proportional to $\tilde{\alpha}$.

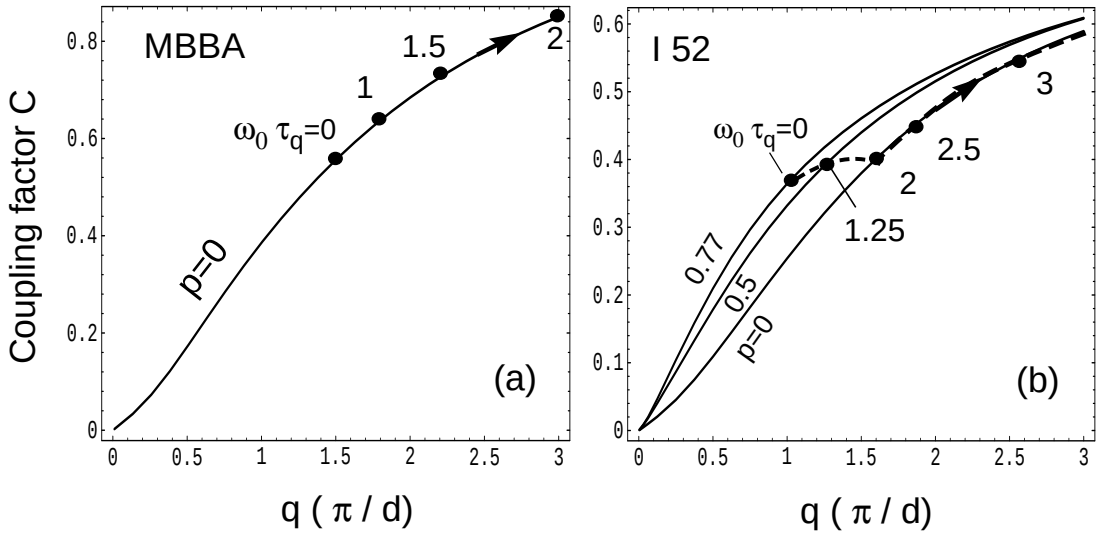

Figure 5.5 Plot of Eq.(5.43) for the coupling factor C in the 2×2 equations (5.38). (a) is for MBBA parameters and $p_c = 0$. The dots on the curve give, for $\omega_0 \tau_q = 0, 1.0, 1.5,$ and 2, the actual value of q_c where C is calculated. The three curves in (b) are for I 52 at 30°C with p_c values corresponding to $\omega_0 \tau_q = 0$, 1.25, and with $p_c = 0$ corresponding to $\omega_0 \tau_q > 2.0$. The kink at the Lifshitz point $\omega_{\rm lif} \tau_q = 2.0$ in the dashed trajectory in (b) translates into a kink in the curves for the Hopf frequency in Fig 5.11a). The slope $\frac{\partial C}{\partial q}$ is the main contribution to the group velocity $\frac{\partial \omega}{\partial q}$.

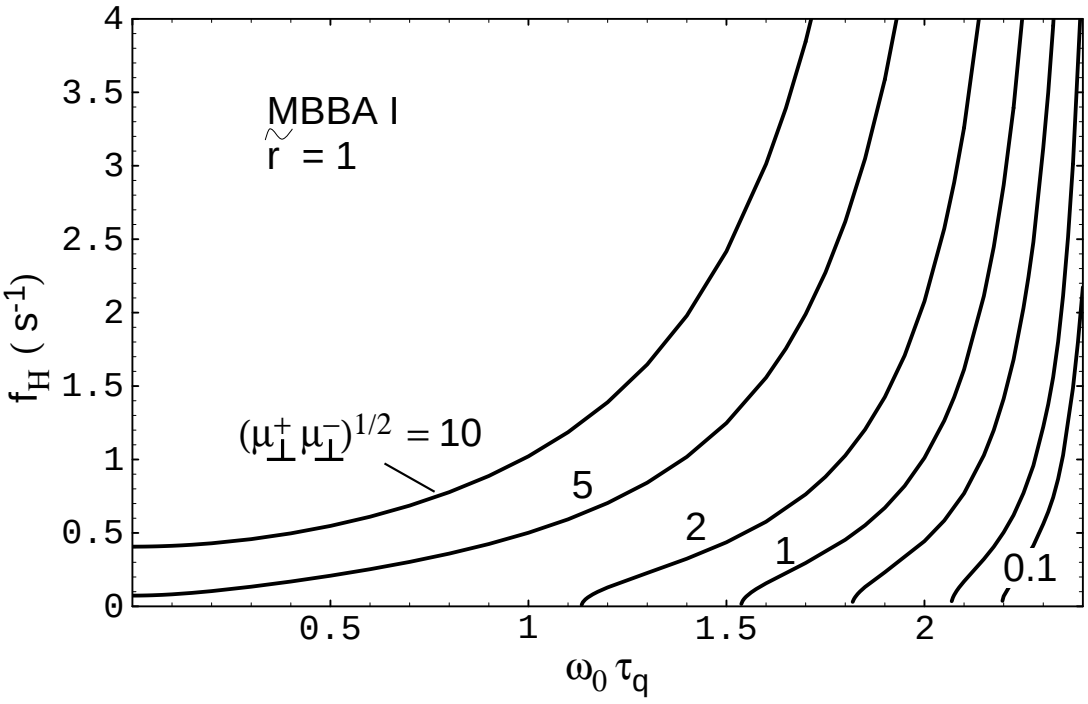

Figure 5.6 Hopf frequency $f_H = (2\pi)^{-1}\omega_H$ in physical units, Eq. (5.53), as a function of the external frequency for the parameter set of MBBA I with $\sigma_\perp = 10^{-8}(\Omega\mathrm{m})^{-1}$ and $d = 13\ \mu$m (as in Ref. [39]), and an assumed recombination rate of $\tau_{\mathrm{rec}} = \tau_d$ (i.e., $\tilde{r} = 1$). Parameter is the geometric mean of the mobilities with the values, from left to right, $10, 5, 2, 1, 0.5, 0.2$, and 0.1 in units of $10^{-10}\mathrm{m}^2/(\mathrm{Vs})$. For other values of d, $\sigma_\perp$, $\sqrt{\mu_\perp^+\mu_\perp^-}$, and τ_{rec}, the form of the curves (especially the codimension-two point where $\omega_H \to 0$) scales with $\tau_{\mathrm{rec}}\tilde{\omega}^{\mathrm{phys}} \propto \tilde{\alpha}/\tilde{r} \propto \sqrt{\mu_\perp^+\mu_\perp^-}\tau_{\mathrm{rec}}/(\sqrt{\sigma_\perp}d^3)$, and the Hopf frequency scales with $\sqrt{\mu_\perp^+\mu_\perp^-}/(\sqrt{\sigma_\perp}d^3)$.

and the condition $\lambda_n = -\lambda_\sigma$ leads to a threshold shift

$$\Delta\epsilon \equiv \frac{R_c}{R_c^{\rm SM}} - 1 = \begin{cases} |\lambda_\sigma|\tau_0^{\rm SM} \approx \tilde{r}\tau_0^{\rm SM} & |\lambda_\sigma| \le \tilde{\omega} \\ \frac{\tilde{\omega}^2\tau_0^{\rm SM}}{|\lambda_\sigma|} \approx \frac{\tilde{\omega}^2\tau_0^{\rm SM}}{\tilde{r}} & |\lambda_\sigma| > \tilde{\omega} \end{cases}, \tag{5.50}$$

where all quantities are taken at threshold. The only source for a shift of the wave vector with repect to the SM model lies in the q dependence of λ_σ which is proportional to $\tilde{\alpha}^2$ and extremely small, in accordance with experiments [39], see also Chapter 6.3.3.

The approximations in the Eqs. (5.49) and (5.50) are valid for $R_c\tilde{\alpha}^2/(1+\omega'^2) << \tilde{r}$. For the I 52 experiments, $R_c\tilde{\alpha}^2/(1+\omega'^2)$ is of the order of 0.01 or smaller and $\tilde{\omega}$ is of the order of 0.2; so there exists a fairly large range where this approximation is fulfilled.

For $\epsilon_a = \alpha_3 = p = 0$, the expression (5.48) for $\tilde{\omega}$ simplifies to

$$\tilde{\omega}\tau_0^{\rm SM} = \tilde{\alpha}\sqrt{(\eta_{zz}-1)/\sigma_a}. \tag{5.51}$$

5.4.4 Dependence on the system parameters

The Equations (5.48) – (5.50) are the main analytic result of this Chapter. Apart from the SM parameters, they contain the mobility parameter $\tilde{\alpha}$ and the recombination rate $\tilde{r}$ in units of the inverse director relaxation time. In physical units, the Eqs. (5.48) and (5.49) read (in the approximation $\lambda_\sigma \approx -\tilde{r}$)

$$\tilde{\omega}^{\rm phys} = \pi C \frac{\epsilon_0\epsilon_\perp}{d^3}\frac{\overline{V}^2}{1+\omega'^2}\sqrt{\frac{\mu_\perp^+\mu_\perp^-}{\gamma_1\sigma_a^{\rm eq}}}, \tag{5.52}$$

$$\omega_H^{\rm phys} = \tilde{\omega}^{\rm phys}\sqrt{1 - \frac{1}{(\tau_{\rm rec}\tilde{\omega}^{\rm phys})^2}}. \tag{5.53}$$

while Eq. (5.50) is valid for physical units as well. This implies the following predictions.

- The Hopf condition scales with $d^{-3}(\sigma_\perp^{\rm eq})^{-1/2}$. This means, that a Hopf bifurcation is favoured for thin cells and low conductivities, i.e. for clean materials and/or low temperatures. If the condition is (fairly) well satisfied, the Hopf frequency scales with $d^{-3}(\sigma_\perp^{\rm eq})^{-1/2}$ as well.

- If the Hopf condition is well satisfied, the Hopf frequency $\omega_H \approx \tilde{\omega}$ depends only on one combination of non-SM parameters , $\sqrt{\mu_\perp^+\mu_\perp^-}$, and this dependence is of a simple multiplicative form. Actually, as shown in the inset of Fig. 5.8, the

influence of the recombination can be neglected (i.e. the Hopf condition is "well satisfied") if $\tilde{r}$ is smaller than about half the Hopf frequency for zero external frequency. One could, at least in principle and when the SM parameters are known, "measure" the geometric mean of the mobilities by measuring the Hopf frequency.

- The function $\tilde{\omega}(\omega_0)$ is proportional to $C(q(\omega_0))R_c(\omega_0)/(1+\omega'^2)$, a fixed function for a given NLC at a given temperature containing only SM parameters. The dependence on C is rather weak, so the behaviour of $\tilde{\omega}$ with ω_0 is primarily determined by the factor $R_c/(1+\omega'^2)$. This factor is nearly constant for $\epsilon_a = 0$ (compare Eq. (5.21) with $R_c \approx R_c^{\mathrm{SM}}$), but increases (decreases) with ω_0 for $\epsilon_a < 0$ ($\epsilon_a > 0$). For $\epsilon_a = \alpha_3 = p = 0$, Eq. (5.51) implies that $\tilde{\omega}$, in units of the zero-field relaxation rate $(\tau_0^{\mathrm{SM}})^{-1}$ of the director, is equal to $\tilde{\alpha}\sqrt{\sigma_\perp/\sigma_a}$ times a factor of the order of unity (see Fig. 5.2). This order-of-magnitude estimate remains valid for nonzero values of ϵ_a, α_3, and p.

- The threshold shift increases with $\tilde{r}$ to a maximum of $\Delta\epsilon = \tau_0^{\mathrm{SM}}\tilde{\omega}$ at the codimension-two point ($|\lambda_\sigma| = \tilde{\omega}$) of travelling rolls and stationary rolls ($\Delta\epsilon \approx$ 3 % for I 52.) For higher $\tilde{r}$ (stationary-roll regime), the shift $\Delta\epsilon = \tau_0^{\mathrm{SM}}\tilde{\omega}^2/\tilde{r}$ decreases and goes to zero in the SM limit $\tilde{r} \to \infty$.

5.5 Comparison with experiments

5.5.1 Travelling normal rolls in MBBA

Travelling rolls in MBBA were observed e.g., in [40, 41, 97, 98]. The advantage of MBBA for testing the WEM is the fact that all SM parameters are known and there exist also some reported data for the mobilities (Table 3.1). In this subsection I test the WEM on the results of Rehberg, Rasenat, and Steinberg [41]. The thickness of the cell was $d = 15\ \mu$m and the cutoff frequency at about 450 Hz corresponds to $\sigma_\perp = 4 \times 10^{-8}(\Omega\mathrm{m})^{-1}$. Their Fig. 4, containing the results of the Hopf-frequency measurements, is reproduced here as Fig. 5.7 (Courtesy of I. Rehberg). Travelling waves were observed for all frequencies. Comparison with the inset of Fig. 5.8 suggests that the unknown recombination rate is sufficiently small ($\tilde{r} < 0.3$ or $\tau_{\mathrm{rec}}^{-1} < 0.3\tau_d^{-1}$) to assume $\omega_H = \tilde{\omega}$. Another experiment described in Chapter 6 [39] leads to the stronger condition $\tilde{r} < 0.1$ ($\tau_{\mathrm{rec}} > 3$s), and supports this assumption. At f_0 =190 Hz ($\omega_0\tau_q = 1.1$), the measured Hopf frequency $\omega_H/(2\pi)$ was 0.345 Hz.

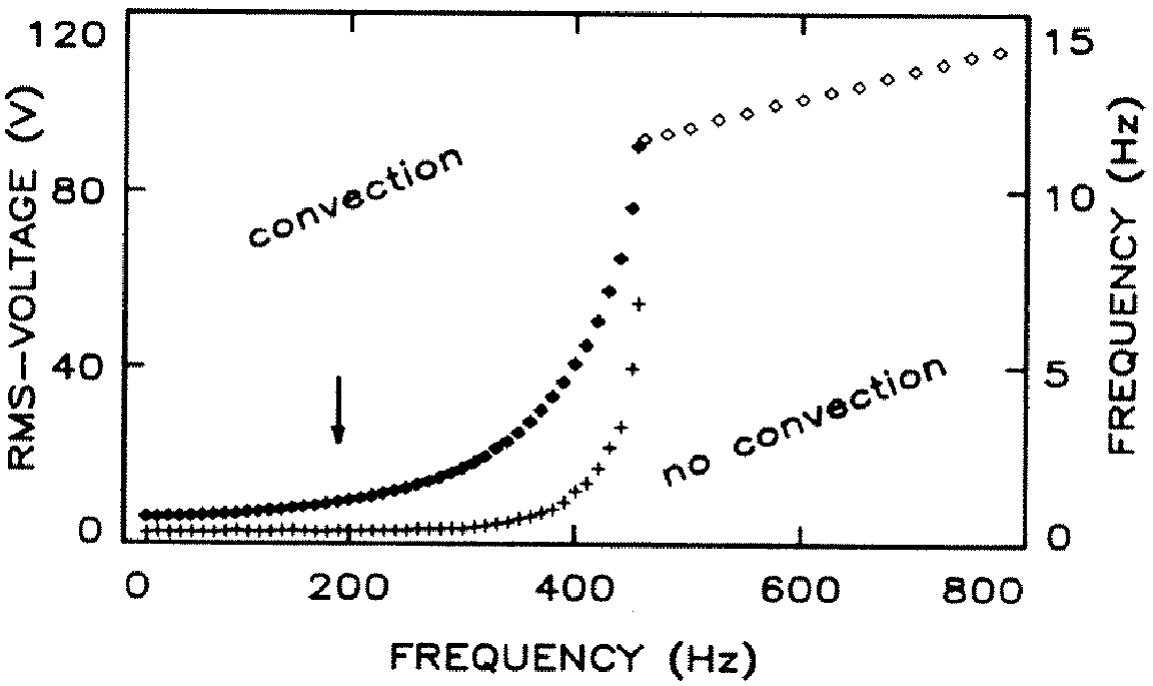

Figure 5.7 Experimental results for a 15 μm cell of MBBA for the Hopf frequency (crosses) and the threshold voltage (solid diamonds for the conductive regime and open diamonds for the dielectric regime). The figure is taken from Ref. [41] (Courtesy of I. Rehberg).

Fitting $\sqrt{\mu_\perp^+ \mu_\perp^-}$ in the WEM prediction (5.52) leads (at 25°C) to

$$\sqrt{\mu_\perp^+ \mu_\perp^-}^{(MBBA)} = 1.6 \times 10^{-10} \mathrm{m}^2/(\mathrm{Vs}), \tag{5.54}$$

consistent with the values given in Table 3.1.

Figure 5.8 shows the WEM prediction for the Hopf frequency as function of the external frequency for the above mobilities and a vanishing recombination rate. The comparison with the measured values of Fig. 5.7 shows nearly a quantitative agreement. Note, that once $\sqrt{\mu_\perp^+ \mu_\perp^-}$ is fixed, all other points of the theoretical curve are determined by the known SM parameters (Appendix A.1).

5.5.2 Travelling oblique rolls in I 52

The NLC I 52 is more stable than MBBA and the drift in time of the material parameters (especially the conductivity) is slow compared to MBBA or Phase 5 [78]. This enables quantitative measurements at different temperatures. Since $\sigma_\perp$, the

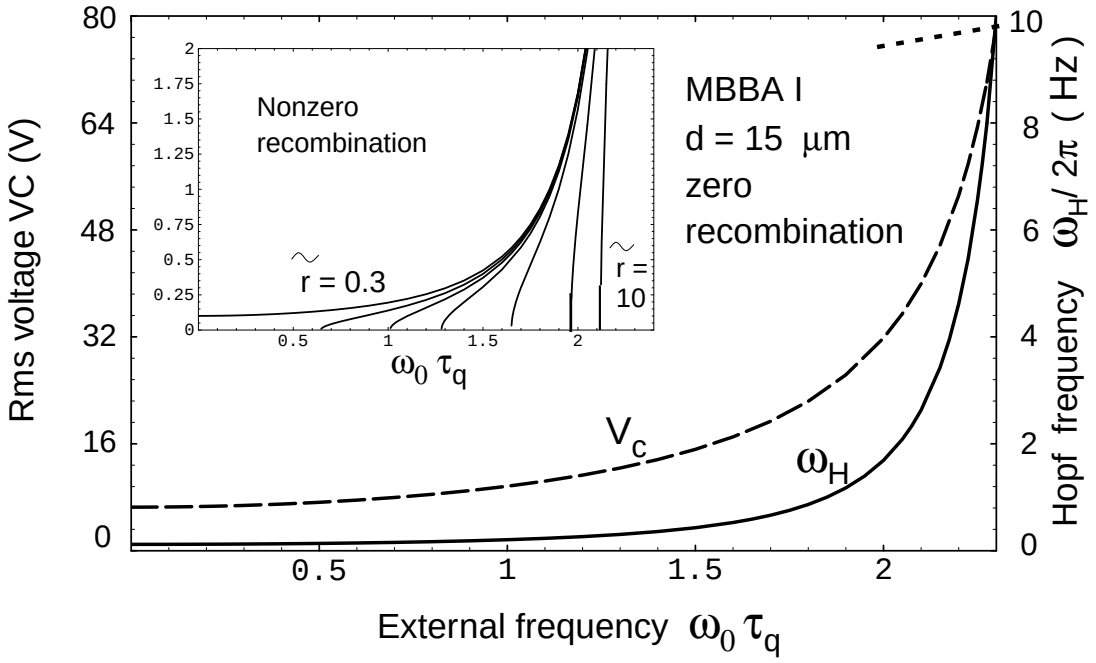

Figure 5.8 Hopf frequency (solid lines) and threshold voltage (dashed) as function of the external frequency for a MBBA cell with the parameters of Ref. [41] (parameter set MBBA I, Appendix A.1 with $\sigma_\perp = 4 \times 10^{-8}(\Omega\mathrm{m})^{-1}$ and $d = 15\ \mu$m), to be compared with Fig. 5.7. Shown is the whole conductive regime. The experimental crossover to the dielectric mode at $\overline{V}_c \approx 80V$ is shown schematically as dash-pointed line (it is not calculated). The scaled frequency $\omega_0\tau_q = 1.1$ (vertical arrow) corresponds in physical units to about 190 Hz (vertical arrow in Fig. 5.7). In the main plot, a negligible recombination rate (in fact $\tilde{r} < 0.3$), is assumed and the geometric mean of the mobility is fitted to the measured Hopf frequency [41] of 0.34 Hz at $\omega_0/2\pi = 190$ Hz ($\omega_0\tau_q = 1.1$) with the result $(\mu_\perp^+\mu_\perp^-)^{1/2} = 1.6 \times 10^{-10}\mathrm{m}^2/(\mathrm{Vs})$. The inset shows the effect of a nonzero recombination while the other parameters are unchanged. The recombination parameter is, from left to right, $\tilde{r} = 0.3, 0.5, 0.7, 1, 2, 5$, and 10. The curve for $\tilde{r} = 0.3$ can be hardly distinguished from that for $\tilde{r} = 0$.

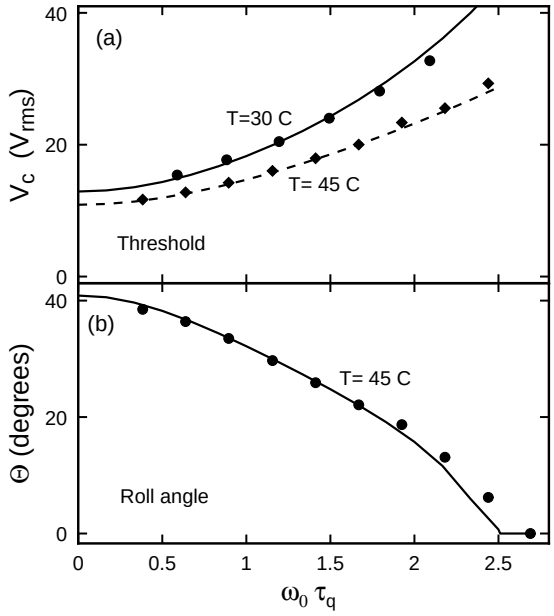

Figure 5.9 Threhold voltage $\overline{V}_c$ and angle Θ of the wavevector with respect to the director, as a function of the dimensionless applied frequency $\omega_0\tau_q$ for the I 52 experiments of Ref. [42]. (a) $\overline{V}_c$ for $T = 30°$C (circles, solid line) and 45°C (diamonds, dashed line). The symbols (lines) are the experimental (theoretical) result. The $\omega_0\tau_q \to 0$ limit is used to determine the temperature dependence of $\sigma_a/\sigma_\perp$, given in the Appendix (A.1). (b) Θ for $T = 45°$C. The temperature dependence of Θ is relatively weak.

viscosities, and ϵ_a have a rather strong temperature dependence, one obtaines qualitatively different Hopf-frequency curves (as function of the external frequency) for different temperatures. Provided that the temperature dependence of the material parameters is known, one can test the WEM on several curves without introducing new unknown parameters.

The experiments were performed by Dennin, Ahlers, and Cannell with cells of 28 μm and 57 μm thickness for six different temperatures [42, 30, 31]. In contrast to MBBA, the bifurcation is to oblique rolls, apart from very high external frequencies (Fig. 5.9). Unfortunately, the relative conductivity anisotropy $\sigma_a(T)/\sigma_\perp(T)$, two

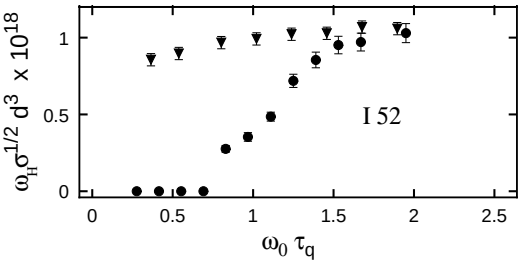

Figure 5.10 $\omega_H \sigma^{1/2} d^3$ as a function of $\omega_0\tau_q$ for one cell of thickness $d = 28$ μm and $\sigma_\perp = 8.5 \times 10^{-9}$ ohm^{-1} m^{-1} (triangles) and one with $d = 57$ μm and $\sigma_\perp = 1.1 \times 10^{-8}$ ohm^{-1} m^{-1} (circles) taken from Ref. [42]. Both cells were at $T = 50°$C. For high frequencies the data scale as predicted by the WEM: $\omega_H \propto \sigma^{-1/2} d^{-3}$. The sharp decrease in ω_H as ω_0 is decreased for the thicker cell is predicted by the WEM and fixes the unknown recombination rate.

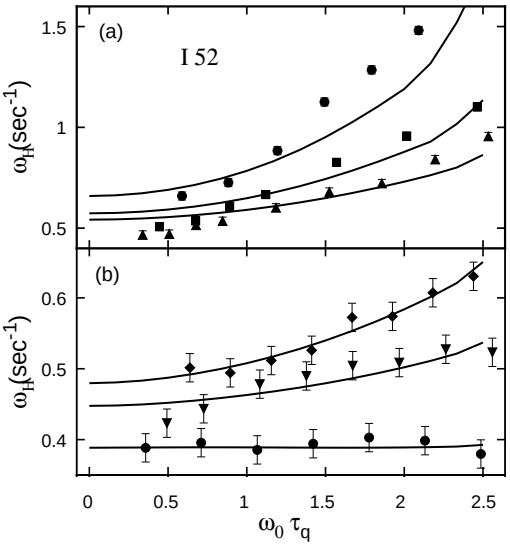

Figure 5.11 Measured and calculated values of the Hopf frequency ω_H as a function of $\omega_0\tau_q$. (a) is for $T = 30$ (circles), 35 (squares), and 40°C (triangles). (b) is for $T = 45$ (diamonds), 50 (triangles), and 60°C (circles). The corresponding results for the WEM model are shown by the solid lines. In both (a) and (b), the abrupt change of slope in the theoretical curves corresponds to the Lifshitz point.

elastic constants, and three viscosities, are not known for I 52. They were fitted to the threshold curves and the curves of the roll angle for all six temperatures. Typical examples of the fits are shown in Fig. 5.9.

Eq. (5.52) predicts $\tilde{\omega} \propto \sigma_\perp^{-1/2} d^{-3}$. If $\tilde{\omega} > 2|\lambda_\sigma|$, this is approximately valid for the Hopf frequency as well. Figure 5.10 compares results from the 28 μm cell with that from a 57 μm thick cell of slightly different conductivity, both at 50°C. We find the expected scaling with d for high values of ω_0 where, indeed, $\tilde{\omega} > 2|\lambda_\sigma|$ (which can be shown *a posteriori* after determining λ_σ). While $\sigma_\perp^{1/2} d^3$ differs by a factor of 9.6 between the two cells, the product $\omega_H \sigma_\perp^{1/2} d^3$ differs by less than 10 % for high values of ω_0. The relaxation rate $\tau_{\rm rec}^{-1}$ can be found with the help of Eq. (5.53) by identifying for the thick cell (index 1) $\tau_{rec,1}^{-1} = \tilde{\omega}_1^{\rm phys}$ at the external frequency where the Hopf frequency goes to zero ($\omega_0\tau_q = 0.7$ in Fig. 5.10). Since $\omega_{H,2}^{\rm phys} \approx \tilde{\omega}_2^{\rm phys} = 9.6\tilde{\omega}_1^{\rm phys}$ for the thin cell (index 2), the recombination rate can be determined by measuring the Hopf frequency of the thinner cell at the same scaled external frequency, $\tau_{\rm rec} = 1/\tilde{\omega}_1^{\rm phys} = 9.6/\tilde{\omega}_2^{\rm phys} \approx 20$s. Presumably, the recombination rate does depend only on the temperature and not on the cell thickness, so this is the recombination rate for both cells.

Fig. 5.11 shows the measured and predicted Hopf frequencies for a thin $d = 28$ μm cell as function of the external frequency with six temperatures as parameter. The relaxation time calculated above corresponds to $\tilde{\omega}/|\lambda_\sigma| > 3$ for any temperature and external frequency, so the theoretical $\omega_H \approx \tilde{\omega}$ is computed using Eq. (5.53) with only one adjustable parameter, $\sqrt{\mu_\perp^+ \mu_\perp^-}$, for each temperature. The fitted values increased

monotonically with T and were all in the range (see Table A.2)

$$\sqrt{\mu_\perp^+ \mu_\perp^-}^{(I52)} = (0.40...0.47) \times 10^{-10} \mathrm{m}^2/(\mathrm{Vs}), \tag{5.55}$$

The discrepancy (up to 15%) at the lower temperatures (Fig. 5.11a) is related primarily to experimental uncertainties in the very small measured conductivity. For most of the data, experiment and theory agree to within 5% of ω_H.

The WEM captures a number of features of the experiment which are independent of the uncertainties in the material parameters. Both in the model and the experiment, the ω_0 dependence of ω_H is determined mostly by ϵ_a. For $\epsilon_a < 0$ ($T < 60°\mathrm{C}$), ω_H increases with ω_0, and for $\epsilon_a \approx 0$ ($T = 60°\mathrm{C}$), it is essentially constant (Fig. 5.11). In addition, the model predicts $\omega_H \propto \sigma_\perp^{-1/2} d^{-3}$. The correct dependence on temperature in Fig. 5.11 reflects the $\sigma_\perp^{-1/2}$ scaling. Note that $\sigma_\perp$ varies by a factor of 5 over the temperature range $30°\mathrm{C} \leq T \leq 60°\mathrm{C}$. Fig. 5.10 shows the correct d^{-3} scaling for two cells with a ratio of d^3 of about 8. The decrease of ω_H to zero for the thicker cells is predicted by the WEM as well. It fixes the recombination rate. Since, to my knowledge, there are no independent quantitative measurements of τ_{rec}, this last aspect can be considered only as a qualitative agreement. Further work is needed to test the theory in this regime since (in contrast to MBBA) an extremely fine tuning of τ_{rec} is required to match the experiment. This is the result of the nearly vanishing dielectric anisotropy.

5.6 Comparison with other systems showing a Hopf bifurcation

I rely on intuition

A. Einstein

A characteristic feature of the WEM is the interplay between a primary instability mechanism and a slower stabilizing mechanism as shown in the top row of Fig. 5.12. A negative director bend $-iq\delta n_z$ leads *via* $\sigma_a^{(\mathrm{eff})}$ to a charge accumulation $\delta\rho$ and to an electric volume force driving the fluid motion $\delta\boldsymbol{v}$. The orientational viscosities close the destabilizing feedback loop by coupling back velocity gradients to the director bend. The gradients of the charge accumulation, however, excite also the charge-carrier mode whose feedback tends to decrease the charge. This second mechanism is only relevant if the σ mode can build up, i.e., the relaxation of this mode (symbolically shown by the arrow with the broken line in the diagram in the top row of Fig. 5.12) is slow.

As shown in Fig. 5.12 for three systems of thermal convection, this interplay seems to be a common scenario for generating travelling waves by a Hopf bifurcation The primary destabilizing mechanism in all three systems is that of the "classical" Rayleigh–Bénard convection for isotropic one-component fluids. The buoyancy force of a volume element of hotter fluid ($\delta\theta > 0$) acts as driving force for the fluid motion $\delta\boldsymbol{v}$ which, in turn, advects this element into colder regions thus increasing the relative temperature difference and the buoyancy force.

In thermal convection in a homeotropically aligned NLC cell (second row in Fig. 5.12), the fluid motion excites, in addition, a director distortion δn_x. If the anisotropy of the thermal conductivity is positive (which is nearly always the case), this leads to a positive divergence of the thermal heat flux in the warmer region, i.e., to a cooling of this region corresponding to a stabilizing feedback [99, 61]. The relaxation time of the director is larger than that of the fluid and the temperature by factors of $\tau_{visc}/\tau_d \approx 10^6$, and $P\tau_{visc}/\tau_d$, respectively (P is the Prandtl number and τ_d is defined analogously as in the planar geometry).

In the "thermohaline" convection experiments in salt water (third row in Fig. 5.12), the BC are such that in the basic state, besides the imposed temperature gradient, there is a gradient of the salt concentration with a higher salt concentration near the bottom [100]. So, the fluid element is not only transported into colder regions increasing the relative temperature difference and the buoyancy caused by thermal expansion, but also transported to regions of a lower salt concentration increasing the relative salt concentration and leading to a negative contribution of the buoyancy (the density of the fluid increases with the salt concentration). The time scale of the concentration field is set by the molecular diffusion time $\tau_D = d^2/D$ of the salt concentration (where D is the diffusion coefficient), which is very long compared to other time scales (note that neglect of molecular diffusion, as done in this chapter for the charge carriers, corresponds to an infinitely long diffusion time).

At last, the bottom row of Fig. 5.12 shows thermal convection in a binary mixture of fluids for the case where the Soret effect leads to a negative separation ratio ψ [22, 54, 9], i.e., temperature inhomogenities induce a mass flux $\propto \psi\boldsymbol{\nabla}T$ of the more dense component, which is directed towards the warmer regions. The BC of impenetrable walls together with the imposed temperature gradient lead in the basic state to a linear concentration profile where the concentration of the heavier fluid component decreases with z. The stabilizing concentration mode [101] is excited in two ways, i) by advection through the concentration gradient of the basic state, as in the thermohaline system; ii) directly by the Soret effect where the temperature inhomogeneity of the linear mode induces a flux of the more dense component into

the warmer regions. The time scale of the concentration mode is governed by the concentration diffusion time τ_D, related to the thermal diffusion time $\tau_{th} = d^2/\kappa$ (κ is the thermal diffusion coefficient) by the "Lewis number" $\mathcal{L} = \tau_{th}/\tau_D$ which is $\approx 10^{-2}$ or smaller for liquid mixtures.

The parameters $-\psi$ and $\mathcal{L}$ are, in some way, the analog of $\tilde{\alpha}$ and $\tilde{r}$ in the WEM. The excitation of the concentration mode (of the WEM carrier density mode) is proportional to $-\psi$ ($\tilde{\alpha}^2$), while its relaxation is proportional to $\mathcal{L}$ ($\tilde{r}$). A Hopf bifurcation occurs if $\sqrt{-\psi} > c_1\mathcal{L}$ ($\tilde{\alpha} > c_2\tilde{r}$) with c_1, c_2 of the order of unity, and if the condition is well satisfied (and $\sqrt{-\psi} <\approx 0.3$), the Hopf frequency is $\propto \sqrt{-\psi}$ ($\propto \tilde{\alpha}$); see, e.g., Fig. 5.2. in Ref. [9] for binary mixtures. In contrast to the WEM, the interesting parameter ranges near the codimension-two curve or near the tricritical curve are, at least for usual liquid mixtures, extemely narrow (typically, $0 > \psi \geq -10^{-4}$) and therefore experimentally hard to attain.

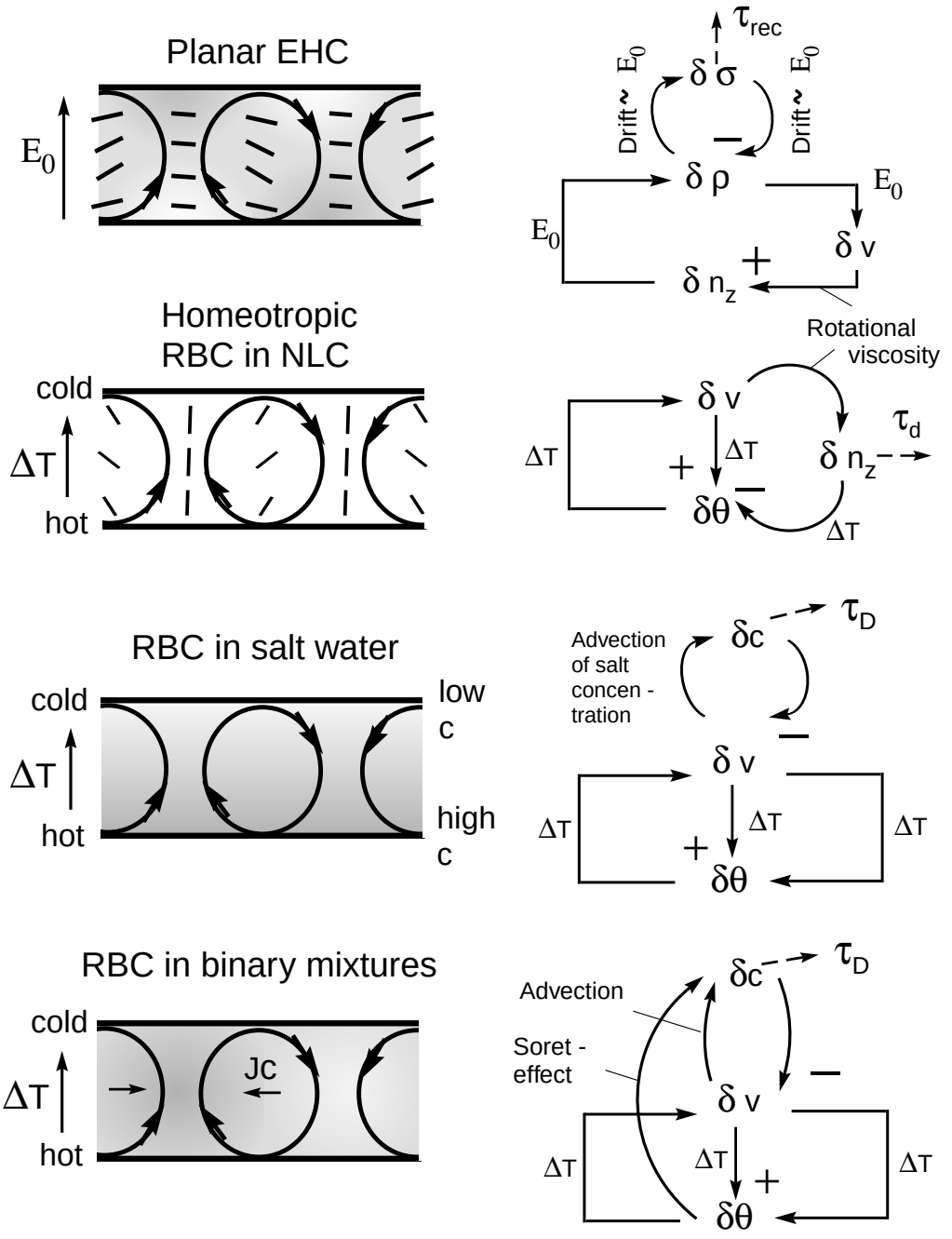

Figure 5.12 Comparison of the WEM mechanism to that of three Rayleigh–Bénard systems which also show a Hopf bifurcation, at least in certain parameter ranges. In each case, the basic destabilizing feedback cycle (straight lines) is coupled to a stabilizing one with a slower time scale (curved lines). The time scale of the stabilizing fields due to relaxation is indicated by arrows with a broken line. In each example, the physical effects providing the coupling to the stabilizing cycle are given. The symbols E_0 or ΔT indicate that the corresponding effect of one field onto the next is proportional to the external driving.

Chapter 6

Weakly nonlinear analysis

Never I encountered a problem which did not become more complicated on careful examination

P. Anderson

The linear analysis of the WEM presented in the previous chapter predicts a threshold shift with respect to the SM and, for sufficiently low recombination rates, a Hopf bifurcation to travelling rolls. Further questions can be treated at the weakly-nonlinear level. Is the bifurcation continuous (forward) or hysteretic (backward)? If it is forward, which combinations of degenerate linear modes will be selected by the dynamics? For instances, for a Hopf bifurcation, the dynamics can select travelling waves or standing waves, i.e., a superposition of left and right travelling waves. In the oblique-roll regime, isolated regions of "zig" or "zag" modes, or a superposition of both, can be favoured; for travelling oblique waves there are even more possibilities. Furthermore, how does the frequency of the travelling waves depend on the reduced control parameter $\epsilon = R/R_c - 1$? Finally, can the observation of chaos at onset [30, 31] be explained within the framework of the weakly-nonlinear analysis?

If the bifurcation is hysteretic, there is the question of the amplitude and of the type (e.g., stationary or oscillatory) of the nonlinear final state, and of the range of the control parameters where hysteresis effects take place. Upon decreasing the control parameter, when does the system jump back to the unstructured state?

The basic idea of the weakly-nonlinear analysis [1, 102, 103] is to reduce the phase space of the system to that of the slowly relaxing "dynamically active" modes. The remaining fast degrees of freedom are "slaved" [1] to these modes. This idea uses the fact that, if one starts with general initial conditions (with a general point in the phase space of the system), the state in phase space will approach on a fast time scale the subspace spanned by the slowly relaxing degrees of freedom, and the

subsequent dynamics will take place on this subspace. For recent reviews see, e.g., [9, 50, 24] or [104].

The (still infinitely dimensional) set of these dynamically active degrees of freedom can be constructed from modes on the same dispersion branches as the critical modes, with wave vectors close to the critical wave vectors. In addition, this set may contain slowly relaxing modes generated by the nonlinearities.

In Chapter 6.1, I discuss the Ginzburg–Landau approach and give the (uncoupled) complex Ginzburg–Landau equation (CGL) for the WEM in the special case of a one-dimensional dynamics of left-travelling waves (LTW) (or, equivalently, right-travelling waves).

Chapter 6.2 gives analytic expressions for the coefficients of this CGL. Rather than providing quantitative numerical results, the goal is a qualitative (at most semi-quantitative) understanding of the nonlinear behaviour of the WEM. In particular, the intricate influence of the WEM mobility parameter $\tilde{\alpha}$ and the recombination parameter $\tilde{r}$ on the dynamics will be elucidated by means of analytic expressions containing explicitely these parameters.

In Chapter 6.3, I summarize the weakly-nonlinear results of the WEM by phase diagrams in the WEM parameter space $(\tilde{\alpha}, \tilde{r})$ and by an expression for the change of the oscillation frequency with the control parameter in the Hopf regime. The predictions are compared with experiments on MBBA and I 52. Furthermore, I give estimates for the nonlinear amplitude in the stationary-hysteretic regime assuming no WEM effects in the nonlinear state. Most results agree, within factors of about two with the experiments.

Chapter 6.4 gives a discussion of the weakly-nonlinear results.

6.1 Ginzburg-Landau equations for the WEM

With at most discrete degeneration of the critical mode, the near-threshold dynamics can be described, for a continuous bifurcation, by a set of third-order coupled Ginzburg–Landau equations (CCGL) for the envelopes (or amplitudes) $A_m(x, y, t)$ of wave packets with wave vectors near that of the mth mode in the set of the degenerated critical modes. For oblique travelling rolls, this involves a total of four amplitudes for the modes of the right and left-travelling "zig" and "zag" rolls. For a hysteretic bifurcation, one needs at least fifth-order CCGLs with a stabilizing fifth-order term to counteract the destabilizing third-order contribution.

For simplicity, I restrict the treatment to one lateral dimension, x, and to modes near the critical mode $\propto e^{i(\mathbf{q}\cdot\mathbf{x}+\omega t)}$ for left-travelling waves (LTW) leading to a one-

dimensional uncoupled CGL. Some relevant experimental results (especially those for I 52 [30, 31]) are for the regime of oblique rolls and the weakly-nonlinear description for, say, the wave packet of the LTWs with $p_c > 0$, would require a two-dimensional CGL. Nevertheless, one can expect that, like q_c and ω_H in the linear regime, many weakly-nonlinear aspects of the oblique-roll regime can be described, at least semi-quantitatively, by dropping the y dependence. [1]

Restricting to left-travelling rolls (and to $p > 0$ for oblique rolls), the set of slowly-relaxing modes can be represented as a wave packet with wave vectors around that of the critical LTW,

$$\begin{aligned} \boldsymbol{u} &= \boldsymbol{u}^{(1)} + \text{higher order terms}, \\ \boldsymbol{u}^{(1)} &= A(\boldsymbol{x},t)\tilde{\boldsymbol{u}}(z,\omega_0 t)e^{i[\mathbf{q}_c\cdot\mathbf{x}+\omega(\mathbf{q}_c,\epsilon)t]} + \text{c.c.} \end{aligned} \tag{6.1}$$

The complex amplitude $A(\boldsymbol{x},t)$ varies slowly in x, y and in time but the y dependence will be dropped. The spatial variation $e^{i\mathbf{q}_c\cdot\mathbf{x}}$ of the critical mode and its frequency (the imaginary part of the linear growth rate) at $\boldsymbol{q} = \boldsymbol{q}_c$ and at the *actual* value of the control parameter is separated out. The function $\tilde{\boldsymbol{u}}$ is the Floquet function, Eq. (5.14), for the LTW at threshold and contains the z dependence and the periodicity with the external field. Within the lowest-order Floquet and Galerkin expansions, $\tilde{\boldsymbol{u}}$ is given by Eq. (5.15) where $(\sigma^{(0)}, \phi^+, \phi^-, n_z^{(0)}, \cdots)$ is the eigenvector composed of the Galerkin coefficients, given by Eq. (5.17) for $\boldsymbol{q} = \boldsymbol{q}_c$, $R = R_c$, and $\lambda = i\omega_H$. For quantitative statements about nonlinear (or stochastic) properties, the normalization of the eigenfunctions is important. It is chosen such that $|A|$ gives directly the maximum director angle $\arctan(n_z) \approx n_z$ at $z = 0$, which can be measured directly by the shadowgraph method [105],

$$n_z(\boldsymbol{r},t) = |A(x,t)|\cos z \cos[\boldsymbol{q}_c\cdot\boldsymbol{x} + \omega(\epsilon,\boldsymbol{q}_c)t + \phi_A] \tag{6.2}$$

with $\phi_A = \arg(A)$. For the coefficients of the one-mode expansion (5.15), this corresponds to $n_z^{(0)} = (\pi/8)^{1/2}$.

The form of the amplitude equation is determined completely by symmetry constraints [9],

$$\tau_0(\partial_t - v_g\partial_x)A = [\epsilon + \xi_0^2(1+ib)\partial_x^2]A - g(1+ic)|A|^2A. \tag{6.3}$$

There are several ways to derive the coefficients. These include the introduction of multiple scales and a subsequent systematic expansion, or the use of "order-parameter equations in $\boldsymbol{q}$ space together with projection techniques employing the "slaving principle" [1].

[1] The nonlinear selection of the zig and zag modes, of course, cannot be described by this approximation.

The multiscale approach was first applied to RBC in simple fluids [102]. Other systems include, e.g., lasers [106] or EHC [48]. For reviews see, e.g., [104, 24, 10].

The order-parameter approach has been applied, e.g., for thermal convection in simple fluids [103], thermal convection in homeotropically aligned EHC, [107, 108], and to EHC [50].

It turns out that the linear coefficients are obtained most easily by using the projection method which, in this case, reduces to an expansion of the growth rate around the threshold (Chapter 6.2.1). The nonlinear coefficients g and c can be calculated easier with the multiple-scale method (Chapter 6.2.2).

6.2 Coefficients of the one-dimensional complex Ginzburg-Landau equation

In addition to the asumptions made in Chapter 5 (adiabatic elimination of the charge and the velocities, lowest-order Galerkin and Floquet expansions), I consider external frequencies satisfying (in physical units) $\omega_0\tau_q << 1$ and $\omega_0\tau_d >> 1$.

The decisive new nonlinearity of the WEM is the term $\boldsymbol{v}\cdot\boldsymbol{\nabla}\sigma$ associated with advection of the carrier density, Eq. (3.28). It can be argued that the saturation of the $\pm q_c$ modes of all SM fields is not altered by WEM effects. Furthermore, I neglect the interaction of the σ modes with intermediate modes excited by second-order SM nonlinearities. This last assumption (whose validity has yet to be investigated) allows an adiabatic elimination of ρ and $\boldsymbol{v}$ also for the nonlinear case by generalizing the effective quantities in Eq. (5.38) to allow for an amplitude dependence. [2]

With these assumptions, the Eqs. (3.28) and (3.29) can be written as

$$\begin{aligned}\left(\partial_t-\hat{\lambda}_\sigma\right)\sigma-R\tilde{\alpha}^2\hat{\sigma}_a^{(\mathrm{eff})}\,\partial_x\partial_z n_z &= -(\boldsymbol{v}\cdot\boldsymbol{\nabla})\sigma \\ &- R\tilde{\alpha}^2\hat{\sigma}_a^{(\mathrm{eff})}\,g^{\mathrm{SM}}|A(x,t)|^2\partial_x\partial_z n_z, \qquad (6.4)\\ -\frac{R\hat{C}^2}{\hat{\sigma}_a^{(\mathrm{eff})}}\partial_z\sigma+\left(\partial_t-\hat{\lambda}_n\right)\partial_x n_z &= -g^{\mathrm{SM}}|A(x,t)|^2\left(\frac{\partial_x n_z}{\tau_0^{\mathrm{SM}}}+\frac{R\hat{C}^2}{\hat{\sigma}_a^{(\mathrm{eff})}}\partial_z\sigma\right), \qquad (6.5)\end{aligned}$$

where $g^{\mathrm{SM}}=0.48$ for MBBA at $\omega_0\tau_q << 1$ and for the normalization (6.2) [48]. The left-hand sides contain the linear terms; the quantities $\hat{\lambda}_\sigma$, $\hat{\sigma}_a^{(\mathrm{eff})}$, $\hat{C}$, and $\hat{\lambda}_n$ are operators which reduce to the corresponding effective quantities λ_σ, $\sigma_a^{(\mathrm{eff})}$, C and λ_n of Chapter 5, if applied to the SM modes. For other modes, they are understood

[2] This is a standard method in nonlinear optics. If, e.g., in laser-active dielectric materials, the time scales of the polarization and inversion fields are much shorter than that of the optical field $\boldsymbol{E}$, one can introduce an effective dielectric permittivity which is $\propto(1+g|\boldsymbol{E}|^2)^{-1}$ [106].

Table 6.1: Linear coefficients of the Ginzburg Landau equation in the approximation $R\tilde{\alpha}^2 << 1$

Quantity	Hopf range	Stationary range
τ_0	$2\left(\frac{1}{\tau_0^{\mathrm{SM}}} - \frac{R\tilde{\alpha}^2\epsilon_q}{\sigma_q(1+\omega'^2)}\right)^{-1} \approx 2\tau_0^{\mathrm{SM}}$ *	$\tau_0^{\mathrm{SM}} \frac{\left(1-\frac{\tilde{\omega}^2}{\lambda_\sigma^2}\right)}{1+2\tau_0^{\mathrm{SM}}\frac{\tilde{\omega}^2}{\lambda_\sigma}}$
ξ_0^2	$\xi_{0,\mathrm{SM}}^2$	$\xi_{0,\mathrm{SM}}^2 - \frac{(\tau_0^{\mathrm{SM}})^3\tilde{\omega}^4}{\tau_0^2\lambda_\sigma^3}\left(\frac{\partial_q C^2}{C^2}\right)^2$ †
b	$\frac{\lambda_\sigma}{\omega_H} + \frac{\tau_0^{\mathrm{SM}}}{\xi_{0,\mathrm{SM}}^2\omega_H}\left(v_g^2 - \partial_q(\tilde{\omega}\partial_q\tilde{\omega})\right)$ **	$--$
v_g	$\frac{\tilde{\omega}\partial_q\tilde{\omega}}{\omega_H}$ **	$--$
$\frac{\partial\omega}{\partial\epsilon}$	$\frac{\tilde{\omega}^2}{\omega_H} + \frac{\lambda_\sigma}{2\tau_0^{\mathrm{SM}}\omega_H}$	$--$
*The first expression is without the approximation $R\tilde{\alpha}^2 << 1$ †Approximation $\tilde{\omega} << 1/\tau_0^{\mathrm{SM}}$ **Approximation $R\tilde{\alpha}^2 << \tilde{\omega}$		

as numbers resulting from the Galerkin approximations for the actual modes (see below). For the Galerkin approximation (5.39) and (5.40) of critical modes, the left-hand side reduces to Eq. (5.38).

The nonlinear terms are on the right-hand sides. The only second-order nonlinearity is the advection term $-\boldsymbol{v}\cdot\boldsymbol{\nabla}\sigma$ in Eq. (6.4). The term $\propto \partial_x n_z$ in Eq. (6.5) is the saturating SM nonlinearity. The other two terms $\propto R$ describe the saturation of the coupling from the σ to the n_z mode, and *vice versa*. The coupling is mediated by the charge density and it can be shown [109], that the saturation of the SM mode is primarily due to the nonlinearities in the charge focussing effect of the director bend. So I assume that this coupling saturates like the SM mode.

6.2.1 Linear coefficients

The linear coefficients of the CGL (6.3) can be obtained directly by the projection method. With the ansatz $\overline{\boldsymbol{u}} = \bar{A}_{\mathbf{q}-\mathbf{q}_c}(t)\tilde{\boldsymbol{u}}e^{i\omega(\mathbf{q}_c,\epsilon)t}$, the eigenvalue problem for the growth rate of the critical branch can be written as

$$\partial_t \bar{A}_{\mathbf{k}} = \left[\lambda(\boldsymbol{q}_c+\boldsymbol{k},\epsilon) - i\omega(\boldsymbol{q}_c,\epsilon)\right]\bar{A}_{\mathbf{k}}, \tag{6.6}$$

where $\boldsymbol{k} = \boldsymbol{q} - \boldsymbol{q}_c$. Taking, in lowest order, the Floquet function $\tilde{\boldsymbol{u}}$ at $\boldsymbol{q} = \boldsymbol{q}_c$, an inverse Fourier transformation of the ansatz back to real space results in Eq. (6.1) with

$$\partial_t A(\boldsymbol{x}, t) = \left[\lambda(\boldsymbol{q}_c - i\boldsymbol{\nabla}, \epsilon) - i\omega(\boldsymbol{q}_c, \epsilon)\right] A(\boldsymbol{x}, t). \tag{6.7}$$

The linear coefficients of the one-dimensional CGL are obtained in terms of the linear growth rate by comparing Eq. (6.3) with the Taylor expansion of Eq. (6.7) with respect to $q_c - i\partial_x$ and ϵ around $\boldsymbol{q} = \boldsymbol{q}_c$ and $\epsilon = 0$. The result is $\tau_0^{-1} = \partial_\epsilon \sigma|_c$, $v_g = \partial_q \omega|_c$, and $\xi_0^2(1 + ib) = -\frac{\tau_0}{2}\partial_q^2 \lambda|_c$, where $\lambda = \sigma + i\omega$ and $|_c$ stands for the critical point $\boldsymbol{q} = \boldsymbol{q}_c$ and $\epsilon = 0$. In addition, one obtains the linear frequency shift, $\Delta\omega := \omega(\boldsymbol{q}_c, \epsilon) - \omega_H = \epsilon \partial_\epsilon \omega|_c$.

Table 6.1 gives approximate analytic expressions for these coefficients using Eq. (5.47) for the growth rate, both for the Hopf regime $\tilde{\omega} > |\lambda_\sigma|$, and for the stationary regime $\tilde{\omega} < |\lambda_\sigma|$, separated by the codimension-two (C2) curve.

The Figures 6.1 and 6.2 show the real and imaginary CGL coefficients for I 52 parameters. Remarkably, the correlation time τ_0 in the Hopf regime is nearly twice the time in both the SM and in the stationary regime not too near to the C2 curve. This can be seen directly from the real part of the growth rate (5.47) which is $\sigma = (\lambda_\sigma + \lambda_n)/2$ in the Hopf regime, while it is $\sigma \approx \lambda_n$ in the stationary regime far away from the C2 curve. For most situations, the ϵ dependence $\propto \tilde{\alpha}^2$ of λ_σ, Eq. (5.41), is negligible compared to that of λ_n. This leads to the factor of 2 in $\tau_0 = (\partial_\epsilon \sigma)^{-1}$.

The correlation time goes to zero and the correlation length diverges if one approaches the C2 curve from the stationary side (Figures 6.1a and 6.1b). This is caused by the dependence of the square root in Eq. (5.47) on, respectively, ϵ and $\boldsymbol{q}$, together with the divergence of the gradient of the square root at the C2 point. Approaching the C2 point from the Hopf region, the diverging gradient leads to vanishing factors of ω_H in the denominators of the expressins for $\frac{\partial \omega}{\partial \epsilon}$, v_g, and b, causing the singularities of these quantities at the C2 point

If the Hopf condition is well satisfied and $\omega_0 \tau_q << 1$, the group velocity $v_g \approx R_c \tilde{\alpha} \frac{\partial C}{\partial q}|_c$ has the same sign as the phase velocity ω_H/q_c of the critical mode; the ratio $v_g/(\omega_H/q_c) = C^{-1}\frac{\partial C}{\partial q}|_c$, is slightly smaller than 1, both for MBBA and I 52 (Fig. 5.5). For most parameters, the expression for the dispersion coefficient b is mainly determined by the negative relaxation term $\lambda_\sigma/\tilde{\omega}$. For very small recombination rates or very high mobility parameters, the term $\propto \partial_q(\tilde{\omega}\partial_q\tilde{\omega})$ becomes important; it is essentially proportional to the negative curvature of $C(q)$, i.e., positive for both MBBA and I 52 (Fig. 5.5). The divergence of b at the C2 point is due to the v_g^2 term.

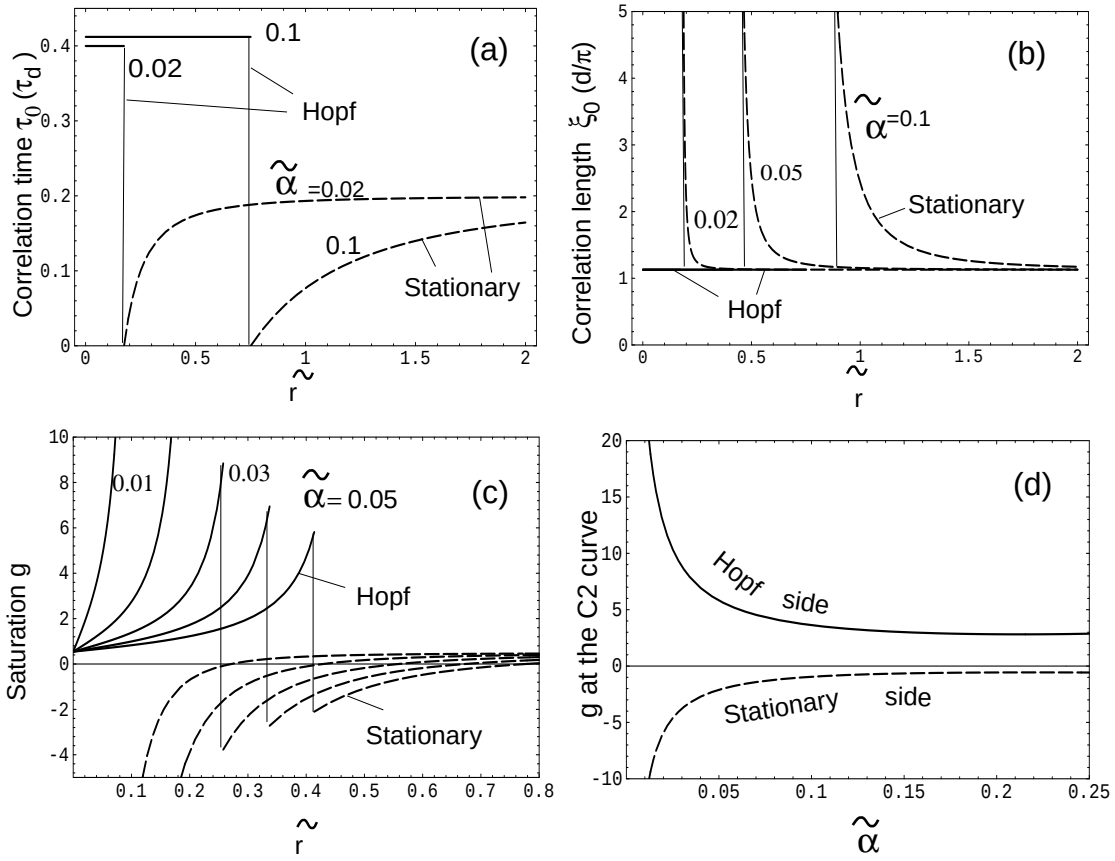

Figure 6.1 (a)-(c) plots of the real Ginzburg–Landau coefficients τ_0 and ξ_0^2 (Table 6.1), and g (Table 6.2) for I 52 at 45°C and for $\omega_0\tau_q << 1$. The full lines are for the Hopf regime of travelling waves and the dashed lines for the stationary regime. Parameter is the mobility parameter $\tilde{\alpha}$, where $\tilde{\alpha} = 0.01 \cdots 0.04$ is the order of magnitude in the MBBA and I 52 experiments, and $\tilde{\alpha} = 0.1$ corresponds to very thin cells.
(d) Nonlinear saturation g along the C2 curve approaching the C2 curve from the Hopf regime (full line) and from the stationary regime (dashed). Several approximations have been applied in calculating the nonlinear coefficients, see the main text.

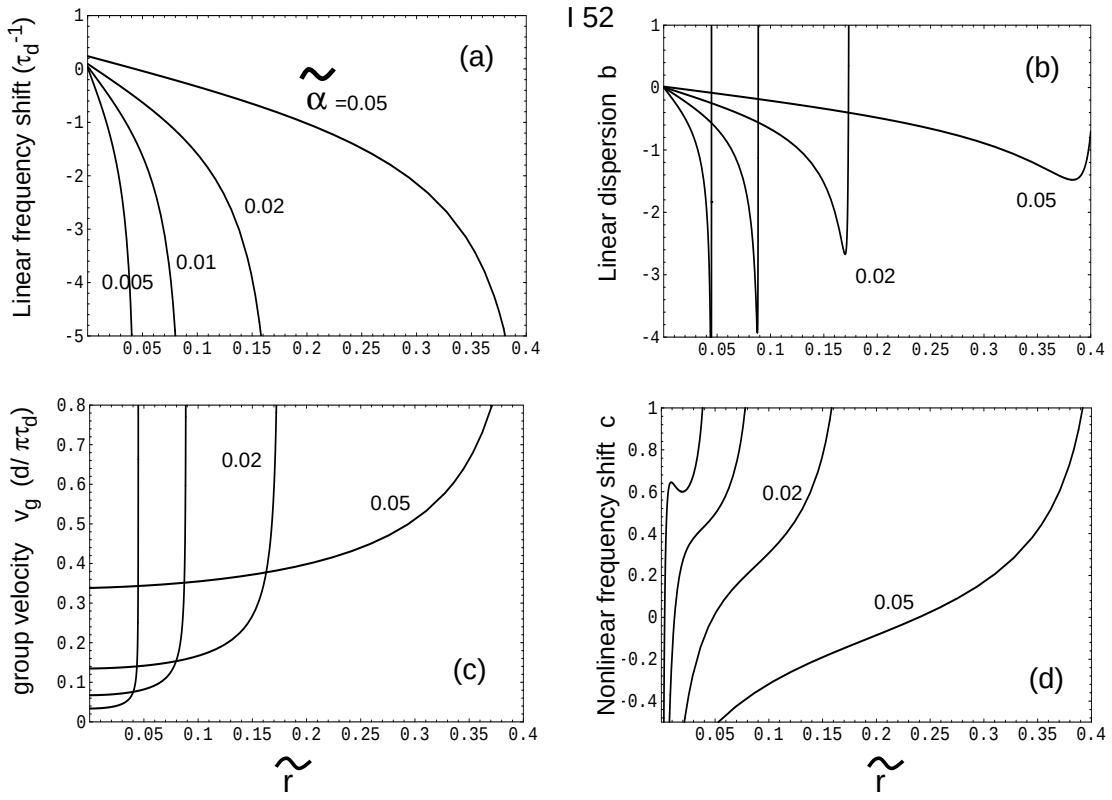

Figure 6.2 (a) linear frequency shift; (c) group velocity, and (b), (d), the imaginary parameters of the CGL in the Hopf regime for I 52 at 45°C and for external frequencies satisfying $\omega_0\tau_q << 1$. The linear dispersion b is proportional to $\frac{\partial^2\omega}{\partial q^2}$, and the nonlinear frequency shift c is proportional to $-\frac{\partial\omega}{\partial|A|^2}$.

At last, the linear frequency shift is negative, apart from the case of very small recombination rates or high values of $\tilde{\alpha}$, where the positive term $\propto \tilde{\omega}^2/\omega_H$ becomes the main contribution. This term reflects the dependence of the coupling $\tilde{\omega} = R\tilde{\alpha}C$ on R.

6.2.2 Nonlinear coefficients

Now I derive the saturation coefficient g and the nonlinear frequency shift c of the CGL (6.3) by a systematic multiple-scale expansion. In this method (a pedagogical example can be found in Ref. [10]), one starts with the ansatz

$$\boldsymbol{u} = \boldsymbol{u}^{(1)} + \boldsymbol{u}^{(2)} + \boldsymbol{u}^{(3)} + \cdots, \tag{6.8}$$

where $\boldsymbol{u}^{(1)}$ is given by Eq. (6.1) in terms of the amplitude, and $\boldsymbol{u}^{(i)}$ is of the order of $|A(x,t)|^i$. Inserting this ansatz into the nonlinear basic equations assuming

$$\mathcal{O}(\partial_t - v_g\partial_x) = \mathcal{O}(\partial_x^2) = \mathcal{O}(|A|^2) = \mathcal{O}(\epsilon) \tag{6.9}$$

for all derivatives acting onto A, and separating into orders of $\epsilon, \epsilon^{3/2}, \cdots$ leads to a hierarchy of linear inhomogeneous equations of the form $\underline{\underline{\tilde{L}}}\boldsymbol{u}^{(i)} = I^{(i)}$. The operator $\underline{\underline{\tilde{L}}}$ contains all linear parts of the basic equations; the inhomogenities $I^{(i)}$ are given in terms of $\boldsymbol{u}^{(i-1)} \cdots \boldsymbol{u}^{(1)}$, calculated already in terms of A and $\tilde{\boldsymbol{u}}$ in the previous steps.

These inhomogeneous equations can be solved nontrivially only, if the $I^{(i)}$ are not in the kernel (null space) of $\underline{\underline{\tilde{L}}}^\dagger$, the operator adjoint to $\underline{\underline{\tilde{L}}}$ (Fredholm alternative). These "compatibility conditions" determine the amplitude equation to the desired order.

Now I apply this method to the "basic equations" (6.4) and (6.5). The solvability condition at $\mathcal{O}(\epsilon)$ leads to $\partial_t A - \frac{\partial\omega}{\partial q}|_c \partial_x A + \mathcal{O}(\epsilon^{3/2}) = 0$ defining $v_g = \frac{\partial\omega}{\partial q}|_c$. [3] This result has been obtained already more directly by the projection technique and will not be shown explicitely here. [4] The solvability condition at the next order $\epsilon^{3/2}$ determines the remaining coefficients of the CGL (6.3).

Since I am interested only in the nonlinear parts $\propto |A|^2 A$ which are already of order $\epsilon^{3/2}$, I neglect all derivatives acting on A ("exact resonance") and show the systematic expansion by starting, instead of Eq. (6.1), with the zero-dimensional ansatz[5]

$$\boldsymbol{u}^{(1)} = A(t)\tilde{\boldsymbol{u}}(z,\omega_0 t)e^{i(\mathbf{q}_c\cdot\mathbf{x}+\omega_H t)} + \text{c.c.}, \tag{6.10}$$

$$\tilde{\boldsymbol{u}}(z,\omega_0 t) \equiv \begin{pmatrix} \tilde{\sigma} \\ \tilde{n}_z \end{pmatrix} = \frac{1}{2}\begin{pmatrix} \sigma^{(0)}\sin z \\ \cos z \end{pmatrix}; \quad \sigma^{(0)} = \left.\frac{iq_c R_c \tilde{\alpha}^2 \sigma_a^{(\text{eff})}}{\lambda_\sigma - i\omega_H}\right|_c. \tag{6.11}$$

[3] In stationary pattern-forming systems like RBC or the SM of EHC, the solvability condition at this order is, usually, fulfilled automatically.

[4] An example of a nontrivial solvability condition at this order is given, e.g., in Ref. [106].

[5] This is the usual way to derive normal forms for low-dimensional systems ("Landau equations")

The inhomogeneous equations at order ϵ read

$$\left(\partial_t - \hat{\lambda}_\sigma\right)\sigma^{(2)} \quad -R\tilde{\alpha}^2\hat{\sigma}_a^{(\mathrm{eff})}\,\partial_x\partial_z n_z^{(2)} \quad = -\boldsymbol{v}^{(1)}\cdot\boldsymbol{\nabla}\sigma^{(1)}, \tag{6.12}$$

$$-\frac{R\hat{C}^2}{\hat{\sigma}_a^{(\mathrm{eff})}}\partial_z\sigma^{(2)} \quad +\left(\partial_t - \hat{\lambda}_n\right)\partial_x n_z^{(2)} \quad = 0. \tag{6.13}$$

For the Hopf regime, the second-order inhomogeneity is

$$\begin{aligned}\boldsymbol{v}^{(1)}\cdot\boldsymbol{\nabla}\sigma^{(1)} &= \frac{\pi(K^{(\mathrm{eff})})^2\eta^{(\mathrm{eff})}\,\tilde{\alpha}^2}{8\tilde{\omega}^2}\Big\{(\lambda_\sigma + i\omega_H)A^2e^{2i(\mathbf{q}_c\cdot\mathbf{x}-\omega_H t)}f_1(z) + \text{c.c.}\\ &- 2\sqrt{\frac{2}{\pi}}\lambda_\sigma|A|^2\partial_z\left[C_1(z)\sin z\right]\Big\}.\end{aligned} \tag{6.14}$$

The inhomogeneity for a stationary bifurcation is obtained by the substitutions $\tilde{\omega}^2 \to \lambda_\sigma^2$, and $\omega_H \to 0$. The function $f_1(z) = (2/\pi)^{1/2}[C_1(z)\cos z - \sin z\partial_z C_1(z)]$ has strong variations only near the boundaries (it would be equal to 1 for free BC).

This inhomogeneity does not lie in the kernel of the adjoint linear operator and drives the second-order charge-carrier modes. Solving Eqs. (6.12) and (6.13) with the BCs $\partial_z\sigma^{(2)} = n_z^{(2)} = 0$ for quasi-stationary conditions (i.e., the dynamics of the excited modes is fast compared to that of A), results, in the lowest-order Galerkin approximation, in two types of modes,

$$\begin{aligned}\boldsymbol{u}^{(2)} = \boldsymbol{u}_0^{(2)} + \boldsymbol{u}_2^{(2)} &= C_0^{(2)}\begin{pmatrix}\sqrt{\frac{2}{\pi}}\cos 2z\\ 0\end{pmatrix}|A|^2\\ &+ C_2^{(2)}\begin{pmatrix}\sqrt{\frac{1}{\pi}}\\ 0\end{pmatrix}A^2e^{2i(\mathbf{q}_c\cdot\mathbf{x}+\omega_H t)} + \text{c.c.},\end{aligned} \tag{6.15}$$

with the amplitudes

$$C_0^{(2)} = -\frac{\pi I_0(K^{(\mathrm{eff})})^2\eta^{(\mathrm{eff})}\,\tilde{\alpha}^2\lambda_\sigma}{4\tilde{\omega}^2\lambda_0^{(2)}}, \tag{6.16}$$

$$C_2^{(2)} = \frac{\pi I_2(K^{(\mathrm{eff})})^2\eta^{(\mathrm{eff})}\,\tilde{\alpha}^2(\lambda_\sigma + i\omega_H)}{4\sqrt{2}\tilde{\omega}^2\lambda_2^{(2)}}, \tag{6.17}$$

the growth rates

$$\lambda_0^{(2)} = -(\tilde{r} + 4R_c\tilde{\alpha}^2), \quad \lambda_2^{(2)} = -(\tilde{r} + 2i\omega_H), \tag{6.18}$$

and the projection integrals

$$I_0 = \frac{2}{\pi}\langle\cos 2z\;\partial_z\left[\sin z\;C_1(z)\right]\rangle = 0.658, \quad I_2 = \frac{2}{\pi}\langle\cos z\;C_1(z)\rangle = 0.787. \tag{6.19}$$

Again, the expressions for the stationary regime are obtained by substituting $\tilde{\omega}^2 \to \lambda_\sigma^2$ and $\omega_H \to 0$ in the Eqs (6.15) - (6.18).

Both excited modes are pure charge-carrier modes. The mode $\boldsymbol{u}_0^{(2)}$ is homogeneous in x, so the corresponding effective viscosity $\hat{\eta}^{(\mathrm{eff})}$ [Eq. (5.28) for $q = 0$ and appropriate projection integrals] diverges. This leads in Eq. (6.13) for very small q to $\hat{C}^2/\hat{\sigma}_a^{(\mathrm{eff})} = \epsilon_\perp \alpha_3 q^2/(\sigma_\perp \eta_2)$ times some projection integrals, i.e., the coupling of σ to n_z vanishes for $q = 0$. The σ part of $\boldsymbol{u}_2^{(2)}$ does not excite the director either, because this mode has no z dependence and the couplings are $\propto \partial_z \sigma$ and $\partial_z n_z$. The inhomogeneity (6.14) excites further modes, e.g., a mode with $(\sigma, n_z) \propto (\cos 2z, n_2 \sin 2z) e^{2i(\mathbf{q}_c \cdot \mathbf{x} + \omega_H t)}$. These modes, however, relax faster and the couplings have smaller projection integrals; they will be neglected.

At order $\epsilon^{3/2}$, the inhomogeneous system for $\sigma^{(3)}$ and $n_z^{(3)}$ reads

$$\underline{\underline{\tilde{L}}} \begin{pmatrix} \sigma^{(3)} \\ n_z^{(3)} \end{pmatrix} \equiv \boldsymbol{I}^{(3)} = - \begin{pmatrix} \boldsymbol{v}^{(1)} \cdot \boldsymbol{\nabla} \sigma^{(2)} + R_c \tilde{\alpha}^2 \sigma_a^{(\mathrm{eff})}\, g^{\mathrm{SM}} |A|^2 \partial_x \partial_z n_z^{(1)} \\ g^{\mathrm{SM}} |A|^2 \left(\frac{\partial_x n_z^{(1)}}{\tau_0^{\mathrm{SM}}} + \frac{R_c C^2}{\sigma_a^{(\mathrm{eff})}} \partial_z \sigma^{(1)} \right) \end{pmatrix}. \tag{6.20}$$

where $\underline{\underline{\tilde{L}}}$ denotes the matrix-differential operator on the left-hand sides of the Eqs. (6.4) and (6.5). The advection term of the excited charge-carrier density is given (within the lowest-order Galerkin expansion) by

$$\boldsymbol{v}^{(1)} \cdot \boldsymbol{\nabla} \sigma^{(2)} = \frac{1}{2} R_c \tilde{\alpha}^2 \sigma_a^{(\mathrm{eff})}\, \gamma_\sigma i q_c |A|^2 A \sin z e^{i(\mathbf{q}_c \cdot \mathbf{x} + \omega_H t)} + \text{c.c.} + \text{nonresonant terms}, \tag{6.21}$$

where γ_σ describes, both for the Hopf ($\tilde{\omega}^2 = \omega_H^2 + \lambda_\sigma^2$) and stationary ($\omega_H \to 0$) regimes, the nonlinearities originating from the σ modes,

$$\gamma_\sigma = \frac{|\lambda_\sigma|}{(\omega_H^2 + \lambda_\sigma^2)(\tau_0^{\mathrm{SM}})^2} \left(\frac{I_0^2}{\lambda_0^{(2)}} + \frac{I_2^2 (1 + \frac{i\omega_H}{\lambda_\sigma})}{\lambda_2^{(2)}} \right) g_\sigma, \tag{6.22}$$

$$g_\sigma = \frac{\pi}{4} \left(\frac{K^{(\mathrm{eff})}\, \tau_0^{\mathrm{SM}}}{q_c} \right)^2. \tag{6.23}$$

Note, that the prefactor $|\lambda_\sigma|/[\tau_0^{\mathrm{SM}}(\omega_H^2 + \lambda_\sigma^2)]$ can be written as $\Delta\epsilon/(\tilde{\omega}\tau_0^{\mathrm{SM}})^2$ for both regimes where the threshold shift $\Delta\epsilon$ is given by Eq. (5.50).

Since the inhomogeneity $\boldsymbol{I}^{(3)}$ in Eq. (6.20) has "resonant" terms in the kernel of the adjoint linear operator, there is a nontrivial solvability condition yielding the Landau equation $\partial_t A = \epsilon A - g(1+ic)|A|^2 A$, whose nonlinear terms are also that of the CGL (6.3). The canonical procedure consists in projecting $\boldsymbol{I}^{(3)}$ onto the eigenvector of the adjoint linear problem with the eigenvalue λ^*. Here I present a more intuitive approach stressing the concept of the amplitude-dependent effective coefficients that is equivalent.

Substituting in Eq. (6.20) the fields $(\sigma^{(1)}, n_z^{(1)}) = e^{i\mathbf{q}_c\cdot\mathbf{x}}(\overline{\sigma}, \overline{n}_z)$ where $\overline{\sigma}$ and $\overline{n}_z$ are given by the Galerkin approximations (5.40) and (5.39), projecting separately the upper line of Eq. (6.20) onto $(2/\pi)^{1/2}\sin z$ and the lower line onto $(2/\pi)^{1/2}\cos z$, [6] and adding the nonresonant linear terms, gives a quasi-linear generalization of the 2×2 system (5.38),

$$\begin{array}{rrl} (\partial_t - \lambda_\sigma)\, A_\sigma(t) & +R\tilde{\alpha}^2\sigma_a^{(\mathrm{eff})}\ (1-(\gamma_\sigma + g^{\mathrm{SM}})|A|^2)\, A_n(t) & = 0, \\ -\frac{RC^2}{\sigma_a^{(\mathrm{eff})}}\,(1-g^{\mathrm{SM}}|A|^2)\, A_\sigma(t) & + \left(\partial_t - \lambda_n + \frac{g^{\mathrm{SM}}}{\tau_0^{\mathrm{SM}}}|A|^2\right) A_n(t) & = 0, \end{array} \tag{6.24}$$

where A_n is related to the CGL amplitude by

$$A_n(t) = \bar{A}_{\mathbf{q}-\mathbf{q}_c}(t)e^{i\omega(\mathbf{q}_c,\epsilon)t}. \tag{6.25}$$

The determinantal condition of Eq. (6.24) gives, as generalization of Eq. (5.47), the amplitude-dependent growth rate λ_{NL}

$$\begin{aligned} \lambda_{\mathrm{NL}} &= \frac{\lambda_\sigma + \tilde{\lambda}_n}{2}\ \overset{+}{(-)}\ \sqrt{\frac{(\tilde{\lambda}_n - \lambda_\sigma)^2}{4} - \tilde{\omega}^2\,(1-(\gamma_\sigma + 2g^{\mathrm{SM}})|A|^2)} \\ &+ \mathcal{O}(|A|^4), \end{aligned} \tag{6.26}$$

$$\tilde{\lambda}_n = \lambda_n - \frac{g^{\mathrm{SM}}|A|^2}{\tau_0^{\mathrm{SM}}}. \tag{6.27}$$

In analogy to the linear case, the amplitude equation is given, to order $\epsilon^{3/2}$, by Eq. (6.7) with the Taylor expansion of λ replaced by that of λ_{NL} around $\boldsymbol{q} = \boldsymbol{q}_c, \epsilon = 0$ and $|A|^2 = 0$.

Comparing the Taylor expansion with Eq. (6.3) leads to the nonlinear contributions

$$g(1+ic) = -\tau_0\frac{\partial\lambda_{\mathrm{NL}}}{\partial|A|^2}. \tag{6.28}$$

Evaluating Eq. (6.28) with the Eqs. (6.26), (6.22), (6.23), (6.18), and (6.19) finally gives the nonlinear CGL coefficients, summarized in Table 6.2.

The Figures 6.1c, 6.1d, and 6.2d give, for I 52 parameters, plots of these expressions as functions of $\tilde{\alpha}$ and $\tilde{r}$. The chosen $\tilde{\alpha}$ and $\tilde{r}$ values are in the experimentally relevant range (for 28 μm cells of I 52, values of $\tilde{\alpha}$ consistent with the measured Hopf frequency vary from $\tilde{\alpha} = 0.011$ at 60°C to $\tilde{\alpha} = 0.038$ at 30°C).

Remarkabally, the saturation coefficient g^{stat} in the stationary regime is negative near the C2 curve indicating a hysteretic bifurcation. Intuitively, the advection "washes away" the σ fields thus decreasing the threshold shift connected with them. For increasing $\tilde{r}$, the σ field cannot build up to amplitudes causing a significant threshold shift, and eventually, the bifurcation becomes forward. For increasing $\tilde{\alpha}$,

[6] This is just the lowest-order Galerkin approximation of the system (6.20).

Table 6.2: Nonlinear coefficients of the complex Ginzburg–Landau equation (6.3)

Regime	Coefficient	Expression for $R_c\tilde{\alpha}^2 << 1$
Hopf	g	$g^{\mathrm{SM}} + \frac{(\tilde{r}+2\lvert\lambda_\sigma\rvert)I_2^2}{\tau_0^{\mathrm{SM}}(\tilde{r}^2+4\omega_H^2)} g_\sigma$
	gc	$\frac{\lvert\lambda_\sigma\rvert}{\omega_H \tau_0^{\mathrm{SM}}} \left[\frac{I_0^2}{\tilde{r}+4R_c\tilde{\alpha}^2} + \frac{I_2^2\left(\tilde{r}+\frac{2\omega_H^2}{\lambda_\sigma}\right)}{\tilde{r}^2+4\omega_H^2} \right] g_\sigma + \left[\frac{2\tau_0^{\mathrm{SM}}\tilde{\omega}^2}{\omega_H} - \frac{\lvert\lambda_\sigma\rvert}{\omega_H} \right] g^{\mathrm{SM}}$
Stationary	g^{stat}	$\left(1 - \frac{2\tau_0^{\mathrm{SM}}\tilde{\omega}^2}{\lvert\lambda_\sigma\rvert}\right) g^{\mathrm{SM}} - \frac{\tilde{\omega}^2}{\tau_0^{\mathrm{SM}}\lambda_\sigma^2} \left(\frac{I_0^2}{\tilde{r}+4R_c\tilde{\alpha}^2} + \frac{I_2^2}{\tilde{r}} \right) g_\sigma$

the drift velocity of the charge carriers increases with respect to the fluid velocity at a given ϵ, so that the advection effects get weaker causing an increasing g^{stat} at points with a constant distance $\tilde{r} - \tilde{r}_{\mathrm{C2}}$ from the C2 point. This is true especially at the stationary side of the C2 curve itself, shown in Fig. 6.1d.

On the Hopf side, the saturation is *stronger* than in the SM ($g > g^{\mathrm{SM}}$), and the frequency decreases with increasing amplitude ($b > 0$), unless the recombination rate is very small. The frequency decrease can be made plausible with the help of the nonlinear growth rate (6.26). For not too high $\tilde{\alpha}$, the term $\propto \gamma_\sigma |A|^2$ in Eq. (6.26) dominates. The real part of γ_σ describes the decrease of the $\sigma - n_z$ coupling and leads to a decrease of the oscillation frequency, in analogy to decreasing the oscillation frequency of a spring by decreasing the spring constant.

6.3 Comparison with experimental results

In this Section, I compare the weakly-nonlinear results of Chapter 6.2 with experiments on I 52 [42, 30, 31] and with some results of the the group of Rehberg on MBBA [39, 44, 41, 40].

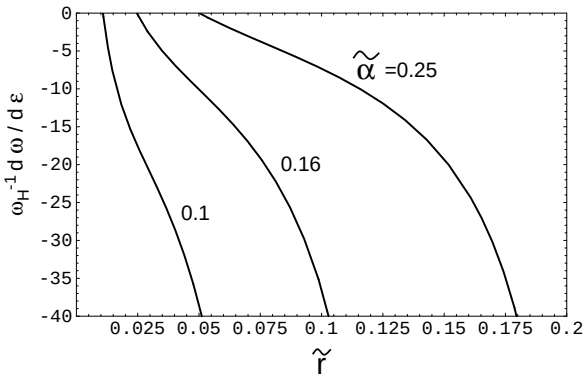

Figure 6.3 Frequency decrease $\frac{1}{\omega_H}\frac{d\omega}{d\epsilon} := -\Delta^{-1}$ due to the linear and nonlinear frequency shifts, calculated from Eq. (6.29) as function of $\tilde{\alpha}$ and $\tilde{r}$ for I 52 parameters. The value $\tilde{\alpha} = 0.16$ corresponds to $T = 49°$C where the frequency decrease was measured.

6.3.1 Decrease of the oscillation frequency with the control parameter

On increasing the control parameter above its threshold value in the Hopf regime, a decrease of the frequency of the travelling rolls was measured. In MBBA, the decrease, in units of the Hopf frequency, was $\Delta^{-1} := -\frac{1}{\omega_H}\frac{d\omega_H}{d\epsilon}|_c \approx 2.1$ for a 15 μm cell at $\omega_0\tau_q = 1.1$ [41] and ≈ 15 in Ref. [40]. In I 52, $\Delta^{-1} \approx 11$ for a 28 μm cell at $\omega_0\tau_q = 1.34$ and 49°C [31] was measured. Note that Δ defines the control parameter ϵ at which a linear extrapolation of the frequency decrease would lead to stationary patterns.

The theoretical dependence of ω on the control parameter is composed of the linear and the nonlinear frequency shifts, $\frac{d\omega}{d\epsilon} = \frac{\partial\omega}{\partial\epsilon} + \frac{\partial\omega}{\partial|A|^2}\frac{\partial|A|^2}{\partial\epsilon}$, where $\frac{\partial\omega}{\partial|A|^2} = -gc/\tau_0$. For stationary conditions (not to be confused with the stationary regime), the amplitude of the critical mode is $|A|^2 = \epsilon/g^{\rm stat}$ leading to the theoretical prediction

$$\frac{d\omega}{d\epsilon} = \frac{\partial\omega}{\partial\epsilon} - \frac{c}{\tau_0}, \tag{6.29}$$

whith $\frac{\partial\omega}{\partial\epsilon}$ and c from the Tables 6.1 and 6.2.

Fig 6.3 shows that the frequency decrease depends rather strongly on $\tilde{r}$. The experimental value of $\Delta^{-1} = 11$ in the I 52 experiments ($\tilde{\alpha} = 0.016$) is consistent with $\tilde{r} = 0.045$ corresponding to a recombination time of about 10 sec. This has to be compared with the result $\tau_{\rm rec} = 20$s obtained from the C2 point in Chapter 5. While this factor of two can be attributed to the approximations (e.g., $\omega_0\tau_q << 1$) made in calculating the nonlinear CGL coefficient b, further work is needed to clarify if the strong dependence of Δ^{-1} and c on $\tilde{r}$ is an artefact of the approximations. In particular, c gets negative for very small recombination rates which is rather unsure.

Generally, the magnitude of the change of the relative oscillation frequency decreases with increasing $\tilde{\alpha}$, in qualitatve agreement with the lower value for MBBA corresponding to $\tilde{\alpha} = 0.025$.

6.3.2 Phase diagrams

The figures 6.4 and 6.5 show, for I 52 parameters and for $\omega\tau_q << 1$, the typical weakly-nonlinear regimes in the $(\tilde{\alpha}, \tilde{r})$ space, predicted by the WEM. The codimension-two curve $|\lambda_\sigma| = \tilde{\omega}$ separating the Hopf regime from the stationary regime (labelled with "C2") derives already from the linear considerations in Chapter 5.4. With the Eqs. (5.41) and (5.48), the condition for a Hopf bifurcation can be formulated as $\tilde{r} < R_c\tilde{\alpha}(C - \tilde{\alpha}\epsilon_q/\sigma_q)/(1+\omega'^2)$, i.e., there is always a Hopf bifurcation for sufficiently small reombination rates, apart from extreme values of $\tilde{\alpha}$.

Neighbouring the C2 curve on the stationary side is a region where the bifurcation is hysteretic. Further away from the C2 curve, the bifurcation gets forward at the tricritical curve "TC", and, in the limit $\tilde{r} \to \infty$, the asymptotic dynamics is that of the SM. For small $\tilde{\alpha}$, the tricritical curve is approximately given by $\tilde{r}_{\rm tri} = [g_\sigma(I_0^2 + I_2^2)/(\tau_0^{\rm SM} g^{\rm SM})]^{1/3}\tilde{\omega}^{2/3}$. For a higher SM saturation $g^{\rm SM}$ or a lower g_σ (increasing $g^{\rm SM}/g_\sigma$ by a factor of four, or more), the TC curve would cross the C2 curve. In this case, there exists a range of values for $\tilde{\alpha}$ where the bifurcation is forward for all values of $\tilde{r}$.

In contrast to the SM parameters entering most aspects of the dynamics in the conductive regime only as relative quantities ($\sigma_a/\sigma_\perp$, etc.), the WEM parameters $\tilde{\alpha}$ and $\tilde{r}$, defined in Table 3.4, depend on the thickness d and on the absolute values of the SM parameters which are changed by the temperature as a "third control parameter" besides R and ω_0. Varying the temperature and using different cells, a representative part of the phase diagram is accessible with only one type of NLC. The mobility parameter $\tilde{\alpha} \propto (\gamma_1/\sigma_\perp)^{1/2} d^{-1}$ can be increased by choosing lower temperatures (increasing γ_1, decreasing $\sigma_\perp$) or by a thinner cell; by contrast, the recombination parameter $\tilde{r} \propto \gamma_1 d^2/(K_{11}\tau_{\rm rec})$ decreases by choosing a thinner cell. Presumably, $\tilde{r}$ increases with temperature, for example, by an activation-energy like behaviour of the equilibrium ion density $n_0 \propto \tilde{r} \propto 1/\tau_{\rm rec}$ (Table 3.4).

The cross in the upper left corner of Fig. 6.4 indicates the point in parameter space corresponding, for an assumed recombination rate of 20 s, to $d = 28$ μm and 30°C. The thick arrow pointing to the stationary-hysteretic region shows the change in $(\tilde{\alpha}, \tilde{r})$ space expected when going to a 56 μm cell at the same temperature. The experimentally observed bifurcation for such cells is, indeed, stationary, but this has been used in Chapter 5.5.2 to determine the recombination time. Independent from the recombination time, however, is the fact that the stationary bifurcation is hysteretic near the C2 point and that the Hopf bifurcation is always continuous. [7]

The dotted arrow shows the change in $(\tilde{\alpha}, \tilde{r})$ space caused by heating the 28 μm I 52 cell to 60°C under the (questionable) assumption of a constant recombination time of 20 s. If the recombination time decreased with temperature, e.g., in parallel

[7] There exist measurements on MBBA which have been interpreted as a hysteretic Hopf bifurcation [39]. They will discussed in Chapter 6.3.3.

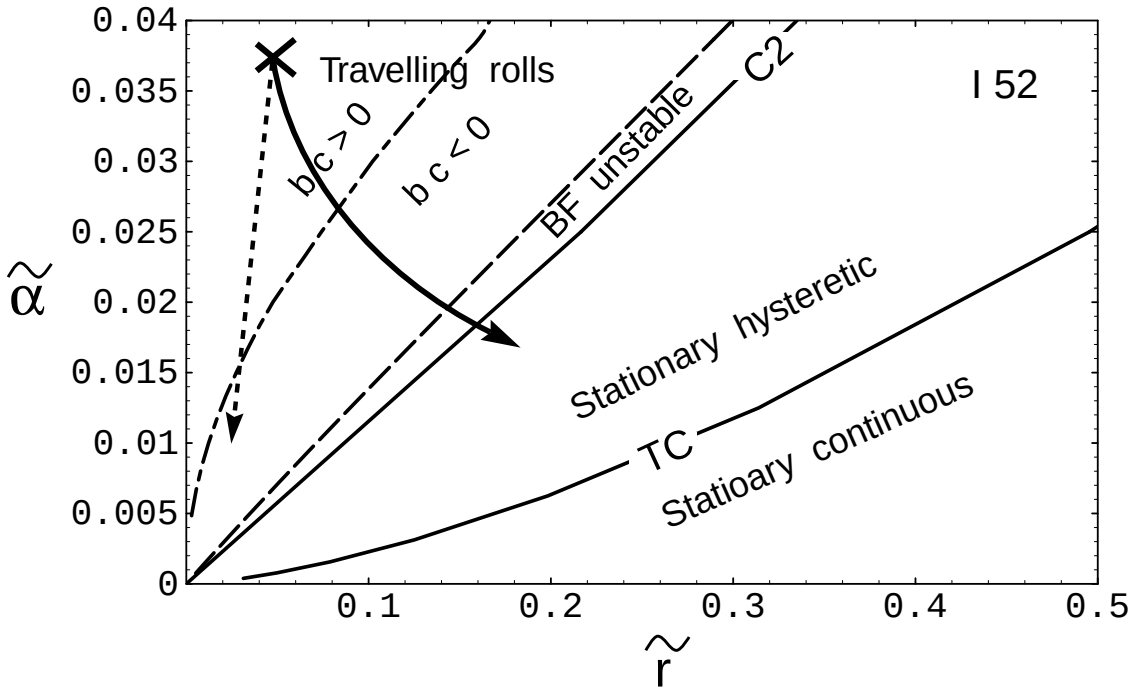

Figure 6.4 Phase diagram of the weakly-nonlinear behaviour in the parameter space $(\tilde{\alpha}, \tilde{r})$ for I 52 parameters at 45°C, and for external frequencies satisfying $\omega_0 \tau_q << 1$. The curve labelled with C2 is the codimension-two curve $|\lambda_\sigma| = \tilde{\omega}$ separating the Hopf regime of travelling waves from the stationary regime. At the stationary side, the bifurcation is hysteretic in a rather large region bounded by the C2 curve and the tricritical curve labelled "TC". For large $\tilde{r}$ or low $\tilde{\alpha}$, the bifurcation becomes continuous and, in the limit $\tilde{r} \to \infty$, the SM behaviour is recovered. In the Hopf regime, the product bc of the dispersion coefficient and of nonlinear frequency shift is positive for very small recombination rates $\tilde{r}$ Approaching the C2 curve it becomes negative at the dashed-pointed curve and in the neighbourhood of the C2 curve there is a small "baloon" bounded by the dashed curves, where the one-dimensional Benjamin-Feir criterion $bc < -1$ is fulfilled.

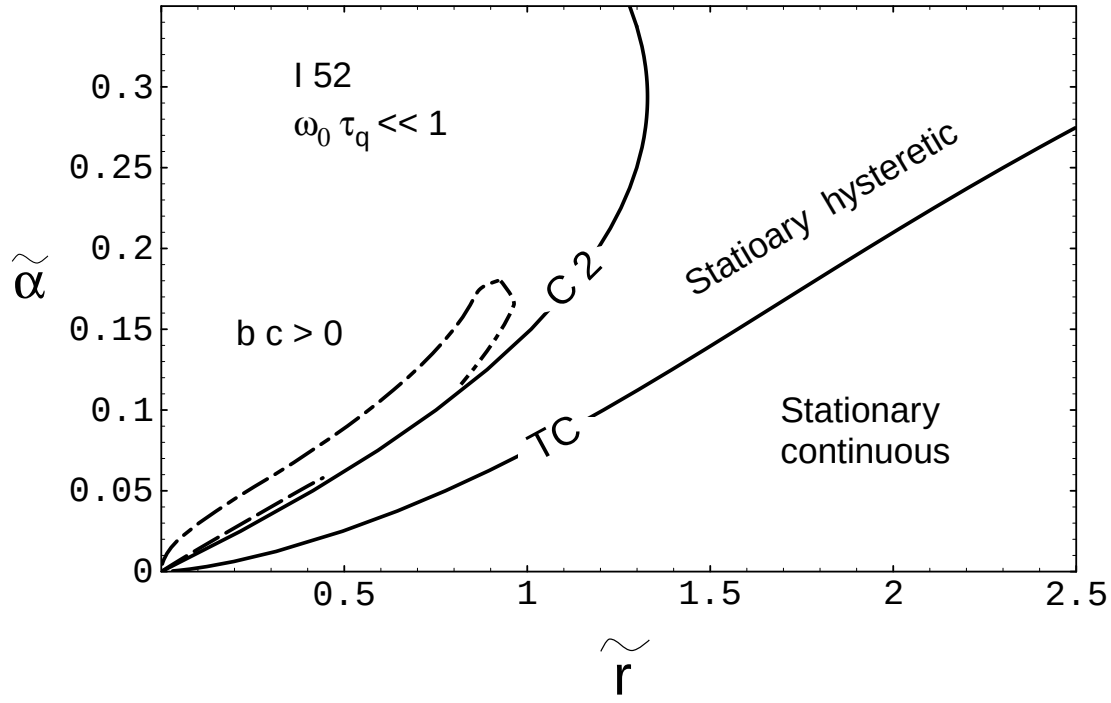

Figure 6.5 Phase diagram for the same parameters as in Figure 6.4, but for larger values of $\tilde{\alpha}$ and $\tilde{r}$, relevant for thinner cells and/or higher recombination rates. The bending of the C2 curve is due to the $\tilde{\alpha}^2$ term in the growth rate of the σ mode, Eq. (5.41). Above $\tilde{\alpha} = 0.018$, there are severeal $\tilde{r}$ values where the product bc changes the sign, but where, in general, $|bc| << 1$.

with the director relaxation time (both times are related to activation-energy processes), the arrow would point more to the right. For $\tau_{\rm rec} < 5s$, one would obtain a stationary bifurcation at T>60°C, in accordance with some measurements [30, 31]. There are, however, some intricacies connected with this observation which will be discussed in the next Chapter 6.3.3.

There is a very thin tongue in the Hopf regime (dashed lines in the Figures 6.4 and 6.5) where the one-dimensional Benjamin–Feir (BF) criterion $bc < -1$ is fulfilled. Within the one-dimensional CGL, all plane-wave solutions are unstable against long-wavelength modulations in this region, resulting in spatiotemporal chaos (STC) [11] for the envelope of the travelling waves. Experimentally, one found in I 52 at $T > 50$°C a Hopf bifurcation to STC. [8] At these temperatures, one is, indeed, nearer to the BF unstable region than for lower temperatures or crosses even the BF unstable region (arrow with the dashed line in Fig. 6.4), but the range, where STC is observed, is much broader than this region. The one-dimensional BF condition, however, is only a *sufficient* criterion for STC if there is more than one spatial dimension or if couplings to other critical modes are relevant. For instances, if the coupling (which has yet to be investigated) is such that a small change in the coupling coefficients leads to a nonlinear selection of a different mode configuration (e.g., oblique rolls *vs* square patterns if the roll angle is not too different from 45 degrees), the BF criterion for STC gets weaker with the extreme case $bc < 0$ [110]. In the Figures 6.4 and 6.5, the larger region where $bc < 0$ is bounded by the dashed lines and by the immediate neighbourhood of the C2 curve (not resolved on the plots). It corresponds semiquantitatively to the parameter ranges where STC is observed in I 52.

6.3.3 Hysteretic effects

Stationary regime

In the I 52 experiments, stationary bifurcations were always hysteretic, in accordance with the WEM predictions not too far away from the C2 curve. The amplitude (maximum director angle) of the nonlinear state right after the jump was found to be 200 mrad ($|A_{\rm NL}| = 0.2$) in a 57 μm cell at 47°C [31].

Strictly speaking, with a third-order CGL like Eq. (6.3), nothing more can be said about hysteretic effects beyond the fact that the bifurcation *is* hysteretic or not. Some properties specific to the WEM, however, enable some predictions on this level. The effects of the σ fields always stabilize the system, so an upper limit of the amplitude $|A_{\rm NL}|$ of the nonlinear state after the hysteretic jump is set by the SM amplitude. Moreover, both the excitation and the relaxation of the σ fields take place on long time scales. This translates to small hysteretic jumps to nonlinear amplitudes

[8] At lower temperatures, one observed localized (and also irregular) states.

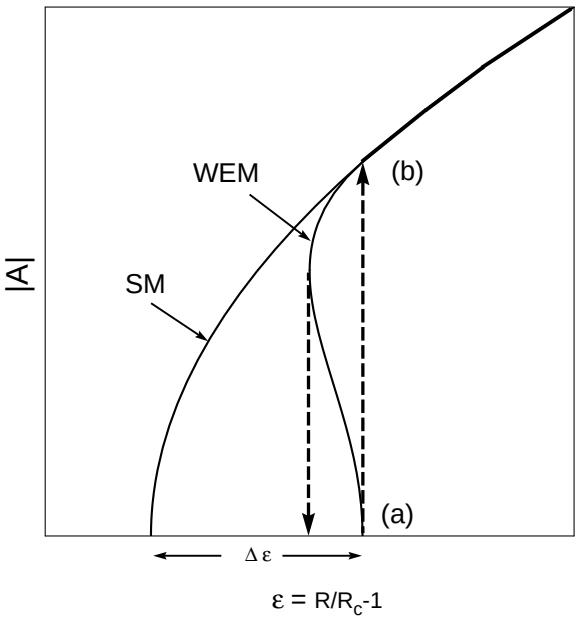

Figure 6.6 Schematic illustration of a hysteretic bifurcation from the linear WEM state (a) to a nonlinear state (b). $\Delta\epsilon$ denotes the linear threshold shift separating the neutral-stability curves of the SM and the WEM at threshold. Shown is a situation where, at the point (b), the SM and WEM amplitudes are not distinguishabel, i.e., the σ fields have no influence on the nonlinear state.

where, presumably, the amplitude equation of the SM is still valid. At last, if the condition for a hysteretic bifurcation is well satisfied by, say, $g^{\rm stat}_{\rm WEM}/g^{\rm SM} < -1$ (one is not too near the TC curve), it is plausible that the advection homogenizes the carrier density in the nonlinear state so that this state is presumably described by the SM.

With these assumptions, it can be seen from Fig. 6.6, that the amplitude in the nonlinear state (b) is that of the weakly-nonlinear SM with $\epsilon^{\rm SM} = R/R_c^{\rm SM} - 1$ equal to the linear threshold shift,

$$|A_{\rm NL}|^2_{\rm stat} = \frac{\Delta\epsilon}{g^{\rm SM}} = \frac{\tilde{\omega}^2\tau_0^{\rm SM}}{|\lambda_\sigma| g^{\rm SM}}. \tag{6.30}$$

The highest jump takes place on the (stationary side of) the C2 curve with $A_{\rm NL}|^2_{\rm stat} \approx \tau_0^{\rm SM}/(g^{\rm SM}\tau_{\rm rec})$.

The experimental parameters used for the hysteresis measurements in I 52 correspond to a point near the C2 curve. This can be seen from Fig. 5.10 where the lower curve is for a cell of a comparable thickness at a comparable temperature. With $\tau_0^{\rm SM} = 0.33$ s and $\tau_{\rm rec} = 20$ s, Eq. (6.30) gives at the C2 point the theoretical result $|A_{\rm NL}| = 0.184$.

Hopf regime

The WEM always predicts a continuous bifurcation in the Hopf regime. Indeed, one observes in I 52, that the initial bifurcation to oscillating states is continuous. At

a rather small value $\epsilon_{\rm jp}$, however, the travelling-wave state with the amplitude $|A_{\rm jp}|$ and the finite oscillation frequency $\omega_{\rm jp} < \omega_H$ jumps hysteretically to a stationary state with a much higher amlitude $|A_{\rm NL}|$ (see Fig. 6.7). For $d = 28$ μm , $\epsilon_{\rm jp}$ varied from 0.1 at 44°C to 0.02 at 59°C [31]. At even higher temperatures, a *hysteretic* stationary bifurcation was observed as primary bifurcation. Due to the large steps of the reduced control parameter ($\delta\epsilon \approx 0.01$) in this experiment, it could not be excluded, however, that the initial bifurcation is actually a *continuous Hopf* bifurcation with a subsequent jump to a nonlinear stationary state at a very small $\epsilon_{\rm jp}$ which could not be resolved.

In MBBA, the bifurcations appeared continuous in experiments without excessive sensitivity in optical contrast and resolution in ϵ [41, 111, 112]. In other very careful investigations, primarily devoted to thermal fluctuations below threshold and discussed in Chapter 7 [44, 39], one observed hysteretic bifurcations to a nonlinear stationary state. The amplitude was about 150 mrad in the experiment of Ref. [39]. The spatiotemporal correlations of *sub-threshold* fluctuations in the same cells, however, can be explained only by assuming a Hopf bifurcation for the linear dynamics, with a very small Hopf frequency of $\omega_H/(2\pi) = 0.044$ s in Ref. [39] and 0.05 s in Ref. [44] (see Chapter 7 for more details). Can this "hysteretic Hopf bifurcation" be explained by assuming, again, a continuous Hopf bifurcation in a regime $0 < \epsilon < \epsilon_{\rm jp}$ which cannot be resolved experimentally?

To describe the dynamics of this scenario with Ginzburg–Landau equations seems hopeless. One needed a seventh-order (!) CGL, and the amplitudes where the higher-order terms come into play, would be higher than the range were a CGL description is even *qualitatively* correct. By contrast, a semi-quantitative description seems possible for the hysteresis by exploiting the quasi-linear 2×2 equations (6.24) and assuming, again, that the amplitude of the nonlinear state is given by the amplitude equation of the SM.

From the determinantal condition of the system (6.24) for zero growth, $\lambda = i\omega$, one obtains, neglecting terms $\propto |A|^4$,

$$-\omega^2 + \frac{\lambda_\sigma}{\tau_0^{\rm SM}}(\epsilon^{\rm SM} - g^{\rm SM}|A|^2) + \tilde{\omega}^2\left(1 - ({\rm Re}\gamma_\sigma + 2g^{\rm SM})|A|^2\right) = 0, \qquad (6.31)$$

$$\omega\left(\lambda_\sigma + \frac{\epsilon^{\rm SM} - g^{\rm SM}|A|^2}{\tau_0^{\rm SM}}\right) - \tilde{\omega}^2 {\rm Im}\gamma_\sigma |A|^2 = 0, \qquad (6.32)$$

where γ_σ is given by Eq. (6.22) with ω_H replaced by the actual oscillation frequency ω. The roots of the system (6.31), (6.32) determine the generalized neutral curves. For the oscillatory branch, the result is (Note that $\epsilon^{\rm SM} = \epsilon + |\lambda_\sigma|\tau_0^{\rm SM}$)

$$\epsilon_{\rm osc} = g(\omega)|A|^2, \qquad (6.33)$$

$$\omega^2 = \omega_H^2 - \frac{|\lambda_\sigma| g(\omega)}{\tau_0^{\rm SM}}\left(1 + \frac{\omega c(\omega)}{|\lambda_\sigma|}\right)|A|^2, \qquad (6.34)$$

where $g(\omega)$ and $c(\omega)$ are the nonlinear CGL coefficients in Table 6.2 with ω_H replaced by ω. For the stationary branch $\omega = 0$ one obtains

$$\epsilon^{\mathrm{stat}} = \Delta\epsilon^{\mathrm{stat}} + g^{\mathrm{stat}}|A|^2, \qquad \Delta\epsilon^{\mathrm{stat}} = \frac{\tau_0^{\mathrm{SM}}\omega_H^2}{|\lambda_\sigma|}. \tag{6.35}$$

Figure 6.7 illustrates schematically the resulting hysteresis curves. For small amplitudes, the oscillatory branch has the lowest threshold. On increasing ϵ, the amplitude is given initially by $|A|^2 = \epsilon/g$ and the frequency decreases initially with the rate $\frac{d\omega}{d\epsilon}$, Eq. (6.29). The bending of the amplitude curve is due to the frequency dependence of $g(\omega)$. With $g(\omega) > g > g^{\mathrm{SM}}$, this branch has comparatively small amplitudes. The stationary branch is the same as in the stationary regime; it is extremely hysteretic since g^{stat} (Table 6.2) becomes more negative for decreasing $\tilde{r}$ (the dashed curves in Figure 6.1c have to be extrapolated to $\tilde{r} < |\lambda_\sigma|$).

Because of the frequency mismatch, the system cannot cross over from the oscillatory curve to the stationary curve at the point B in Fig. 6.7. The actual point where the jump takes place, has not yet been determined, so the points C and D in Figure 6.7 are qualitative and based on experiments where the jump takes place at an oscillation frequency of about half the Hopf frequency [31].

For very small Hopf frequencies as in Ref. [39], an upper bound can be given for the control parameter at the hysteretic jump ϵ_{jp} (see Figure 6.7), $\epsilon_{\mathrm{jp}} \approx \Delta/2 \propto (\tilde{\omega}\tau_0^{\mathrm{SM}})^2$. ϵ_{jp} decreases strongly with $\tilde{r}$. For $\tilde{r} = 0.5\tilde{\omega}$, it is smaller than the step size $\delta\epsilon = 0.001$ of the experiment so that a forward Hopf bifurcation may go unnoticed. Besides, the amplitude $|A|^2_{\mathrm{jp}} = \epsilon_{\mathrm{jp}}/g \approx 13$ mrad at the jump is very small; it is only three times larger than typical rms values in the subcritical regime of (thermal) fluctuations (!). This is caused by the combined effects of a small value of ϵ_{jp}, and a high saturation coefficient, $g/g^{\mathrm{SM}} = 6.5$ for $\tilde{r} = 0.5\tilde{\omega}$. In contrast, the nonlinear amplitude $|A_{\mathrm{NL}}|^2 = (\epsilon_{\mathrm{jp}} + \Delta\epsilon)/g^{\mathrm{SM}} \approx 100$ mrad increases with $\tilde{r}$, caused by the increased linear threshold shift.

6.4 Discussion

The weakly-nonlinear analysis of the WEM agrees qualitatively and sometimes quantitatively with the experiments. At first, the calculation of the CGL coefficients brought two linear results. The correlation time τ_0 in the Hopf regime is twice that of the SM while the correlation length is the same in both models. Both results fit well to experimental values obtained for cells of 13 μm [39] and 23 μm [44] thickness from the oscillating dynamics in the subcritical stochastic regime. There seem to be no measurements of τ_0 in I 52.

The phase diagram of the weakly-nonlinear behaviour agrees qualitatively. In particular, the Hopf bifurcations are always continuous and the stationary bifurcations

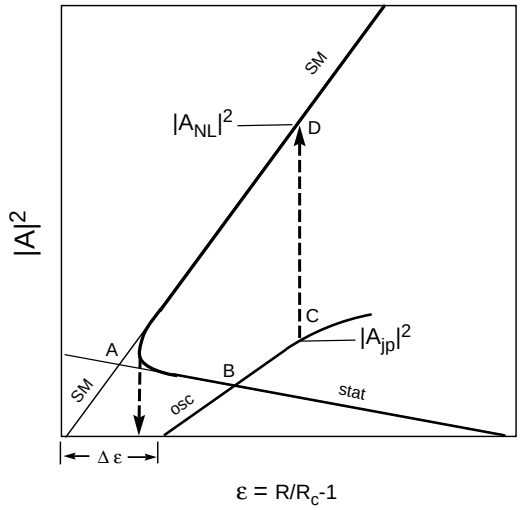

Figure 6.7 Hysteretic secondary bifurcation in the Hopf regime (schematically). The curve labelled "stat" is the stationary backwards-bifurcating branch of zero growth rate which exists also in the stationary regime. At the point A (where the amplitude is of the order of $|A| \approx |\lambda_\sigma|$), the stationary branch crosses over to the SM branch "SM". The curve labelled "osc" is the oscillatory branch starting with the Hopf frequency. The oscillation frequency decreases with ϵ until the curve ends at zero frequency. At the point C, the state jumps from the continuous Hopf branch to the nonlinear SM state D.

are hysteretic if one is near the C2 curve. The observed STC for higher temperatures in I 52 is compatible with the area in phase space where the WEM predicts $bc < 0$. This can possibly be explained by a Benjamin–Feir like long-wavelength instability.

Both, linear and nonlinear results for I 52, are compatible with a recombination time of 10 to 20 s. The decrease of the oscillation frequency of travelling waves with the control parameter is compatible with $\tau_{\rm rec} = 10$ s. The amplitude of the nonlinear state in the stationary-hysteretic regime requires $\tau_{\rm rec} \approx 15$ s. Comparing the C2 curve with the external parameters (cell thickness, temperature, ω_0) where the Hopf frequency decreases to zero, gives $\tau_{\rm rec} \approx 20$ s. In MBBA, the condition $|\lambda_\sigma| < \tilde{\omega}$ required $\tau_{\rm rec} > 1/\omega_H = 3.5$ s in the experiment of Ref. [39].

The oscillatory behaviour observed for MBBA in the subcritical stochastic regime, while a hysteretic jump to stationary patterns is observed above threshold [39], seems puzzling. Even this seems to be consistent with the WEM assuming a continuous Hopf bifurcation, but a jump to a stationary state at a small but positive control parameter $\epsilon_{\rm jp}$ which cannot be resolved experimentally. For typical experimental resolutions $\delta\epsilon < 0.001$, this implies $\tilde{r} \geq 0.4$ or $\tau_{\rm rec} \leq 8$ s. The reason for the small $\epsilon_{\rm jp}$ is the small Hopf frequency where Eq. (6.29) together with the CGL coefficient c in Table 6.2 lead to $\epsilon_{\rm jp} \approx \Delta/2 \propto (\tilde{\omega}\tau_0^{\rm SM})^2$. Recent experiments on the nematic mixture Merck Phase 5 confirm this interpretation [113].

An interesting prediction of the theory is that the nonlinear dispersion c becomes negative for very small recombination rates, i.e., the oscillation frequency should increase with the amplitude (the linear frequency shift can be neglected for small $\tilde{r}$), which has never been observed. Possibly this is due to the dynamics of the excited charge-carrier modes which become dynamically independent for small recombination rates so that the CGL is valid only in a very small range of ϵ. The CGL requires that all excited modes relax much faster than the amplitude itself, $\tau_0^{-1}\epsilon << |\lambda_0^{(2)}|$, $|\lambda_2^{(2)}|$, or

$$\epsilon << \tau_0\tilde{r} \approx 2\Delta\epsilon. \tag{6.36}$$

The CGL of the WEM is valid, if the distance from threshold is much smaller than the linear threshold shift. For I 52, this gives $\epsilon << 0.02$ (Table 6.3), and in MBBA, e.g., $\epsilon << 0.01$ for the cell in Table 6.3 assuming $\tilde{r} = 0.5\tilde{\omega}$. With a typical resolution of $\delta\epsilon = 10^{-3}$, this range is experimentally accessible.

Chapter 7

Thermal fluctuations in pattern-forming instabilities

Statistics is the physics of numbers.

P. Diaconis

Thermal fluctuations result from deterministic chaos in 10^{23} *dimensions.*

I. Rehberg

The material in this chapter has been published as Ref. [114]. Landau's method of hydrodynamic fluctuations is developed in a form suitable for pattern-forming systems. The resulting scheme is applied to RBC, to Taylor-Couette flow and to the SM of EHC. Using the WEM would lead to a factor of two (two critical left- and right travelling modes instead of one stationary mode) that is cancelled by the correlation time in the denominator of Eq. (7.41), which the WEM predicts to be twice as long as in the SM (Chapter 6.4).

7.1 Introduction

Recent experiments in several hydrodynamic systems confirm that pattern-forming instabilities in extended nonequilibrium systems exhibit some features reminiscent of equilibrium-phase transitions. Fluctuations of the field variables become measurable near threshold and both their amplitudes and the correlations in space and time increase as one approaches the threshold. Two questions arise. Are the measured fluctuations of internal origin, i.e., due to thermal or quantum-mechanical noise (the latter is predominant in lasers [115]) or are they the result of external noise from the experimental setup? Can one theoretically describe thermal fluctuations in pattern-forming systems in an unified way, as in equilibrium systems? A positive answer

to the second question means extending the theory of fluctuations near equilibrium phase transitions [68] to nonequilibrium systems. If in addition the predictions are confirmed by experiments as discussed in the Sections 5 and 6 of this chapter, it is safe to say that one actually measured thermal fluctuations. Each additional source would increase the fluctuations.

Theoretical predictions for the effects of thermal noise in pattern-forming systems were given for Rayleigh–Bénard convection (RBC) in simple fluids [116, 117, 118] and recently for RBC in binary mixtures [119], for electrohydrodynamic convection (EHC) in nematic liquid crystals (NLC) [120] and for Taylor–Couette flow (TCF) [121, 122, 123]. In all this work, the dynamical (macroscopic) equations are supplemented with stochastic terms accounting for the microscopic degrees of freedom and determined from the assumption of local equilibrium. Near threshold the resulting Langevin equations are reduced to a stochastic generalization of the usual normal form equations. These equations are simple enough to be solved for the amplitude (and phase) fluctuations and may provide a basis for an unified description of fluctuations of patterns in nonequilibrium systems. Once the amplitude fluctuations are known the determination of the fluctuations of the physical fields and their measurable effects is straightforward.

The crucial assumption in this approach is that of local equilibrium in systems which are typically far from global equilibrium. This implies that the external forces driving the system out of equilibrium, e.g., shear, director rotation, electric and magnetic fields, and also the ensuing fields of the macroscopic patterns, are small compared to the internal fields effective on a molecular scale. In the hydrodynamic regime this should be always fulfilled.

In the next two sections I describe the method in a form applicable to a large class of pattern-forming systems including quasi one-dimensional (1D) and quasi two-dimensional (2D) systems and the interesting case of symmetry-induced degeneracy where several deterministic solutions become simultaneously unstable at the primary threshold. In Section 4 I calculate the fluctuations of planar EHC and compare them with fluctuations of RBC patterns in simple liquids and axisymmetric vortices in TCF. Chapter 7.5 describes relevant experiments which are compared to the theory in the last section.

7.2 Macroscopic stochastic equations for thermal noise

With the assumption of local equilibrium one can use locally the fluctuation-dissipation theorem (FDT) which essentially states that thermal fluctuations are always connected with dissipation and vice versa. So I start by writing down the ensemble-averaged entropy production of the macroscopic system as an integrated sum of

products of Onsager forces and currents (summation over doubly occurring indices is implied)

$$\langle \dot{S} \rangle = \int_V d^3\boldsymbol{r} \left\{ F_\alpha(\boldsymbol{r},t) \langle J_\alpha(\boldsymbol{r},t) \rangle \right\}. \tag{7.1}$$

For macroscopic hydrodynamic systems near local equilibrium this quantity is extensive and the forces and ensemble-averaged currents, F_α and $\langle J_\alpha \rangle$, are linearly related,

$$\langle J_\alpha \rangle = M_{\alpha\beta} F_\beta := J_\alpha - \tilde{J}_\alpha, \tag{7.2}$$

where $M_{\alpha\beta}$ are the components of the Onsager matrix $\underline{\underline{M}}$, given by the constitutive material equations. We allow for fluctuations $\tilde{J}_\alpha$ of the currents, $J_\alpha = \langle J_\alpha \rangle + \tilde{J}_\alpha$ with $\langle \tilde{J}_\alpha \rangle = 0$, and will determine them with the FDT. Introducing auxiliary field variables $x_\alpha(\boldsymbol{r},t)$ by $J_\alpha = \dot{x}_\alpha$ (Ref. [68]) one can write the constitutive relations (7.2) with fluctuations as Langevin equation for x_α,

$$\dot{x}_\alpha = M_{\alpha\beta} F_\beta + \tilde{J}_\alpha. \tag{7.3}$$

Expressing the entropy $S[\boldsymbol{x}] = \int_V d^3\boldsymbol{r} s(\boldsymbol{x}(\boldsymbol{r}))$ in terms of $\boldsymbol{x}$ ($\boldsymbol{x}$ is a shorthand for all x_α) and comparing the averaged entropy production $\langle \dot{S}\,[\boldsymbol{x}] \rangle = \int_V d^3\boldsymbol{r} \frac{\partial S}{\partial x_\alpha} \langle \dot{x}_\alpha \rangle$ with (7.1), one sees that the forces are the variables conjugate to x_α, $F_\alpha = \frac{\partial S}{\partial x_\alpha}$, and (7.3) can be written in a "generalized potential form" $\dot{x}_\alpha = M_{\alpha\beta} \frac{\partial S}{\partial x_\beta} + \tilde{J}_\alpha$. For a given small volume element ΔV_r around $\boldsymbol{r}$, the corresponding Fokker-Planck equation allows a canonical stationary distribution $W_{\infty,r}[\boldsymbol{x}] \propto e^{S_r/k_B}$ with $S_r = \int_{\Delta V_r} d^3\boldsymbol{r} s(\boldsymbol{x}(\boldsymbol{r})) \approx s\Delta V_r$, if the probability currents are zero (detailed balance) and the fluctuations are given by the fluctuation-dissipation theorem $\langle \tilde{J}_\alpha(\boldsymbol{r},t) \tilde{J}_\beta(\boldsymbol{r'},t') \rangle = k_B (M_{\alpha\beta} + M_{\beta\alpha})(\Delta V_r)^{-1} \delta_{rr'} \delta(t-t')$ [68, 124]. In the continuum limit this becomes

$$\langle \tilde{J}_\alpha(\boldsymbol{r},t) \tilde{J}_\beta(\boldsymbol{r'},t') \rangle = k_B (M_{\alpha\beta} + M_{\beta\alpha}) \delta(\boldsymbol{r}-\boldsymbol{r'}) \delta(t-t'). \tag{7.4}$$

Thus the FDT is a consequence of the postulated canonical distribution. Note that this ansatz implies the existence of "mesoscopic" volume elements which are large enough so that the entropy can be treated as extensive quantity and small enough to neglect spatial variations of the macroscopic fields.

Typical sources contributing to the density $\dot{s}$ of the entropy production (7.1) are $\dot{s}^{(v)}$ related to the viscous flow and $\dot{s}^{(th)}$ related to thermal conductivity. In fluids with finite electric conductivity there is a contribution $\dot{s}^{(el)}$ due to Ohmic heating, and in NLCs an additional contribution $\dot{s}^{(n)}$ from the orientational relaxation of the director field $\boldsymbol{n}(\boldsymbol{r},t)$ [72]. These sources are [120, 58, 125]

$$\begin{aligned} T\,\dot{s}^{(v)} &= \sigma^{(s)}_{ij} v_{ij}, & T\,\dot{s}^{(n)} &= -\sigma^{(as)}_{ij} \Omega_{ij}, \\ T\,\dot{s}^{(th)} &= -\tfrac{1}{T} \boldsymbol{j}^{(th)} \cdot \boldsymbol{\nabla} T, & T\,\dot{s}^{(el)} &= \boldsymbol{j}^{(el)} \cdot \boldsymbol{E}, \end{aligned} \tag{7.5}$$

where $v_{ij} = (\partial_i v_j + \partial_j v_i)/2$ is the symmetrical fluid shear-rate tensor $n_j \Omega_{ij} = n_j(\partial_i v_j - \partial_j v_i)/2 + (\partial_t + \boldsymbol{v}\cdot\boldsymbol{\nabla})n_i$ is the rotation of the director relative to the moving fluid, $\sigma_{ij}^{(s)}, \sigma_{ij}^{(as)}$ are the symmetric and antisymmetric parts of the stress tensor and $\boldsymbol{j}^{(th)}$ and $\boldsymbol{j}^{(el)}$ are the dissipative parts of the heat and electric current. This list is not complete; for example in binary mixtures there is an additional mixing-entropy term proportional to the negative concentration gradient times the mass flux density of one component, see e.g., [119, 126, 58].

There is some freedom in choosing the Onsager forces and currents. If one takes as currents

$$\{J_\alpha\} = (\sigma_{ij}^{(s)},\ \ \sigma_{ij}^{(as)},\ \ j_i^{(th)},\ \ j_i^{(el)}) \tag{7.6}$$

then the conjugate forces are

$$\{F_\alpha\} = \left(\frac{v_{ij}}{T},\ \ -\frac{\Omega_{ij}}{T},\ \ -\frac{\partial_i T}{T^2},\ \ \frac{E_i}{T}\right), \tag{7.7}$$

and the Onsager matrices can be found by comparing the dissipative part of the constitutive material equations with the definitions of the currents and forces.

For NLCs the constitutive equations are (Chapter 2 and [57, 58])

$$\begin{pmatrix} \sigma_{ij}^{(s)} \\ \sigma_{ij}^{(as)} \\ j_i^{(th)} \\ j_i^{(el)} \end{pmatrix} = \begin{pmatrix} T\eta_{ij,kl} & T\eta_{ij,kl}^{(n)} & 0 & 0 \\ T\eta_{kl,ij}^{(n)} & T\gamma_{ij,kl} & 0 & 0 \\ 0 & 0 & T^2\lambda_{ik} & -T\lambda_{ik}^{(el)} \\ 0 & 0 & -T\lambda_{ik}^{(el)} & T\sigma_{ik}^{(el)} \end{pmatrix} \begin{pmatrix} v_{kl}/T \\ -\Omega_{kl}/T \\ -\partial_k T/T^2 \\ E_k/T \end{pmatrix}, \tag{7.8}$$

with the NLC-Onsager matrix as first term on the right-hand side. The viscosity tensor $\eta_{ij,kl}$, the rotational viscosity tensor $\gamma_{ij,kl}$ and the fluid-director coupling $\eta_{ij,kl}^{(n)}$ contain a total of five independent coefficients (for $\eta_{ij,kl}$ see Eq. (2.20), for the other tensors see Eq. (B1) in [120]). The thermal and electric conductivities λ_{ik} and $\sigma_{ik}^{(el)}$ and the Peltier coefficients $\lambda_{ik}^{(el)}$ are uniaxial tensors of the form $\lambda_\perp \delta_{ik} + \lambda_a n_i n_k$.

To get the noise terms of the macroscopic equations themselves, one identifies all parts which may contain dissipative effects and writes them in terms of the Onsager currents. Typically these equations, written in terms of the perturbations $\boldsymbol{u}(\boldsymbol{r},t)$ of the macroscopic fields from the unstructured state, can be cast into the symbolic form (the field variables $\boldsymbol{u}$ should not be confused with the auxiliary variables $\boldsymbol{x}$ in the derivation of the FDT),

$$[\underline{\underline{S}}^R(\boldsymbol{\nabla},\boldsymbol{r},t)\partial_t + \underline{\underline{L}}^R(\boldsymbol{\nabla},\boldsymbol{r},t)]\boldsymbol{u}(\boldsymbol{r},t) + \boldsymbol{N}^R(\boldsymbol{u},\boldsymbol{\nabla},\boldsymbol{r},t) = \boldsymbol{\xi}(\boldsymbol{r},t), \tag{7.9}$$

with the noise term $\boldsymbol{\xi}$ to be determined. The linear matrix-differential operators $\underline{\underline{S}}^R$ and $\underline{\underline{L}}^R$ and the nonlinear deterministic term $\boldsymbol{N}$ depend on a control parameter R and may depend explicitely on $\boldsymbol{r}$ if the basic state is nontrivial (e.g., in TCF or

Non–Boussinesq RBC) or periodically on time in the case of periodic forcing as in EHC. Recall from chapter 2 that the mascroscopic equations are either conservation laws or balance equations for slowly relaxing variables or broken-symmetry variables; the latter are e.g., director variations in NLC. The first class of equations contains gradients of the currents (examples 1 and 2 below), the second one some linear combination of the currents themselves. In both cases, the left-hand side of Eq. (7.9) can be written symbolically as

$$(\underline{\underline{S}}^R\partial_t + \underline{\underline{L}}^R)\boldsymbol{u} \equiv -\underline{\underline{D}}\langle \boldsymbol{J}\rangle + \text{conservative terms}, \tag{7.10}$$

where $\boldsymbol{J}$ contains all Onsager currents and $\underline{\underline{D}}$ is a matrix-differential operator for conservation laws and a matrix for other balance equations. The stochastic forces are accordingly

$$\boldsymbol{\xi}(\boldsymbol{r},t) = \underline{\underline{D}}\tilde{\boldsymbol{J}}(\boldsymbol{r},t). \tag{7.11}$$

In summary, the Langevin equations (7.9) are a stochastic generalization of the deterministic basic equations. The fluctuating forces $\boldsymbol{\xi}$ have zero mean and their second moments are given in terms of $\underline{\underline{D}}$ and the Onsager matrix $\underline{\underline{M}}$ by (7.11) and (7.4). $\underline{\underline{M}}$ is defined *via* the constitutive material equations (Eqs. (7.8) for NLCs)) and $\underline{\underline{D}}$ by the basic equations themselves (see examples below). Note that $\underline{\underline{M}}$ and $\underline{\underline{D}}$ may depend on broken-symmetry variables and in addition $\underline{\underline{M}}$ on scalar fields (temperature etc.) of the basic equations, giving rise to multiplicative parts of $\boldsymbol{\xi}$ in terms of the macroscopic field variables. As an example, the constitutive NLC material tensors depend on the director $\boldsymbol{n}$, which is also a macroscopic variable in the EHC equations.

Now I give some examples for $\underline{\underline{D}}$.

1. Navier-Stokes equations for an incompressible fluid, $\rho_m(\partial_t + \boldsymbol{v}\cdot\boldsymbol{\nabla})\boldsymbol{v} + \boldsymbol{\nabla}p - \boldsymbol{\nabla}\langle\underline{\underline{\sigma}}\rangle - \boldsymbol{f}_{vol} = \boldsymbol{\xi}^{(v)}$. All dissipative effects are contained in $\boldsymbol{\nabla}\underline{\underline{\sigma}}$, which can be written (in Cartesian coordinates) as $(\boldsymbol{\nabla}\underline{\underline{\sigma}})_i = \partial_j(\sigma_{ji}^{(s)} + \sigma_{ji}^{(as)}) = D_{i,jk}(\sigma_{jk}^{(s)} + \sigma_{jk}^{(as)})$ with $D_{i,jk} = \delta_{ik}\partial_j$. Hence $\xi_i^{(v)} = D_{i,jk}(\tilde{\sigma}_{jk}^{(s)} + \tilde{\sigma}_{jk}^{(as)})$.

2. Heat equation (conservation of energy) $\rho_m c_v(\partial_t + \boldsymbol{v}\cdot\boldsymbol{\nabla})T + \boldsymbol{\nabla}\cdot\langle\boldsymbol{j}^{(th)}\rangle = \xi^{(th)}$. Obviously $\underline{\underline{D}} = -\boldsymbol{\nabla}$ and $\xi^{(th)} = -\boldsymbol{\nabla}\cdot\tilde{\boldsymbol{j}}^{(th)}$. Things are analogous for the charge conservation equation.

3. Director equations in EHC (balance of local angular momentum), $\boldsymbol{n}\times\boldsymbol{\Gamma} = \boldsymbol{\xi}^{(n)}$, where $\boldsymbol{\Gamma}$ is the molecular field introduced by De Gennes [25]. Here the dissipative terms are not so obvious. They are proportional to the antisymmetric part of the stress tensor, $(\boldsymbol{n}\times\boldsymbol{\Gamma})_i = (\boldsymbol{n}\times\boldsymbol{\Gamma})_i^{(cons)} + \epsilon_{ijk}\langle\sigma_{jk}^{(as)}\rangle$, i.e., $\xi_i^{(n)} = -\epsilon_{ijk}\tilde{\sigma}_{jk}^{(as)}$ [72, 120, 127], where ϵ_{ijk} is the total-antisymmetric third-rank unity tensor.

7.3 Stochastic amplitude equations

Amplitude equations (normal forms), valid near threshold in systems with a continous bifurcation, are universal in a way that they only depend on the symmetries of the pattern and on the quasi-dimensionality of the system. *Stochastic* amplitude equations seem a natural way to generalize this universality to fluctuations of patterns, and compare them to equilibrium fluctuations near continous phase transitions. We define as quasi-dimensionality D the number of dimensions (0, 1 or 2) where the system is translationally invariant and infinite. Of course "infinite" means sufficiently large so that boundaries play no role; for stationary patterns this means a system size much larger than the correlation length of the pattern; for travelling waves the precise conditions are not yet well understood, but seem to be more stringent [9]. Denoting the infinite directions with $r_\parallel$ and the other "perpendicular" directions with $r_\perp$, a space point is given for $D = 2$ by $\boldsymbol{r} = (r_{\parallel 1}, r_{\parallel 2}, r_{\perp 1})$ and for $D = 1$ by $\boldsymbol{r} = (r_{\parallel 1}, r_{\perp 1}, r_{\perp 2})$. The $r_\perp$-coordinates are allowed to be curvilinear. We will use vector notation for $r_\parallel, r_\perp$ only if they explicitely have more than one component.

The symmetries of the correlations of the fluctuating pattern below threshold are determined by the branches of the linear deterministic growth rate $\lambda(\epsilon, k) = \mathrm{Re}\lambda(\epsilon, k) - i\omega(\epsilon, k)$ for the modes $\boldsymbol{u}_k = e^{\lambda t} e^{ik\cdot r_\parallel}\ \boldsymbol{f}^R(k, r_\perp, t)$ becoming first unstable at threshold, where $\boldsymbol{f}^R$ is periodic in t in systems with periodic driving like AC-driven EHC. The reduced control parameter $\epsilon = (R - R_c)/R_c$ and the threshold, $\lambda(\epsilon = 0, k_c) = -i\omega_c$, are defined as usual. A bifurcation is stationary if $\omega_c = 0$, and degenerate if the growth rate of the critical branch becomes simultaneously unstable around several k_c values or if there are several critical dispersion branches, e.g., associated with a Hopf bifurcation $\lambda(\epsilon = 0, k_c) = \pm i\omega_c$.

The amplitude equations are usually derived by a multiple-scale perturbation around threshold [9, 10], but for the linear part the resulting solvability conditions determining the amplitude are equivalent to projecting the basic equations onto the critical eigenfunctions. We extend now this projection to the stochastic system and add, if necesary, the nonlinear deterministic terms *ad hoc*. The director-dependent parts of the fluctuating forces, described in the paragraph after Eq. (7.11), will lead to additional multiplicative noise terms also in the amplitude equation. Reference [120] gives plausibility arguments that within the range of validity of the amplitude equation they are negligible compared to the additive noise.

We show this projection for autonomous systems with non-degenerate bifurcations and make some remarks about more general cases later. Inserting the ansatz

$$\boldsymbol{u}(\boldsymbol{r}, t) = \int d^D k' e^{i(k'\cdot r_\parallel - \omega t)} \psi(k', t) \boldsymbol{f}^R(k', r_\perp) \tag{7.12}$$

in the linear part of (7.9) and projecting these equations onto the eigenfunctions of

the adjoint linear problem gives a stochastic linear equation for the mode amplitudes,

$$\partial_t \psi(k,t) = \lambda(\epsilon,k)\psi(k,t) + \Gamma(k,t). \tag{7.13}$$

The noise term is

$$\Gamma(k,t) = \frac{[\boldsymbol{f}^{\dagger R}, \boldsymbol{\xi}(t)]}{[\boldsymbol{f}^{\dagger R}, \underline{\underline{S}}^R(\nabla_\parallel \to ik, \nabla_\perp, r_\perp)\boldsymbol{f}^R]}, \tag{7.14}$$

where $\nabla_\parallel$ and $\nabla_\perp$ are the components of the nabla operator in the $r_\parallel$ and $r_\perp$ directions, respectively. The brackets denote the scalar product

$$[\boldsymbol{\phi}, \boldsymbol{\eta}] := \frac{1}{C}\int_C d^{3-D} r_\perp \phi^*_\alpha(r_\perp)\eta_\alpha(r_\perp), \tag{7.15}$$

for vector functions $\boldsymbol{\phi}$ and $\boldsymbol{\eta}$ containing fields of the basic equations and defined in C where C is the cross-section for $D = 1$ and the thickness for $D = 2$. The Hermitean conjugate operators in the adjoint linear problem $(\underline{\underline{S}}^{R\dagger}\partial_t + \underline{\underline{L}}^{R\dagger})e^{-i(k\cdot r_\parallel - \omega t)}\boldsymbol{f}^{\dagger R}(k, r_\perp) = 0$ are defined with respect to this scalar product.

Inserting (7.11) and (7.4) into (7.14) gives $\langle\Gamma\rangle = \langle\Gamma\Gamma\rangle = \langle\Gamma^*\Gamma^*\rangle = 0$ and the noise strength [120]

$$\langle\Gamma^*(k,t)\Gamma(k',t')\rangle = Q^R(k)(2\pi)^{-D}\delta(k-k')\delta(t-t'), \tag{7.16}$$

$$Q^R(k) = \frac{1}{C}\frac{[\boldsymbol{f}^{\dagger R}, \underline{\underline{Q}}(ik, \nabla_\perp, r_\perp)\boldsymbol{f}^{\dagger R}]}{|[\boldsymbol{f}^{\dagger R}, \underline{\underline{S}}^R(ik, \nabla_\perp, r_\perp)\boldsymbol{f}^R]|^2}. \tag{7.17}$$

The noise-correlation matrix of the basic equations, defined (in real space) as $\langle\boldsymbol{\xi}(\boldsymbol{r},t)\boldsymbol{\xi}(\boldsymbol{r'},t')\rangle = \underline{\underline{Q}}(\boldsymbol{\nabla}, \boldsymbol{r})\delta(\boldsymbol{r}-\boldsymbol{r'})\delta(t-t')$, is given by

$$\underline{\underline{Q}}(\boldsymbol{\nabla}, r_\perp) = k_B \underline{\underline{D}}(\underline{\underline{M}} + \underline{\underline{M}}^T)\underline{\underline{D}}^\dagger. \tag{7.18}$$

where $\underline{\underline{D}}^\dagger$ is the Hermitean conjugate of $\underline{\underline{D}}$ with respect to the scalar product (7.15). The intensity of stationary fluctuations of the modal amplitudes resulting from Equation (7.13) with (7.16) is

$$\langle|\psi(k)|^2\rangle = \frac{Q^R(k)}{2(2\pi)^D \mathrm{Re}(-\lambda)}. \tag{7.19}$$

The above eqations are valid in the linear regime and in particular for any k and $\epsilon \le \epsilon_{NL} < 0$ (for all practical purposes $\epsilon_{NL} \approx 0$, see [118]). Now I specialize to the vicinity of the threshold and consider only contributions near $\pm k_c$ since the stationary mode fluctuations (7.19) are large only in these regions. Expanding the linear modal growth rate $\lambda(\epsilon, k)$ to lowest nontrivial order around threshold and evaluating the

stochastic terms at threshold one obtains from (7.13) the main result of this section, the amplitude equation in real space,

$$\begin{aligned} \tau_0(\partial_t + v_g \cdot \nabla_\parallel)A(r_\parallel,t) &= (\epsilon + \xi_{ij}\nabla_{\parallel i}\nabla_{\parallel j})A(r_\parallel,t) \\ &+ \tau_0\sqrt{Q}\ \eta(r_\parallel,t), \qquad (7.20) \\ Q &= Q^{R_c}(k_c). \qquad (7.21) \end{aligned}$$

The amplitude $A(r_\parallel,t)$ is defined by its Fourier tansform, $A(q,t) = \psi(k_c+q,t)$. The deterministic coefficients $\tau_0^{-1} = \partial_\epsilon\lambda$, $v_g = \nabla_k\omega$ and $\xi_{ij} = -\frac{\tau_0}{2}\partial_{k_i}\partial_{k_j}\lambda$ (τ_0, ξ_{ij} in general complex) come from the expansion of $\lambda(\epsilon, k_c - i\nabla_\parallel) + i\omega_c$ to lowest nontrivial order around threshold and $\eta(r_\parallel,t)$ is a complex Gaussian noise source with $\langle\eta\eta\rangle = \langle\eta^*\eta^*\rangle = 0$ and $<\eta^*(r_\parallel,t)\ \ \eta(r'_\parallel,t')>= \delta(r_\parallel - r'_\parallel)\delta(t-t')$.

An example of the resulting equal-time correlations $<A^*(r_\parallel + \Delta r_\parallel,t)A(r_\parallel,t)>$- $= \int d^D r_\parallel e^{iq\Delta r_\parallel} Q/(2(2\pi)^D \mathrm{Re}\lambda)$ for 1D with $r_\parallel = x$ and real coefficients is

$$\langle A^*(x+\Delta x,t)A(x,t)\rangle = \frac{Q\tau_0 e^{-\left|\frac{\Delta x\sqrt{-\epsilon}}{\xi_0}\right|}}{8\xi_0\sqrt{-\epsilon}}. \qquad (7.22)$$

Since (7.20) is an inhomogeneous equation, the precise connection with the physical quantities is essential. We get from (7.12) near threshold

$$\boldsymbol{u}(\boldsymbol{r},t) = A(r_\parallel,t)\boldsymbol{f}(r_\perp)e^{i(k_c\cdot r_\parallel - \omega_c t)} + \text{c.c.} + \text{h.o.t.} \qquad (7.23)$$

Now I discuss some generalizations.

For discretely degenerated bifurcations, e.g., zig and zag rolls $(\omega_c, k_{cx}, k_{cy}) = (0, k_{cx}, \pm k_{cy})$ in EHC in the oblique-roll regime[48], left and right travelling waves $(\pm\omega_c, k_{cx}, 0)$ in EHC in thin and clean cells [97] or in 1D-RBC in binary mixtures and other sytems, or both degeneracies [30], there are amplitude equations of the form (7.20) for each set $\pm k_c$ of modes around the critical k vectors. They are independent in the linear regime if the different (ω_c, k_c) values are sufficiently separated.

For isotropic systems e.g., RBC in isotropic fluids, EHC or RBC in homeotropically aligned EHC (see e.g., [23]) or optical vortices in large-aperture class A lasers [128] λ is of the form $\lambda = \lambda(\boldsymbol{k}^2, \epsilon)$. Inverse Fourier transform of (7.13) and substituting for the growth rate a generic isotropic expression approximating λ near threshold to $\mathcal{O}(k^2 - k_c^2)^2$ and $\mathcal{O}(\epsilon)$, gives with the same approximations as above the stochastic Swift-Hohenberg (SSH) equation

$$\tau_0\partial_t\psi(\boldsymbol{r}_\parallel,t) = \left(\epsilon - \tilde{\xi}_0^4(k_c^2 + \nabla_\parallel^2)^2\right)\psi + \tau_0\sqrt{Q}\eta(\boldsymbol{r}_\parallel,t), \qquad (7.24)$$

where $\tilde{\xi}_0^4 = -\frac{\tau_0}{2}\partial^2\lambda(k^2)/\partial(k^2)^2|_{k=k_c}$. The amplitude ψ, defined as the inverse spatial Fourier transform of $\psi(k,t)$, is related to the physical quantities in the case of stationary bifurcations by

$$\boldsymbol{u} = \psi(\boldsymbol{r}_\parallel,t)\boldsymbol{f}(r_\perp) + \text{h.o.t.} \qquad (7.25)$$

and its modes in k space have the fluctuation intensity (7.19). In contrast to the difficulties with the deterministic version of this equation in the weakly nonlinear regime (see e.g., [9]) it should be correct in describing subcritical fluctuations.

Nonautonomous systems with a periodic driving force like AC-driven EHC can be reduced (using the Floquet theorem and a discrete Fourier transformation in time) to an infinite set of autonomous equations for the components of $\boldsymbol{u}$ proportional to $e^{\pm in\omega_0 t}$, with the external driving frequency ω_0 and integer n [120]. Truncating at some $n = n_{max}$ gives an effectively autonomous system.

Note that expression (7.21) is valid for both the amplitude and the SSH equations and for any boundary conditions (BC) including lateral through flow. The actual value of Q changes because the eigenfunctions (and eventually $\underline{\underline{S}}$) depend on the BC and on the through flow. As shown in the next section, the fluctuations of the physical quantities, obtained from the amplitude fluctuations with (7.23) or (7.25), do not depend on the normalizations of $\boldsymbol{f}$ or $\boldsymbol{f}^\dagger$. They are, as equilibrium fluctuations calculated with the equipartition theorem, inversely proportional to the thickness (D=2) or to the cross section (D=1).

7.4 Theoretical results

At first I show how the method works by applying it to RBC in isotropic fluids, a pattern-forming system with one of the simplest basic equations. Then I calculate fluctuations of axisymmetric vortices in TCF, an example for an 1D system with curvilinear geometry and a nontrivial basic flow leading to an explicit $r_\perp$ dependence in the linearized basic equations. Finally I calculate the stochastic term of the anisotropic amplitude equation of quasi two-dimensional planar EHC. Here the basic equations are far more complex and depend (due to the periodic driving) explicitely on time. The calculations are rather lengthy but as straightforward as in the other systems.

7.4.1 Rayleigh–Bénard convection

We consider both a quasi two-dimensional system with a thickness d, $r_\parallel = (x, y)$, $r_\perp = z$, and an 1D system with a rectangular cross-section $L_y d$, $r_\perp = (x, y)$ and $r_\parallel = x$ where L_y and d are of the same order and so small that the unstable mode branch $\boldsymbol{f}^R(k, r_\perp)$ is well separated from the branches of other perpendicular modes. As order-parameter equations one can take for the 2D system the SSH equation (7.24) which has in this classical case real coefficients, and for the 1D system the amplitude equation (7.20), which specializes without through flow to

$$\tau_0 \partial_t A = (\epsilon + \xi_0^2 \partial_x^2) A + \tau_0 \sqrt{Q} \eta(r_\parallel, t). \tag{7.26}$$

If the one-dimensional system has periodic BC in the y direction then τ_0 and Q are the same and ξ_0 is related to the SSH length $\tilde{\xi}_0$ by $\xi_0^2 = 4k_c^2\tilde{\xi}_0^4$. The coefficients can be written as integrals of the eigenfunctions over the cross section [9] and depend via the eigenfunctions on the BC. The basic equations (7.9) are the Navier-Stokes, heat balance and continuity equations for the deviations $(\boldsymbol{v}, \theta, p)$ of the velocity, temperature and pressure from the unstructured state $(\boldsymbol{v}_0, T, p_0)$ [9], where $\boldsymbol{v}_0 = 0$ without through flow.

The heat balance equation, written in terms of the temperature deviation, couples only to v_z and has the same stochastic term as in Example 2 in Section 2 above. By applying twice the curl operation on the Navier-Stokes equations and taking the z component an equation for v_z is obtained (see Eq (A.4) in [118]), which couples only to the temperature deviation and has the fluctuating force (compare with Example 1 in Section 2) $\xi_z = [\boldsymbol{\nabla} \times (\boldsymbol{\nabla} \times \boldsymbol{\xi}^{(v)})]_z = [\boldsymbol{\nabla} \times (\boldsymbol{\nabla} \times \boldsymbol{\nabla}\underline{\underline{\tilde{\sigma}}})]_z$.

We gather the ingredients $\underline{\underline{D}}, \underline{\underline{M}}$ and $\underline{\underline{D}}^\dagger$ of the noise-correlation matrix. For incompressible isotropic fluids the dissipative transport coefficients in (7.8) reduce to $\eta_{ij,kl} = \nu\rho_m(\delta_{ik}\delta_{jl} + \delta_{il}\delta_{jk})$, $\eta^{(n)}_{ij,kl} = 0$ and $\lambda_{ik} = c_v\rho_m\kappa\delta_{ik}$ where ν is the kinematic viscosity, κ the heat diffusion coefficient and c_v the specific heat per mass. The components of the Onsager matrix are $M^{(vv)}_{ij,kl} = T\nu\rho_m(\delta_{ik}\delta_{jl} + \delta_{il}\delta_{jk})$ for the velocity equations, $M^{(th,th)}_{ij} = c_v\rho_m T^2\kappa\delta_{ij}$ for the temperature balance, and zero for the mixed components. Writing ξ_z as $D^{(vv)}_{jk}\tilde{\sigma}_{jk}$ with $D^{(vv)}_{jk} = (\partial_z\partial_k - \delta_{3k}\boldsymbol{\nabla}^2)\partial_j = -D^{(vv)\dagger}_{jk}$ (all indices run from 1 to 3) and $D^{(th,th)} = -\boldsymbol{\nabla} = -\boldsymbol{D}^{(th,th)\dagger}$ from example 2 one gets $O^{(vv)} = -2k_BT\nu\rho_m(\partial_x^2 + \partial_y^2)\boldsymbol{\nabla}^4$, $O^{(th,th)} = -2k_BT^2\kappa c_v\rho_m\boldsymbol{\nabla}^2$, and zero for the two nondiagonal elements. To calculate the Hermitean conjugates I used the fact that $\boldsymbol{v}$ and θ vanish at the boundaries.

It is convenient to scale space by d, time by d^2/η and temperature by $P\Delta T/R$ with the Prandtl number $P = \eta/\kappa$ and the Rayleigh number $R = \Delta T g\alpha d^3/(\kappa\nu)$ where α is the heat expansion coefficient and $g = 9.81\text{ms}^-2$. Choosing $\boldsymbol{k}_c = k_c\hat{\boldsymbol{x}}$ and inserting in (7.21) the noise-correlation matrix $\underline{\underline{Q}}$ and the time-derivative coefficients $S^{(vv)} = -\boldsymbol{\nabla}^2$, $S^{(th,th)} = P$ and $S^{(th,v)} = S^{(v,th)} = 0$ gives the noise intensity of both the nondimensionalized SSH and amplitude equations,

$$\begin{aligned} Q^{(R)} &= 2Q_0^{(R)} \\ &\times \frac{\int_{C'} d^{3-D}r_\perp \{f_z^{\dagger *}(k_c^2 - \partial_y^2)(k_c^2 - \nabla_\perp^2)^2 f_z^\dagger + \alpha^{(R)} f_\theta^{\dagger *}(k_c^2 - \nabla_\perp^2) f_\theta^\dagger\}}{|\int_{C'} d^{3-D}r_\perp \{f_z^{\dagger *}(k_c^2 - \nabla_\perp^2) f_z + P f_\theta^{\dagger *} f_\theta\}|^2}, \end{aligned} \tag{7.27}$$

with the (small) parameter

$$Q_0^{(R)} = \frac{k_BT}{\rho_m d\nu^2}. \tag{7.28}$$

The integrals go over the scaled cross section C' ($C' = 1$ for 2D, L_y/d for 1D and L_xL_y/d^2 for one Fourier mode) and f_z and f_θ denote the v_z and θ components of the eigenfunction at threshold. The relative contribution of the temperature fluctuations

turns out to be negligible for usual fluids [117, 118], but an analog will be essential in Taylor–Couette flow, so I will keep it.

If one multiplies equation (7.27) by a scalar product of any of the nonzero eigenfunction components f_z, f_x and f_θ (f_z and f_θ can be chosen real here and $iqf_x = -\partial_z f_z$) then the right-hand sides of the resulting equations are manifestly independent of the normalizations. Furthermore some scalar products relate the resulting equations directly to measurable effects of the fluctuations as can be seen from the left-hand sides of the following examples with (7.25) or (7.23) and $\langle\psi^*\psi\rangle$ (or $\langle A^*A\rangle$) $\propto Q$. Multiplying equation (7.27) with $([f_z, f_z] + [f_x, f_x])\rho_m C'/2$ makes its sides proportional to $\rho_m/2 \int d^{3-D}r_\perp \langle v^2\rangle$, the mean energy per length (2D) or per area (1D), contained in the velocity fluctuations (see below). Multiplying both sides with $C'[f_\theta, f_\theta]$ relates them to the cross-section integrated temperature fluctuations proportional to the shadowgraph signal as discussed in Section 5. The simplest expression is obtained by multiplying (7.27) with $[f_z, f_\theta]$, relating the sides to the relative increase $N - 1 = R_c^{-1}[f_z, f_\theta]\langle|\psi|^2\rangle$ of the heat transport due to convection (N is the Nusselt number) which is again a (globally) measurable quantity. This gives

$$[f_z, f_\theta]Q^{(R)} = \frac{2Q_0^{(R)}(1+\alpha^{(R)})}{C'\tau_0^{2(R)}}. \tag{7.29}$$

For 2D and free-slip BC (or 1D with additional periodic BC at $\pm L_y/2$ and $\partial_y = 0$), one has $\tau_0 = 2(P+1)/(3\pi^2)$ and Eq. (7.29) is (after taking care of the different scalings and relations to the physical variables) the classic result of Graham [117, 129]. For no-slip BC $\tau_0 = (P + 0.512)/19.65$ [118] and (7.29) is the result of van Beijeren and Cohen [130]. The BC and the dimensionality enter *via* τ_0 and the projection integral. In particular, cross-section integrated fluctuating quantities rather than the fluctuations themselves are independent of the transverse system size.

As an example I give for the 1D system with periodic BC and $\alpha^{(R)} = 0$ the average line energy density

$$\langle E'\rangle = \frac{\rho_m}{2}\int_C dy\; dz \langle \boldsymbol{v}^2\rangle = \rho_m \nu^2 C' \left([f_x, f_x] + [f_z, f_z]\right)\langle|A|^2\rangle \tag{7.30}$$

of the fluctuations in physical units,

$$\langle E'\rangle_{RBC} = \frac{k_B T}{4d\xi_0\sqrt{|\epsilon|}(-\lambda_0\tau_0)} \tag{7.31}$$

where $\lambda_0 = \lambda(\epsilon = -1, k = k_c)$ is the equilibrium-growth rate of the mode becoming unstable at threshold and, for no-slip BC, $\xi_0 = 0.38$ and $-\lambda_0\tau_0 = 1 + 1.93P$. In deriving (7.31) I used (7.23), the stationary fluctuations (7.22) of the scaled 1D amplitude equation, expressed f_x in terms of f_z and used (7.29) with $I_{z\theta} := [f_z, f_z]/[f_z, f_\theta]$ given below in (7.34) and an analogous integral expression for λ_0. There is an additional

factor $e^{-|x/\xi|}\cos k_c x$ with the correlation length $\xi = \xi_0/\sqrt{-\epsilon}$ for two-point equal-time velocity correlations with separation x. For 2D and near threshold the corresponding energy per area is $k_c/2$ times the line energy density (7.31) [131].

Equation (7.31) states that in 1D the mean kinetic energy of velocity fluctuations in a volume with unscaled cross section C and twice the unscaled correlation length ξd is $\frac{1}{2}k_BT(\tau_0|\lambda_0|\epsilon)^{-1}$. In 2D the corresponding volume is d times the area $(\xi d)(4\lambda_{roll}/\pi)$ with $\lambda_{roll} = \pi/k_c$. This appears, especially for $P \to 0$ ($\lambda_0\tau_0 \to -1$), similar to equipartition-theorem fluctuations. Indeed, calculating the average energy of velocity fluctuations contained in one Fourier-mode pair with (7.19) and (7.16) gives, for arbitrary vertical BC and Prandtl numbers and periodic BC in x and y,

$$\frac{\rho_m}{2}\int_V d^3r\langle(|\boldsymbol{v}_k|^2 + |\boldsymbol{v}_{-k}|^2)\rangle = \frac{k_BT}{|\epsilon|}\begin{cases} 1 & P = 0 \text{ or } \epsilon = -1, \\ (|\lambda_0|\tau_0)^{-1} & \epsilon \to 0_-, \end{cases} \tag{7.32}$$

where V is the volume of the system. Without temperature gradient ($\epsilon = -1$) the kinetic energy contained in these fluctuations fulfills the equipartition theorem (two physical degrees of freedom per wave-vector pair). For zero Prandtl number the fluctuations increase like $-1/\epsilon$ if a temperature gradient is applied.

7.4.2 Taylor–Couette flow

The system consists of two concentric cylinders of inner and outer radii R_1 and R_2, rotating at angular frequencies Ω_1 and Ω_2, respectively. We scale lengths and time as in RBC, where d is now the gap width $R_2 - R_1$, and take as control parameter the dimensionless inner rotation $\omega_1 = \Omega_1 d^2/\nu$. The outer rotation $\omega_2 = \Omega_2 d^2/\nu$ and the radius ratio $\eta = R_1/R_2$ are fixed parameters. The system is effectively one-dimensional and described best in cylindrical coordinates $r_\parallel = z$ and $r_\perp = (r, \phi)$. In a range of the control parameters where the first instability of the basic Couette flow leads to axisymmetric vortices [9], the amplitude equation for $A(z,t)$ without through flow is the same as Eq. (7.26) for 1D-RBC. With axial through flow there is an additional group velocity term $v_g\partial_x A$ where v_g is 1.23 times the mean axial velocity of the through flow (1.05 times the phase velocity of the vortices) and furthermore the other coefficients have very small imaginary parts [132].

The only noise source in the basic equations [73] comes from the stress tensor in the Navier-Stokes equations for the deviations of the velocity from the basic Couette flow. In cylindrical coordinates one gets (the indices take the values r, ϕ, and z) $(\boldsymbol{\nabla}\underline{\sigma})_i = D^{(vv)}_{i,jk}\sigma_{jk}$ with $D^{(vv)}_{ij,k} = (\delta_{ik}r^{-1}\partial_j r + r^{-1}\delta_{k2}(\delta_{i2}\delta_{j1} - \delta_{i1}\delta_{j2}))$. The Hermitean conjugates with respect to (7.15) are $D^{\dagger(vv)}_{jk,i} = -\delta_{ik}\partial_j + r^{-1}\delta_{k2}(\delta_{i2}\delta_{j1} - \delta_{i1}\delta_{j2})$. A straightforward calculation of Eq. (7.21) gives an expression for the noise strength of the TCF amplitude equation which is similar to (7.27). Instead of writing it down (see [121, 122]) I use the fact that for $\omega_2 > 0$ the Taylor system can be mapped onto

RBC to second order in the gap width $1-\eta$ yielding explicit analytic expressions in terms of RBC parameters [122]. The resulting noise intensity of the amplitude equation is

$$[f_r, f_r]Q^{(T)}(\omega_2, \eta) \approx \frac{Q_0^{(R)}(1+\alpha^{(T)})I_{z\theta}}{\pi\overline{r}\tau_0^{2(R)}|_{P=1}}, \tag{7.33}$$

where

$$I_{z\theta} = \frac{[f_z, f_z]}{[f_z, f_\theta]} = \frac{k_c^2[f_z, f_z]}{[f_z, (k_c^2 - \partial_z^2)^2 f_z]}, \tag{7.34}$$

$$\alpha^{(T)} = \frac{4\omega^2(\overline{r})}{R_c}, \qquad \overline{r} = \frac{R_1 + R_2}{2d}. \tag{7.35}$$

The radial eigenfunction f_r corresponds to f_z in the RBC system and $\omega(\overline{r})$ denotes the squared dimensionless angular velocity of the basic Couette-flow $\omega(\overline{r})$ [73] in the middle of the gap. For no-slip BC ($R_c = 1708$, $\tau_0^{(R)} = 0.077$, $I_{z\theta} = 0.013$) the error with respect to a calculation of (7.21) using numerically obtained eigenfunctions [121] is less than 2.5% for $\eta = 0.738$ and all $\omega_2 \geq 0$ [122]. Smaller gaps (larger η) should make the approximation even better since the mapping onto RBC gets exact for $\eta \to 1$.

Eqation (7.33) states that, if one relates the amplitude to v_r in TCF and to v_z in RBC, the noise strength of the amplitude equation for axisymmetric TCF vortices is $(1+\alpha^{(T)})/(1+\alpha^{(R)}) \approx (1+\alpha^{(T)})$ times the noise strength of 1D-RBC with $P = 1$, a width $2\pi\overline{r}$, and periodic BC in y. While in RBC the relative influence $\alpha^{(R)}$ of the temperature fluctuations is negligible, the relative influence $\alpha^{(T)}$ of v_ϕ fluctuations on fluctuations of the axisymmetric Taylor vortices dominates for large corotation rates ω_2. Velocity fluctuations, integrated over the respective cross sections, should be comparable in both systems if they are at the same (small, negative) distance ϵ from threshold [133]. For the mean line energy $\langle E' \rangle_{TCF} = \frac{\rho_m}{2} \int_C r \; dr d\phi \langle v_r^2 + v_z^2 \rangle^{(T)}$, contained in the fluctuations of the velocity components v_r and v_z which correspond to v_z and v_x in RBC, one obtains

$$\langle E' \rangle_{TCF} = \frac{k_B T}{(4d\xi_0\sqrt{|\epsilon|})} \frac{(1+\alpha^{(T)})}{(-\lambda_0^{(R)}\tau_0^{(R)})} \left(\frac{\tau_0^{(T)}}{\tau_0^{(R)}}\right). \tag{7.36}$$

With $\tau_0^{(T)}/\tau_0^{(R)} = \xi_0^2/\xi_0^{2(R)}$ (Ref. [122]) the mean energy per length is effectively $(1+\alpha^{(T)})(\tau_0^{(T)}/\tau_0^{(R)})^{1/2}$ times the RBC line energy density which is $\langle E' \rangle_{RBC} = 0.225 k_B T/(d\sqrt{|\epsilon|})$ for no-slip BC.

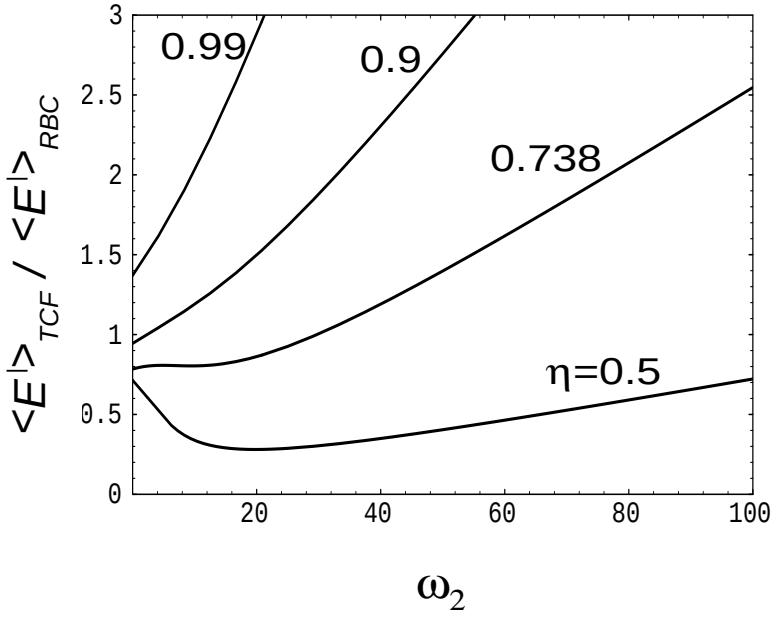

FIGURE 7.1. Average line energy contained in the fluctuations of the radial and axial velocity components of axisymmetric Taylor vortices with realistic no-slip BC. The plot shows the enhancement factor $(1+\alpha^{(T)})(\tau_0^{(T)}/\tau_0^{(R)})^{1/2}$ of the line energy density with respect to that of the equivalent one-dimensional Rayleigh–Bénard system with Prandtl number $P=1$ and the same distance ϵ from threshold. The hoerizontal axis is the dimensionless corotation $\omega_2 = \Omega_2 d^2 \rho_m/\nu$ of the outer cylinder. Parameter is the radius ratio η.

Figure 7.1 shows a plot of this enhancement factor for various outer corotation rates ω_2 and radius ratii η. For the outer cylinder at rest ($\omega_2 = 0$) and a radius ratio $\eta = 0.738$ as in [121], the line energy is nearly the same as for RBC with $P = 1$ (factor 0.94). Without external stress ($\omega_1 = \omega_2 = \alpha^{(T)} = 0$) one recovers again equipartition-theorem results .

7.4.3 Planar electrohydrodynamic convection

The system consists of a thin liquid crystal cell (thickness d) sandwiched between two planar electrodes. The external stress is an applied AC voltage $V(t) = \sqrt{2}V_0 \cos\omega_0 t$; the control parameter is V_0^2 for fixed ω_0 and $\epsilon = V_0^2/V_c^2 - 1$. We assume planar BC $\boldsymbol{n} = (1,0,0)$ making the system anisotropic in the infinite directions and consider

a range of ω_0 and of the material parameters, where the first instability at V_c is to normal rolls $\boldsymbol{k}_c = (q_c, 0)$ (roll axis normal to equilibrium director orientation) with an essentially time independent splay-bend director mode (conductive regime) [48]. The system is quasi two dimensional. Choosing $r_\parallel = (x, y), r_\perp = z$, the amplitude equation (7.20) reduces to

$$\tau_0 \partial_t A(x, y, t) = (\epsilon + \xi_{0x}^2 \partial_x^2 + \xi_{0y}^2 \partial_y^2) A + \tau_0 \sqrt{Q} \eta(x, y, t). \tag{7.37}$$

The basic charge conservation, director, and nematic Navier–Stokes equations for the deviations $(\phi, \delta\boldsymbol{n}, \boldsymbol{v})$ of the basic state $(\sqrt{2} V_0 \frac{z}{d} \cos \omega_0 t, \boldsymbol{n}_0, 0)$ have periodic coefficients [48]. Stochastic forces come from the fluctuations of $\boldsymbol{j}^{(el)}$ in the charge equation (see example 2 at the end of Section 2), from the antisymmetric stress tensor $\sigma_{ij}^{(as)}$ in the director equation (example 3) and from both parts of σ_{ij} in the fluid equation (example 1). The noise correlation matrix $\underline{\underline{Q}}$ from equation (7.18), calculated with the anisotropic Onsager matrix (7.8) without the temperature components, is given in [120], Equation (67).

To calculate the threshold and the eigenfunctions in (7.21) I apply the lowest-order time-Fourier expansion for the conductive mode and lowest-order trial functions satisfying no-slip planar BC's for the z dependencies of all fields [120]. Furthermore I eliminate the velocities adiabatically. With lengths scaled by d and times by the director relaxation time $\tau_d = \gamma_1 d^2/(K_{11}\pi^2)$ (K_{11} is the splay elastic constant and γ_1 the rotational viscosity), a straightforward but lengthy calculation of (7.21) gives eventually for the parameter set of MBBA I [120],

$$[f_{n_z}, f_{n_z}]Q = \frac{2Q_0^{(E)}|\lambda_0|}{C'K} \left(\frac{1 + \alpha^{(E)}}{(\tau_0 \lambda_0)^2} + O(\frac{\omega_0}{\omega_{cutoff}})^2 \right), \tag{7.38}$$

where $|\lambda_0|/K = 1.84$, $\alpha^{(E)} = 14.9 P_1$, $|\lambda_0|\tau_0 = 1 + 9.3 P_1$ and $P_1 = \tau_{el}/\tau_d \approx 2.81(\mu m/d)^2$. The left-hand side of (7.38) is proportional to the fluctuations of n_z, a quantity which is related to the fluctuations of light modulations in the shadowgraph method, see Section 5.

The quantity $|\lambda_0|/K$ with $K = [f_{n_z}, (K_{33}q^2/K_{11} - \partial_z^2) f_{n_z}]/[f_{n_z}, f_{n_z}]$ is the ratio of the energy dissipation rate to the elastic energy of the fluctuating mode. The ratio P_1 of the time scales $\tau_{el} = \epsilon_0 \epsilon_\perp / \sigma_\perp$ and τ_d of the electric and director subsystems is the analog of the Prandtl number in RBC. The relative contribution $\alpha^{(E)}$ of the charge fluctuations is the analog of the temperature fluctuations in RBC and the v_ϕ fluctuations in TCF. Since both, $\alpha^{(E)}$ and P_1, are proportional to d^{-2}, charge fluctuations become important for thin cells. In principle there is a second time-scale ratio $d^2 \rho_m/(\nu \tau_d)$ of the time scales of the fluid and director subsystems but it turns out to be negligibly small ($\approx 10^{-6}$). This justifies the adiabatic elimination of the velocities and implies that the velocity fluctuations, which play the main role in RBC, are negligible here.

The prefactor

$$Q_0^{(E)} = \frac{k_B T}{K_{11} d} \approx 10^{-3} \frac{\mu\mathrm{m}}{d} \tag{7.39}$$

is much larger than in RBC or TCF making EHC the best candidate for quantitative fluctuation measurements.

As in the other systems one can calculate the mean line and area densities of the orientational-elastic energy contained in the fluctuations of the splay-bend director modes. Although typical EHC systems have large aspect ratios and are quasi two dimensional, the line energy density $\langle E' \rangle_{EHC} = \frac{1}{2} \int_C dy\, dz \{K_{11}(\partial_z n_z)^2 + K_{33}(\partial_x n_z)^2\} = \frac{1}{2} K_{11} K C'[f_{n_z}, f_{n_z}] \langle |A|^2 \rangle$ (proportional to the integrated director fluctuations) makes sense if interpreted as energy contained in all Fourier modes with $k_y = 0$. Indeed it is this quantity which was measured in the experiments of reference [97] as described in the next section. With the 1D version of (7.37), (7.38) and (7.22) one obtains

$$\langle E' \rangle_{EHC} = \frac{k_B T}{4 \xi_0 d \sqrt{|\epsilon|}} \beta \tag{7.40}$$

with

$$\beta = \frac{1 + \alpha^{(E)}}{|\lambda_0| \tau_0}, \tag{7.41}$$

remarkably similar to (7.31) and (7.36) although the energy itself is quite different in nature, here an elastic energy while in RBC and TCF a kinetic energy.

There is no simple expression for the energy per area in the 2D system [134]. Very near to the Lifshitz point where the correlation length ξ_{0y} vanishes [48], dimensional arguments lead to an $|\epsilon|^{-1/4}$ behavior (for the 1D case a crossover from $|\epsilon|^{-1/2}$ to $|\epsilon|^{-3/4}$ is predicted [120]).

Finally one can again compare the mean orientational-elastic energy of the critical (discrete) Fourier-mode pair with the equipartition theorem. With (7.19) and the 0D version of (7.38) for a volume $V = L_x L_y d$ and periodic BC in x and y one obtains near threshold

$$\langle E_{k_c}^{(E)} + E_{-k_c}^{(E)} \rangle = \frac{k_B T}{|\epsilon|} \beta. \tag{7.42}$$

The factor β comes from the electric degrees of freedom, both stochastic (relative influence of charge fluctuations $\propto \alpha^{(E)}$) and deterministic ($\lambda_0 \tau_0 \neq -1$ due to two comparable time scales). The relative influence $\beta - 1$ of the electric degrees of freedom onto the director fluctuations vanishes for $P_1 = 0$, i.e., if the electric variables can be adiabatically eliminated. A more general calculation for $\boldsymbol{k} \neq \boldsymbol{k}_c$ and $0 > \epsilon \geq -1$ with (7.17) shows that $\beta(\boldsymbol{k}, P_1, \epsilon \to -1) \to 1$, i.e., without external stress the equipartition-theorem result is recovered.

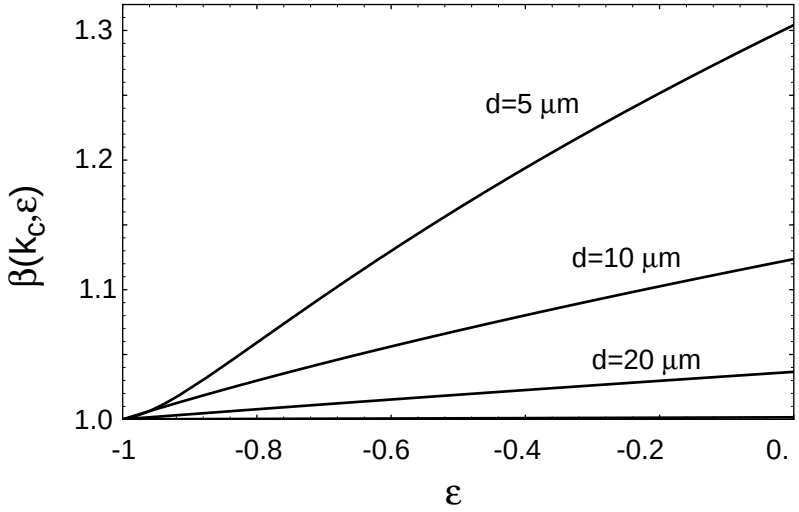

FIGURE 7.2. Influence of the electric degrees of freedom (charge fluctuations and change of the relaxation time) on director fluctuations of EHC for external frequencies much smaller than the cutoff frequency and relatively small charge relaxation times. The plot shows the enhancement factor $\beta(k_c, \epsilon)$ for the energy of the critical splay-bend Fourier mode with respect to $k_B T/(2|\epsilon|)$ which would be obtained by adiabatically eliminating the charge and neglecting charge fluctuations. The horizontal axis denotes the reduced control parameter where $\epsilon = -1$ (no external stress) corresponds to an equilibrium system. Parameter is the cell thickness $d \propto (\tau_d/\tau_q)^{1/2}$. For $\epsilon \to 0$, β is given by Eq. (7.41).

Figure 7.2 shows a plot of the enhancement factor $\beta(k_c, \epsilon)$ as a function of ϵ for some values of the cell thickness ($P_1 \propto d^{-2}$).

Note that even for negligible charge fluctuations the conductivity and thus the nonequilibrium property is essential since it influences the relaxation time. Without electric conductivity, but leaving the other MBBA parameters unchanged, the stabilizing effect of the negative dielectric anisotropy would lead to decreased instead of enhanced fluctuations for increasing V_0.

7.5 Experimental results

A common difficulty in measuring thermal fluctuations in pattern-forming system is their small magnitude, expressed by the prefactors $Q_0^{(R)}$ and $Q_0^{(E)}$. To measure the fluctuations directly, one needs a system with a favourable Q_0 and as little imperfections as possible, to be able to go very near threshold.

Both $Q_0^{(R)}$ and $Q_0^{(E)}$ can be increased by decreasing the thickness and $Q_0^{(R)}$ also by decreasing ρ_m making gasses (ν comparable with fluids) the favourable RBC system. A lower limit for the thickness in RBC is set by the temperature difference $\propto \nu/d^3$ needed to reach the threshold together with the requirement that there is no freezing at the top and boiling at the bottom. In EHC the critical voltage of the conductive mode is independent of the thickness (at least as long as the ratio of the charge relaxation time to the director relaxation time, $P_1 \propto d^{-2}$, is much smaller than unity [48]) and the limiting factor for d is electric breakthrough. In addition, for small d the director relaxation time becomes comparable with τ_q, a regime which is not yet investigated systematically.

In general the conditions for EHC are more favourable than in the RB systems. So up to very recently EHC was the only system where thermal fluctuations could be measured directly [97, 135, 113]. In reference [97] director fluctuations of a thin ($d = 13$ μm) cell of MBBA with an aspect ratio of about 1000 (quasi-2D) were determined with the shadowgraph method [39], i.e., by measuring intensity modulations of transmitted light. This method uses the dependence of the refractive index on the director orientation. For small fluctuations around the equilibrium alignment $\boldsymbol{n}_0 = (1, 0, 0)$, the light modulations $\tilde{I}(x, y, t) = I(x, y, t)/I_0 - 1$ are proportional to the z integrated director bend, $\tilde{I} = -\delta_{EHC}\partial_x \overline{n}_z$ with $\overline{n}_z(x, y, t) = \int dz n_z(\boldsymbol{r}, t)$ and known shadowgraph sensitivity δ_{EHC} [39, 136]. If one normalizes f_{n_z} to $\int dz f_{n_z} = 1$, the theoretically calculated structure function $S(\Delta x, \Delta y, \Delta t) := \langle \tilde{I}(x + \Delta x, y + \Delta y, t + \Delta t)\tilde{I}(x, y, t)\rangle$ is related to the correlations of the amplitude fluctuations in the case of stationary normal rolls by

$$\begin{aligned} S(\Delta x, \Delta y, \Delta t) &= 2q_c^2\delta_{EHC}^2\langle A^*(x, y, t)A(x + \Delta x, y + \Delta y, t + \Delta t)\rangle \\ &\quad \cos q_c\Delta x. \end{aligned} \tag{7.43}$$

The photodetector integrated in y over a length $L_y = 13.4d$, which is larger than the actual correlation length in y for typical ϵ values. So it measured in this direction effectively the discrete Fourier component at $k_y = 0$, $\tilde{I}(x, t) = L_y^{-1}\int_0^{L_y} dy\ \tilde{I}(x, y, t)$. The measured 1D-correlations $S(\Delta x, \Delta t)$ should correspond to the amplitude correlations of an 1D system with cross-section dL_y and periodic BC in y, i.e., effectively to the 1D version of (7.37) with $\partial_y = 0$ and a noise strength $Q_{1D}^{(E)} = L_y^{-1}Q_{2D}^{(E)}$.

Recall that all considerations about fluctuations in EHC in this chapter are based onto the SM. In the above system, however, one observes travelling waves above threshold and consistent with this, the observed fluctuations oscillate in time, see

Fig.4 of [97]. For all time delays the correlations were reflection symmetric in x showing that they are caused by fluctuations of right and left travelling waves in statistically equal proportions indicating a Hopf bifurcation [137].

In the simplest case this can be captured by assuming for the two waves $(\pm\omega_c, k_c, 0)$ two independent 1D-stochastic amplitude equations of the form (7.37) with group-velocity terms $\pm v_g \partial_x A$ added on their left-hand sides. The structure function then has two contributions of the form (7.43) with $\cos q_c \Delta x$ replaced by $\cos(q_c \Delta x \mp \omega_c \Delta t)$. Analytically calculated correlations of the amplitude equations [97] lead to a structure function which agrees, as function of space and time delay, very well with the measured one.

The structure function shows the predicted symmetries and the increase of fluctuation intensity and correlation lengths and times, as one approaches the threshold. The equal-time correlations (7.22) for each of the waves, $< A^*(x,t)A(x+\Delta x,t) > = \langle |A|^2 \rangle e^{-\xi|\Delta x|}$ with $\langle |A|^2 \rangle = Q/(8\tau_0 \xi_0 \sqrt{|\epsilon|})$ have the predicted correlation length $\xi = \xi_0 |\epsilon|^{-1/2}$ and an intensity $\propto |\epsilon|^{-1/2}$ consistent with the measured equal-time structure function $S(\Delta x,\, \Delta t = 0)$. The decay of $S(\Delta x = 0, \Delta t)$ with time delay is also in good agreement with the prediction. The oscillations of S have about the same wavelength and frequency as the deterministic pattern above threshold. In addition the *absolute* fluctuation intensity agrees within a factor of about 1.3 with the theoretical prediction (7.40). The measured intensity corresponds to $\beta_{exp} \approx 1.44$ while the theoretical prediction (7.41) can be taken from Fig. 7.2 yielding $\beta = 1.1$ for $d = 13\mu$m and $\epsilon = 0$.

Similar good agreement is found in [135] by measuring the shadowgraph signal in a MBBA cell with 23μm thickness. In agreement with (7.42) both the correlation time and the intensity as obtained from the Fourier-mode pair with the critical wave vector are $\propto |\epsilon|^{-1}$. The measured absolute intensity, $\beta_{exp} = 1.3$, was 30% above equipartition-theorem estimates while the theory predicts $\beta = 1.03$.

Hörner et al [113] have measured spatial correlations of fluctuations in a cell filled with the nematic Merck Phase V. For low external frequencies this material has a (deterministic) bifurcation to oblique rolls, i.e., a degenerated bifurcation to zig and zag rolls.

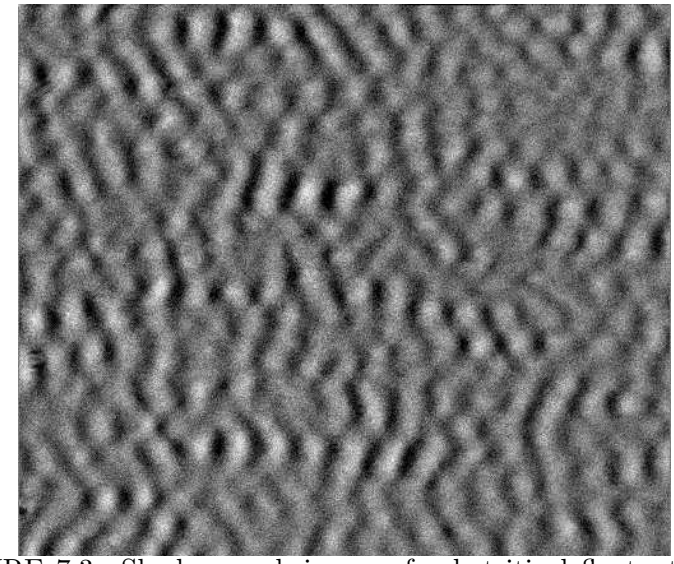

FIGURE 7.3. Shadowgraph image of subctritical fluctuations near the threshold of electroconvection of the nematic Merck Phase V in a frequency regime where there would be oblique rolls above threshold. (Courtesy of I. Rehberg and F. Hörner).

Figure 7.3 shows a snapshot of the resulting shadowgraph intensity. According to theory the equal-time structure function (spatial correlation) has now two contributions of the form (7.43) with $\cos q_c \Delta x$ replaced by $\cos(q_c \Delta x \pm p_c \Delta y)$ and the amplitude equation has the general form (7.20) with real coefficients and $v_g = 0$. The spatial Fourier transform of the theoretically calculated structure function, $S(k_x, k_y)$, has four peaks at the wave vectors $\pm \boldsymbol{k}_{zig}$ and $\pm \boldsymbol{k}_{zag}$. The structure function obtained from Fig. 7.3 shows qualitative agreement with the theoretical prediction.

Recently, fluctuations were measured directly in effectively two-dimensional RBC in gaseous CO_2 at elevated pressures [131] and in an effectively one-dimensional convection channel in a binary mixture of ethanol and water [138]. In the CO_2 experiment, $Q_0^{(R)}$ is larger than in liquids but nevertheless the measured signal required extensive processing. As in the EHC experiments, the fluctuations were measured with the shadowgraph technique. Here the refractive index depends on the density and on the temperature *via* the expansion coefficient. The shadowgraph signal for light, incident in the z direction, is $\tilde{I}(x, y, t) = -\delta_{RBC} \nabla_\perp^2 \overline{\theta}$ with $\overline{\theta} = \int dz \theta$ and known sensitivity δ_{RBC}[131]. Near threshold the relevant contributions to the fluctuating

pattern include all wave vectors with $|k| \approx k_c$. With f_θ normalized to $\int dz f_\theta = 1$, the modulation amplitude $\tilde{I} = \delta_{RBC} k_c^2 \psi$ is directly proportional to the amplitude of the stochastic Swift–Hohenberg equation and the theoretically determined structure function $S(\Delta x, \Delta y, \Delta t) = \delta_{RBC}^2 k_c^4 \langle \psi^* \psi \rangle$ is given by the amplitude correlations. The measured spatial Fourier transform of the equal-time structure function agreed well with the theoretical prediction near threshold, $S(\boldsymbol{k}) = S_0/((k - k_c)^2 + |\epsilon|)$ [131] with $S_0 = \delta_{RBC}^2 k_c^4 Q \tau_0/(2(2\pi)^2)$ from Eq. (7.19). In particular it is isotropic, large in a ring of radius k_c and the peak at k_c is proportional to $|\epsilon|^{-1}$. In real space, both the absolute intensity of the temperature fluctuations and the $|\epsilon|^{-1/2}$ behavior agreed perfectly with the theoretical prediction $\propto \int d^2k S(\boldsymbol{k})$ for high pressures where the Boussinesq approximation holds. For lower pressures the experimental values were up to 20% *smaller*.

In the experiment on binary mixtures [138], the fluctuations are observed in a parameter regime where the first instability is a Hopf bifurcation leading to travelling waves because these time–dependent patterns can be observed with a better signal–to–noise ratio than stationary ones. The fluctuation intensity shows the correct $|\epsilon|^{-1/2}$ behavior of 1D systems and the magnitude is of the same order as idealized theoretical estimates.

So far I described direct measurements. A possibility to overcome the difficulties with the small signal are indirect measurements where the fluctuations are enhanced by some amplifying mechanism prior to measurement.

The amplification mechanism can be external by applying control–parameter ramps in time going from sub- to supercritical values. As soon as the control parameter is supercritical, the small, initially subcritical, fluctuations grow exponentially until they become measurable. Measurements on RBC with this method gave the first experimental evidence of stochastic effects in pattern–forming systems [139, 140]. As in the direct measurements, the structure factor in Fourier space had a maximum along a ring with radius k_c. The intensity, however, was about a factor of 2×10^4 larger than predicted for thermal fluctuations.

Another possibility is internal amplification in space in the convectively unstable regime in systems with a nonzero group velocity [123]. Above the convective instability fluctuations are amplified as they travel through the system. If one is also above the absolute threshold, they would grow in the whole system to nonlinear saturation and eventually the system would reach a deterministic attractor. Below the absolute threshold, however, the propagation velocity of perturbations, determined by the growth rate and the spreading by diffusion, is smaller than the group velocity so that fluctuations are convected away faster than they can grow. So at least in parts of the system the fluctuations are both linear and much larger than the subcritical ones, and the resulting "noise–sustained structures" [132] can be measured. Typically systems with nonzero group velocity have a Hopf bifurcation or are open

systems, e.g., RBC or TCF with throughflow.

The Hopf bifurcation of RBC in binary–fluid mixtures with a negative separation ratio [9] was used to measure fluctuations in an quasi–1D cell [141, 138]. Theoretically this system is described by two stochastic 1D complex amplitude equations similar to the ones used in EHC above. The dissipative effect of mass diffusion leads (compare Eqs. (7.21) and (7.18)) to an additional term in the RBC fluctuation strength (7.27) which has been calculated in [119] and was found to be small [142]. The interpretation is difficult because the fluctuations described by these stochastic equations depend strongly on the boundary conditions which in the experiment correspond to ramps consisting of decreasing height on both sides of the cell. Analytic calculations with an effective cell length [141] lead to a fluctuation intensity in accordance with the experiment whereas numerical calculations taking into account more realistic BC by introducing a space dependent control parameter at each side lead to fluctuation intensities about two orders of magnitude smaller than the measured ones [143]. A possible explanation of this large discrepancy is the exponential dependence of the intensity on the assumed effective cell length in the analytic calculation together with the fact that there is no obvious way to define this length.

Things are easier to interprete in open–flow systems where there is only one travelling wave and the downstream BC is irrelevant (in the convectively unstable regime information cannot travel upwards). Numerical simulations showed that the fluctuations are even rather insensitive to the upstream BC. Even if one sets the upstream fluctuations at the inlet equal to zero, the stochastic volume force would create fluctuations which after a short distance from the inlet are nearly the same as with more realistic equilibrium fluctuations at the inlet [121]. In any case the fluctuations are amplified on their way through the system until they become measurable and eventually saturate at the "healing length". In a way the experiments in open–flow systems are the analog in space to the ramping experiments in time. In the former, time is translated to space by the group velocity. Measurements of the rms value of axial velocity fluctuations in TCF with through flow with a laser–Doppler interferometer [121] agreed with theory in all aspects except the absolute fluctuation intensity which was by a factor of 270 larger than the predicted value $\nu^2/d^2 \times [f_z, f_z] Q^{(T)} \tau_0 / (4\xi_0 \sqrt{-\epsilon})$ for thermal fluctuations.

7.6 Discussion

In this chapter I tried to provide an understanding of fluctuations near pattern–forming transitions in nonequilibrium extended systems starting from stochastic hydrodynamics, an approach formulated by Landau [68] to describe equilibrium hydrodynamic fluctuations in simple fluids. The *rationale* to extend this approach to nonequilibrium systems is that it requires only local equilibrium which is fulfilled

in many hydrodynamic systems which are far from global equilibrium. In addition the separation of scales between the microscopic and macroscopic degrees of freedom justifies the assumption that the fluctuating forces are δ correlated.

Fluctuating hydrodynamics makes definite predictions about the fluctuations as a function of the quasi–dimensionality and the distance from threshold. The correlation functions of the fluctuations oscillate as function of space and time separation with about the same period as the deterministic pattern and below threshold they retain all symmetries of the system. Correlation lengths and times, and the fluctuation intensity, increase with the proximity to the deterministic threshold, with scaling exponents which depend on the symmetries and the quasi–dimensionality. This means that the fluctuations in real space consist of patches with the size of about the correlation length, living for about one correlation time. Each patch is a wave packet of one degenerate mode out of the uniformly distributed set of critical modes. The fluctuations anticipate, in a way, the possible deterministic patterns above the primary threshold.

In 1D systems, many of these features are analogous to equilibrium fluctuations. The scaling exponents of correlation lengths, times and of the intensity are the same. In 2D, pattern–forming systems with continous degeneracy (RBC or EHC at the transition from normal to oblique rolls) offer new and fascinating symmetry classes of transitions. If only one field is dynamically active (e.g., n_z for normal rolls in EHC with $P_1 \to 0$ or v_z for RBC with $P \to 0$), the average energy contained in the fluctuations of one Fourier mode or, equivalently, the energy in a fluid element of half the size of the correlation length in 1D systems, is $|\epsilon|^{-1}$ times the equipartition–theorem fluctuations $k_B T/2$. This is again as in equilibrium, for example below the splay–bend Fréedericksz transition in planar EHC. Additional dynamically active fields lead both to new fluctuating forces summarized in the terms proportional to $\alpha^{(R)}$, $\alpha^{(T)}$ and $\alpha^{(E)}$ in Eqs. (7.29), (7.36) and (7.40) with (7.41), and to a deterministic influence on the relaxation rate, making $(-\lambda_0\tau_0)$ unequal to unity, from Sec. 4 $(-\lambda_0\tau_0) = 1 + 1.93P$ in RBC, $2.93\tau_0^{(T)}/\tau_0^{(R)}$ in TCF and $1 + 9.3\tau_{el}/\tau_d$ in EHC. The net effect on the fluctuations can be increasing as in the case of charge fluctuations in EHC, decreasing as for the temperature field in RBC, or dependent on a second control parameter as in TCF.

The above predictions agree with experiments. One sees patches of zig and zag rolls in the oblique–roll regime of EHC, areas of left and right travelling waves if there is a Hopf bifurcation, and isotropically distributed roll directions in RBC in simple fluids corresponding to a ring in k space.

The above features are predicted for *any* noise source if its correlations in space and time are much smaller than the macroscopic scales. To show that *thermal* fluctuations are involved and that stochastic hydrodynamics provides the correct thermodynamical description of nonequilibrium systems near a phase transition, the

absolute value of the fluctuation intensity must agree with the experiment. This is the case in the direct measurements of the EHC and RBC systems described above. [The fact that the measured fluctuations in the RBC experiments are up to 20% smaller for low pressures, can probably be explained by using the non–Boussinesq equations in Eqs. (7.21) and (7.18).]

An open question is the observed fluctuation intensity in the indirect experiments. In the open-flow experiment [132], the observed fluctuation intensity is more than two orders of magnitude too large; in the time-ramping experiments [139, 140] the discrepancy is even four orders of magnitude, and in the binary-mixture experiment using travelling waves as amplification mechanism [141] it is difficult to interpret. An investigation primarily aimed at describing nonlinear transient patterns in the splay Fréedericksz transition of NLCs with positive dielectric anoisotropy [144] shows that in a situation similar to the above indirect measurements (jump of the control parameter to above threshold) even in nematics the experimental noise strength is much larger than that of thermal noise. Specifically the initial (subcritical) amplitude of the homogeneous mode obtained from the experimental fit to the nematodynamic equations is about two orders of magnitude larger than predicted by Eq. (7.42). This is strikingly similar to the time-ramping experiments [139, 140] (the intensity is equal to the square of the amplitude).

All this seems to indicate that the assumption of stochastic hydrodynamics together with local equilibrium is valid only in stationary situations. However, one has to be aware that in all indirect experiments the logarithm of the noise strength rather than the noise strength itself is measured. In the time-ramping experiments, errors in determining the effective time difference from the initial subcritical fluctuations to saturation contribute exponentially. The same is true for the effective travelling length to saturation ("healing length" l_h) in the open-flow and travelling-wave experiments and, in all three indirect experiments, for the uncertainty in the distance from the convective threshold. We take as an example the TCF experiment [132] in the regime of convective instability $0 < \epsilon \leq \epsilon_a$. The fluctuation intensity is roughly $e^{2\beta z}$ times the fluctuations at the inlet $z = 0$ where the spatial growth rate β increases monotonically with ϵ and is essentially proportional to ϵ if one is not too close to the absolute threshold [121]. If one assumes at the inlet *a priori* thermal equilibrium fluctuations $\langle \overline{\theta}^2 \rangle = \gamma Q$ with known constant γ (and not larger inlet fluctuations due to additional experimental noise), the intensity at the nonlinear saturation for typical threshold distances is about nine orders of magnitude larger. The fluctuations were measured only in the region where the intensity is more than 0.01 times the saturation value, so, experimentally, the strength of the fluctuating forces is essentially inferred from the healing length l_h by $\gamma Q_{exp} = \langle \overline{\theta}^2(z=0) \rangle = e^{-2\beta l_h} \langle \overline{\theta}^2 \rangle_{sat}$. With known saturation fluctuations and assuming $\beta \propto \epsilon$, the error in the decadic logarithm of the experimental noise strength, $\Delta(\log_{10} Q_{exp})$, is $9(\Delta\epsilon/\epsilon)$ and $9(\Delta l_h/l_h)$ due to the relative errors in the threshold distance and the healing length, respectively.

A relative error of 0.22 in one of these quantities would lead to a factor of 100 in the measured noise strength. Note that β depends also on other parameters of the amplitude equation like τ_0 and ξ_0 [121], whose errors contribute similarly.

Chapter 8

Conclusion

Even if someone found the ultimate truth, he would not know. Everything is interspersed with assumptions. K. R. Popper

Now I discuss some open questions and give suggestions for future research. The main unresolved issue with the WEM is the unknown value of $\tau_{\rm rec}$ which must be rather long (of the order of 10 seconds). A direct determination of both $\tau_{\rm rec}$ and the mobilities is desirable, e.g., by measuring the transient current response to various voltage signals in cells with well-defined boundary conditions (blocking electrodes) [84, 86, 83]. Furthermore, one would like to know, at least for one material, the complete set of the SM parameters, together with measurements of the threshold (q_c, p_c, $\overline{V}_c$, ω_H), of the frequency decrease $d\omega/d\epsilon$, and of all CGL parameters.

On the theoretical side, a (numerical) weakly-nonlinear analysis of the full set of WEM equations is needed. In further steps, one could generalize the resulting two-dimensional CGL to include the coupling to the other critical modes (e.g., couplings between the amplitudes of right and left travelling rolls), and also to include couplings to slowly-relaxing modes that are excited in higher order by the nonlinearities.

As discussed in Chapter 5.6, the role of the *linear* charge-carrier modes for producing a *Hopf bifurcation* is reminiscent of the role of the concentration field for the Hopf bifurcation in binary fluid convection. There, the *nonlinearly excited* concentration modes were found to be important for the production of *pulses* [145, 146]. I expect, that coupled equations for the amplitudes of critical and slow nonlinear modes will be similar to the "extended CGL", which was derived by Riecke [146] to describe the dynamics of the pulses. Are these pulses related to the "worms" observed for low temperatures in I52 [30, 42]?

Finally, a nice feature of EHC is that the Hopf bifurcation is continuous and that one observes spatio-temporal chaos (STC) right at onset [30]. It would be fascinating to explain this in the framework of CGLs by the Benjamin–Feir instability [11] enabling quantitative experimental tests of the predictions of one of the most simple and generic equations producing STC.

Appendix A

A.1 Material parameters for MBBA and I 52

Table A.1. Material parameters for MBBA at 25°C [147, 148], and for I 52 at 30°C – 60°C [32] as used in Ref. [42]

Parameter		MBBA	I 52
Orientational elasticities in units of 10^{-12} N	K_{11} K_{22} K_{33}	6.66 4.2 8.61	18.4 * 12.65 * 23
Conductivities in units of $10^{-8}(\Omega\mathrm{m})^{-1}$	$\sigma_\perp$ σ_a	1.0 0.5	$0.28 \cdots 1.41$ & $0.073 \cdots 0.63$ & *
Dielectric permittivities in units of $\epsilon_0 = 8.8542 \times 10^{-12} \frac{As}{Vm}$	$\epsilon_\perp$ ϵ_a	5.25 -0.53	$3.01 \cdots 2.90$ & $0.056(T - 63°\mathrm{C})/(38°\mathrm{C})$
Viscosities in units of $10^{-3} \frac{Ns}{m^2}$ **	α_1 α_2 α_3 α_4 α_5 α_6	-18.1 -110.4 -1.1 82.6 77.9 -33.6	$0.1\gamma_1$ * $-0.9\gamma_1$ † $0.1\gamma_1$ * 2η $0.65\gamma_1$ †† $-0.15\gamma_1$ *
mobilities in units of $10^{-10}\mathrm{m}^2/(\mathrm{Vs})$	$\sqrt{\mu_\perp^+ \mu_\perp^-}$	1.6	$0.4 + 0.07(T - 30°\mathrm{C})/(30°\mathrm{C})$
recombination rate (1/sec)	τ_{rec}^{-1}	≈ 0.2&&	≈ 0.1&&

* Value fitted to the experimental threshold and roll-angle curves
** If not given in terms of γ_1 or η
† $\alpha_2 = \alpha_3 - \gamma_1$ †† Onsager relation $\alpha_5 = \alpha_6 - \alpha_2 - \alpha_3$
& Left value for 30°C; right value for 60°C, see Table A.2.
&& Fits of the WEM predictions to experiments

As decribed in detail in Chapter 5, the mobility parameter is fitted to the measured Hopf frequencies as function of the external frequency (in I 52 for each temperature). The recombination parameter was estimated in Chapter 6.

The rotational viscosity γ_1, the bulk viscosity $\eta = \alpha_4/2$, and $\epsilon_\perp$ where measured for I52 in Ref. [149] as function of the temperature. Interpolations to the temperatures relevant in this work are given in Table A.2 below. The conductivity as function of the temperature was measured in Ref. [30]. The anisotropy of the conductivity was fitted, for each temperature, to the measured values of $\overline{V}_c$ in the limit of small external frequencies. All viscosities with the exception of the isotropic $\alpha_4 = 2\eta$ are assumed to have the same temperature dependence as γ_1. The prefactors, in units of γ_1, were determined to fit the threshold and roll angles.

Table A.2 Temperature dependence of the material parameters of I 52

Temperature (°C)	30	35	40	45	50	60
$\epsilon_\perp(\epsilon_0)$	3.01	2.99	2.98	2.96	2.94	2.90
$\gamma_1(10^{-3}\frac{Ns}{m^2})$	207	163	130	105	87	65
$\eta = \alpha_4/2(10^{-3}\frac{Ns}{m^2})$	19.8	15.8	12.8	10.7	9.2	7.7
$\sigma_\perp(10^{-8}(\Omega\mathrm{m})^{-1})$	0.28	0.37	0.49	0.65	0.85	1.41
$\sigma_a/\sigma_\perp$	0.26	0.3	0.34	0.38	0.42	0.45

A.2 Linearization of the WEM equations for nonzero diffusivities and with respect to a nontrivial basic state

The WEM equations (3.18) and (3.19) are expressed in terms of α and D instead of $\tilde{\alpha}$ and $\tilde{D}$, where α and D are defined in the Eqs. (4.4) and (4.5). The resulting equations are linearized around a nontrivial basic state of the functional form given by Eq. (4.1). Denoting the z derivatives of the fields of the basic state with a prime ($\delta\rho_0 = \delta\phi''$), the result for the Fourier modes with wavevector $\boldsymbol{q} = (q, p)$ is given by

$$
\begin{aligned}
P_1\partial_t(\hat{\epsilon}_q\overline{\phi} \;&+\; \epsilon_a E_0 iq\overline{n}_z) \\
&= \left[-\sigma_0\hat{\sigma}_q + \sigma_0'\partial_z - 2Ds_1\hat{\sigma}_q\hat{\epsilon}_q\right]\overline{\phi} - \left[E_0\partial_z + \delta\rho_0 + \alpha^{-1}Dd_1\hat{\sigma}_q\right]\overline{\sigma} \qquad \text{(A.1)} \\
&+ \left\{-\sigma_a\sigma_0 E_0 + D\left[\alpha^{-1}d_1\sigma_a\sigma_0' + 2s_1(\sigma_a\delta\rho_0' - \hat{\sigma}_q\epsilon_a E_0)\right]\right\} iq\overline{n}_z - P_1\delta\rho_0'\overline{v}_z, \\
P_1\partial_t\overline{\sigma} = \;& \alpha\left\{-\alpha s_1\left[(E_0\hat{\epsilon}_q - \delta\rho_0')\partial_z + \delta\rho_0(\hat{\sigma}_q + \hat{\epsilon}_q + 2r\hat{\epsilon}_q)\right]\right. \\
&- d_1\left[\sigma_0\hat{\sigma}_q - \sigma_0'\partial_z + Ds_1\hat{\sigma}_q\hat{\epsilon}_q - r\sigma_0\hat{\epsilon}_q\right]\Big\}\overline{\phi} \\
&- \left[\alpha d_1(E_0\partial_z + \delta\rho_0(1-r)) + Ds_2\hat{\sigma}_q + 2r\sigma_0\right]\overline{\sigma} \\
&+ \left\{\alpha d_1\left[-\sigma_0\sigma_a E_0 + Ds_1(\sigma_a\delta\rho_0' - \hat{\sigma}_q\epsilon_a E_0) + r\sigma_0\epsilon_a E_0\right]\right. \qquad \text{(A.2)}
\end{aligned}
$$

$$+ \quad \alpha^2 s_1 E_0 \left[-\delta\rho_0\sigma_a - \epsilon_a(2\delta\rho_0(1+r) + E_0\partial_z)\right] + Ds_2\sigma_a\sigma_0'\Big\} iq\overline{n}_z - P_1\sigma_0'\overline{v}_z,$$

with the (homogeneous) BCs

$$[E_0 - \alpha^{-1}Dd_1\partial_z]\overline{\sigma} + [\sigma_0 - 2Ds_1\partial_z^2]\partial_z\overline{\phi} = 0, \tag{A.3}$$

$$[D\partial_z - \alpha E_0 d_1]\overline{\sigma} - \alpha[d_1\sigma_0 + 2\alpha s_1(\delta\rho_0 + E_0\partial_z)]\partial_z\overline{\phi} = 0. \tag{A.4}$$

The operators $\hat{\epsilon}_q$ and $\hat{\sigma}_q$ are given by Eq. (5.10). The linearized director and momentum-balance equations are given by the Eqs. (5.5) – (5.8) with the volume force $E_0\hat{\epsilon}_q\overline{\phi}$ in Eq. (5.8) replaced by $(\sqrt{2R}\cos\omega_0 t - \delta\phi_0')\hat{\epsilon}_q\overline{\phi} - \delta\rho_0\phi_0'$. The electric field is given by $E_0 = \sqrt{2R}\cos\omega_0 t - \delta\phi_0'$.

A.3 The 3 × 3 eigenvalue system of the one-mode approximation of the linearized WEM equations

Inserting the adiabatically eliminated charge density (5.20), and the velocities (5.18) and (5.19), into the Galerkin projection of the linearized WEM equations (5.4), (5.5), and (5.6) with v_x replaced by $(i\partial_z v_z - pv_y)/q$, leads to following eigenvalue system for modes $\propto e^{\lambda t}$,

$$(\lambda - \lambda_\sigma)\sigma^{(0)} + \tilde{\alpha}^2 R\sigma_a^{(\mathrm{eff})}\, iqn_z^{(0)} = 0, \tag{A.5}$$

$$-\frac{RC_z^2}{\sigma_a^{(\mathrm{eff})}\,(1+\omega'^2)}\sigma^{(0)} + (\lambda - \lambda_z)iqn_z^{(0)} + \frac{p}{q}\left(m_{zy}\partial_t - \lambda_{0z}\frac{k_{zy}}{K_{yy}}\right)qn_y^{(0)} = 0, \tag{A.6}$$

$$\frac{p}{q}\left[\frac{RC_y^2}{\sigma_a^{(\mathrm{eff})}\,(1+\omega'^2)}\right]\sigma^{(0)} + \frac{p}{q}\left[m_{yz}\partial_t - \lambda_{0y}\left(\frac{k_{zy}}{K_{yy}} + \frac{R}{R_{0y}}\right)\right] iqn_z^{(0)} + (\lambda - \lambda_{0y})qn_y^{(0)} = 0, \tag{A.7}$$

where

$$m_{zy} = -\frac{\lambda_{0z}}{K_{zz}}\left(\frac{a_2 a_2'\eta_{zy}}{\eta_{yy}\eta_z^{(\mathrm{eff})}} + \frac{\alpha_2\alpha_3 I_2}{\eta_{yy}q}\right), \quad m_{yz} = \frac{\lambda_{0}y}{\lambda_{0z}}\frac{K_{zz}}{K_{yy}}m_{zy}. \tag{A.8}$$

The growth rate λ_z of the SM for normal rolls is given by

$$\lambda_z = \lambda_{0z}\left(1 - \frac{R}{R_{0z}}\right), \tag{A.9}$$

where R_{0z} is given by Eq. (5.21) for $p = 0$.

The parameter R_{0y} is given by

$$R_{0y} = \frac{K_{yy}\eta_{yy}\eta_z^{(\mathrm{eff})}}{a_2'\sigma_a^{(\mathrm{eff})}\,\eta_{zy}}. \tag{A.10}$$

Bibliography

[1] H. Haken, *Synergetics*, Springer-Verlag, (Berlin 1978).

[2] H. Poincaré, *Les Methodes Nouvelles de la Méchanique Céleste*, Gautiers-Villars, (Paris 1892). In English: N.A.S.A. Translation TT F-450/452 (U.S. Fed. Clearinghouse, Springfield,1967).

[3] See, e.g., H. G. Schuster, *Deterministic Chaos*, Physik-Verlag, (Weinheim, Germany 1984).

[4] B. Mandelbrot, *Fractals*, Freeman, (San Francisco 1977).

[5] D. Ruelle and F. Takens, Comm. Math. Phys. **70**, 167 (1971).

[6] P. Manneville and Y. Pomeau, Phys. Lett. **75 A**, 1 (1979).

[7] M. J. Feigenbaum, Los Alamos Sci. **1**, 4 (1980).

[8] H. D. Abarbanel, R. Brown, I. Sidorowich, and L. S. Tsimring, Rev. Mod. Phys. **65**, 1331 (1993).

[9] M. C. Cross and P. C. Hohenberg, Rev. Mod. Phys. **65**(3), 851 (1993).

[10] P. Manneville, *Dissipative Structures and Weak Turbulence*, Academic Press, (NY 1990).

[11] T. Benjamin and J. Feir, J. Fluid mech. **27**, 41 (1967).

[12] Kardar, Parisi, and Zhang, Phys. Rev. Lett. **56**, 889 (1986).

[13] A. T. Bergerud, Scientific Am. **319/2** (1984).

[14] A. Gierer and H. Meinhard, Kybernetik **12**, 30 (1972).

[15] B. Mandelbrot, *Fractals in Nature*, Freeman, (San Francisco 1977).

[16] F. H. Busse, Fundamentals of thermal convection, in W. R. Peltier, editor, *Mantle convection, Plate Tectonics and Global Dynamics*, Gordon and Breach, (1989).

[17] F. Busse and C. Carrigan, Science **191**, 81 (1976).

[18] R. Kühne, Physikalische Blätter **47**, 201 (1991).

[19] L. P. Glass, P. Hunter, and A. McCulloch, *Theory of Heart*, Springer, NY, 1991. For further references see also [9].

[20] Lord Rayleigh, Proc. R. Soc. London Ser. A **93**, 148 (1916).

[21] H. Bénard, Ann. Chim. Phys. (Ser. 23) **7**, 62 (1900).

[22] J. K. Platten and J. C. Legros, *Convection in Liquids*, Springer, (NY 1984).

[23] G. Ahlers, Experiments on thermally driven convection, in L. Kramer and A. Buka, editors, *Pattern Formation in Liquid Crystals*, Springer, (NY 1995).

[24] L. Kramer and W. Pesch, Annu. Rev. Fluid Mech. **27**, 515 (1995).

[25] P. de Gennes and J. Prost, *The Physics of Liquid Crystals*, Clarendon, (Oxford 1993).

[26] J. L. Ericksen, Arch. Ration. Mech. Anal. **4**, 231 (1960).

[27] F. M. Leslie, Quart. J. Mech. Appl. Math. **19**, 357 (1966).

[28] L. M. Blinov, *Electrooptical and Magnetooptical Properties of Liquid Crystals*, John Wiley, (NY 1983).

[29] L. M. Blinov and V. G. Chigrinov, *Electrooptical Effects in Liquid Crystal Materials*, Springer, (NY 1994).

[30] M. Dennin, D. S. Cannell, and G. Ahlers, Mol. Cryst. Liq. Cryst **261**, 377 (1995).

[31] M. Dennin, *A Study in Pattern Formation: Electroconvection in Nematic Liquid Crystals*, Phd dissertation, University of Santa Barbara, (1995).

[32] M. Dennin, G. Ahlers, and D. S. Cannell, Measurement of material parameters of the nematic crystal I52, in P. Cladis and P. Palffy-Muhoray, editors, *Spatio-temporal patterns in nonequilibrium complex systems*, page 343, Addison-Wesley, (NY 1994).

[33] E. F. Carr, Mol. Cryst. Liq. Cryst. **7**, 253 (1969).

[34] W. Helfrich, J. Chem. Phys. **51**, 4092–4105 (1969).

[35] R. Williams, J. Chem. Phys **39**, 384 (1963).

[36] A. Kapustin and L. Larinova, Kristallografya **9**, 297 (1963).

[37] A. Joets and R. Ribotta, J. Phys.(Paris) **47**, 595–606 (1986).

[38] S. Kai and K. Hirakawa, Prog. Theor. Phys. Suppl. **64**, 212 (1978).

[39] I. Rehberg, S. Rasenat, M. de la Torre Juarez, W. Schöpf, F. Hörner, G. Ahlers, and H. R. Brand, Phys. Rev. Lett **67**, 596 (1991).

[40] I. Rehberg, B. L. Winkler, M. de la Torre Juarez, S. Rasenat, and W. Schöpf, Advances in Solid State Physics **29**, 35 (1989).

[41] I. Rehberg, S. Rasenat, and V. Steinberg, Phys. Rev. Lett. **62**, 756–59 (1989).

[42] M. Dennin, M. Treiber, L. Kramer, G. Ahlers, and D. Cannell, Phys. Rev. Lett. **76**, 319 (1996).

[43] I. Rehberg, F. Hörner, and G. Hartung, J. Stat. Phys. **64**, 1017 (1991).

[44] I. Rehberg, F. Hörner, L.Chiran, H. Richter, and B. Winkler, Phys. Rev. A **44**, 7885 (1991).

[45] Orsay Liquid Crystal Group, Phys. Rev. Lett. **26**, 1642 (1970).

[46] P. A. Penz and G. W. Ford, Phys. Rev. A **6**, 414 (1972).

[47] W. Zimmermann and L. Kramer, Phys. Rev. Lett. **55**, 402–5 (1985).

[48] E. Bodenschatz, W. Zimmermann, and L. Kramer, J. Phys. France **49**, 1875 (1988).

[49] L. Kramer, E. Bodenschatz, W. Pesch, W. Thom, and W. Zimmermann, Liquid Crystals **5**(2), 699–715 (1989).

[50] L. Kramer and W. Pesch, Electrohydrodynamic instabilities in nematic liquid crystals, in L. Kramer and A. Buka, editors, *Pattern Formation in Liquid Crystals*, Springer, (NY 1996).

[51] S. Chandrasekhar, *Liquid Crystals*, University Press, (Cambridge 1977).

[52] W. Zimmermann, On travelling waves in electrohydrodynamic convection in nematics, in J. M. Coron, J. Ghidaglia, and F. Helein, editors, *Nematics: Mathematical and Physical Aspects*, volume 332 of *C*, page 401, Kluwer Acad. Publishers, (Dordrecht 1991).

[53] C. W. Oseen, Trans.Far.Soc. **29**, 883 (1933); H. Zöcher, Trans.Far.Soc. **29**, 945 (1933); F.C. Frank, Disc.Far.Soc. **25**, 19 (1958).

[54] L. D. Landau and E. M. Lifshitz, *Fluid Mechanics*, Addison Wesley, (Reading, MA 1959).

[55] D. Forster, *Hydrodynamic Fluctuations, Broken Symmetry and Correlation Functions*, Benjamin, (Reading, MA 1975).

[56] P. Martin, O. Parodi, and P. Pershan, Phys. Rev. A **6**, 2401 (1972).

[57] M. Liu, Phys. Rev. Lett. **70**, 3580 (1993).

[58] H. Pleiner and H. R. Brand, Hydrodynamics and electrohydrodynamics of nematic liquid crystals, in L. Kramer and A. Buka, editors, *Pattern Formation in Liquid Crystals*, Springer, (NY 1996).

[59] K. Henjes and M. Liu, Ann. Phys. **223**, 243 (1993).

[60] For recent reviews on RBC in NLC's, see e.e. P. J. Barrat, *Liquid crystals* **4**, 3 (1989) or Ref. [23].

[61] E. Dubois-Violette, Solid State Commun. **14**, 767–71 (1974).

[62] Q. Feng, *Patterns and Instabilities of Rayleigh–Bénard Convection in Nematic Liquid Crystals*, Phd dissertation, University of Bayreuth, (1992).

[63] M. Liu, Phys. Rev. Lett. **70**, 3580 (1993).

[64] R. B. Meyer, Phys. Rev. Lett. **22**, 918 (1969); N. Madhusudana and G. Durand, J. Phys. Paris **46**, L 195 (1985).

[65] W. Decker and W. Pesch, J.Phys.II France **4**, 493 (1994).

[66] R. B. Meyer, Phys. Rev. Lett. **22**, 918 (1969); N. Madhusudana and G. Durand, J. Phys. Paris **46**, L 195 (1985). It seems that one usually measures a combination of the usual static and a dynamic flexoelectric effect with unknown ratio. Often, not even the sign of the flexoelectric coefficients is known. (H. R. Brand, private communication).

[67] L. Onsager, Phys. Rev. **37**, 405 (1931).

[68] L. D. Landau and E. M. Lifshitz, *Statistical Physics*, Pergamon, (London 1958).

[69] N. G. V. Kampen, *Stochastic processes in physics and chemistry*, North-Holland, (Amsterdam 1990).

[70] E. Dubois-Violette, G. Durand, E. Guyon, P. Manneville and P. Pieranski, *Solid State Phys.*, Edited by L. Liebert, Academic Press, 1978, Suppl. 14.

[71] S. DeGroot and P. Mazur, *Nonequilibrium thermodynamics*, Dover, (NY 1984).

[72] M. J. Stephen and J. P. Straley, Rev. Mod. Phys. **46**, 617 (1974).

[73] S. Chandrasekhar, *Hydrodynamic and Hydromagnetic Stability*, Clarendon, (Oxford 1961).

[74] O. Parodi, J. Phys.(Paris) **31**, 581 (1970).

[75] F. H. Busse and E. W. Bolton, J. Fluid mech. **146**, 115 (1984).

[76] A. Hertrich, *Elektrohydrodynamische Instabilitäten in nematischen flüssigen Kristallen mit nichttrivialen Grundzuständen*, Phd dissertation, University of Bayreuth, (1995).

[77] M. Kaiser, *Amplitudengleichungen für die elektrohydrodynamische Instabilität in nematischen Flüssigkristallen*, Phd dissertation, University of Bayreuth, (1992).

[78] Eber, private communication.

[79] L. I. Bergé, G. Ahlers, and D. S. Cannell, Phys. Rev. E **48**, 3236 (1993).

[80] R. Chang and J. Richardson, Mol. Cryst. Liq. Cryst **28**, 189 (1973).

[81] R. Turnbull, J. Phys. **D6**, 1745 (1973).

[82] N. Felici, Revue générale de l' electricité **78**, 717 (1969).

[83] G. Brière, R. Herino, and F. Mondon, Mol. Cryst. Liq. Cryst. **19**, 157 (1972).

[84] H. Naito, M. Okuda, and A. Sugimura, Phys. Rev. A **44**, 3434 (1991).

[85] H. Naito, K. Yoshida, and A. Sugimura, J. Appl. Phys **73**, 1119 (1993).

[86] A. Sugimura, et al., Phys. Rev. B **43**, 8272 (1991).

[87] D. Gennes, Comments on Solid State Physics **3**(5), 148 (1971).

[88] D. Diguet, et al., Compt. Rend. **271B**, 954 (1970).

[89] R. Zwanzig, J. Chem. Phys. **38**, 1603 (1963).

[90] P. Atten and J. Lacroix, Journ. Mec. **18**, 511 (1979).

[91] M. Treiber, unpublished.

[92] M. Treiber and L. Kramer, Mol. Cryst. Liq. Cryst **261**, 311 (1995).

[93] A. Hetrich and M. Treiber, unpublished.

[94] W. Thom, W. Zimmermann, and L. Kramer, Liq. Cryst. **4**, 309 (1989).

[95] W. Pesch, private communication.

[96] C. Oldano, Phys. Rev. Lett **56**, 1098 (1986); W. Zimmermann and L. Kramer, Phys. Rev. Lett **56**, 2566 (1986).

[97] I. Rehberg, S. Rasenat, M. de la Torre Juarez, W. Schöpf, F.H. Hörner, G. Ahlers and H. Brand, Phys. Rev. Lett **67**, 596 (1991).

[98] H. Richter, *Elektrisch induzierte Instabilitäten in homöotrop und planar angeordneten nematischen Flüssigkristallen*, Phd dissertation, University of Bayreuth, (1994).

[99] H. Lekkerkerker, J. Phys. France Lett. **38**, 277 (1977).

[100] See e.g., P. Coullet and E. A. Spiegel, SIAM J. Appl. Math **43**, 716, or (in German), M. G. Velarde and C. Normand, in *Chaos und Fraktale*, Spektrum der Wissenschaft, 1989, pp. 38.

[101] D. Hurle and E. Jakeman, J. Fluid Mech. **47**, 667 (1971).

[102] A. C. Newell and J. A. Whitehead, J. Fluid Mech. **38**, 279 (1969).

[103] M. C. Cross, Phys. Fluids **23**, 1727 (1980).

[104] A. C. Newell, T. Passot, and J. Lega, Annu. Rev. Fluid Mech. **25**, 399 (1993).

[105] S. Rasenat, G. Hartung, B. Winkler, and I. Rehberg, Exp. in Fluids **7**, 412 (1989).

[106] A. C. Newell and M. Moloney, *Nonlinear Optics*, Addison Wesley, (NY 1992).

[107] Q. Feng, W. Pesch, and L. Kramer, Phys. Rev. A **45**, 7242–56 (1992).

[108] Q. Feng, W. Decker, W. Pesch, and L. Kramer, J. Phys. France **II 2**, 1303 (1992).

[109] M. Treiber, unpublished.

[110] L. Kramer, private communication.

[111] H. Richter, A. Buka and I. Rehberg, "Convection in a Homeotropically Aligned Nematic", to be published (homeotropically aligned specimens with $\epsilon_a < 0$ behave in many respects similar to planarly aligned ones).

[112] I. Rehberg, S. Rasenat, M. de la Torre Juarez, and V. Steinberg, Phys. Rev. Lett. **61**, 2448 (1988).

[113] F. Hörner, private communication.

[114] M. Treiber, Thermal fluctuations in pattern forming instabilities, in L. Kramer and A. Buka, editors, *Pattern Formation in Liquid Crystals*, Springer, (NY 1996).

[115] H. Haken, *Light*, North-Holland, (NY 1981).

[116] V. Zaitsev and M. Shliomis, Zh. Eksp. Teor. Fiz. **59**, 1583 (1970). [Sov.Phys.-JETP **32**, 866 (1971)].

[117] R. Graham, Phys. Rev. A **10**, 1762 (1974).

[118] P. C. Hohenberg and J. B. Swift, Phys. Rev. A **46**, 4773 (1992).

[119] W. Schöpf and W. Zimmermann, Phys. Rev. E **47**, 1739 (1993).

[120] M. Treiber and L. Kramer, Phys. Rev. E **49**, 3184 (1994).

[121] J. Swift, K. Babcock, and P. Hohenberg, Physica A **204**, 625 (1994).

[122] M. Treiber, Phys. Rev. E **53**, 577 (1996).

[123] R. J. Deissler, J. Stat. Phys. **54**, 1459 (1989).

[124] C. W. Gardiner, *Handbook of Stochastic Methods*, Springer, (NY 1990).

[125] M. Treiber, *Einfluß von Fluktuationen auf feldgetriebene Übergänge in Flüssigkristallen*, Diploma thesis, University of Bayreuth, (1991).

[126] W. Schöpf and I. Rehberg, Europhys. Lett. **17**, 321 (1992).

[127] There is a misprint in [120], Eq. (65). Drop the factor of 2 on the right-hand side of $\xi_i^{(n)}$.

[128] G. Feng, J. Moloney, and A. Newell, Phys. Rev. Lett. **71**, 705 (1993).

[129] R. Graham, Phys. Rev. A **45**, 4198 (1992).

[130] H. van Beijeren, J. Stat. Phys. **53**, 77 (1988).

[131] M. Wu, G. Ahlers, and D. S. Cannell, Phys. Rev. Lett. **75**, 1743 (1995).

[132] K. L. Babcock, G. Ahlers, and D. S. Cannell, Phys. Rev. E **50**, 3670 (1994).

[133] The definition of the reduced control parameter is ambiguous. With $1+\epsilon$ proportional to the rotation ω_1 of the inner cylinder as in Ref. [121], we get for resting outer cylinder $\tau_0^{(T)} = \tau_0^{(R)}/2$ whereas with ϵ defined in terms of the Taylor number $T \propto \omega_1^2$ as $T/T_c - 1$ we have $\tau_0^{(T)} = \tau_0^{(R)}$.

[134] The expression obtained from Eq. (7.37) would even (logarithmically) diverge. This is due to the contributions at very high wave numbers where this equation is not valid.

[135] I. Rehberg, F.H. Hörner, L.Chiran, H. Richter and B.L. Winkler, Phys. Rev. A **44**, 7885 (1991).

[136] In deriving this result, geometrical optics was applied. It is valid if $\lambda_r^2/(\lambda_L L) >> 1$, where $\lambda_r = \pi/k_c$ is the size of one roll, λ_L is the wavelength of the light source and L the distance from the cell to the imaging plane.

[137] A recent generalization of the standard equations, the weak-electrolyte model, appears to explain the Hopf bifurcation in EHC, see Chapter 6, M. Treiber and L. Kramer, Mol. Cryst. Liq. Cryst. **261**, 311 (1995) and M. Dennin, M. Treiber, L. Kramer, G. Ahlers and D.S. Cannell, Phys. Rev. Lett., in Press (1996).

[138] G. Quentin and I. Rehberg, Phy. Rev. Lett. **74**, 1578 (1995).

[139] C. W. Meyer, G. Ahlers, and D. S. Cannell, Phys. Rev. Lett, **59**, 1577 (1987).

[140] C. W. Meyer, G. Ahlers, and D. S. Cannell, Phys. Rev. A **44**, 2514 (1991).

[141] W. Schöpf and I. Rehberg, J. Fluid Mech. **2717**, 235 (1994).

[142] W. Schöpf, *Theoretische und experimentelle Untersuchungen zur Konvektion in binären Flüssigkeiten*, Phd dissertation, University of Bayreuth, (1992).

[143] G. Ahlers, private communication.

[144] A. Buka and L. Kramer, Phys. Rev. A **45**, 5624 (1992).

[145] H. Riecke, Physica D **61**, 253 (1992).

[146] H. Riecke, Phys. Rev. Lett. **68**, 301 (1992).

[147] W. H. de Jeu, W. A. P. Classen, and A. M. J. Spruijt, Mol. Cryst. Liq. Cryst. **37**, 269 (1976).

[148] H. Kneppe, F. Schneider, and N. K. Sharma, J. Chem. Phys. **77**, 3203 (1982).

[149] U. Finkenzeller, T. Geelhaar, G. Weber, and L. Pohl, Liquid Crystals **19**, 123 (1992).

Acknowledgements

It is a pleasure for me to thank my advisor Professor Lorenz Kramer for providing me with many insightful ideas for my thesis work, for leaving me much freedom, and, not at the least, for having encouraged me to tackle this long-time unresolved problem. I thank him also for giving me the possibility to flee some of the grueling Bayreuth winters which I spent in Santa Barbara and Tucson.

I also would like to thank Prof. G. Ahlers in Santa Barbara and Prof. A. Newell in Tucson for their hospitality. I am also indebted to Gunther Ahlers for providing me with some experimental results prior to publication and giving me a careful overview of the experimental situation of thermal fluctuations and to Ingo Rehberg for helpful discussions.

I thank Armin Hertrich for providing me with a fortran code for the nontrivial basic state; he also showed me some tricks in using computers.

I thank M. Schmögner for showing me the ropes of the drawing program "topdraw". I was always able to get help at once, whenever I encountered a computer problem.

Special thanks to my parents Hanskarl and Christine Treiber for encouraging and supporting me in any aspect. I can not imagine better parents.